



Provided by the author(s) and University of Galway in accordance with publisher policies. Please cite the published version when available.

Title	The role of matrix properties and extrinsic loading in osteoblast-osteocyte differentiation in tissue engineered scaffolds
Author(s)	Mc Garrigle, Myles
Publication Date	2018-02-05
Item record	http://hdl.handle.net/10379/7128

Downloaded 2024-04-24T10:00:56Z

Some rights reserved. For more information, please see the item record link above.



The Role of Matrix Properties and Extrinsic Loading in Osteoblast-Osteocyte Differentiation in Tissue Engineered Scaffolds

Myles J. Mc Garrigle B.E. (2012)



A thesis submitted to the National University of Ireland as fulfilment of the requirements for the degree of Doctor of Philosophy

2017

Biomedical Engineering
College of Engineering and Informatics
National University of Ireland, Galway

Supervisor of Research: Prof. Laoise M. McNamara

Abstract

Bone tissue engineering is a promising field with the potential to generate tissue substitutes, by taking advantage of mesenchymal stem cells ability to grow and produce tissue substitutes under specific physical conditions. However, to date the development of functional tissue substitutes has been limited, due to inconsistent tissue formation. Moreover, it has not yet been possible to establish osteoblast and osteocyte networks using existing tissue engineering approaches *in vitro*, albeit that these cell networks play a vital role in bone regeneration and long term maintenance of the bone microenvironment *in vivo*. Extracellular cues from the extracellular matrix have been shown to regulate osteocyte differentiation in two dimensional (2D) environments *in vitro*. Cell-seeding strategies (e.g. seeding density, peripheral seeding or cell encapsulation), govern tissue formation on TE scaffolds, but it has not yet been established what the optimal seeding approach is to achieve the phenotypic shift from osteoblasts to osteocytes and to establish a 3D cellular network. Mechanical stimulation in the form of fluid perfusion or mechanical strain can enhance cell distribution, osteogenic differentiation, nutrient and waste transport and hence overall bone tissue formation. However, the specific mechanical cues (both matrix-derived and extrinsically applied) required for osteoblast-osteocyte differentiation have not been identified. Therefore, the objective of this PhD thesis is to develop a bone regeneration strategy that optimises cell seeding and mimics *in vivo* mechanical stimulation, in particular extracellular matrix properties, compression and fluid flow, to investigate how such stimuli regulate both osteoblast and osteocyte phenotypes within porous TE constructs.

The first study of this thesis investigated the effect of extracellular mechanical cues in a 3D environment and cell seeding density on osteoblast-osteocyte differentiation. MC3T3-E1 pre-osteoblastic cells were encapsulated at varied cell densities (0.25, 1 and 2×10^6 cells/mL) within microbial transglutaminase (mtgase) gelatin hydrogels of low (0.58 kPa) and high (1.47 kPa) matrix stiffnesses. It was found that osteocyte differentiation and the formation of an interconnected network between dendritic cells was significantly increased within low stiffness 3D matrices, when seeded at high cell densities,

compared to cells within high stiffness matrices and those in the same matrices at low cell seeding density. This osteocyte-like network was interconnected and connected with osteoblast-like cells at the matrix surface. This study showed for the first time the role of the 3D physical nature of the ECM and cell density in regulating osteocyte differentiation and the formation of an osteocyte network *in vitro*.

The second study of this thesis investigated the effect of (1) delayed osteogenic differentiation, (2) scaffold stiffness and (3) 3D scaffold porosity on cell distribution, mineralisation and the formation of an osteoblast-osteocyte network. The results of this study showed for the first time that porous gelatin-mtgase hydrogels provide a surface area for encapsulated MC3T3-E1 cells to migrate from within the 3D gel and spread over the surface, whilst also maintaining cells surrounded by a 3D matrix within a porous structure. Furthermore, after 32 days of culture, it was observed that a homogenous distribution of both osteoblasts and osteocytes was achieved with the porous scaffold. Taken together, the results of chapters 3 and 4 provided a novel *in vitro* strategy that developed porous hydrogels containing encapsulated cells, which was shown to result in homogenous distribution of osteocyte cells in 3D environments, but also osteoblast cell attachment and spreading at the surface, representative of the osteoblast-osteocyte networks within trabecular bone *in vivo*.

The third study of this thesis sought to design and fabricate a compression perfusion bioreactor system capable of applying controlled mechanical stimulation to porous TE scaffolds. The system was designed based on a previous computational study, which provided predictions of the appropriate experimental conditions required to enhance bone tissue formation in 3D TE scaffolds (Zhao et al. 2014; Zhao et al. 2015). This novel system was a perfusion-compression bioreactor that allowed for precise control of fluid velocities and uniaxial compressive strains applied to cells within TE scaffolds. The bioreactor is capable of maintaining an appropriate temperature and gas mixture (37 °C, 5% CO₂), minimising the risks of outside contamination and continuous support of cell growth. Finally, real time imaging was integrated into the bioreactor design, thus allowing for live cell imaging during the application of mechanical stimulus.

Moreover, the bioreactor is compatible with inverted microscopes allowing for live cell imaging during the application of mechanical stimulus.

The final study of this thesis investigated whether the combination of (1) matrix-based cues and (2) the application of extrinsic compression and perfusion stimuli could enhance both osteoblast and osteocyte differentiation within the same porous scaffolds. This chapter built upon the results from chapters 3-4 and incorporated these constructs into the bioreactor system developed in Chapter 5, which was capable of applying combined perfusion and compression stimulus to the constructs. The results of this study show that applying combined oscillatory compression-perfusion stimulus to a porous trabecular-like hydrogel containing encapsulated osteoblasts led to osteocyte differentiation and mineralisation, supporting increased construct mechanical properties.

Publications

The following publications have been generated from this thesis:

Published Journal Articles:

- Mc Garrigle M.J., Mullen C.A., Haugh M.G., Voisin M.C. and McNamara L.M. “Osteocyte Differentiation and the Formation of an Interconnected Cellular Network *In Vitro*” (2016) *European Cells and Materials*, 31(353), pp.323–340

Journal Articles in Submission/Preparation:

- Mc Garrigle M.J., Zhao F., McNamara L.M. Design, fabrication and validation of a perfusion-compression bioreactor integrated with microscopy for TE scaffolds (*Applying for patent protection*)
- Mc Garrigle M.J., Zhao F., McNamara L.M. Combined compression and perfusion stimulus promotes osteocyte differentiation (*In preparation*)
- Zhao F., Vaughan T.J., Mc Garrigle M.J., McNamara L.M. A multiphysics model to investigate the migration of bone cells in a tissue engineering scaffold, *Submitted*.
- Zhao F., Mc Garrigle M.J., Vaughan, T.J., McNamara L. M. In silico study of bone tissue regeneration in a porous hydrogel scaffold under mechanical loadings. *Submitted*

The following publications have been generated separate to this thesis:

- Verbruggen, S.W., Mc Garrigle M.J., Haugh M.G., Voisin M.C., McNamara L.M. Altered Mechanical Environment of Bone Cells in an Animal Model of Short- and Long-Term Osteoporosis (2015). *Biophysical Journal*, 108(7), pp.1587–1598.

Conference Presentations:

- Mc Garrigle, M.J., Mullen C.A., Haugh, M.G., Voisin, M.C., McNamara, L.M. Osteoblast-osteocyte differentiation within a three dimensional matrix is

determined by matrix stiffness and intercellular separation. *TERMIS World Congress*, September 2015, Boston, USA. (Poster presentation)

- Mc Garrigle, M.J., Mullen C.A., Haugh, M.G., Voisin, M.C., McNamara, L.M. Osteoblast-osteocyte differentiation within a three dimensional matrix is determined by matrix stiffness and intercellular separation. *Biomedical Engineering in Ireland 21 (BINI21) Conference*, January 2014, Maynooth, Ireland. (Podium presentation)
- Mc Garrigle, M.J., Haugh, M.G., Voisin, M.C., McNamara, L.M. Substrate stiffness and the timing of cell differentiation regulate bone tissue formation within gelatin scaffolds. *Annual Meeting of Orthopaedic Research Society (ORS)*, March 2014, New Orleans, US. (Poster presentation)
- Mc Garrigle, M.J., Haugh, M.G., Voisin, M.C., McNamara, L.M. Substrate stiffness and the timing of cell differentiation regulate bone tissue formation within gelatin scaffolds. *BINI20 Conference*, January 2014, Limerick, Ireland. (Podium presentation)
- Mc Garrigle, M.J., Verbruggen, S.W., McNamara, L.M. The Effect Of Substrate Stiffness And Delayed Cell Differentiation On Bone Tissue Formation Within Uniform Gelatin Scaffolds. Anatomical society meeting, July 2013, Dublin, Ireland. (Poster presentation)
- Mc Garrigle, M.J., Verbruggen, S.W., McNamara, L.M. Design and Fabrication of a micro-loading device integrated with confocal microscopy to Investigate bone cell mechanics. *BINI19 Conference*, January 2013, Meath, Ireland. (Poster presentation)

Acknowledgements

I would like to express my sincerest thanks to all of those who inspired and helped me over the last few years. First and foremost to my supervisor Prof. Laoise McNamara, whose guidance, support and encouragement inspired me throughout my studies. I am deeply grateful to her constant drive in achieving the highest standard of research, attention to detail and work ethic providing a constant source of inspiration. You have taught me so much, both in research and critical thinking. Thank you Laoise.

A particular thanks to all members of the McNamara group. First of all, the great post docs Muriel, Matt, Ted and Jessica whose assistance helped me through the different stages of my PhD. Thanks for all your support, knowledge and patience in answering my awkward questions. A big special thanks to all the other members of the group, who were always there for a “quick” talk or troubleshooting experimental problems. An extra special thanks to Feihu, who it was a pleasure to collaborate with and at the same time introduced me to tasty world of Asian cuisine. Finally I would like to thank all the help and technical assistance from the skilled technical officers within the engineering building.

I would also like to take the time to acknowledge the great research crew from the Engineering building for providing constant banter and excursions (Long tea breaks, cube parties, blackrock, adventure trips and great nights out). Finally I would like to thank my parents, brother and sister for their support and constant words of inspiration “are you finished yet”. Only joking, thanks guys.

Nomenclature

Roman Letters

<i>Ca</i>	Calcium
<i>d</i>	Pore size
<i>E</i>	Young's modulus
<i>k</i>	Permeability
<i>m</i>	Mass
<i>p</i>	Pressure
<i>R</i>	Radius
<i>t</i>	Time
<i>V</i>	Volume

Greek Letters

μ	Dynamic viscosity
ρ_f	Density of fluid
ρ_s	Density of solid
ε_{app}	Compressive strain

Acronyms

ALP	Alkaline phosphatase
BCs	Boundary conditions
BM	Basic medium
BMP	Bone morphogenic protein
BSA	Bovine serum albumin
BDI	Butane diisocyanate
CaP	Calcium phosphate
CD	Cluster of differentiation
CFD	Computational fluid dynamics
CC	Chondrocytes
COX2	Cyclooxygenase-2
DMEM	Dulbecco's modified Eagle medium
DNA	Deoxyribonucleic acid
DPBS	Dulbecco's phosphate-buffered saline
ECM	Extracellular matrix
DMP-1	Dentin matrix protein -1

FB	Fibroblasts
FSI	Fluid structure interaction
FSS	Fluid shear stress
GAG	Glycosaminoglycan
hASCs	Human adipose stem cells
MC3T3-E1	Mouse calvarial osteoblastic cell line
M-CSF	Macrophage colony-stimulating factor
MEMS	Micro-electro-mechanical systems
micro-CT	Micro-computed tomography
MSCs	Mesenchymal stem cells
OB	Osteoblasts
OCN	Osteocalcin
OM	Osteogenic medium
OPG	Osteoprotegrin
OPN	Osteopontin
PDMS	Polydimethylsiloxane
PGE2	Prostaglandin E2
PINP	Procollagen Type I N-terminal propeptide
PLA	Poly(lactic acid)
PLGA	Poly(lactide-co-Glycolide)
PMMA	Poly(methyl methacrylate)
PU	Polyurethane
RANKL	Receptor activator of nuclear factor κ β ligand
RUNX2	Runt-related transcription factor 2
SF	Stress fibre
TEM	Transmission electron microscopy
TE	Tissue engineering
USDFLD	User defined field
WSS	Wall shear stress
2D	Two dimensional
3D	Three dimensional

Table of contents

Abstract.....	i
Publications	iv
Acknowledgements	vi
Table of contents	ix
Table of figures.....	xiii
Table of tables	xx
1 Introduction	1
1.1 Musculoskeletal tissue engineering	1
1.2 Bone Tissue Engineering for large bone defects.....	2
1.2.1 Current treatments for large bone defects	3
1.2.2 Bone tissue engineering applications for large bone defects	3
1.3 Objectives and Hypotheses	7
1.4 Thesis Structure.....	8
2 Literature Review	9
2.1 Bone.....	9
2.1.1 Insight into bone biology and characterises	9
2.1.2 Bone tissue composition	9
2.1.3 Bone Structure and Hierarchical organisation	10
2.1.4 Bone cells and formation of bone extracellular matrix.....	11
2.2 Bone diseases and disorders	16
2.3 Bone tissue engineering	17
2.3.1 Background	17
2.3.2 Types of biomaterial for bone TE	19
2.3.3 Gelatin as a biomaterial	20
2.3.4 Hydrogel scaffolds in TE.....	20
2.3.5 Achieving a porous scaffold architecture	21
2.3.6 Varying scaffold stiffness through crosslinking	22
2.3.7 Measuring mechanical properties	24
2.3.8 Commercially available biomaterials for bone tissue engineering.....	25
2.3.9 Combining cells with biomaterial scaffolds (In vitro)	26
2.3.10 Clinical success of cells combine with scaffold biomaterials	27
2.4 Mechanical/biophysical stimulation and bone regeneration	30
2.4.1 2D Substrate / 3D matrix stiffness.....	30
2.4.2 Fluid flow	32
2.4.3 Matrix strain	33
2.4.4 Combined stimuli.....	33
2.5 Bioreactors in bone tissue engineering	34

2.5.1	Clinical success of bioreactors	37
2.6	Summary	40
3	Osteocyte differentiation and the formation of an interconnected cellular network in vitro	42
3.1	Introduction	42
3.2	Methods	44
3.2.1	Gelatin–mtgase hydrogel preparation	44
3.2.2	Gelatin–mtgase hydrogel mechanical properties	45
3.2.3	Cell culture embedded in 3-dimensional mtgase hydrogels	46
3.2.4	DNA content	47
3.2.5	Morphological analysis of cell phenotype	47
3.2.6	Live cell imaging to track exploratory dendrites	48
3.2.7	DMP-1 immunofluorescent staining	49
3.2.8	Extracellular ALP content	49
3.2.9	Mineralisation	50
3.2.10	Statistics	50
3.3	Results	51
3.3.1	Compressive modulus	51
3.3.2	DNA content	52
3.3.3	Morphological analysis of cell phenotype	52
3.3.4	DMP-1 immunofluorescent staining	60
3.3.5	ALP activity of cells	61
3.3.6	Mineralisation	62
3.4	Discussion	64
3.5	Conclusion	69
4	An <i>in vitro</i> model for trabecular bone, recapitulating both osteoblast and osteocyte differentiation in porous TE scaffolds	70
4.1	Introduction	70
4.2	Methods	75
4.2.1	Cell culture	75
4.2.2	Mechanical testing	75
4.2.3	Cell number	75
4.2.4	Peripheral seeding	76
4.2.5	Cell encapsulation	80
4.3	Statistical Analysis	83
4.4	Results	84
4.4.1	Peripheral seeding	84
4.4.2	Cell encapsulation	89
4.5	Discussion	95
4.6	Conclusion	100

5	Design, fabrication and validation of a perfusion-compression bioreactor integrated with microscopy for TE scaffolds	101
5.1	Introduction	101
5.2	Materials & Methods	104
5.2.1	Bioreactor design criteria, component selection and analysis	104
5.2.2	Bioreactor design	114
5.2.3	Bioreactor in-house fabrication and construction	117
5.2.4	Design changes and final bioreactor design	121
5.3	Bioreactor Validation	122
5.3.1	Microscopy and live cell imaging setup.....	122
5.3.2	Compression Validation	123
5.3.3	Perfusion Validation	125
5.4	Bioreactor evaluation (Results and conclusion).....	130
6	Combined compression and perfusion stimulus promotes osteoblast and osteocyte differentiation.	134
6.1	Introduction	134
6.2	Materials and Methods.....	138
6.2.1	Combined perfusion-compression bioreactor and moulds	138
6.2.2	Cell culture and porous cell-laden gelatin-mtgase hydrogels fabrication	139
6.2.3	Mechanical stimulation procedure	140
6.2.4	Cell viability.....	141
6.2.5	Cell morphology and DMP-1 immunofluorescent staining.....	141
6.2.6	Extracellular ALP activity	142
6.2.7	Micro-CT.....	143
6.2.8	Mineralisation	143
6.2.9	Mechanical testing	143
6.3	Results	144
6.3.1	Cell viability.....	144
6.3.2	Cell morphology and DMP-1 immunofluorescent staining.....	145
6.3.3	Extracellular ALP activity	147
6.3.4	Micro-CT.....	147
6.3.5	Mineralisation	149
6.3.6	Mechanical testing	150
6.4	Discussion	151
6.5	Conclusion.....	155
7	Discussion and Conclusion	157
7.1	Introduction	157
7.2	Main findings of the thesis.....	157
7.3	Implications for the fields of bone mechanobiology and bone tissue engineering	159

7.4	Future Work.....	164
7.4.1	Combine low and high matrix stiffness in cell encapsulated hydrogels..	164
7.4.2	Improvements of bioreactor operating design, usability and a larger range of tissue testing	165
7.4.3	Adjustment of stimulus in conjunction with new tissue formation in scaffolds	166
7.4.4	Bioreactor technology in the pharmaceutical industry	166
7.5	Conclusion	167
	References.....	169
1	Appendix.....	198
1.1	Bioreactor in-house fabrication and construction.....	198
1.1.2	Bioreactor fabrication cost	206
2	Appendix.....	208

Table of figures

Figure 2-1: Hierarchical organisation of bone with different length scales, illustrating (a) collagen fibrils and hydroxyapatite crystals forming (b) lamellar bone consisting of (c) osteons and Haversian canals within (d) cortical and trabecular bone (Vaughan et al. 2012).	11
Figure 2-2: Schematic representation of MSC differentiating into pre-osteoblasts and producing osteoid on the bone surface. A fraction of these osteoblast become embedded, differentiating into early stage osteocytes, and hence into mature osteocytes as the osteoid mineralisation.	12
Figure 2-3: Schematic representation of the approach employed in bone tissue engineering. Cells and signalling molecules combined with a scaffold <i>in vitro</i> to enhance tissue formation before being implanted.	17
Figure 2-4: Illustration of the uniaxial stress-strain curve for an elastomeric cellular solid in compression. The graph shows the linear elastic region up to approximately 5% strain, the pore collapse plateau and densification regimes up to 80% (Harley et al. 2007).....	24
Figure 2-5: Schematic of a stir plate bioreactor, scaffolds suspended in culture while media is circulated through a stir plate (Yeatts & Fisher 2011) (A). Rotating wall bioreactor, two concentric cylinders within each other. One cylinder is stationary while the second rotates. The space between the two cylinders is filled with media were the rotation provides mixture of centrifugal and gravitational forces (Yeatts & Fisher 2011) (B). Media is perfused through a growth chamber containing the seeded scaffold (Jaasma et al. 2008) (C).	36
Figure 2-6: <i>Ex vivo</i> bone compression bioreactor (Zetos system) (Davies et al. 2006) (A) and BioDynamic chamber for compression of Polyurethane open cell foam scaffolds (Sittichockechaiwut et al. 2009).....	37
Figure 3-1: Hydrogel fabrication method for mechanical testing. Unconfined compression testing was performed on samples using a custom made platen attached to a 10 N load cell.....	46
Figure 3-2: Mechanical properties of a 3 % Gelatin hydrogel crosslinked with 0.15, 0.03, 0.06, 0.08, 0.15, 0.2 % mtgase after 1 hour of incubation at 37 °C, n = 8 per group. ^a p<0.05 relative to 0.03 % mtgase hydrogel.	51
Figure 3-3: DNA content of each group at 2.5 hours, 3, 21 and 56 days (n = 6 samples per group per time-point). ^a p<0.05 representing a statistical difference between low (0.58 kPa) and high (1.47 kPa) stiffness. Error bars denote standard deviation.....	52
Figure 3-4: Actin staining of cell morphology after 2.5 hours of culture comparing spherical vs dendritic (Red arrows) morphology (A). Also shown is the percentage of spherical vs dendritic cells (B) and average dendritic cell span (C) within low (0.58 kPa) and high (1.47 kPa) stiffness matrices. ^a p<0.05 representing a statistical difference between low (0.58 kPa) and high (1.47 kPa) stiffness at the same density group. Scale bar = 50 µm, same for all images.	53
Figure 3-5: Actin staining of cell morphology after 21 hours of culture comparing spherical vs dendritic (Red arrows) morphology (A). Also shown is the percentage of spherical vs dendritic cells (B) and average dendritic cell span (C) within low (0.58 kPa) and high (1.47 kPa) stiffness matrices. ^a p<0.05 representing a statistical	

difference between low (0.58 kPa) and high (1.47 kPa) stiffness at the same density group. Scale bar = 50 μm , same for all images.	55
Figure 3-6: Section views of cell morphologies and interconnections at 56 days. Fluorescent images represented as 3D stacks in low stiffness matrix group. Scale bar = 50 μm	57
Figure. 3-7: Section view images of low stiffness matrix and high cell density comparing cell morphologies and interconnections at 2.5 hours and 56 days. After 2.5 hours cells form dendrites throughout the hydrogel. By 56 days, cells proliferate on surface, exhibiting a spread and confluent morphology (red arrows), progressing from the hydrogel surface cells become dendritic and forming interconnections (red circle). Scale bar = 50 μm	58
Figure 3-8: Actin staining and particle analysis illustrations of cell morphology after 56 days of culture comparing spherical vs dendritic morphology (A) within low (0.58 kPa) and high (1.47 kPa) stiffness matrices. Also shown is the percentage of spherical vs dendritic cells (B), average cell dendrite length (C) and percentage of interconnections formed between cells (D). ^a $p < 0.05$ representing a statistical difference between low (0.58 kPa) and high (1.47 kPa) stiffness at the same density group. Scale bar = 100 μm	59
Figure 3-9: (A) Live cell imaging of a low stiffness matrix at a high cell density show cells (green cells) to be highly dynamic and constantly sending out exploratory dendrites (red arrow) throughout the study, while at the later timepoints the same cells formed interconnections with neighbouring cells (blue cells). Furthermore cells that became balled up and encapsulated (Black arrows), were observed to remain balled up within the hydrogel throughout the 56 days culture period and were classified as dormant. (B) Fluorescent imaging at day 56 show interconnections formed between cells (blue arrow).	60
Figure 3-10: Immunofluorescent images of DMP-1 from cells encapsulated in a hydrogel at a low matrix stiffness (0.58 kPa). (A) Negative controls were performed by omitting the primary antibody and no DMP-1 staining was observed. (B) DMP-1 staining was observed within the proximity of dendritic and interconnected cells at a medium cell density (10x magnification). At a low (C, D) and high (E, F) cell density, DMP-1 staining was observed within matrices at day 21 and 56 (40x magnification). DMP-1 staining, at the high cell density (E, F) was observed as dispersed nodules within the surrounding matrix of dendritic and interconnected cells (Blue arrows, 40x magnification). Images were taken at approximately 50 μm below the hydrogel surface. Scale bar for 10x (A, B) = 120 μm ; 40x (C, D, E, F) = 50 μm	61
Figure 3-11: Extracellular ALP activity of each group at day 3, 21 and 56 (n = 6 samples per group per time-point). ^a $p < 0.05$ relative to the other cell density groups at the same timepoint and ^b $p < 0.05$ representing a statistical difference between low and high stiffness. Error bars denote standard deviation.	62
Figure 3-12: Calcium content of each group at days 21 and 56 (n = 6 samples per group per time-point). ^a $p < 0.05$ relative to the other cell density groups at the same timepoint. ^b $p < 0.05$ relative to the other matrix stiffness groups at the same timepoint. Error bars denote standard deviation.	63
Figure 4-1: Scanning electron microscope (SEM) image of a dry porous GG scaffold....	77
Figure 4-2: Cell nuclei distribution within a scaffold section (A). ImageJ software was used to threshold and perform particle analysis to determine coordinates of	

individual cell nuclei (B), allowing for a graph of cell distribution to be created (C).	78
Figure 4-3: Illustrates the fabrication method of gelatin-mtages hydrogels (diameter 12.7 x 4 mm). A coverslip and custom made moulds were inserted within the 24 well-plate and the hydrogel solution added. The moulds were removed and media added. The hydrogel could then be removed by lifting the coverslip.....	80
Figure 4-4: Illustrates a hydrogel (A) and a porous hydrogel (B). Scanning electron microscope (SEM) image of a hydrogel (C) and brightfield image of a porous hydrogel (D). Scale bars 50 μm (C) and 2 mm (D).....	81
Figure 4-5: Concentration of EDAC crosslinking and mechanical properties of GG scaffolds. $n=8$ per group. ^a $p<0.05$ relative to EDAC 3 crosslinked GG scaffold. ...	84
Figure 4-6: Cell number within GG scaffolds at 2 hrs, 7, 21 and 28 days. ^a $p<0.05$ versus corresponding 0.5 kPa stiffness group at the same time point, ^b $p<0.05$ versus corresponding stiffness group at 2 hrs and ^c $p<0.05$ ($n = 6$ samples per group per time-point). Error bars denote the standard deviation.	85
Figure 4-7: Cell distribution in GG scaffolds after 2 hours, 7, 21 and 28 days illustrating cell attachment around the periphery (Red arrows) of the scaffolds with migration towards the centre (Black arrows) over the course of 28 days ($n=2$).	86
Figure 4-8: Extracellular ALP activity at day 7, 21 and 28. ^a $p<0.05$ versus corresponding 1.4 kPa stiffness group at the same time point. ^b $p<0.05$ versus corresponding stiffness groups at the same time point. ^c $p<0.05$. Error bars denote the standard deviation ($n = 3$).	87
Figure 4-9: Calcium content at 2 hours, 21 and 28 days. ^a $p<0.05$ versus corresponding stiffness at the same timepoint. Error bars denote the standard deviation ($n = 3$)....	88
Figure 4-10: Alizarin red stain showing mineral distribution at 2 hours, 21 and 28 days ($n = 2$), with black arrows denoting the periphery of the scaffold and red arrows the start location of mineral. Scale bar 300 μm	89
Figure 4-11: Compressive properties of 6 % gelatin encapsulated and porous encapsulated hydrogels crosslinked with 0.03% and 0.08% mtgase. ^a $p<0.05$ relative to 0.03 % mtgase hydrogel ($n = 8$). Error bars denote the standard deviation.	90
Figure 4-12: Cell number within encapsulated and porous encapsulated hydrogels at 2 hours and 7 days (B) ($n = 6$). Error bars denote the standard deviation.	91
Figure 4-13: Actin (Green) and dapi (Blue) staining of cell nuclei and cytoskeleton illustrating cell distribution ($n = 4$) after 2 hours within low stiffness encapsulated and porous encapsulated hydrogels. Encapsulated hydrogels had a homogenous distribution of cells throughout the construct. Porous encapsulated hydrogels groups showing homogenous distribution of cells throughout pores/struts of construct (Red dashed lines). Scale bar is 500 & 100 μm for 4 and 20 x magnifications respectively.	92
Figure 4-14: Actin (Green) and DAPI (Blue) staining of cell nuclei and cytoskeleton illustrating cell distribution and morphology after 7 days in encapsulated and porous encapsulated hydrogels at low and high hydrogel stiffnesses. Cells within all hydrogels groups remained homogeneously distribution throughout constructs. In low stiffness porous hydrogels after 7 days of culture, cells were observed to spread over the pore surface along with expressing a bipolar morphology (Red arrows), while cells within the struts (white arrows) remained surrounded by the 3D hydrogel matrix. Scale bar is 500 & 100 μm for 4 and 20 x magnifications respectively.	93

Figure 4-15: After 32 days, immunofluorescent images of DMP-1 (Red arrows) from cells spread over pore surface (Blue arrow) and encapsulated in the porous hydrogel at 20x (A), 40x (B, C) and 60 x (D) magnifications. Scale bar for 20x = 200 μm ; 40x = 100 μm ; 60x = 100 μm	94
Figure 4-16: Representative images of alizarin red stain in a low stiffness (0.58 kPa) porous hydrogel showing mineral distribution at 32 days in low stiffness porous hydrogels at magnifications of 20x (A) and 40x (B) (n = 2). Scale bar for 20x = 200 μm ; 40x = 100 μm	95
Figure 5-1: Porous platens allow for direct homogenous compression of a TE scaffold (Red porous block) confined on 5 sides, while also allowing for fluid perfusion (Blue arrows) to occur through the TE scaffold (A). A sintered filter element (B) contains a porous structure allowing for fluid to pass through while providing a rigid structure for compressive loading (C).	105
Figure 5-2: Computational models predicted for a porous hydrogel with a porosity of ~50% and idealised pore size of ~500 μm a peak flow rate of 0.3 mL/min (fluid velocity $v = 250 \mu\text{m/s}$) and a compressive strain of 0.5% at 1 Hz was required for osteogenic differentiation to occur through mechanical stimulus. Furthermore, a low flow rate of 0.05 mL/min was determined for nutrients and waste exchange (Zhao et al. 2014; Zhao et al. 2015).	107
Figure 5-3: Illustration of a Ballscrew (A). During rotation the ball bearings circulate along threaded slots in the ballscrew and ballnut, allowing low friction and high accuracies during high loads.....	108
Figure 5-4: Stepper motor (C) combined with planetary gearing (B) and flexible motor couple (A) forming connection with ballscrew shaft.....	109
Figure 5-5: Diaphragm sealing method to prevent leaking during compressive loading. Membrane in the shape of a washer (Red) with both ends held in place forming a seal, while still allowing for movement between the two sealed ends during compression.	112
Figure 5-6: Olympus inverted microscope, containing a removable disk from the stage, leaving behind a circular opening which acted as template for the bioreactor base (A). Standard microscope endoscope allowing for low magnification of scaffolds at the global level (B). A 3D model of the microscope stage was created to determine the bioreactor size restrictions (B), such as the TE constructed limited to 1 mm above the objective (C).	113
Figure 5-7: The full bioreactor system (170 x 125 mm) consists of two main parts, the bioreactor chamber and the compression rig (A). An exploded illustration of all parts within the bioreactor perfusion chamber (B) and compression rig (C). The bioreactor chamber holds four samples with full sealing achieved through the diaphragm membrane and gaskets during loading. Direct observation of samples can be achieved at low and high magnification. Compression rig provides the main compression power transmission system. Aluminium mounts were used for holding the transmission system.	115
Figure 5-8: Plan and end view of bioreactor stimuli operation. Homogenous perfusion (Blue) is applied through an inlet port and hence diverges in the 4 channels with the compression arm before entering the porous platens and scaffolds. Fluid perfuses out through the scaffold and the fixed platen before re-converging and exiting the bioreactor. Perfusion flow can be fully reversed. Homogenous compression applied externally to samples through a compression shaft (Red) and internally applied to	

samples by four compression arms containing platens. Fixed platens on the opposite side of the sample restrict movement during compression.	116
Figure 5-9: Two porous platens after degreasing and passivation.....	117
Figure 5-10: Custom machined ballscrew (A) with thrust and support bearing axially fixed to the ballscrew shaft (B).	118
Figure 5-11: CNC machining carried out on four sides of the bioreactor chamber stock block. Bioreactor windows were machined and thread milling performed (A-C). Machining of side 2 formed a slot for the compression chamber (D-F). Machining of side 3 formed 2 mm channels for fluid flow (G-I). Finally machining of side 4 preformed for observation window and scaffold holding slots (J-K).	119
Figure 5-12: Compression rig control box (A). The microcontroller is connected to external AC-DC power supply, with a 9 pin connector connected from the micro controller to stepper motor. The micro controller connects to laptop through RS485 cable and hence through USB connections. Nanopro software allows for full control over the stepper motor travel distance by the number of steps (B), motor speed (C) and repetitions of the same motion. Reversing motor direction (D) allows for oscillatory compression profile. While, a graph (E) shows real time feedback of motor position during operation.....	120
Figure 5-13: 3D CAD illustration of bioreactor versus assembled fabricated bioreactor.	121
Figure 5-14: Bioreactor compression rig redesigned to accommodate a second bioreactor chamber system that can be attached, compressive loading 8 samples concurrently.	122
Figure 5-15: Bioreactor setup within the live cell microscope (A), imaging at low, medium and high magnification, identifying the global scaffold geometry, pore structure and individual cells (B). Microscope objective capable of moving between samples, while endoscope allows for low magnification images (C). Bioreactor system remains fixed in place during loading.	123
Figure 5-16: After programming the geared stepper motor to revolve 720 steps a corresponding output of 14.4 degree was observed (A). Calibration points machined in bioreactor chamber objective window, allowing for visualisation of 20 μm displacement applied to the porous platen (B). Compressive loading was calibrated to the correct displacement by microscopy imaging allowing for the visualisation of platen displacement during loading (C, D, E)	124
Figure 5-17: Illustrates controlled displacement applied to the porous platen and hence to the porous test sample (Blue arrows) (A). Real time videos were acquired of the strut deformation under controlled displacement (B).....	125
Figure 5-18: Validation of first bioreactor design showed an uneven flow profile across the 4 channels in the bioreactor chamber at peak flow rate of 1.2 mL/min.....	126
Figure 5-19: Computational and experimental testing of the old and new bioreactor flow profile. Fluid (stain with red dye) enters through the bottom of the four channels and permeates through the channels before re-converging and exiting the bioreactor chamber. A homogenous flow profile was observed across the 4 channels in the final design compared to the first design.	127
Figure 5-20: Real time video frames shows red dye being perfused through the bioreactor chamber under a steady flow rate of 1.2mL/min. Small changes in flow profiles were observed between the 4 channels containing porous platens and scaffolds (A). Global fluid perfusion was observed through the compressive porous platens and	

hence through the test sample before exiting through the fixed porous platen (B). Magnified of the scaffold structure shows red dye perfusing through pores and out through the porous platens (White arrows) (C)..... 129

Figure 6-1: Custom design moulds for static and osteogenic constructs. Constructs receiving mechanical stimulus were moulded in the bioreactor chamber..... 139

Figure 6-2: Live/dead staining showed viable cells within all groups after 32 days. Viable cells (Red arrows) were observed encapsulated in the hydrogel and on the surface of pores (Red circle). Dead cells were observed encapsulated in the hydrogel. Calcein AM, staining live cells (Green) and Eth-1 staining dead cells (Red) (n=2). Scale bar is 500 μm 144

Figure 6-3: Cells within porous hydrogels were observed to proliferate and spread over the surface of pores (Blue arrows), while cells within hydrogels remained encapsulated in 3D hydrogel matrix. DMP-1 expression from cells was observed as dispersed nodules within the surrounding matrix of spread and encapsulated cells. DMP-1 staining in all groups, however a higher intensity of staining was observed in the combined group (Red arrows). Scale bar for 20x = 200 μm ; 40x = 100 μm 145

Figure 6-4: Positive control bovine sample stained for DMP-1 (A). DMP-1 expression observed in cells encapsulated in porous hydrogels subject to combined compression and perfusion stimulus, at 20x magnification (B). DMP-1 staining was observed within the proximity of dendritic cells, 40x magnification (C). DMP-1 was observed to be secret from cell nucleus and along dendrites (Blue arrows) (D). Scale bar for 20x = 200 μm ; 40x = 100 μm 146

Figure 6-5: Extracellular alkaline phosphatase activity of each group (n = 6) after 32 days..... 147

Figure 6-6: Average mineral volume within an 11.4 mm³ section from a construct after 32 days in each group determined from Micro CT scans. 148

Figure 6-7: Representative micro-CT images of mineral distribution (red arrows) in an 11.4 mm³ sections after 32 days of culture in each group. 149

Figure 6-8: Alizarin red stain showing mineral distribution at 32 days in all groups at 20x magnification (n = 2). Dark red patches arise from Alizarin red staining of calcium deposits/nodules. Scale bar 200 μm 150

Figure 6-9: Bulk compressive modulus of control sample containing no cells and constructs in all groups after 32 days of culture. ^ap<0.05 relative to control..... 151

Figure 7-1: Graphical illustration of the work conducted as part of this thesis with respect to key studies used in hypotheses formation. 160

Figure 7-2: Graphical representation of thesis findings, which developed osteoblast-osteocyte networks in 3D constructs and applied mechanical stimulus to porous trabecular-like constructs, ultimately promoting both osteoblast and osteocyte differentiation as determined from chapters 3, 4, 5 and 6. 164

Figure 1-1: Haas TM1P CNC Toolroom mill used to automatically machine bioreactor parts 198

Figure 1-2: A model of CNC vice used for the development machining paths boundary conditions and zero coordinate offset (A). Sample toolpaths generated for machining out geometries bioreactor (B). Multiple bioreactor chamber parts, machined out using a “Sprue” machining approach from three different stock blocks (C). 201

Figure 1-3: Tools setup on carousel (A&B) and hence all tool heights to the same offset using a pressure height gauge (C&D). Stock coordinate position and parameters

setup with CNC vice and zero reference coordinate taken from fixed end of vice (E).	202
Figure 1-4: Polycarbonate and aluminium stock purchased parts (A) cut to rough stock dimensions using vertical (B) and horizontal band saw (C). Subsequently, precise face milling (E) carried out of stock parts forming parallel sides and smooth surfaces (F) for CNC machining.	203
Figure 1-5: Machining of bioreactor chamber parts using the “sprue” technique. Precise stock blocks were loaded in the CNC vice with machining preformed on two sides. Nine parts were created from A and three from B.	204
Figure 1-6: After removal of parts from the “sprue” further machining was performed (A), such as threading of the compression arm and nut (B & C). To allow for fluid flow 2 mm high channels were machined out with a 2mm end mill cutter (D).	204
Figure 1-7: CNC machining carried out on four sides of the bioreactor chamber stock block. Bioreactor windows were first machined out with thread milling performed (A-C). Machining of side 2 formed a slot for the compression chamber (D-F). Machining of side 3 formed 2 mm channels for fluid flow (G-I). Finally machining of side 4 preformed for observation window and 1 mm channels for calibration points through 1 mm End mill and 45° chambering (J-K).	205
Figure 1-8: Fabrication of the compression rig. Five aluminium parts machined out using the “sprue” method (A). Subsequently, machining performed on two side of the polycarbonate compression rig frame (B-C)	206

Table of tables

Table 1: Table of commercially available bone scaffolds substitutes.....	26
Table 2: Reported outcomes of in vivo studies exploring the potential of cell –seeded biomaterial scaffolds cultured <i>in vitro</i> prior to implantation.....	29
Table 3: Cell combined with biomaterial scaffolds and culture <i>in vitro</i> using bioreactor based approaches before implanting <i>in vivo</i>	39
Table 4: Table of different tools, spindle speeds and feed rates used in the fabrication of bioreactor parts.....	200
Table 5: Illustrates the approximate amount of the components and equipment required to fabricate one bioreactor device. This does not include labour and manufacturing costs.....	207

Chapter 1: Introduction

1.1 Musculoskeletal tissue engineering

Musculoskeletal conditions are responsible for severe long term pain and disability in 20-30% of adults in Europe, who are affected by long-term muscle, bone and joint diseases such as osteoporosis, rheumatism and arthritis (Woolf 2007). A report from EUMUSC.Net summarised that musculoskeletal conditions are among the top 5 diagnostic groups in Europe in terms of health care costs (EUMUSC 2014). In Germany the estimated cost of diseases of the musculoskeletal system and connective tissue in 2008 was €28,545 million (11% of total illness costs), whereas in Ireland expenditure on drugs for musculoskeletal conditions was €3,048 million euros (6% of total drug expenditure) (EUMUSC 2014). From 2004 to 2006 the direct medical costs related to musculoskeletal conditions were \$576 billion in the USA (Summers et al. 2015). Clinical treatment to re-establish function in musculoskeletal tissues requires transplanting tissue grafts from another part of the patient or from a donor. However, accessing viable tissue within the patient is challenging and there is also a scarcity of suitable donors. As such there is a strong healthcare rationale for the development of functional substitutes for damaged or diseased musculoskeletal tissues.

Tissue engineering has been widely explored as a solution for treatment of patients suffering from musculoskeletal conditions and the field strives to generate tissue substitutes by combining biomaterials with biological cells and thereby take advantage of their natural capacity to grow and produce tissue constituents. By 2019 the total market for tissue engineering products for musculoskeletal applications is expected to exceed \$39 billion in the USA. The global cell culture market is expected to exceed \$19,000 million by 2020, a large proportion of which will be consumed for research into tissue engineering/regeneration and pharmaceutical drug development. Skin tissue engineered substitutes, such as Biobrane® and Matriderm®, are clinically used for treatment of damaged skin layers (Wen et al. 2016; Shevchenko et al. 2010; Priya et al. 2008; Min et al. 2014). However, although significant advances have been made in developing *in*

in vitro bone and cartilage graft substitutes using biomaterial-based approaches (Gleeson et al. 2010; Alhag et al. 2012; Schubert et al. 2013; Kim et al. 2014; Matsumoto et al. 2012; Yamada et al. 2013; Dumas et al. 2012; Thorpe et al. 2013; C. C. Wang et al. 2012; R. Zheng et al. 2013; Ando et al. 2007; Cunniffe et al. 2015), current strategies for musculoskeletal applications are limited because of the inability to provide functional and mechanically suitable tissue grafts for clinical applications (Keogh et al. 2011; Lyons et al. 2010; Arano et al. 2010; Smith & Grande 2015)

1.2 Bone Tissue Engineering for large bone defects

Bone is an essential, dynamic and adaptive mineralised tissue, which facilitates body movement, and stability, defining shape and protecting organs. Bone has a unique capacity to constantly adapt and remodel itself due to mechanical loading from everyday activities (McNamara 2011). In normal bone there is an equilibrium between bone formation and resorption that maintains bone strength throughout life. Bone cells are responsible for maintaining the precisely ordered and structured environment of bone, through the remodelling process. Specifically, osteoblasts are regarded as the main cells responsible for bone formation as they secrete collagen, growth factors, cytokines and several proteins to support mineralisation (Cowin 1989), whereas osteocytes are the most abundant cells in mature bone and are believed to be the most important mediators of mechanical stimulation and thereby act as regulators of bone mass and structure throughout life (Verbruggen et al. 2012; McNamara 2011). In mature bone, osteocyte cells form a complex communication network that plays a vital role in regulating bone health (Burger & Klein-Nulend 1999).

Bone has a high capacity to regenerate itself after experiencing a minor fracture or defect. However, natural regeneration capabilities are limited by the size of the defect, which can be restricted in severe trauma or bone tumour removal and thereby require clinical treatment to repair these critical size defects. Moreover, bone diseases can significantly affect the normal equilibrium in the body.

1.2.1 Current treatments for large bone defects

Current treatment approaches for bone defects include autografts and allografts. Autografts are taken from a non-essential bone of the patient's body and reused at an affected site. This method is considered an ideal clinical treatment, as the autografts naturally incorporate both osteogenic cells and an osteoconductive mineral (Jahangir et al. 2008; Ebraheim et al. 2001). An example of this involves autologous tissue transplantation from the patient's iliac crest, ribs or calvarium. However, with large defects induced by tumours, infectious diseases or trauma, the size of such bone sections may not be sufficient (Kasper et al. n.d.; Salgado et al. 2004; A.R. Amini et al. 2012). Furthermore, additional surgery may be required, increasing costs, pain and risk of rejection (Seiler & Johnson 2000; Reid 1968; Myeroff & Archdeacon 2011; Arrington et al. 1996; Ebraheim et al. 2001). Allografts involve transplanted tissue from cadavers or other living donors, which can provide greater amounts of graft tissue compared to autografts. However, there is the risk of infection or an immune response for the donor. The grafts are usually processed to reduce the risk of infection, though this can weaken the biological and mechanical properties initially present in the tissue (Dick & Strauch 1994; Mankin et al. 2005; Brydone et al. 2010). Despite the early success with the use of autografts and allografts, which have shown good compatibility and recognition by the host tissue, there have been concerns about second site morbidity and infection of such tissues (Yarlagadda et al. 2005). Therefore, alternative solutions are being sought to recreate these properties under laboratory conditions and resolve the risks associated with current therapies for clinical treatments of large bone defects.

1.2.2 Bone tissue engineering applications for large bone defects

Bone tissue engineering (TE) is a promising scientific field with significant potential to repair injured, aged or damaged diseased skeleton tissue through the development of *in vitro* bone tissue substitutes, using biomaterial scaffolds and the patient's own cells, hence ruling out the potential of rejection and the need for revision surgery (Langer & Vacanti 1993). Biomaterial scaffolds act as an artificial extracellular matrix and a template of the physical architecture and thereby provide structural support, facilitate cell adhesion, proliferation, differentiation, cell interactions and formation of new tissue (Mitchell & Tojeira

2013). To date, fully functional and mechanically suitable tissue grafts are not yet widely available for clinical applications, as most constructs developed are susceptible to core degradation, absence of a vascular network or inconsistent tissue formation. Moreover, there has been minimal evidence of the development of an osteocyte network within such constructs. This is a distinct limitation as osteocytes are crucial for long-term maintenance of bone and as such will be required in regenerated bone.

A possible solution to overcome such limitations is to reproduce bone constructs with an osteocyte network in place. Extracellular mechanical cues are recognised as regulators of a variety of cell behaviours such as migration (Zaman & Trapani 2006), proliferation (Hadjipanayi et al. 2009), and differentiation (Tan et al. 2014; Lo et al. 2000). The extracellular mechanical environment can partially direct osteogenic differentiation and mineralisation of a variety of cells including myoblasts (Tan et al. 2014), osteoblasts (Chatterjee et al. 2010), MSCs (Engler et al. 2006; Huebsch et al. 2010; L. S. Wang et al. 2012) and embryonic stem cells (Evans et al. 2009). Osteogenic differentiation of human mesenchymal stem cells (MSCs) and pre-osteoblasts (MC3T3-E1) has been studied on 2D surfaces (Engler et al. 2006; Przybylowski et al. 2012) and on 3D biomaterials (Keogh, O'Brien, et al. 2010; Gleeson et al. 2010; Curtin et al. 2012; Correia et al. 2012) and it has been shown that substrate (2D) (Mullen et al. 2013; Engler et al. 2004) and matrix (3D) (Tan et al. 2014) stiffnesses are important physical factors that induce a phenotypic shift towards osteogenic or osteoblast-osteocyte differentiation. Cell seeding density has also been shown to be a critical parameter controlling cell proliferation, matrix synthesis and osteogenic signal expression, as it dictates the paracrine signalling distance between cells (Mullen et al. 2013; Kim et al. 2009; Zhou et al. 2011). However, although osteocyte differentiation has been studied in 2D (Mullen et al. 2013), it is not known how biophysical cues, such as matrix stiffness and cell density, control the phenotypic shift from osteoblasts to osteocytes in a 3D environment. To address this problem, the first research hypothesis to be investigated in this PhD thesis is *“Osteocyte differentiation is regulated by ECM stiffness and cell density within a 3D environment”*.

Biomaterial scaffolds strive to mimic *in vivo* properties of bone, and specific porous scaffolds mimic the physical architecture of trabecular bone, to facilitate cell adhesion, proliferation, differentiation and elicit new tissue formation (Wu et al. 2014; O'Brien 2011; Sopyan et al. 2007). Long term *in vitro* cultivation of bone cells on porous biomaterials (Gleeson et al. 2010; Keogh et al. 2011; Keogh, O'Brien, et al. 2010; Curtin et al. 2012; Correia et al. 2012; Kim et al. 2007; O'Brien 2011) and hydrogel biomaterial scaffolds (Castillo Diaz et al. 2014; Chatterjee et al. 2010; Tan et al. 2014; Shin et al. 2014) can sustain substantial cell numbers, viability and mineral content and thereby promote osteogenic differentiation and higher mechanical properties compared to an unseeded scaffold (Keogh, O'Brien, et al. 2010; Sittichokechaiwut et al. 2009; Kim et al. 2007; Correia et al. 2012; Naito & Dohi 2011). *In vivo*, trabecular bone has a complex 3D structure containing osteoblasts spread out over the strut surface with 3D embedded osteocytes interconnecting throughout the bone tissue, which play a vital role in maintaining bone health by monitoring mechanical stimulation (McNamara et al. 2009; Wang et al. 2007) and initiating bone formation and resorption (Rho et al. 1998; Franz-Odenaal et al. 2006; Burger & Klein-Nulend 1999). Certain biomaterials, such as gelatin and collagen hydrogels, have been shown to promote *in vitro* osteoblast to osteocyte differentiation (Mc Garrigle et al. 2016; Gerald J Atkins et al. 2009; Uchihashi et al. 2013). However, *in vivo* newly formed tissue in the scaffold can act as a barrier to remodelling and osseointegration with the host tissue (Lyons et al. 2010; Alhag et al. 2012), restricting the establishment of a mechanically solid interface between the material and the host tissue (Anselme 2000). Furthermore, current biomaterial scaffolds have not demonstrated simultaneous recapitulation of both osteoblasts and osteocytes within porous scaffolds (Mc Garrigle et al. 2016; Gerald J Atkins et al. 2009; Uchihashi et al. 2013; Keogh et al. 2011; McCoy et al. 2012; Murphy et al. 2010). To address this problem, the second research hypothesis to be investigated is ***“initial cell seeding density and stiffness in 3D will promote uniform cell distribution and subsequently tissue formation throughout TE scaffolds”*** The third hypothesis is ***“porous gelatin scaffolds represent the structurally different mechanical environments of trabecular bone in vivo (pores and struts) and will thereby promote both osteoblast and osteocyte development”***

Osteoblasts and osteocytes reside within complex micro-environments, such as trabecular bone (Burger & Klein-Nulend 1999), and sense and respond to mechanical loading and thereby orchestrate bone formation or resorption and play a vital role in bone physiology (McNamara 2011; Burger & Klein-Nulend 1999; Schaffler et al. 2014). Matrix stiffness, fluid flow and matrix strain all provide biophysical stimulation of osteoblasts and osteocytes *in vivo* (Chan et al. 2009; Wittkowske et al. 2016; Keogh et al. 2011; Jaasma et al. 2008; Ban et al. 2011; Owan et al. 1997; You et al. 2001; Smalt et al. 1997; Gomes et al. 2003; Zhang et al. 2006; Klein-Nulend et al. 2012; Saunders et al. 2006; Bacabac et al. 2004; Mullen et al. 2013; Engler et al. 2004; Tan et al. 2014; Jungreuthmayer et al. 2009). Bioreactors, are engineering devices that influence biological processes, which have shown great potential to control process parameters, such as fluid flow velocity and mechanical compression, and thereby regulate culture conditions for new tissue development (Keogh et al. 2011; Gardel et al. 2013; Thorpe et al. 2010; Schulz et al. 2008). However, existing systems do not strive to translate *in vivo* levels of mechanical stimuli to the *in vitro* porous scaffold environment (e.g. fluid shear stress, mechanical strain) (Keogh et al. 2011; Sittichokechaiwut et al. 2009). Recent computational studies, using a multiphysics approach, have been able to simulate mechanical stimuli on TE scaffolds consisting of different geometries and structures, and thereby predict the desired level of mechanical stimulation to elicit tissue formation within specific biomaterial scaffolds (Zhao et al. 2015; Zhao et al. 2014). Specifically, it has been predicted that a combination of perfusion and compression can amplify mechanical stimulus in scaffolds and enhance osteogenic differentiation (Zhao et al. 2015; Zhao et al. 2014). However, no experimental study has sought to investigate whether such stimuli will indeed promote both osteoblast and osteocyte differentiation with TE scaffolds. Moreover, the role of matrix stiffness, when combined with extrinsic mechanical loading, has not been investigated. To address this problem, the fourth research hypothesis to be investigated is “***A combination compression and perfusion mechanical stimuli will regulate both osteoblast and osteocyte differentiation***”. This hypothesis combines chapter 5 and 6.

1.3 Objectives and Hypotheses

The global objective of this Thesis is to develop an *in vitro* tissue regeneration strategy that can promote the development of both osteoblasts and osteocytes phenotypes within a porous trabecular-like structure. The first specific objective of this thesis is to investigate the effect of a 3D cell environment, extracellular matrix (ECM) stiffness and cell density on osteoblast-osteocyte differentiation *in vitro*. The second specific objective of this thesis is to investigate the effect of (1) delayed osteogenic differentiation, (2) scaffold stiffness and (3) 3D scaffold porosity on cell distribution, mineralisation and the formation of an osteoblast-osteocyte network. The third specific objective of this thesis is to design and fabricate a compression perfusion bioreactor system capable of applying combined compression and perfusion stimulus to TE scaffolds. The final specific objective of this thesis is to investigate the effect of combined matrix stiffness, oscillatory compression and perfusion mechanical stimuli on osteoblast and osteocyte differentiation within a porous TE scaffold. To address these objectives, four hypotheses have been defined, each of which will be underpin the research of Chapters 3-6 of this Thesis.

Hypothesis 1: Osteocyte differentiation is regulated by ECM stiffness and cell density within a 3D environment (Chapter 3).

Hypothesis 2: Initial cell seeding density and stiffness in 3D will promote uniform cell distribution and subsequent tissue formation throughout TE scaffolds (Chapter 4).

Hypothesis 3: Porous gelatin scaffolds represent the structurally different mechanical environments of trabecular bone *in vivo* (pores and struts) and will thereby promote both osteoblast and osteocyte development (Chapter 4).

Hypothesis 4: A combination of compression and perfusion mechanical stimuli will regulate both osteoblast and osteocyte differentiation in porous gelatin scaffolds (Chapter 5 and 6).

By testing each of these hypotheses, the research objectives outlined above can be answered and the proposed research will deliver significant advances in the understanding of osteoblast-osteocyte differentiation, bone tissue engineered scaffold development and bioreactor technology for bone regeneration approaches.

1.4 Thesis Structure

This thesis comprises the work completed for the duration of the candidate's PhD studies. A review of current literature is presented in Chapter 2, providing an in depth introduction to bone function and composition, bone cells and tissue development, and current approaches for bone tissue engineering. In particular previous bone tissue regeneration strategies incorporating bioreactor based technologies for tissue formation in TE scaffolds are presented. Chapter 3 investigates the effect of a 3D cell environment, extracellular matrix (ECM) stiffness and cell density on osteoblast-osteocyte differentiation *in vitro*, testing Hypothesis 1 of the Thesis. Chapter 4 investigates the effect of (1) delayed osteogenic differentiation, (2) scaffold stiffness and (3) 3D scaffold porosity on cell distribution, mineralisation and the formation of an osteoblast-osteocyte network, testing Hypothesis 2 and 3. Chapter 5 involves the design and fabrication of a compression-perfusion bioreactor system capable of applying controlled stimulation to TE scaffolds. Chapter 6 investigates the effect of combined compression and perfusion mechanical stimuli on osteoblast and osteocyte differentiation within TE scaffolds, using the bioreactor system designed in chapter 5, addressing the final Hypothesis of this Thesis. Finally Chapter 7 outlines the main findings of the thesis, places these in the context of current bone tissue engineering strategies and outlines recommendations for future research in this field.

Chapter 2: Literature Review

2.1 Bone

2.1.1 *Insight into bone biology and characteristics*

The skeleton provides a solid structure to support vital organs within the body and to bear the loads experienced during everyday activities, while maintaining a lightweight structure for efficient movement. Bone tissue is the main supporting structure of the skeletal system providing rigidity, strength and lightweight properties. These mechanical properties are attributed to organic proteins and mineral crystals, which are precisely ordered and structured to form a mineralized organic matrix that makes up bone tissue, as is described in detail below. Bone is a highly active material with the ability to reshape and remodel in response to external stimuli and thereby accommodates biomechanical forces imposed by everyday activities.

2.1.2 *Bone tissue composition*

Bone tissue is a porous composite material made up of an organic phase (35%) and a mineral phase (65%). The organic phase consists of 90% Collagen Type 1 and 10% noncollagenous proteins (NCPs). The collagen in bone is principally collagen Type I, along with trace amounts of Type III, IV and VI. Collagen is synthesized by osteoblast cells during the initial phase of bone formation, when polypeptide chains are released and assembled together into a right-handed coil, known as a triple helix, containing a structure that is stabilized by hydrogen bonds. NCPs such as osteocalcin, osteonectin, osteopontin and bone sialoprotein are the most abundant proteins in bone, which are also produced by osteoblasts. NCPs provide bonds between collagen fibrils, while also facilitating mineralisation and playing an important role in the calcification process by regulating the growth of mineral crystals in bone (Cowin 1989). The mineral phase is in the form of small crystals located within and between the collagen fibres. The crystals are made of impure hydroxyapatite, which are bound together between the collagen fibrils, see Figure 2-1. The mineral is produced by osteoblast

cells and occupies the spaces between the collagen (Cowin 1989). The physical attributes of each of these phases (i.e. quantity, quality, mechanical properties and interactions) determine bone structural and mechanical integrity. The overall size and distribution of these minerals is dependent on the spacing present in the collagen matrix, and thus plays an important role in determining the mechanical strength and load bearing capability of the human skeleton (Cowin 1989; McNamara 2011). Matrix formation occurs as collagen fibres cross-link together forming a solid scaffold for bone minerals and proteins. Regulation of the matrix is believed to be controlled by noncollagenous proteins, such as osteocalcin, osteopontin, alkaline phosphatase, fibronectin, bone sialoprotein, osteoprotegerin, osteonectin, and thrombospondin which can direct attachment of cells and hence control cellular activity (Cowin 1989).

2.1.3 Bone Structure and Hierarchical organisation

Bone is a complex and hierarchical solid that contains structures at multiple length scales (Cowin 1989), which work in concert to perform diverse mechanical, biological and chemical functions (Rho et al. 1998). At the organ level, structural organisation is dependent on the anatomical location and type of bone involved, see Figure 2-1. However, at the macrostructural level variances between bone types is dependent on the organisation of layers, or lamellae (Rho et al. 1998), see Figure 2-1. These lamellae are organised either into circumferential layers of bone (osteons), which surround the blood vascular supply (Haversian canal), or into single trabeculae, which are not vascularised (McNamara 2011).

In an adult skeleton 20% of bone tissue is known as trabecular bone while the other 80% is cortical bone. Cortical bone makes up the denser part, with a low porosity level between 5-10%. This is commonly found in long bones, making up the outer shafts and both ends of bone. At the micro-scale, cortical bone contains osteons, comprised of concentric layers of compact bone tissue containing a central blood vessel, located within the Haversian canal (Cowin 1989). The Haversian canal facilitates nutrients supply to osteocytes orientated about the canals (Cowin 1989).

Trabecular bone (spongy bone) is highly porous varying from 75-95% (Rho et al. 1998). It is mainly found in the interior ends of long bones, where it creates

a complex, three-dimensional structure. This structure is composed of plates and rods, known as trabeculae, and cavities filled with bone marrow. Cavities created by trabeculae allow for the supply of nutrients and removal of waste generated by the activities of bone cells. It has been hypothesized that the trabeculae tend to orientate themselves in the same direction as that where physiological forces are applied (Behrens et al. 2009; Wolff 1986; Frost 1990). This allows bone to withstand loads experience during everyday activities, while also providing a lightweight structure. Studies have reported elastic modulus of trabecular and cortical tissue in the range of 0.75 to 30 GPa (Choi et al. 1990; Rho et al. 1997; Townsend et al. 1975; Teo et al. 2006; Rho et al. 1993; McNamara 2011; McNamara et al. 2006).

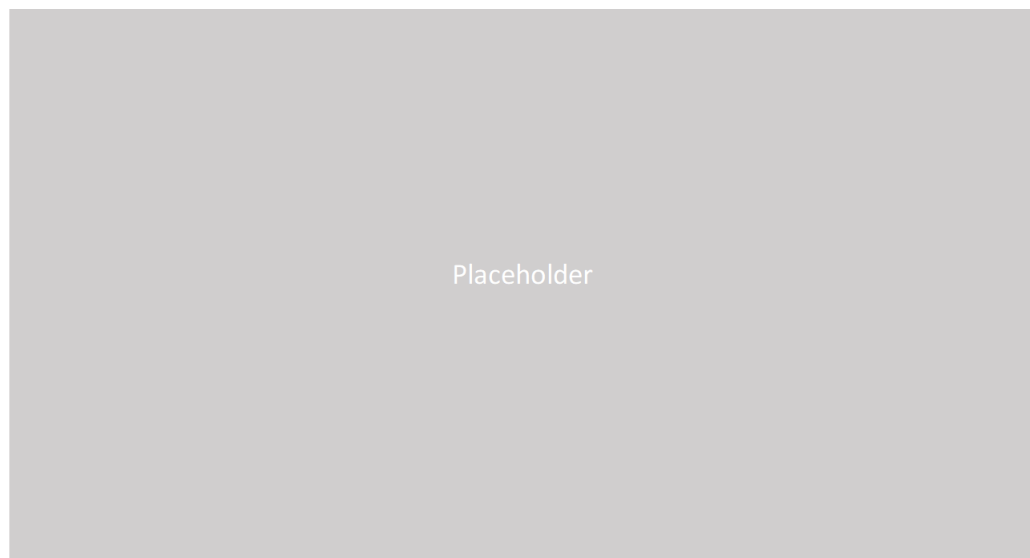


Figure 2-1: Hierarchical organisation of bone with different length scales, illustrating (a) collagen fibrils and hydroxyapatite crystals forming (b) lamellar bone consisting of (c) osteons and Haversian canals within (d) cortical and trabecular bone (Vaughan et al. 2012).

2.1.4 Bone cells and formation of bone extracellular matrix

Bone cells are responsible for maintaining the precisely ordered and structured environment of bone, and are primarily cells derived from either the osteogenic lineage (osteoblasts and osteocytes) or the monocyte-macrophage lineage (osteoclasts). This section describes the formation of a mineralised bone matrix from a bone cells perspective, starting off with osteoblasts laying down an organic

matrix, growth of the matrix into a composite material, through mineral crystal precipitation, and the embedding of mature osteocytes within the matrix.

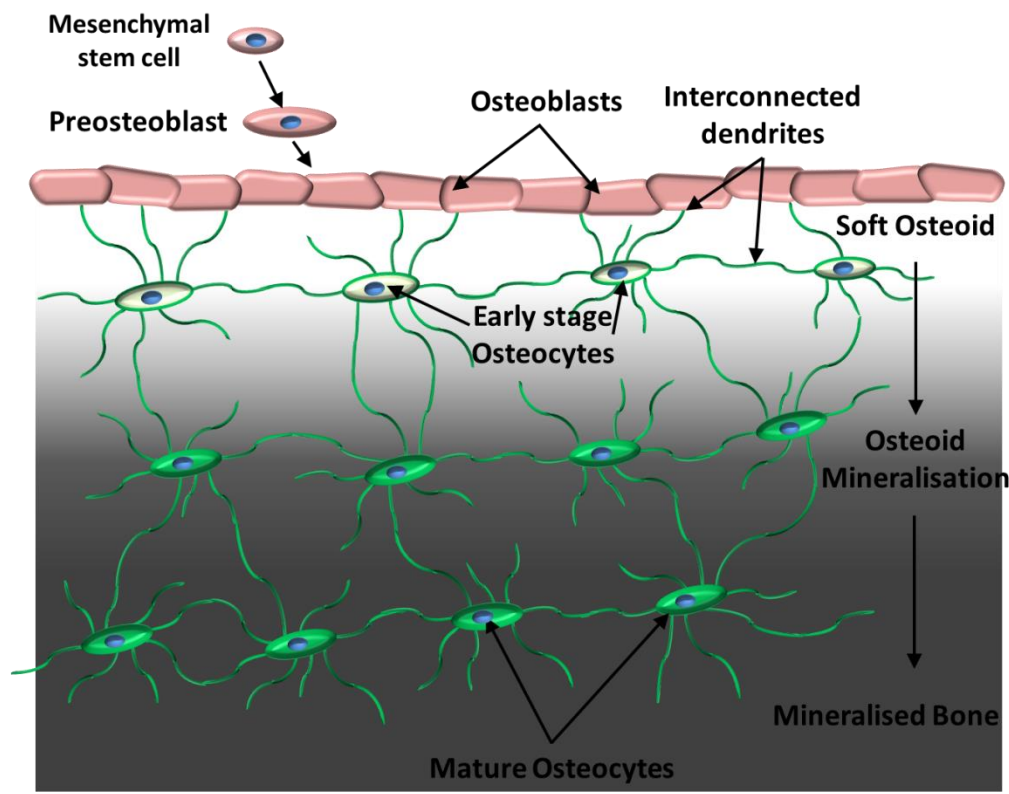


Figure 2-2: Schematic representation of MSC differentiating into pre-osteoblasts and producing osteoid on the bone surface. A fraction of these osteoblast become embedded, differentiating into early stage osteocytes, and hence into mature osteocytes as the osteoid mineralises.

2.1.4.1 Mesenchymal stem cell

Mesenchymal stem cells (MSCs) are multipotent stromal cells located in bone marrow and have the capacity to differentiate into various cell phenotypes, such as osteoblasts, chondrocytes and myocytes (Phinney & Prockop 2007). MSCs are characterised by a fibroblast-like morphology, comprised of a large round cell nucleus and small cell body (Jiang et al. 2002). They are capable of changing their morphology in response to their local environment, such as extending their cytoplasm into the surrounding matrix (McNamara 2011). MSCs start to differentiate towards osteoprogenitors cells when influenced by growth factors, cytokines, and physical stimuli (Undale et al. 2009). Mechanical stiffness represents an essential physical factor in regulating osteogenic differentiation and mineralisation in MSCs. MSCs cultured on 2D substrates of varied stiffness (0.1 –

40 kPa) have been shown to differentiate into various phenotypes, such as brain neurite cells or osteoblasts (Engler et al. 2006). Additionally, in 3D microenvironments, Huebsch et al showed that MSCs committed to osteogenesis in response to the stiffness of 3D environment predominantly at 11–30 kPa (Huebsch et al. 2010).

2.1.4.2 Pre-osteoblasts to mature osteocyte

Mesenchymal stem cells (MSC), located in the bone marrow, have the ability to differentiate into various cell types, such as osteoblasts, chondrocytes and myocytes cells (McNamara 2011). During normal bone physiology, under specific biochemical and mechanical stimuli, MSCs are recruited to the site of bone formation and start to differentiate along the osteogenic pathway to become pre-osteoblast cells. They typically spread out over the flat 2D surface of the bone in a cuboidal morphology, differentiating into active bone matrix-secreting osteoblasts (Franz-Odenaal et al. 2006). Osteoblasts contain a highly developed cytoskeleton, and are regarded as the main cells responsible for bone formation, as they secrete collagen, growth factors, cytokines and several proteins to support mineralisation (Cowin 1989). During the transition to a mature osteoblasts, a 26 fold increase in volume occurs from the osteoblast precursor to a mature osteoblast (Zouani et al. 2013). Mature osteoblasts lay down a soft collagen matrix known as osteoid, followed by mineral crystal deposition (Landis et al. 1996; Barragan-Adjemian et al. 2006). The mineral crystals deposited within this soft osteoid are small undeveloped hydroxyapatite (HA) crystals deposited within the space of the triple helical fibrils of collagen (Sapir-Koren & Livshits 2011). Once associated with collagen, the crystals grow within the collagen fibres, reaching sizes as large as 500 nm before coalescing to form the mineralized matrix (Landis et al. 1996) and will keep proliferating depending on the concentrations of the component ions in solution (Cowin 1989). A variety of proteins and enzymes are associated with this transition stage, including osteonectin, alkaline phosphatase, osteocalcin and bone sialoprotein.

2.1.4.3 Mature Osteoblasts - early stage osteocyte

During the formation of the new layer of osteoid, osteoblasts secrete matrix only at the bone-facing side, pushing themselves away from the surface as they produce matrix (Cowin 1989). Some of these osteoblast cells become trapped

within the secreted osteoid and thereafter differentiate towards early stage osteocytes and extend dendrites throughout the soft matrix, which form channels and interconnections with neighbouring osteoblasts and osteocytes (Dallas & Bonewald 2010). Engler et al, showed that the elastic modulus of this bone osteoid is $\sim 27 \pm 10$ kPa. This was measured by allowing seeded human osteoblasts (hFOB) cells to secreted matrix deposits on glass substrates for 7 days with measurements determined by atomic force microscopy (AFM) (Engler et al. 2006). *In vivo*, after ~ 10 days the soft osteoid matrix begins to increase in stiffness as mineral crystal growth occurs, due to continued release of ion phosphate from the mature osteoblasts on the surface and the differentiating osteocytes, which ultimately calcifies the osteoid (Barragan-Adjemian et al. 2006; Cowin 1989). The calcified osteoid forms a stiff dense mineralised matrix around the osteocyte. However, the osteocyte resides within a space (lacuna) in that matrix and the osteocyte dendrites reside within channels (canaliculi), both of which contain a pericellular noncollagenous matrix and fluid (Bonewald 2011; Dallas & Bonewald 2010). The osteocytes establish integrin connections with the matrix (McNamara et al. 2009).

2.1.4.4 Mature Osteocyte

Osteocytes are the most abundant cells in mature bone and are believed to be the most important regulator of bone mass and structure. Osteocytes are widely understood to act as biological sensors of mechanical forces experienced by the human body, due to physical actions such as walking and running (Verbruggen et al. 2012). Osteocytes are evenly distributed throughout the bone tissue, thus allowing them to communicate with other osteocytes and osteoblasts (McNamara 2011), see Figure 2-2. A study showed that osteocyte-to-osteocyte distance *in vivo* can vary from 10-40 μm in human bone (Hannah et al. 2010). While, osteocyte density can varied from $4 \times 10^4/\text{mm}^3$ close to the Haversian canal to $9 \times 10^4/\text{mm}^3$ at 80% of osteon radius (Hannah et al. 2010). The stiff calcified osteoid acts a mediator of mechanical stimulation to the osteocyte cell-ECM interactions within the lacunar-canalicular system (McNamara et al. 2009; Wang et al. 2007), whereas the pericellular matrix transmits forces due to load induced fluid flow in the pericellular space (Wang et al. 2007; You et al. 2001).

Mature osteocytes *in vivo* have been shown to deform in response to mechanical stimulation resulting in load induced fluid flow and cell-ECM interactions within the lacunar-canalicular system surrounding osteocytes (McNamara et al. 2009; Wang et al. 2007; You et al. 2001; Smalt et al. 1997; Verbruggen et al. 2013). Studies have also shown changes in gene expression that coincide with mechanical loading, where increased levels of early osteocyte markers, such as E11/gp38/podoplanin and dentin matrix protein 1 were expressed (Dallas et al. 2013; Bonewald 2011; Zhang et al. 2006). However, whether mechanical stimuli promote differentiation of early stage osteocytes into mature osteocytes has not been reported.

Osteocyte attachment to the pericellular space is achieved by collagen fibrils that attach directly to the cell process membrane via integrin-attachments (cell adhesion proteins) (You et al. 2004; Wang et al. 2007; McNamara et al. 2009). It has been proposed that integrins play an important role in amplifying the strains perceived by osteocyte dendrites as a result of fluid flow and the matrix stiffness (You et al. 2004; Haugh et al. 2015; Dallas et al. 2013).

As the early stage osteocyte differentiates towards a mature osteocyte, a change in the ultrastructure (ER and Golgi) results in a down regulation of protein synthesis (osteocalcin, bone sialoprotein, collagen type I, alkaline phosphatase, IGFs, integrins and periostin) and secretion, hence down regulation in genes representing bone markers (Franz-Odenaal et al. 2006). It is possible to distinguish between bone cell types by monitoring changes in expression of key bone marker genes (Franz-Odenaal et al. 2006). The changes in gene expression that represent a signature for transition towards an osteocytic phenotype include down regulation of collagen Type I, alkaline phosphatase, osteocalcin, bone sialoprotein, bone morphogenetic protein 2 (BMP-2) and osteoblast specific factor 2 (OSF-2) (Franz-Odenaal et al. 2006; Bonewald 2011; Rosser & Bonewald 2012). Expression of E11/gp38/podoplanin (E11), sclerostin (Sost) and osteocalcin, along with osteocyte specific molecules that regulate phosphate and bio-mineralisation, such as dentin matrix protein 1 (DMP1), fibroblast growth factor 23 (FGF23), matrix extracellular phosphoglycoprotein (MEPE), and PHEX are upregulated (Bonewald 2011; Franz-Odenaal et al. 2006; Barragan-Adjemian et al. 2006; Lee et al. 2014; Zhang et al. 2006; Dallas et al. 2013). Thus,

phenotypic markers, such as collagen Type 1 and OSF-2 in osteoblasts, and E11 and DMP1 in osteocytes, have provided a strong indicator of bone cell differentiation activity in many studies (Mullen et al. 2013; Ducky et al. 1997; Zhang et al. 2006; Krishnan et al. 2010; Rios et al. 2005; Narayanan et al. 2003). DMP-1, dendrite formation, calcium content and ALP have previously been used as an indicator of the osteoblast cell line differentiating towards a more osteocyte-like phenotype (Mullen et al. 2014; Uchihashi et al. 2013; Woo et al. 2011; Krishnan et al. 2010; Dallas & Bonewald 2010). Therefore, these were used in the studies of this PhD as an indicator of osteoblast-osteocyte differentiation.

2.1.4.5 Osteoclasts

Osteoclasts are responsible for bone resorption through their ability to secrete acid and specific degrading enzymes that dissolve bone (McNamara 2010). Osteoclast cells are mononuclear precursor cells originating from haematopoietic stem cells that are typically 20 to 100 μm in diameter and contain up to 50 nuclei (Horne 1995). Osteoclast formation occurs as neighbouring osteoblasts release membrane bound proteins RANKL (Receptor Activator of Nuclear Factor Kappa B Ligand) and macrophage cytokines (M-CSF). After resorption, osteoclasts undergo apoptosis and release growth factors that activate osteoblasts to form a new lay of osteoid within the resorption cavity (McNamara 2011).

2.2 Bone diseases and disorders

The majority of bone injuries (fractures) heal, eventually forming new bone with similar properties to the uninjured bone. However, pathological conditions or severe traumatic injuries, due to high impact loading, such as road accidents, can lead to large bone defects or non-unions that do not repair (Dimitriou et al. 2011). Osteoporosis is a disease in which the loss of bone mass occurs, leading to fractures, deformity, severe pain and in some cases complications that result in death (Johnell et al. 2004). The disease primarily affects post-menopausal women, though it is also seen in men. Common fractures such as hip, spine and wrist can require surgical intervention to somewhat restore bone function. Paget's disease is a chronic disorder that results in oversized and irregular shaped bones, with the added risk of fracture. In Paget's disease, the bone remodelling process is no longer in equilibrium, resulting in increased bone turnover. It is predominant in

the older generation, with a higher occurrence in men (Whyte 2006). Bone cancer is the development of abnormal cells in bone tissue, leading to the development of a tumour. Severe pain, joint and bone swelling are some of the symptoms. Depending on the extent of cancer, treatment may range from chemotherapy to surgery (Luger et al. 2005). In most cases associated with bone diseases or critical sized defects, improvement of patient's wellbeing and health requires specialised methods. Current treatments are based on autografts or allografts showing good compatibility and recognition by the host tissue. However, there have been concerns about second site morbidity, infection, additional surgery and the added risk of rejection (Yarlagadda et al. 2005; Jahangir et al. 2008).

2.3 Bone tissue engineering

2.3.1 Background

Tissue engineering is a fast growing field, which seeks to apply biology and engineering technologies to develop functional substitutes, to improve damaged or diseased tissues (Langer & Vacanti 1993). It strives to engineer tissue substitutes (constructs) derived from biomaterial scaffolds and the patient's own cells within a laboratory environment, hence ruling out the potential of rejection and the need for revision surgery (Langer & Vacanti 1993), see Figure 2-3. There is significant potential for tissue engineering approaches to generate functional *in vitro* bone tissue substitutes, for clinical repair of injured, aged or damaged diseased skeleton tissue.

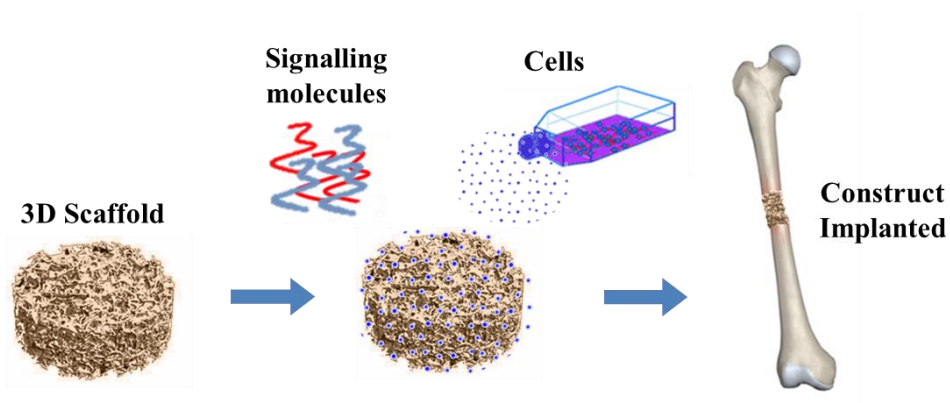


Figure 2-3: Schematic representation of the approach employed in bone tissue engineering. Cells and signalling molecules combined with a scaffold *in vitro* to enhance tissue formation before being implanted.

Bone TE relies heavily on biomaterials to deliver the appropriate environment for the regeneration of tissues (O'Brien 2011). 3D Biomaterial scaffolds act as an artificial extracellular matrix template representing the physical architecture, which strive to enhance cell adhesion, proliferation and differentiation (Mitchell & Tojeira 2013; Murphy et al. 2013) and facilitate cell interactions and the formation of bone-extracellular matrix to provide structural support.

A successful tissue engineered transplant depends on the construct being able to fulfil the function of bone in the environment for which it is needed (Gerhardt & Boccaccini 2010). Replication of key features, such as biocompatibility, biodegradability and scaffold structure are essential for host integration with a biomaterial (Stevens 2008; Matassi et al. 2011; Gerhardt & Boccaccini 2010; O'Brien 2011). A biomaterial can be considered biocompatible if it performs without eliciting an immune or inflammatory response, which may result in future problems or scaffold failure (Rhodes 2004). A biomaterial that is non-toxic, degradable and biologically active will ultimately integrate with the surrounding tissue and in time fully degrade. Whereas, if the biomaterial is toxic, non-degradable and biologically inactive the host tissue surrounding the biomaterial may recognise the scaffold as a foreign body, reject the construct and hence lead to localised necrosis when implanted *in vivo*. Biodegradability enables and controls the rate at which the scaffold degrades over time, allowing the scaffold to remain long enough for extracellular matrix regeneration before being ultimately replaced by native tissue (Haugh 2009; Yin et al. 2003). However, if degradation occurs too fast inflammation may occur. Factors that determine these responses are related to material type and scaffold structure (Gunatillake & Adhikari 2003). The scaffold architecture plays a significant role in the mass transport, and the pore structure helps morphology, growth and differentiation towards the desired phenotype (Haugh 2009). Cell survival and proliferation in the interior of the scaffold relies on nutrient transport upon initial implantation until the onset of vascular invasion (A.R. Amini et al. 2012). Furthermore scaffold architecture also significantly affects the mechanical properties of scaffolds, with porosity determining initial mechanical stability and permeability (W L Grayson et al. 2010). Currently, bone tissue engineering scaffolds are made from a broad range of bulk materials described below.

2.3.2 *Types of biomaterial for bone TE*

Three types of biomaterials are commonly used in bone tissue engineering, ceramic, natural and synthetic biomaterials.

Ceramic scaffolds in tissue engineering comprise of bioactive inorganic materials that replicate innate characteristics of bone, such as hydroxyapatite and calcium phosphate (Yuan et al. 2010; Gerhardt & Boccaccini 2010). However, the brittle nature of ceramics has meant that, when the scaffolds are subjected to load bearing applications *in vivo*, they can fail (Stevens 2008). Ceramic scaffolds tend to be comprised of hard brittle materials such as calcium, giving them high stiffness but low ductility. Due to their chemical composition, which is close to bone, these scaffolds have shown good osteoconductivity (Akita et al. 2004). Hydroxyapatite is a commonly used material, due to controlled degradation rate and osteoinductivity.

Synthetic biomaterials are materials, such as polystyrene, poly-L-lactic acid (PLLA), polyglycolic acid (PGA) and poly-DL-lactic-co-glycolic acid (PLGA) (O'Brien 2011). They can be fabricated into fibrous meshes, porous sponges or foams, composed of tailored architecture, various shapes, with desired pore morphologic features conducive to tissue in-growth (O'Brien 2011; Gunatillake & Adhikari 2003; Matassi et al. 2011; Stevens 2008; Yu et al. 2015). Furthermore, varying of the polymer characteristics allows for control over the degradation characteristics, while fabrication methods, such as injection and compression moulding, mean they can be easily shaped into the desired tissue or organ (Gunatillake & Adhikari 2003; O'Brien 2011). However, synthetic polymers have a risk of rejection due to reduced bioactivity (O'Brien 2011). Also, problems exist with the degradation process of PLLA and PGA reducing the local pH level, and hence leading to an inflammatory reaction, damaging cell and tissue health (Liu et al. 2006).

Natural polymers in tissue engineering are attractive, due to their versatility and the fact that they have received FDA approval for use in joint replacements (Murphy et al. 2013). Their mechanical properties can be tailored to suit various applications, along with being fabricated into various shapes and geometries that are conducive to tissue in-growth (Gunatillake & Adhikari 2003).

Certain natural polymers, such as collagen, gelatin, alginate and fibrin can be found in the ECM in nature (O'Brien 2011; de la Puente & Ludeña 2013). Consequently these materials show great biocompatibility due to their surfaces containing ligands and peptides appropriate for cellular attachment and cellular scaffold interactions (Harley & Gibson 2008). Furthermore, their natural properties make them more biocompatible and biodegradable compared to ceramic biomaterials.

2.3.3 Gelatin as a biomaterial

Gelatin is heat-denatured collagen, formed through hydrolysis, consisting of an almost identical composition to collagen (Yin et al. 2003). The denaturing process can evade the risk of immunogenicity and pathogen transmission associated with collagen (X. Liu et al. 2009). Furthermore, high costs are associated with the purification and large scale production of collagen, making the use of gelatin in place of collagen very desirable in cell culture (Paguirigan & Beebe 2006). Gelatin, at room temperature, forms a physical gel, while at 35 °C, gelatin chains undergo relaxation, becoming labile and gradually diffusing, forming a dissolved solution with a liquid consistency. Studies have commonly used gelatin to form scaffolds or in bone regeneration research (Yamada et al. 2013; X. Liu et al. 2009; Amini & Nair 2012; Sachar et al. 2012; Machado et al. 2007; Y. Liu et al. 2009; Ferreira & Padilla 2013). These studies demonstrated the use of gelatin to fabricate different types of bone TE scaffolds, such as gelatin β -TCP sponges enhancing bone regeneration in large bone defects (Yamada et al. 2013) or 3D nanofibrous gelatin scaffolds seed with osteoblasts demonstrating uniform mineral and collagen distribution (Sachar et al. 2012). While, gelatin gels were shown to promote the adhesion, spreading, and 3D growth of encapsulated MC3T3-E1 cells (Amini & Nair 2012). A composite chitosan–gelatin–chondroitin porous scaffold was shown to provide an environment for osteogenic differentiation of MSCs, while also enhancing cellular proliferation (Machado et al. 2007). For this thesis, gelatin was selected as the main biomaterial in the fabrication of scaffolds.

2.3.4 Hydrogel scaffolds in TE

Hydrogels are 3D networks of long polymer chains that are highly hydrophilic monomeric blocks. Water can penetrate in between the polymer chains of the

polymer network, subsequently causing swelling and the formation of a hydrogel (Peppas et al. 2006; Langer & Peppas 2003) with water forming more than 90% of the hydrogel weight. Hydrogels can be fabricated from natural polymers, such as collagen, agarose, alginate, Matrigel, and gelatin (Thorpe et al. 2013; Liu Tsang et al. 2007; Alsberg et al. 2001; Liang et al. 2011; Chen et al. 2013; Thorpe et al. 2008). An important feature in hydrogels is the direct homogenous encapsulation of cells within a 3D structure. This is related to the mesh size, which is smaller than the cell and therefore “encapsulates” the cells inside the gel (Nicodemus & Bryant 2008; Zisch et al. 2003; Chiu et al. 2011; Sutter et al. 2007). The mesh size is a measure of the distance between crosslinks and influences diffusive properties through the hydrogel. Typical mesh sizes for crosslinked polyethylene glycol (PEG) hydrogels used in cell encapsulation are in the range of ~40 to 200 Å (10^{-10} m) (Nicodemus & Bryant 2008). However, hydrogels are not appropriate for load bearing applications, such as treatment of bone defects, due to their low mechanical properties and load bearing capability (Levato et al. 2014). *In vivo* studies have investigated cell-laden hydrogels as therapeutics for soft tissue defects, such as diabetic ulcers, skin wound healing or salivary glands (Hwang et al. 2013; Chen et al. 2015; Pradhan-Bhatt et al. 2014) or cancer research for tumour growth suppression (Yan et al. 2016).

2.3.5 Achieving a porous scaffold architecture

In bone TE scaffolds, geometry is an important parameter for dictating the mechanical environment within scaffolds (Murphy et al. 2010). Porous scaffolds have shown great potential for temporary support for the transplantation of specific cells and tissues, while acting as three-dimensional analogues of the extracellular matrix (ECM) (Harley et al. 2007; Hou et al. 2003). For porous scaffolds some of the common approaches are gas foaming, leaching and lyophilisation.

A study used gas foaming salt to form a porous poly (L-lactic acid) PLLA scaffold (Nam et al. 2000). A mixture of PLLA-solvent gel, containing ammonium bicarbonate salt particles, was immersed in a hot water solution and permitted the expansion of ammonia and carbon dioxide within the polymer matrix forming interconnected pores (Nam et al. 2000). Hepatocyte cells seeded

on the scaffolds demonstrated about 95% seeding efficiency and up to 40% viability at day 1. Another study created porous scaffolds through microsphere-sintering and porogen-leaching, involving the addition of particles and a solvent (NaCl) to a polymer. The solvent is heated and evaporated and hence the particles are dissolved in water leaching out (A.R. Amini et al. 2012). Porous scaffolds from this study displayed increased oxygen diffusion, pre-osteoblast cell infiltration, proliferation, and survival throughout the entire scaffold, along with homogenous mineralization *in vitro*.

Lyophilisation or freeze-drying is a process that involves freezing a slurry precipitate under a vacuum (O'Brien et al. 2005; Haugh et al. 2010). A change in pressure and temperature causes ice to sublime producing a continuous interpenetrating network of ice and solute. The ice crystal structure mirrors the pore structure of the scaffold, allowing for the pore structure to be controlled by altering the process (the rate of cooling can control the size and volume fraction of the pores). High porosities of 90-99% and pore sizes ranging from 100-350 μm can be achieved using this technique (Haugh et al. 2010). Studies showed a high scaffold porosity of ~99% allowed for high cell efficiencies and numbers to be achieved (Murphy et al. 2010; Haugh et al. 2011), along with upregulation of late stage bone formation markers, osteopontin and osteocalcin and increased levels of mineralisation (Keogh, O'Brien, et al. 2010; Murphy et al. 2015).

2.3.6 Varying scaffold stiffness through crosslinking

Crosslinking can be used to vary and stabilise polymer scaffold mechanical properties by varying the degree of chemical bonds formed between collagen molecules and hence restricting fibres from sliding over each other under mechanical loading (Lee et al. 2001). Crosslinking can also be used to control the degradation rate of scaffolds, as the crosslinks need to be broken down before degradation can occur (Nicodemus & Bryant 2008). Biochemical and biophysical crosslinking are considered the two main groups associated with crosslinking.

Biochemical crosslinking, such as 1-Ethyl-3-(3-dimethylaminopropyl) carbodiimide EDAC crosslinking, forms isopeptide bonds between the carboxyl and amino groups from different residues. The two residues must be in direct contact *in situ*, resulting in no additional components to the final crosslinked

product, and hence referred to as the formation of “zero length” crosslinks. However, the bio-product ammonia is cytotoxic to cells and needs to be removed before the addition of cells. Studies have commonly used EDAC crosslinking to stabilise freeze-dried collagen-glycosaminoglycans (CG) scaffolds for research in bone regeneration (Keogh, O’Brien, et al. 2010; Murphy et al. 2012; Grover et al. 2012; Haugh et al. 2011; Curtin et al. 2012; Murphy et al. 2015).

Certain types of crosslinkers allow for direct crosslinking of scaffolds in conjunction with cells. One study created cell-laden gelatin methacrylate (GelMA) hydrogels, using UV irradiation in the presence of a photoinitiator to crosslink the gelatin (Nichol et al. 2010). However, depending on the duration, UV exposure can be potentially damaging to cells due to photoinitiators molecules and radicals (Nicodemus & Bryant 2008). Another crosslinker, polyethylene glycol (PEG) allows for direct mixing of the crosslinker with cells and the hydrogel solution, allowing for cell encapsulation, tuneable mechanical properties, excellent cell viability and biocompatibility (Liang et al. 2011). However, this type of crosslinking reduces the scaffolds degradation capability *in vivo* (Chen et al. 2013) and cells typically cannot attach too or significantly degrade these crosslinks (Nichol et al. 2010; Chatterjee et al. 2010).

Microbial transglutaminase (mTgase) is an enzyme that catalyses the acyl-transfer reaction between the amino group of lysine and the carboxamide group of glutamine in proteins. Ajinomoto Corporation Inc. Japan has made available a microbial form of transglutaminase, which is suitable for industrial and laboratory use. One unit of enzyme (U) will catalyse the formation of 1.0 μmol hydroxamate per minute from Na-CBZ-Glutaminylglycine and hydroxylamine at pH 6.0 and 37 °C. Studies have shown that enzymatic crosslinking can be achieved in gelatin by catalysing the formation of a crosslink between amino acid residues in adjacent collagen molecules (Chen et al. 2013; Kuwahara & Yang 2009; Yung & Wu 2007; Amini & Nair 2012; Tan et al. 2014). This crosslinker allows for direct cell encapsulation within gelatin hydrogels, while also stabilising gelatin’s low melting temperature (35 °C) and providing control over mechanical properties depending on the crosslinking concentration (Tan et al. 2014). Furthermore, studies have shown good cell survival and biocompatibility within the hydrogels, while also mimicking *in vivo* crosslinking, by creating crosslinks between

collagen molecules without altering the natural characteristics of the material (Bertoni et al. 2006; Yung & Wu 2007; Orban et al. 2004).

2.3.7 Measuring mechanical properties

Compressive testing is a commonly used method to determine the mechanical properties of hydrogels and porous scaffolds in bone tissue engineering (Keogh, O'Brien, et al. 2010; Sittichokechaiwut et al. 2009; Kim et al. 2007; Correia et al. 2012; Naito & Dohi 2011; Hwang et al. 2013; Chatterjee et al. 2010). For soft hydrogels, the material often behaves as a linearly elastic material for strains under 10% and hence the modulus can be determined from the slope of the stress-strain curve in that region (Shin et al. 2014; Chatterjee et al. 2010). However, at strains greater than 10%, the material behaviour is non-linear and is more appropriately analysed as a hyperelastic material, using Neo-Hookean law. Porous scaffolds, such as collagen-glycosaminoglycans (CG) scaffolds, resemble low-density open-cell foams characterised by a linear elastic region (<5 % strain), collapse plateau and densification regimes (<80 % strain) (Harley et al. 2007), see Figure 2-4. The linear elastic-collapse plateau transition is observed at approximately 5% strain. For this reason, studies of the mechanical properties of porous scaffolds determined the compressive modulus in the 2-5% strain region (Harley et al. 2007; Gibson & Ashby 1990). While, in porous hydrogels compressive modulus has been determined at less than 10% strain (Sokic et al. 2014; Hwang et al. 2010).

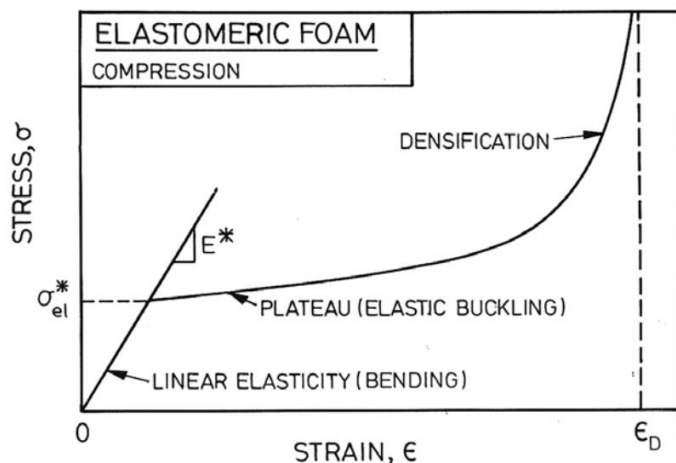


Figure 2-4: Illustration of the uniaxial stress-strain curve for an elastomeric cellular solid in compression. The graph shows the linear elastic region up to

approximately 5% strain, the pore collapse plateau and densification regimes up to 80% (Harley et al. 2007)

2.3.8 Commercially available biomaterials for bone tissue engineering

Currently, numerous scaffold based biomaterials are commercially available for human clinical applications. Table 1 illustrates examples of commercially available non-seed scaffolds for bone regeneration.

Defect type	Company	Scaffold type	Surgery
Infuse	Medtronic	Recombinant engineering bone morphogenic protein on a collagen sponge	Spinal fusion, tibial shaft fractures or oral-maxillofacial
Hydroset	Stryker	Calcium phosphate cement injected as a putty	Fills bony voids or gaps
Vitoss	Stryker	Porous (90%) beta-tricalcium phosphate	Fills bony voids or gaps
Bonesave	Stryker	80% tricalcium phosphate / 20% hydroxyapatite granules	Fills bony voids or gaps
Integra Mozaik	Integra LifeSciences	20% Type I Collagen and 80% Beta-Tricalcium Phosphate	Fills bony voids or gaps
chronOS[®]	DePuy Synthes	Beta-tricalcium phosphate	Oral-maxillofacial, Craniofacial
HydroxyColl	SurgaColl	Collagen-Hydroxyapatite scaffold	Fills bony voids or gaps

Geistlich Bio-Oss	Geistlich Biomaterials	Hydroxyapatite calcium phosphate particles	Oral-maxillofacial
--------------------------	------------------------	--	--------------------

Table 1: Table of commercially available bone scaffolds substitutes.

These commercially available biomaterials have shown favourable results in spinal fusion, tibial shaft fractures, craniofacial or oral-maxillofacial surgery, filling bony voids or gaps created during clinical surgery or due to osseous defects from traumatic injury. However, none of these products have completely replaced bone autografts as the ‘gold standard’, due to limitations with implantation in large size defects or limited load bearing capabilities, as a result of been limited to amorphous pastes, particles and putties (Smith & Grande 2015). Furthermore, *in vivo* animal studies have shown implantation of biomaterial/scaffolds can lead to the host body implementing a foreign-body response and hence forming a fibrous tissue encapsulation around the construct, inhibiting optimal tissue regeneration and integration (Ami R Amini et al. 2012; O’Brien 2011; Lyons et al. 2010; Massari et al. 2015; Polo-Corrales et al. 2014; Anderson 2001). Bone biomaterial scaffolds need to be multi-functional, providing strong bioactivity, compatibility and an osteoconductive matrix for host osteogenic cells to produce bone, and provide faster integration with host tissue (Matassi et al. 2011).

2.3.9 Combining cells with biomaterial scaffolds (*In vitro*)

For scaffolds to reach the next-generation in clinical applications requires further enhancement of their osteogenic capacity to provide faster integration with host tissue compared to non-seeded scaffolds (Matassi et al. 2011). This could be achieved by combining cells with scaffolds and through *in vitro* culturing to synthesize new tissue “constructs” that mimic the ECM for which the desire tissue/organ is required.

Combining cells with scaffolds is mainly achieved through peripheral seeding or cell encapsulation. Peripheral cell seeding involves covering each side of a pre-fabricated scaffold with cells, and hence leaving cells to migrate into the scaffold from the “periphery” (Haugh et al. 2011). Numerous studies used this

approach, as it allows for the fabrication of complex scaffold feature, containing tailored architecture, while maintaining control of the scaffold composition (Yuan et al. 2010; Gerhardt & Boccaccini 2010; Akita et al. 2004; O'Brien 2011; Gunatillake & Adhikari 2003; Matassi et al. 2011; Stevens 2008; Yu et al. 2015; Tierney et al. 2009). Cell encapsulation within scaffolds is achieved by mixing cells with a dissolved polymer solution and allowing the solution to gel, forming a hydrogel scaffold that surrounds the cell in a 3D matrix at the same time as combining the cells (Nichol et al. 2010; Amini & Nair 2012). This method provides a simple, fast method for the homogenous distribution of cells throughout the hydrogel scaffolds. Large scaffolds can be moulded into the shape of tissue or organ, containing high cell seeding efficiencies (Chen et al. 2013).

2.3.10 Clinical success of cells combine with scaffold biomaterials

To date, studies have shown the potential of combining cells with biomaterial scaffolds for successful bone regeneration in human trials. Table 2 illustrate examples of clinical successes using 3D biomaterial scaffolds combined with cells in healing human bone defects.

Defect type	Patient No.	Scaffold	In vitro culture duration	Results/ healing times
Long bone defect (Marcacci et al. 2007)	4	Bone marrow stroma cells seeded onto porous hydroxyapatite scaffolds	Overnight	Complete fusion between the implant and the host bone was observed 5 to 7 months after surgery
Long bone defect (Quarto et al. 2001)	3	Osteoprogenitor bone marrow cells seeded on porous hydroxyapatite scaffolds	Not published	Callus formation along the implants and good integration at the interfaces with the host bones 2 month after surgery.
Maxillary Defect	2	Maxillary bone cells seeded on natural bone	40 days	32% new bone formation observed after 8 months

(Springer et al. 2006)		mineral		
Maxillary defect (Schimmin g & Schmelzeisen 2004)	27	Mandibular periosteum cells seeded on a polymer fleece (Ethisorb, Ethicon)	7 days	18 out of 27 patients revealed mineralized trabecular bone with remnants of the biomaterial proved 3 months after augmentation.
Maxillary Defect (Shayesteh et al. 2008)	6	hMSCs seeded on beta tricalcium phosphate/hydroxy apatite scaffold	1 day	The mean percentage of newly formed bone was 41.34% with clinically osseointegration seen after 4 months.
Mandibular defect (Pradel et al. 2006)	11	Primary osteoblasts seeded on porous collagen matrix/scaffold (Osteovit ®)	3-4 days	After 12 months ossification results had higher mechanical properties compared to controls
Mandibular Defect (Meijer et al. 2007)	10	Hydroxyapatite Scaffold	Not published	New tissue formation only observed in 1 patient.
Mandibular Defect (Meijer et al. 2008)	6	HMSCs seeded on hydroxyapatite scaffolds (Pro-Osteon 500)	7 days	Reduced bone formation in patients with intra-oral osseous defects compared to increased ectopic bone formation in mice.
Mandibular Defect (d'Aquino et al. 2009)	17	Dental pulp stem/progenitor cells seeded on collagen sponge	Cell combined during surgery	Optimal bone regeneration was evident one year after grafting.

scaffold				
Avulsion of the thumb	1	Porous hydroxyapatite (Pro-Osteon 500)	Cell combined during surgery	Functional restoration of a stable and biomechanically sound was achieved
(Vacanti 2001)				

Table 2: Reported outcomes of *in vivo* studies exploring the potential of cell – seeded biomaterial scaffolds cultured *in vitro* prior to implantation

Overall, the results from these studies demonstrate that cells harvested from patients and combined with biomaterial scaffolds have been successfully implanted. However, only in a few studies enhanced integration and bone formation was observed, while others were not able to achieve these results compared to animal studies. Furthermore, none of these constructs were implanted in load bearing areas without the assistance of fixtures or clamps, while the majority were restricted to short term *in vitro* culture (1-3 days), providing limited time for cells to fully populate and produce tissue within the scaffold. Whereas, long term *in vitro* studies have shown that cultivation of scaffolds with bone cells can sustain substantial cell population and mineral content (Gleeson et al. 2010; Keogh et al. 2011; Keogh, O’Brien, et al. 2010; Curtin et al. 2012; Correia et al. 2012; Castillo Diaz et al. 2014; Tan et al. 2014; Chatterjee et al. 2010; Shin et al. 2014; Kim et al. 2007; O’Brien 2011). This newly formed tissue *in vitro*, has been shown to promote increased scaffold mechanical properties (Keogh, O’Brien, et al. 2010; Sittichokechaiwut et al. 2009; Kim et al. 2007; Correia et al. 2012; Naito & Dohi 2011) and after implantation, higher host bone formation compared to native cells only (Eniwumide et al. 2007; Yu et al. 2015). This represents a potential approach for the further enhancement of constructs that could be placed in load bearing locations. However, currently this approach is limited when the tissue in the scaffold acts as a barrier to remodelling and osseointegration with the host tissue (Lyons et al. 2010; Alhag et al. 2012), along with complications in establishing a solid connection between the material’s surface and the host bone tissue (Anselme 2000). Prior to implantation during the *in vitro* culture stage

tissue formation is restricted to areas within the scaffold, leading to inconsistent tissue formation, effecting cell viability in scaffold cores, overall bulk mechanical properties, which at the stage of *in vivo* culture effects integration with the host tissue and the scaffolds load bearing potential (Sikavitsas et al. 2005; Keogh et al. 2011). In order to overcome these deficiencies in TE constructs might require the application of applying appropriate biophysical stimulus through bioreactor technology.

2.4 Mechanical/biophysical stimulation and bone regeneration

Bone tissue repair, regeneration and remodelling is modulated by biophysical stimulation according to the local tissue environment (Chao & Inoue 2003). *In vivo* bone is constantly exposed to biophysical stimulation, in the form of mechanical forces induced by muscular contraction and body movements, resulting in changes in mechanical stimulation at the cellular level, such as hydrostatic pressure, direct cell strain, fluid flow-induced shear stress, and electric fields (Rauh & Milan 2011). Subsequently, these mechanical forces govern bone adaptation to simultaneously maintain its lightweight structure and essential properties (stiffness, energy absorption, tensile, etc). Mechanical forces are ever-present between cells and their surroundings, providing a crucial set of “cues” that are important in controlling cell structure, differentiation, and function (Baker & Chen 2012; Keogh, O’Brien, et al. 2010) and ensuring that the appropriate biological response needed to resolve the situation is implemented. Researches have sought to identify and replicate these cues and hence implement them under *in vitro* conditions.

2.4.1 2D Substrate / 3D matrix stiffness

Substrate (2D) or matrix (3D) stiffness represents an important form of stimuli in the ECM environment. Mechanical stiffness has been shown as an essential physical factor in regulating osteogenic differentiation and mineralisation in cell types such as myoblasts, osteoblasts, MSCs and embryonic stem cells (Mullen et al. 2013; Engler et al. 2004; Tan et al. 2014; Mc Garrigle et al. 2016; Chatterjee et al. 2010; Engler et al. 2006; Huebsch et al. 2010; L. S. Wang et al. 2012; Evans et al. 2009). Furthermore, mechanical stiffness has also been shown to effect a variety of cell behaviours such as migration (Zaman & Trapani 2006),

proliferation (Hadjipanayi et al. 2009), and differentiation (Tan et al. 2014; Lo et al. 2000).

The effect of (2D) substrate stiffness has been demonstrated in the differentiation of MSCs into various phenotypes when cultured on substrates of varied stiffness (0.1 – 40 kPa) (Engler et al. 2006). Cells on soft substrates (0.1 kPa) were found to mimic brain neurite cells, demonstrating a branched morphology, while a stiff substrate illustrated a spread morphology that mimicked an osteoblast morphology (40 kPa). Furthermore, Mullen et al demonstrated the effect of varying 2D substrate stiffness on MC3T3-E1 osteoblastic cells. Cells were shown to favour osteocyte differentiation on relatively soft ECM substrates (0.286 kPa) (confirmed by a dendritic morphology, mineralisation, reduced ALP, Col type 1 and OSF-2 and increased DMP-1 and Sost expression) compared to cells on stiffer substrates (Mullen et al. 2013). Furthermore, 2D substrate stiffness has also been shown to effect the proliferation rate of MSCs seeded on collagen type-1 gels, with soft substrates (1 kPa) reducing the proliferation rate compared to MSCs on stiff substrates (15 kPa) (Park et al. 2011).

The previous research focused on cells seeded on flat 2D surfaces. However, substrate stiffness has been shown to effect cells in 3D porous cell seeded scaffolds. A study showed the influence of scaffold stiffness on osteoblast distribution in peripherally seeded CG scaffolds, showing increased cell number and enhanced cellular distribution in high stiffness scaffolds (1.4 and 1.8 KPa) compared to a low stiffness after 7 days (~0.5 kPa) (Haugh et al. 2011). While, a study also showed that osteoblasts seeded on CG scaffolds at a low scaffold stiffness (0.48 kPa) promotes cell mediate contraction, enhancing mineralisation and mechanical properties, compared to high stiffness scaffolds (1.17 and 1.37 kPa) after 42 days (Keogh, O'Brien, et al. 2010).

In cell encapsulated 3D hydrogels, matrix stiffness has been shown to promote osteogenic protein and mineral production (Castillo Diaz et al. 2014; Tan et al. 2014; Chatterjee et al. 2010; Shin et al. 2014). A study encapsulated myoblasts cells in mtgase-gelatin hydrogels at low (1.58 kPa) and high (32.22 kPa) matrix stiffnesses (Tan et al. 2014). A low stiffness was found to promote cell proliferation, while the high stiffness facilitated osteogenic differentiation

(Tan *et al.*, 2014). Furthermore changes in cell morphology were observed, with osteoblast-like cells became elongated at low stiffnesses of 1.58 kPa and spherical at higher stiffnesses (32.32 kPa) (Tan *et al.*, 2014). Chatterjee et al encapsulated MC3T3-E1 osteoblasts in poly(ethylene glycol) dimethacrylate (PEG) hydrogels at varied stiffness (10-300 kPa) and found gels with moduli over 225 kPa enhanced osteogenesis, as determined by ALP and calcium phosphate expression (Chatterjee et al. 2010).

These studies have shown the effect of 2D substrate and 3D matrix stiffness on cell behaviour and should be taken into account when engineering implantable 3D constructs (Evans et al. 2009). Control of substrate stiffness in TE scaffolds may act as an option for priming scaffolds to apply biophysical stimulus to cell and hence regulate cellular responses on scaffolds during cultivation of a construct *in vitro*.

2.4.2 Fluid flow

In vitro studies have shown that bone cells are sensitive to flow-induced shear stress, as observed in osteoblasts (Keogh et al. 2011; Jaasma et al. 2008; Ban et al. 2011), osteocytes (Owan et al. 1997; You et al. 2001; Smalt et al. 1997) and bone marrow cells (Gomes et al. 2003). Fluid flow is known to induce mechanical stimulation of cells within scaffolds, enhancing matrix production and providing waste and nutrients exchange, negating problems associated with cell death in scaffold cores (Keogh, O' Brien, et al. 2010; Cartmell & Porter 2003; Gardel et al. 2013; Grayson et al. 2008; Jaasma et al. 2008; Partap et al. 2010). As bone is mechanically loaded *in vivo*, fluid within bone experiences a heterogeneous pressurisation in response to the deformation of the matrix, leading to changes in pressure gradients after load removal, forming fluid motions that are dynamic and oscillatory in nature (Du et al. 2009; Jacobs et al. 1998). Oscillatory flow has been shown to induce mechanical stimulation of cells through shear stress within the construct, improving matrix production compared to steady flow (Jaasma et al. 2008), while also enhancing cell distribution and uniformity (Wendt et al. 2003; Du et al. 2009). However, other *in vitro* experiments have shown that pulsating and static flow exhibit higher stimulatory responses compared to oscillating flow

(Bacabac et al. 2004; Fröhlich & Grayson 2009). This suggests that there may be multiple cellular reactions involved in the cell's response to fluid flow.

2.4.3 Matrix strain

Bone cells are also sensitive to mechanical strain, and can transduce these mechanical stimuli into biochemical responses (Zhang et al. 2006; Klein-Nulend et al. 2012; Saunders et al. 2006; Bacabac et al. 2004). Mechanical strain has been shown to promote differentiation of MSCs into osteoblasts (Li et al. 2015), while also increasing the production of calcium (Lohberger et al. 2014). Short term mechanical cyclic loading (0.05 Hz, 4 kPa) has been shown to enhance osteogenic pre-differentiation of human bone marrow-derived stem cells in 3D constructs, resulting in improved osseous integration of tissue engineered grafts in bone defect healing (Matziolis et al. 2011). While, cyclic compressive loading (5% strain, 1 Hz) in polyurethane scaffolds seeded with MLO-A5 osteoblastic cells, led to an upregulated of type 1 collagen, osteopontin (OPN) and osteocalcin (OCN) and an increased in calcium deposition compare to those grown under static conditions (Sittichokechaiwut et al. 2009). Huebsch et al, showed that stem cell behaviour can also be controlled *in vitro* by manipulating the elasticity of hydrogels, demonstrating that MSC osteogenesis *in vitro* can be controlled by modifying the hydrogel's elastic modulus with the higher stiffness hydrogel (60kPa) promoting bone formation (Huebsch et al. 2015)

2.4.4 Combined stimuli

The previous studies illustrate the use of individual stimuli to enhance tissue formation. However, *in vivo* bone regeneration is modulated by a combination of different types of biophysical stimulation according to the local tissue environment (Chao & Inoue 2003). Bouet et al showed by combining perfusion (2 μ L/min) and compression (4 μ m amplitude, at 3 Hz) stimulus to ceramic scaffolds seeded with mouse calvarial cells, lead to osteoblast differentiation and the formation of a mineralised matrix (Bouet et al. 2015). Liu et al demonstrated that compression (10% strain, 0.5 Hz, 4 times/day, 2 h/time with 4 h of rest thereafter) and perfusion (10 ml/min, 0.5 Hz) loading applied to polyurethane-based meniscus scaffolds seeded with human bone mesenchymal stromal cells enhanced

the functional properties (equilibrium modulus, tensile modulus and type III collagen) of constructs (Liu et al. 2012).

These types of stimulus are implemented through the use of engineered systems known as “bioreactors”, which maintain the required cellular environment and the cues (strain, shear stress) needed to improve cultivation conditions.

2.5 Bioreactors in bone tissue engineering

Bioreactors are devices in which biological or biochemical processes are developed under closely monitored and tightly controlled (Arano et al. 2010; Martin et al. 2004). Initial high accuracy and repeatability lead to their use in large scale applications such as water treatment, fermentation and pharmaceuticals (Plunkett & O’Brien 2010). Bioreactor potential in bone tissue engineering has come to light, as a system designed to support/expand a population of cells on a scaffold through dynamic culture and providing a controlled environment for tissue formation (Sladkova & de Peppo 2014). Culturing of cells under static conditions might lead to cell necrosis occurring at the construct centre due to a lack of nutrient delivery and waste removal (Jaasma et al. 2008).

In general, parameters that modulate cell growth include temperature, oxygen concentration, pH, nutrient and waste concentration, and physically relevant mechanical stimuli (Rauh & Milan 2011). The design of a bioreactor is generally adapted to the surrounding of a conventional cell culture incubator with material selection based on its ability to withstand sterilisation and cellular requirements. In terms of a clinically relevant strategy it must greatly minimize the risk of contamination from bacteria and other cells, reduce labour intensity, and reduce costs associated with *in vitro* cell culture (Yeatts & Fisher 2011). Bioreactor operation can be achieved through the integration of mechanical systems with specialised equipment, such as pumps, tensile testers or hydraulics/pneumatics. There are numerous types of bioreactors associated with cellular stimulation. A number of these will be outlined below.

Perfusion bioreactors provide stimulus and nutrient exchange through fluid flow, encompassing bioreactors such as spinner flasks, rotating wall vessels and

perfusion bioreactors (Gaspar et al. 2012). In a spinner flask bioreactor, scaffolds are suspended in cell culture media with a magnetic stir bar creating media flow through the scaffolds, see Figure 2-5. Advantages of this approach are that it enables thorough media mixing and is also shown to increase expression of early osteoblastic marker alkaline phosphatase (ALP), late osteoblastic marker osteocalcin (OC), and calcium deposition as compared to static culture and rotating wall bioreactors (Sikavitsas et al. 2002). However, scaffold size is limited as cell necrosis occurs in the centre of large scaffold due to lack of sufficient nutrient and oxygen (Plunkett & O'Brien 2010). The rotating wall bioreactor was developed by NASA. It provides an upward hydrodynamic drag force that balances with the downward gravitational force (Schwarz et al. 1992). Distribution of nutrients and oxygen shows similar results to fluid flow in the spinner flask bioreactor. Rotating wall bioreactors have been used in the vascularisation of porous 3D polyactic acid scaffolds containing bone marrow MSCs co-cultured with MSC-derived endothelial cells (Nishi et al. 2012). However, scaffolds tend to scatter throughout the bioreactor leading to collisions with the walls hence leading to cell damage (Botchwey 2001). Perfusion bioreactors perfuse media directly through a porous scaffold, which is held in position within a chamber, and can either provide a constant, pulsating or oscillating flow through the scaffold (Jaasma et al. 2008). Constant perfusion of flow through the scaffolds provides a homogeneous distribution of fluid flow compared to the spinner and rotating wall bioreactor. Furthermore, studies have achieved uniform cell distribution in peripherally cell-seeded scaffolds using this approach (Olivares et al. 2012; Keogh et al. 2011). In this system, flow is controlled through a pump, generally a peristaltic pump or syringe pump creating flow profiles such as oscillatory flow within TE scaffolds (Jaasma et al. 2008; Grayson et al. 2011).

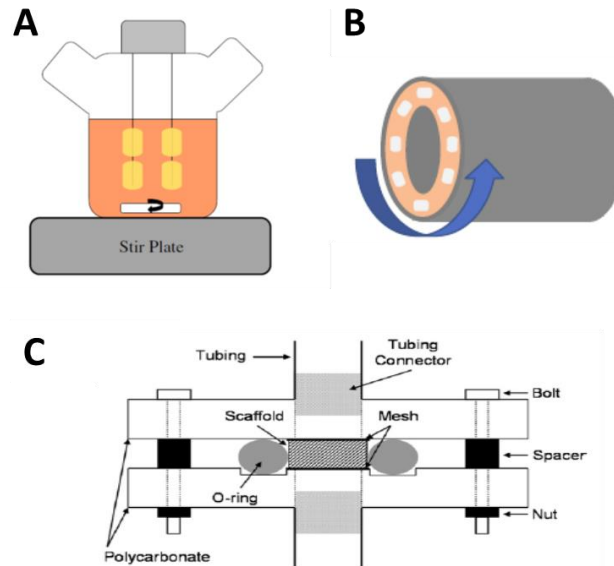


Figure 2-5: Schematic of a stir plate bioreactor with scaffolds suspended in culture while media is circulated through a stir plate (Yeatts & Fisher 2011) (A). Rotating wall bioreactor, two concentric cylinders within each other. One cylinder is stationary while the second rotates. The space between the two cylinders is filled with media where the rotation provides mixture of centrifugal and gravitational forces (Yeatts & Fisher 2011) (B). Media is perfused through a growth chamber containing the seeded scaffold (Jaasma et al. 2008) (C).

Dynamic compression bioreactors allow for direct application of compressive strain to scaffolds. An example of a compression bioreactor used in bone TE is the bioreactor system used by (Sittichockechaiwut et al. 2009), consisting of a BioDynamic chamber mounted on a ELF3200 mechanical testing machine (ElectroForce System Group, Bose, USA), capable of applying compressive strain (5%, 1 Hz) to polyurethane scaffolds. Furthermore, mechanical compression has been used in cartilage development with unconfined axial compression applied to constructs through impermeable platens using a stepper motor and linear stage (ATS0300, Aerotech, USA) with displacement verified using an externally mounted linear variable displacement transducer (PR-812, Macro Sensors, USA) (Mauck et al. 2007; Huang et al. 2010). Similarly, Frank et al designed a custom dynamic mechanical loading system, with a specialised chamber for holding cartilage constructs in six wells. Through an axial stepper motor, it was capable of applying compressive ramps at rates up to 1 mm/s with an applied force up to 400 N (Frank et al. 2000). Another example of a compression bioreactor, was a closed cylindrical polyethylene chamber, where

cell-matrix constructs were mechanically stimulated between two flexible silicon membranes. The system consisted of an upper membrane, that loaded the construct perpendicularly to its surface, while the lower membrane transfers the pressure via a standard infusion tube to a pressure transducer (Matziolis et al. 2011). Furthermore, studies have applied uni-axial loading to TE scaffolds through an externally applied magnetic field ensuring system sterility during operation (Schulz et al. 2008; Park et al. 2006).

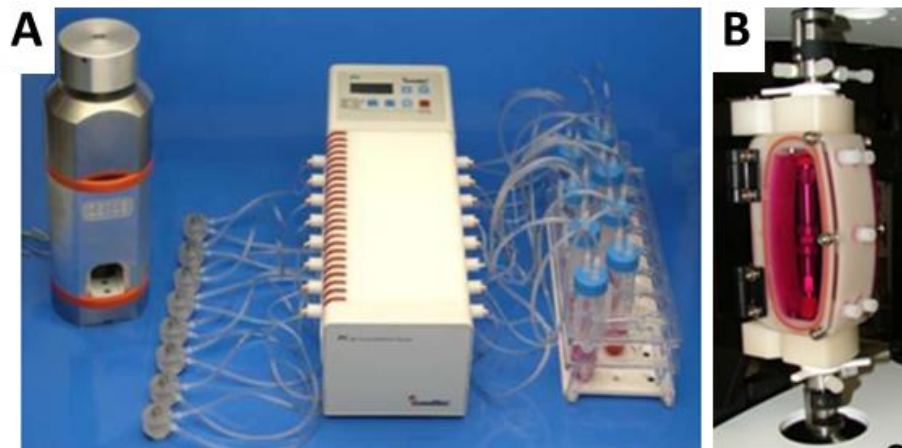


Figure 2-6: *Ex vivo* bone compression bioreactor (Zetos system) (Davies et al. 2006) (A) and BioDynamic chamber for compression of Polyurethane open cell foam scaffolds (Sittichockechaiwut et al. 2009).

The use of bioreactors in laboratories has significantly assisted in the development and enhancement of tissue constructs. However, most bioreactors vary greatly in relation to cost, ease of use, environment recreation, as well as monitoring methods. Bioreactors, such as the spinner flask and rotating wall provide convenient methods for recreating initial culturing environments, but are restricted by their inability to further enhance and adapt the supply of nutrients and essential stimulus.

2.5.1 *Clinical success of bioreactors*

Bioreactor technology has allowed for the development of functional tissue constructs *in vitro* (Keogh et al. 2011; Gardel et al. 2013; Thorpe et al. 2010; Schulz et al. 2008; Sittichockechaiwut et al. 2009; Matziolis et al. 2011). *In vitro*, studies using bioreactors have shown promising results, such as uniform cell distribution, increased osteogenic capacity and tissue formation in bone constructs

(Olivares et al. 2012; Keogh et al. 2011; Jaasma et al. 2008; Grayson et al. 2011; Matziolis et al. 2011; Sikavitsas et al. 2002; Bouet et al. 2015; Sittichockechaiwut et al. 2009), thereby enhancing functional and mechanical properties (Liu et al. 2012; Sittichockechaiwut et al. 2009). Table 3 illustrates examples of scaffolds combined with cells and cultured *in vitro* using bioreactor based approaches before implanting *in vivo* animal models.

Bioreactor type	Cells type	Scaffold	Implant Model	Results
Perfusion (2mL/h) (Uemura et al. 2003)	Rat Osteoblasts	Porous beta-tricalcium phosphate, / collagen-phosphosphoryn sponge	Subcutaneous, rat model	Accelerated the formation of bone
Perfusion (Not published) (de Peppo et al. 2013)	Human-induced pluripotent stem cells	Decellularized cow bone	Subcutaneous, mouse model	Increased expression of osteogenesis and tissue maturation.
Perfusion (400µm/sec) (Braccini et al. 2005)	Bone marrow stromal cells	Porous 3D hydroxyapatite ceramic scaffolds	Ectopically, mouse model	Uniform bone tissue generated
Biaxial rotating (3.8 ml/min) (Zhang et al. 2009)	Human fetal MSCs	Polycaprolactone–tricalcium phosphate scaffolds	Subcutaneous, mouse model	Greater ectopic bone formation compared to static-cultured scaffolds.
Spinner flask	Human bone marrow	Porous silk fibroin scaffolds	Critical sized cranial defects,	Elevated mineral deposition and host

(50 rpm) (Suwandi et al. 2015)	stromal cells		mouse model	bone ingrowth
Perfusion (1 mL/min) (Yeatts et al. 2014)	Human mesenchymal stem cells	Nanofibrous electrospun poly(lactic-co-glycolic acid)/poly(ϵ -caprolactone) scaffolds	Femoral condyle defects, rat model	Higher bone regeneration in defects compared to statically cultured scaffolds and acellular scaffolds.
Perfusion (4 mL/min) (Janssen et al. 2010)	Human bone marrow stromal cells	biphasic calcium phosphate scaffolds	Subcutaneous, mouse model	No difference in bone formation between static and dynamic groups
Perfusion (Not published) (Schliephake et al. 2009)	Human trabecular cells	Three scaffold types: porous calcium carbonate, mineralized collagen, porous tricalcium phosphate	Press fit into non-healing mandibles defects, rat model	Cell seeded scaffolds did not enhance bone formation in mandibular defects.

Table 3: Cell combined with biomaterial scaffolds and culture *in vitro* using bioreactor based approaches before implanting *in vivo*

All these studies demonstrated host tissue formation in constructs subject to mechanical stimulus after implantation. Furthermore, some studies demonstrate accelerated host bone tissue formation and integration within biomaterial scaffolds compared to statics controls, which received no stimulus under normal cell culture conditions. However, in current bioreactor technology, growing clinically relevant volumes of tissue is challenging (Janssen et al. 2010; Hansmann et al. 2013; Sladkova & de Peppo 2014), along with the culturing of

anatomically accurate shapes for patients defect, such as hips (Warren L Grayson et al. 2010). Furthermore, constructs used in these studies still have not reach load bearing capabilities, with constructs mainly implanted subcutaneously or requiring fixed support.

2.6 Summary

This chapter has presented an overview of bone, its cells, function, composition and structure and a brief overview of bone tissue engineering, and the use of bioreactor technology. To summarise, bone is an active material that is constantly adapting and remodelling itself due to mechanical loading from everyday activities with osteocyte cells playing a vital role in maintaining bone health by directing bone formation and resorption. However, natural regeneration capabilities of large defects are limited, as observed in severe trauma or bone tumour removal. Current clinical treatment to re-establish function in bone tissues requires transplanting tissue grafts from another part of the patient or a donor. Furthermore, accessing viable tissue within the patient is challenging and there is also a scarcity of suitable donors. As such there is a rationale for the development of functional substitutes for damaged or diseased bone. Bone tissue engineering is a promising strategy and significant advances have been made in the development of *in vitro* bone graft substitutes through the association of novel biomaterials with cells. However, fully functional and mechanically suitable tissue grafts that can be used for clinical applications are not yet widely available, due to core degradation, achieving substantial osteocyte differentiation and consistent tissue formation. Therefore, a possible solution to overcome such limitations is to produce tissue grafts containing both osteoblasts and osteocyte networks via matrix properties and extrinsically applied stimulus, promoting consistent host matrix formation and integration. To address this, chapter 3 of this PhD thesis investigates the effect of substrate stiffness and cell density on osteoblast-osteocyte differentiation. Chapter 4 investigate the effect of (1) delayed osteogenic differentiation, (2) scaffold stiffness and (3) 3D scaffold porosity on cell distribution, mineralisation and the formation of an osteoblast-osteocyte network. Chapter 5 involves the design and fabrication of a compression-perfusion bioreactor system capable of applying controlled stimulation to TE scaffolds. Chapter 6 investigates whether the application of applying combined

matrix stiffness, compression and perfusion stimulus to scaffolds may generate both osteoblast and osteocyte in porous TE scaffolds.

Chapter 3: Osteocyte differentiation and the formation of an interconnected cellular network *in vitro*

3.1 Introduction

In bone, osteocyte cells form a complex three-dimensional (3D) communication network that plays a vital role in maintaining bone health by monitoring physical cues arising during load-bearing activity and directing the activity of osteoblasts and osteoclasts to initiate bone formation and resorption (Burger & Klein-Nulend 1999). Osteocytes are formed when cuboidal-like osteoblasts become embedded within soft secreted osteoid and start to change morphologically to a dendritic shape characteristic of an osteocyte. This transition is accompanied by a loss of cell volume (reduced organelle content) (Knothe Tate et al. 2004; Palumbo et al. 2004) and an increase in the formation and elongation of thin cytoplasmic projections that interconnect with neighbouring osteocytes within the bone ECM and osteoblasts on the surface of the bone (Palazzini *et al.* 1998; Palumbo 1986; Mullen *et al.* 2013; Prideaux *et al.* 2012; Palumbo *et al.* 2004). Furthermore, as an osteoblast differentiates to an osteocyte, expression of the osteoblast marker enzyme alkaline phosphatase (ALP) is greatly reduced (Jee 2001; Nakano et al. 2004; Mikuni-Takagaki et al. 1995) along with an upregulation in dentin matrix protein-1 (DMP-1) (Rios et al. 2005; Narayanan et al. 2003). During the transformation from soft secreted osteoid to a mineralised ECM, the embedded osteoblast has been shown to extend out thick cell processes that polarise towards the mineralised matrix layer. These cell processes are believed to be involved in the extrusion of calcifying matrix vesicles and hence the formation of a mineralised osteoid matrix. This is followed by the cell extending out dendrites of a longer, thinner nature towards the vascular space, which are believed to have a nutritional function (Palumbo 1986; Barragan-Adjemian et al. 2006). It is believed that osteocyte cell processes play an important role in monitoring mechanical

stimulation of the osteocytes, arising from fluid flow within the lacunar-canalicular network and direct mechanical strain of the bone cell membrane (Weinbaum et al. 1994; Han et al. 2004; Wang et al. 2005; Wang et al. 2007; You et al. 2001; Knothe Tate et al. 2000; Knothe Tate & Niederer 1998; Knothe Tate et al. 1998; Wang et al. 2000; Zeng et al. 1994; McNamara et al. 2009; Anderson & Knothe Tate 2008; Verbruggen et al. 2012).

Osteogenic differentiation of human mesenchymal stem cells (MSCs) and pre-osteoblasts (MC3T3-E1) has been studied on 2D surfaces (Engler et al. 2006; Przybylowski et al. 2012) and on 3D biomaterials (Keogh, O'Brien, et al. 2010; Gleeson et al. 2010; Curtin et al. 2012; Correia et al. 2012), which act as tissue engineering (TE) scaffolds for cell attachment and tissue growth. Through these methods important cellular responses have been identified, in particular regulatory mechanisms for cell proliferation, migration, and matrix production, which provide information that is driving the development of approaches for regenerating bone tissue *in vitro* as a treatment for large bone defects. It has been shown that substrate (2D) (Mullen et al. 2013; Engler et al. 2004) and matrix (3D) (Tan et al. 2014) stiffnesses are important physical factors that induce a phenotypic shift towards osteogenic differentiation. Indeed extracellular mechanical cues are recognised as regulators of a variety of cell behaviours such as migration (Zaman & Trapani 2006), proliferation (Hadjipanayi et al. 2009), and differentiation (Tan et al. 2014; Lo et al. 2000). Moreover the extracellular mechanical environment can partially direct osteogenic differentiation and mineralisation of a variety of cells including myoblasts (Tan et al. 2014), osteoblasts (Chatterjee et al. 2010), MSCs (Engler et al. 2006; Huebsch et al. 2010; L. S. Wang et al. 2012) and embryonic stem cells (Evans et al. 2009). In particular the effect of varying 2D substrate stiffness on cultured osteoblastic cells has been shown to favour osteocyte differentiation on relatively soft ECM substrates (0.286 kPa) (Mullen et al. 2013), whereas culture on a more rigid substrate (20-40 kPa) led to osteogenic differentiation (Engler et al. 2004).

Cell seeding density has also been shown to be a critical parameter controlling cell proliferation, ECM synthesis and osteogenic signal expression, as it dictates the paracrine signalling distance between cells (Mullen et al. 2013; Kim et al. 2009; Zhou et al. 2011). Using a 2D culture of pre-osteoblastic cells seeded on collagen substrates, Mullen et al recently showed that a low cell seeding

density was important for dendrite formation and osteogenic differentiation, as indicated by reduced alkaline phosphatase (ALP) activity and increased mineral production (Mullen et al. 2013). In contrast a high cell density resulted in the attainment of an osteoblastic phenotype, indicated by a spread morphology and high levels of ALP (Mullen et al. 2013).

In vivo osteoblasts and osteocytes primarily exist within a complex three dimensional (3D) environment (Boukhechba & Balaguer 2009), and it is known that 3D environment has a significant effect on cell morphology and geometry, as shown in NIH 3T3 fibroblast (Legant et al. 2010), cardiac cells (Soares et al. 2012) and MC3T3-E1 osteoblasts (Murshid et al. 2007). The process of osteocyte dendrite formation within a 3D environment is highly dynamic as the embedding cells repeatedly extend and retract their dendrites. These “exploratory dendrites” make transient connections with already embedded osteocytes and may allow the osteocyte to position itself an appropriate spacing from other embedded osteocytes to maintain the ordered three dimensional spacing of the osteocyte network (Dallas et al. 2013; Zhang et al. 2006). However, although osteocyte differentiation has been studied in 2D (Mullen et al. 2013), it is not known how biophysical cues, such as matrix stiffness and cell density, control the phenotypic shift from osteoblasts to osteocytes in a 3D environment.

In this study, the hypothesis that osteocyte differentiation is regulated by ECM stiffness and cell density within a 3D environment was tested. The effect of extracellular mechanical cues in a 3D environment for osteoblast-osteocyte differentiation is investigated by encapsulating MC3T3-E1 pre-osteoblastic cells homogeneously within hydrogels of varying matrix stiffnesses. To investigate the effect of cell density, osteoblast cells are cultured at varying cell densities within each of the hydrogels. Osteocyte differentiation is examined by DMP-1 staining and quantifying cellular morphology, matrix mineralisation and ALP activity.

3.2 Methods

3.2.1 *Gelatin–mtgase hydrogel preparation*

Gelatin–mtgase hydrogels, with a final concentration of 3 % w/v gelatin, were prepared by mixing gelatin (type A, 175 Bloom, Sigma–Aldrich, Dublin, Ireland) at 37 °C in α MEM (Sigma–Aldrich) culture medium containing 10 % foetal

bovine serum (FBS) (Sigma–Aldrich), 100 U/mL penicillin (Sigma-Aldrich), 100 g/mL streptomycin (Sigma Aldrich) and 2 mM L-glutamine (Sigma-Aldrich), to obtain a liquid consistency for easier mixing. Gelatin suspensions were sterile filtered through a 0.22 μm filter (Millipore, Cork, Ireland). Microbial transglutaminase (mtgase) (Activa WM; containing 1 % mtgase; Ajinomoto foods Europe S.A.S., Mesnil-Saint-Nicaise, France) crosslinking was carried out by mixing mtgase with the gelatin suspension, allowing to vary hydrogel stiffness by using different concentrations (0.03, 0.06, 0.08, 0.15 and 0.20 %) of mtgase per gram of gelatin.

3.2.2 Gelatin–mtgase hydrogel mechanical properties

Unconfined compression testing was used to determine the stiffness of the hydrogels exposed to different concentrations of crosslinking using a tensile tester (Z009; Zwick/Roell, Ulm, Germany) fitted with a 10 N load cell. Samples were prepared in silicon isolators (Sigma–Aldrich) that contained 8 wells of diameter 9 mm and height 2.5 mm ($n = 8$ per stiffness). Silicon isolators were covered with a coverslip (50 x 24 mm) (EU Thermo Scientific, Loughborough, UK) to produce a flat surface after gelation, see Figure: 3-1. Samples were incubated in a bath of phosphate buffered saline (PBS) (Sigma–Aldrich) for 1 hour at 37 °C before the coverslip and silicon isolators were removed. During mechanical testing the gelatin–mtgase hydrogels were held within a bath of PBS at room temperature. Testing was conducted at a strain rate of 10 % per minute. The modulus was defined as the slope of a linear fit to the stress–strain curve over 2 – 5 % strain (Harley et al. 2007). Based on the results of these tests, a low and high matrix stiffness were chosen to examine the effects of 3D matrix stiffness on osteoblast differentiation and morphology.

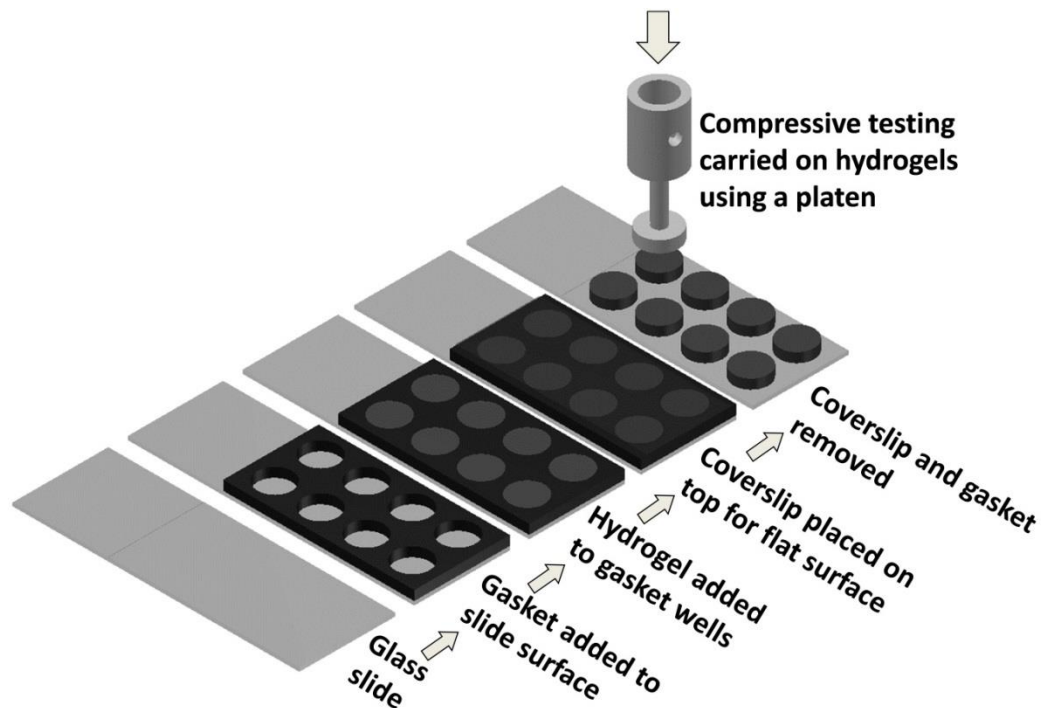


Figure: 3-1: Hydrogel fabrication method for mechanical testing. Unconfined compression testing was performed on samples using a custom made platen attached to a 10 N load cell.

3.2.3 Cell culture embedded in 3-dimensional mtgase hydrogels

MC3T3-E1 pre-osteoblastic cells (Sigma–Aldrich) were cultured under standard conditions (5 % CO₂, 37 °C). Cells were routinely grown to 70% confluency in T175 culture flasks (Sarstedt Ltd, Wexford, Ireland) containing α MEM culture medium (Sigma–Aldrich), 10 % FBS (Sigma–Aldrich), 100 U/mL penicillin (Sigma-Aldrich), 100 g/mL streptomycin (Sigma Aldrich) and 2 mM L-glutamine (Sigma-Aldrich). Before encapsulating, MC3T3-E1 cells (Passage 15-16) were detached using trypsin–ethylenediaminetetraacetic acid (EDTA, Sigma-Aldrich) and suspended in supplemented medium at 2×10^6 cells/mL. Varying cell densities (0.25, 1 and 2×10^6 cells/mL, which is approximately 0.4, 1 and 1.6×10^4 cells/cm²) were prepared in separate suspensions. Cell suspensions were then mixed with 6 % gelatin suspension and low and high concentrations of mtgase at a ratio of 5:4:1 (v:v:v) to give a low and high matrix stiffness. The final concentration of the mixture was 3 % w/v gelatin, (0.25, 1 and 2×10^6 cells/mL) within mtgase concentrations of 0.03 % and 0.08 % per gram of gelatin. Hydrogel suspensions for biochemical assays and morphology analysis were aliquoted into 96-well

plates at 0.071 mL/well. All hydrogels had a height of 2 mm and were allowed to gel at 4 °C for 6 min before media was added.

3.2.4 DNA content

DNA content was evaluated using the Hoechst 33258 DNA assay, which fluorescently labels double-stranded DNA (Sigma-Aldrich), as previously described (Haugh et al. 2011). After 2.5 hours, 3, 21 and 56 days of incubation, cell laden hydrogels were washed twice with PBS, frozen and stored at -80 °C. Samples were then thawed and digested overnight in papain digest (100 mM Sodium Phosphate Buffer containing 10 mM L-cysteine, 125 µg/mL Papain and 5 mM Na₂EDTA (all from Sigma Aldrich) in ddH₂O at pH 6.5 and 60 °C). Once the samples were digested the biochemical assays were performed straight away or stored at - 80 °C until the assays could be performed. Briefly, 200 µL of Hoechst dye solution was added to 20 µL of digested samples / standards in a 96-well plate in triplicate. Fluorescence was then measured (excitation: 355 nm; emission: 460 nm) using a fluorescence spectrophotometer (Synergy HT Multi-mode microplate reader). Readings were converted to DNA content using a standard curve, according to the manufacturer's protocol, with samples containing no cells subtracted as background.

3.2.5 Morphological analysis of cell phenotype

Hydrogel constructs were fixed using 4 % (w/v) paraformaldehyde (Sigma-Aldrich) after 2.5 hours, 21 and 56 days of culture, for 1 hour under rotation. Cells within the hydrogels were permeabilised with 2 mM Sodium Chloride (NaCl), 1.5 mM Magnesium Chloride (MgCl₂), 16 mM Sucrose and 0.5 % Triton-X100 in PBS (all from Sigma-Aldrich) for 10 minutes at 4 °C under rotation and washed with 1% PBS three times. Hydrogels were then stained with phalloidin-Fluorescein Isothiocyanate (phalloidin-FITC) solution at 1.25µg/mL (diluted 1:400, Sigma Aldrich) to stain the actin cytoskeleton and DAPI dilactate (diluted 1:2000, Sigma Aldrich) to stain the nucleus and rinsed again with 1% PBS solution. Confocal scans were taken using a confocal microscope (Olympus Fluoview FV1000) at magnifications of 10x for the hydrogel surface, 20x and 40x for cells below the hydrogel surface.

Maximum intensity images were generated from z-stacks taken at 20x magnification with a distance of 5 μ m between each slice for a thickness of 25 μ m, while 40x magnification z-stacks were taken at a distance of 2.5 μ m between each slice for a thickness of 10 μ m. All stacks were obtained at the same distance of 50 μ m below the hydrogel surface. In total 15 stacks were obtained at each timepoint, for each condition (five on each replicate hydrogel). Cell processes were defined as cellular features composed of actin, located at the cell membrane, which extended for a distance of at least 10 μ m from the cell body, as previously described (Mullen et al. 2014). Cells at later time points, day 21 and 56 that retained a strong fluorescent actin cytoskeleton and also maintained a cell body were classified as “active”, while cells that demonstrated a balled up and encapsulated morphology, showing no evidence of splitting or proliferating with a cell diameter less than 15 μ m were classified as “dormant”. Using this classification method cell morphologies were quantified as follows: (1) “dendritic” cells exhibited the small cell body and long thin cell processes associated with osteocytes, (2) “spherical” cells had no cell processes and exhibited a spherical or cuboidal morphology, (3) “dendritic interconnected” cells represented the number of cell process that formed interconnections with neighbouring cell processes and (4) “dividing cells” represented splitting cells within the hydrogel that remain connected. Cell morphology was quantified using NIH ImageJ software particle analysis. After 2.5 hours and 21 days average cell span was determined from the diameter of the dendritic cell. By day 56, individual dendrites were manually measured and average dendrite length was determined.

3.2.6 Live cell imaging to track exploratory dendrites.

During the 56 days culture period live cell images of the same location within hydrogels were taken at 20x magnification using an Olympus IX50 inverted brightfield microscope. The same cell locations were identified by scoring the bottom of 96-well plates with a grid, indicating the x and y coordinate, and through focusing within the z plane to identify the same cells. Images were taken every 3-4 days at room temperature for no longer than 30 mins.

3.2.7 *DMP-1 immunofluorescent staining*

DMP-1 is a secreted protein that is upregulated during osteoblast to osteocyte differentiation and has been observed in late stage osteoblast (D'Souza et al. 1997; Feng et al. 2002) and early stage osteocytes (Rios et al. 2005; Narayanan et al. 2003; Lee et al. 2014; Dallas & Bonewald 2010). Immunofluorescent staining for DMP-1 was conducted to investigate the phenotypic differentiation of MC3T3-E1 cells.

Hydrogel constructs were fixed using 4% paraformaldehyde (Sigma-Aldrich) after 21 and 56 days of culture for 1 hour under rotation. Cells within the hydrogels were permeabilised with 2mM Sodium Chloride (NaCl), 1.5 mM Magnesium Chloride (MgCl₂), 16 mM Sucrose and 0.5% Triton-X100 in PBS (all from Sigma-Aldrich) for 10 mins at 4°C under rotation and washed in PBS 3 times. Hydrogel constructs were covered with a 10% bovine serum albumin (BSA) / 3% normal goat serum (NGS) (Jackson ImmunoResearch) blocking solution for 1 hour under rotation before incubation with monoclonal anti-DMP1 antibody at a dilution of 1:100 at 4°C overnight (Clone 8G10.3, Millipore). After washing 3 times with 1%BSA/PBS solution, samples were then treated with a Dylight™ 549 conjugate goat anti-mouse secondary antibody at a dilution of 1:100 (Jackson ImmunoResearch) for 1 hour under rotation at room temperature. After secondary staining, samples were rinsed 3 times with 1% BSA/PBS solution. Hydrogels were then further counterstained with phalloidin-FITC at 1.25µg/mL (diluted 1:400, Sigma Aldrich) to stain the actin cytoskeleton and DAPI dilactate (diluted 1:2000, Sigma Aldrich) to stain the nucleus and rinsed again with 1%BSA/PBS solution. Confocal scans were taken using a confocal microscope (Olympus fluoview) at 10x and 40x magnification. Z-stacks were combined together in 2D to form maximum intensity images. Negative controls were performed by omitting the primary antibody incubation step.

3.2.8 *Extracellular ALP content*

Extracellular alkaline phosphatase (ALP) activity was determined using a colorimetric assay of enzyme activity (SIGMAFAST *p*-NPP Kit, Sigma Aldrich), which uses *p*-nitrophenyl phosphate (*p*NPP) (nmol) as a phosphatase substrate, with ALP enzyme (Sigma Aldrich) as a standard. Prior to media change, media

was removed from samples at each timepoint and frozen and stored at $-80\text{ }^{\circ}\text{C}$, $40\text{ }\mu\text{L}$ of the medium was added to a 96-well plate in triplicate with a $50\text{ }\mu\text{L}$ of *p*NPP solution, which contains both *p*NPP and assay buffer. The samples were shielded from direct light at room temperature for one hour. After this, $20\text{ }\mu\text{L}$ of Stop Solution (3 M NaOH) was added to the wells and the plate was read at 405 nm in a Synergy HT Multi-mode microplate reader. Results were then normalised to cell number (μg) as determined through the Hoescht assay outlined above and expressed as $\text{nmol}/\mu\text{g}$.

3.2.9 Mineralisation

Mineralisation within hydrogel constructs was determined from calcium deposition and measured using the Calcium Liquicolour kit (Stanbio Laboratories, Syntec, Dublin, Ireland) according to the manufacturer's protocol. After 21 and 56 days of incubation, cell laden hydrogels were washed twice with PBS, frozen and stored at $-80\text{ }^{\circ}\text{C}$. Hydrogel samples were then thawed and digested by adding $16.6\text{ }\mu\text{L}$ of 6 M hydrochloric acid (HCL) (Sigma-Aldrich) to each well and storing the solution at $4\text{ }^{\circ}\text{C}$, when completely dissolved HCL concentration was adjusted to 0.5 M HCL by adding $183.4\text{ }\mu\text{L}$ of ddH_2O to each sample. $10\text{ }\mu\text{L}$ each of the digested samples and assay standard was added to a 96-well plate and $200\text{ }\mu\text{L}$ of the working solution. The plate was read on a synergy HT Multi-mode microplate reader at an absorbance of 550 nm as previously described (Freeman 2013).

3.2.10 Statistics

All biochemical experiments were conducted in biological triplicate with two independent experiments run for a total of $n = 6$. Cell morphology experiments were conducted in duplicate with two independent experiments run for a total of $n = 4$. Results are expressed as mean \pm standard deviation. For all the biochemical analysis two-way analysis of variance (ANOVA) was conducted, followed by pair-wise multiple comparison procedure (Tukey's HSD test). All analyses were performed with Graphpad Prism 6 (GraphPad software, San Diego, USA). For all comparisons, the level of significance was $p \leq 0.05$.

3.3 Results

3.3.1 Compressive modulus

Compressive testing of varied stiffness of hydrogels increased in stiffness with varied cross-linking concentration after incubation for 1 hour at 37 °C, see Figure 3-2. Mtgase hydrogels containing 0.03, 0.06, 0.08, 0.15, 0.2 % mtgase had compressive moduli of 0.58 ± 0.1 , 0.84 ± 0.1 , 1.47 ± 0.3 , 3.05 ± 0.2 and 3.03 ± 0.4 kPa respectively. The effect of increasing cross-linking density on hydrogel stiffness reached a plateau at 0.15 % mtgase crosslinking. Cells were encapsulated in a similar mechanical environment to a previous studies using 2D substrates (~ 0.3 kPa), which were shown to elicit osteoblast-osteocyte differentiation (Mullen et al. 2013). The compressive moduli 0.58 kPa was the lowest achievable stiffness in this 3D environment, while a higher matrix stiffness (1.47 kPa) was selected from the gels that were crosslinked at different densities, see Figure 3-2, on the basis that it was statistically significantly higher matrix stiffness (1.47 kPa) compared to the low matrix stiffness ($p < 0.0001$).

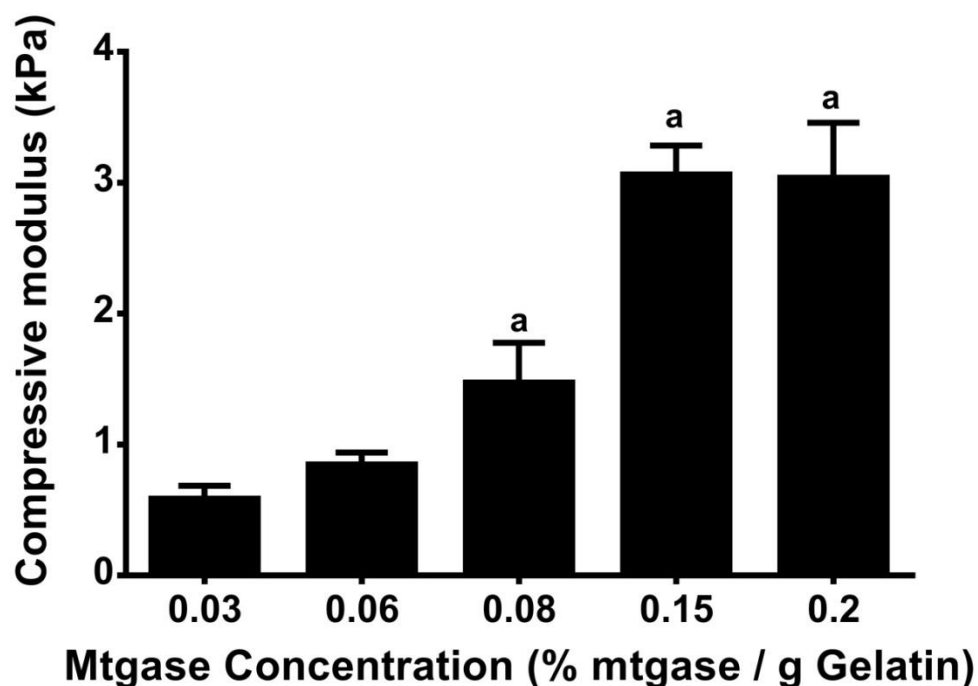


Figure 3-2: Mechanical properties of a 3 % Gelatin hydrogel crosslinked with 0.15, 0.03, 0.06, 0.08, 0.15, 0.2 % mtgase after 1 hour of incubation at 37 °C, n = 8 per group. ^a $p < 0.05$ relative to 0.03 % mtgase hydrogel.

3.3.2 DNA content

DNA content increased significantly in all matrix stiffness and cell density groups from 2.5 hours to 56 days of culture ($p < 0.0001$), see Figure 3-3. By day 56 in the medium cell density group (1×10^6 cells/mL) a significant difference was observed between the low and high matrix stiffness ($3.28 \pm 1.02 \mu\text{g}$ vs. $2.53 \pm 0.55 \mu\text{g}$, $p < 0.03$).

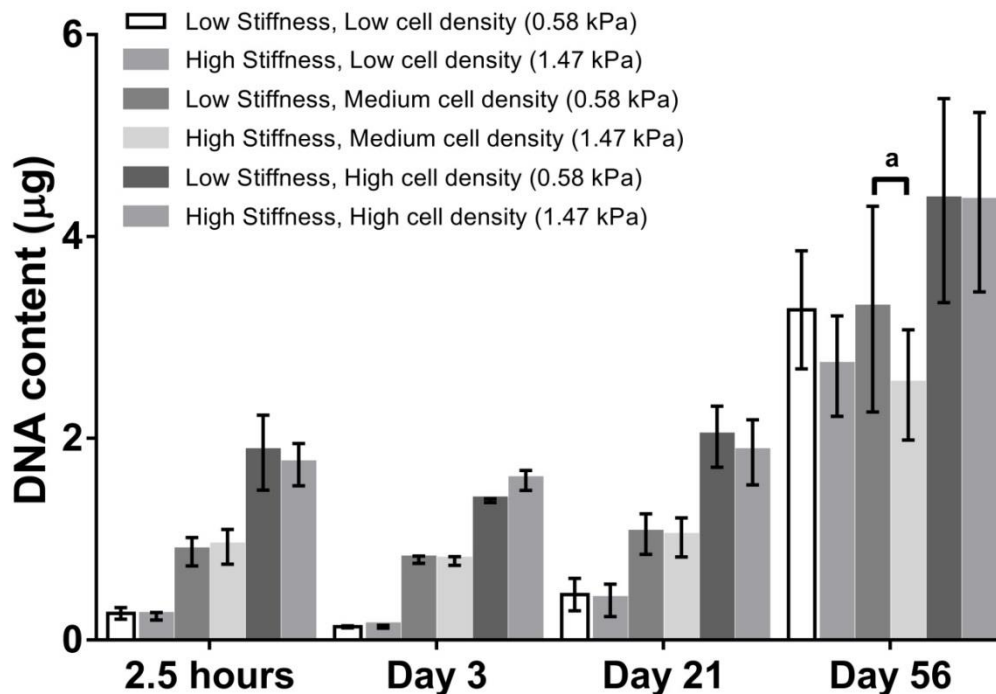


Figure 3-3: DNA content of each group at 2.5 hours, 3, 21 and 56 days ($n = 6$ samples per group per time-point). ^a $p < 0.05$ representing a statistical difference between low (0.58 kPa) and high (1.47 kPa) stiffness. Error bars denote standard deviation

3.3.3 Morphological analysis of cell phenotype

3.3.3.1 MC3T3-E1 morphology and dendritic cell span after 2.5 hours

MC3T3-E1 cells cultured at low and medium cell densities within low stiffness matrices (0.58 kPa) had a similar morphological pattern with approximately 81.5 % classed as spherical and 18.5 % as having a dendritic morphology after 2.5 hours ($p < 0.0001$). However, cells cultured within a high stiffness matrix (1.47 kPa) at a low and medium cell density were classified as being approximately 99 % spherical and 1 % dendritic ($p < 0.0001$). In the high cell density groups, within a low stiffness hydrogel (0.58 kPa), cells were classed to be 71.5 % spherical and

28.5 % dendritic ($p < 0.0001$). In contrast, cells within the high stiffness matrices were classed as 97 % spherical and 3 % dendritic ($p < 0.0001$). Furthermore, for all cell density groups a larger percentage of dendritic cells were observed in the low stiffness matrices compared to the higher stiffness ($p < 0.0012$), see Figure 3-4A for representative images and Figure 3-4B for summarised results.

After 2.5 hours, dendritic cell span in the low stiffness matrices within each cell density had similar cell span lengths, though not significantly different, 58 μm in the low cell density, 56 μm in the medium cell density and 64 μm in the high cell density, while no change occurred in the higher matrix stiffness hydrogels remaining at approximately 24 μm , see Figure 3-4C.

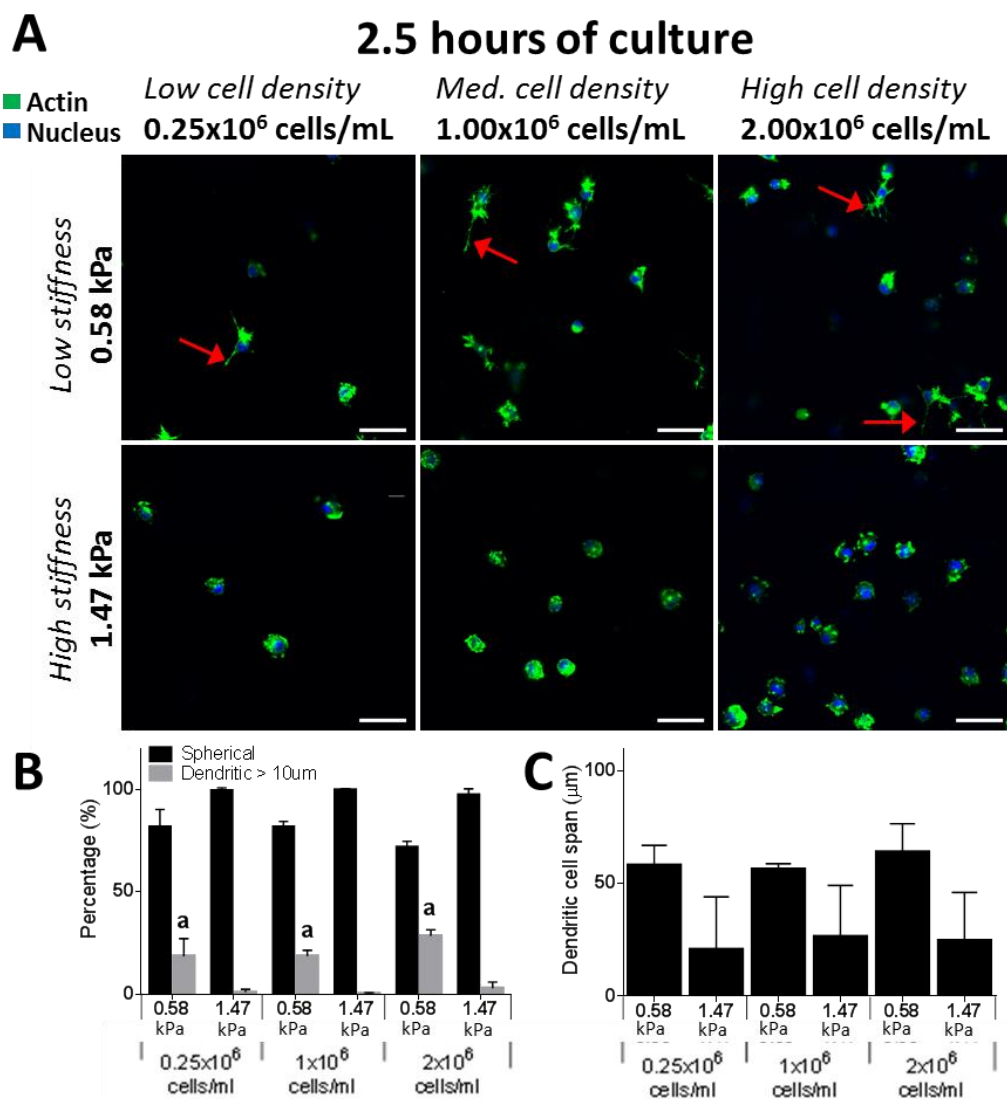


Figure 3-4: Actin staining of cell morphology after 2.5 hours of culture comparing spherical vs dendritic (Red arrows) morphology (A). Also shown is the

percentage of spherical vs dendritic cells (**B**) and average dendritic cell span (**C**) within low (0.58 kPa) and high (1.47 kPa) stiffness matrices. ^a $p < 0.05$ representing a statistical difference between low (0.58 kPa) and high (1.47 kPa) stiffness at the same density group. Scale bar = 50 μm , same for all images.

3.3.3.2 MC3T3-E1 morphology and dendritic cell span after 21 days

For a low cell density and a low stiffness matrix, 52 % of the cells were classified as spherical, while 48 % of cells were dendritic after 21 days. In contrast, for a high stiffness matrix, 82.6 % of cells were spherical, while 17.4 % of cells were dendritic ($p < 0.0001$). Cells cultured at medium and high cell densities within a low stiffness matrix had a similar morphological pattern with approximately 24 % classed as spherical and 76 % as dendritic morphology for both seeding densities ($p < 0.0005$). In contrast within the high stiffness matrix, at a medium and high cell density, approximately 94 % cells were spherical and 6 % dendritic ($p < 0.0001$). Additionally, all cell density groups had a significant increase in the percentage of dendritic cells in the low stiffness matrices compared to the high stiffness ($p < 0.0386$), see Figure 3-5A for representative images and Figure 3-5B for summarised results.

Dendritic cell span in the low stiffness matrices showed a trend of increasing as cell density increased though not significantly different. Specifically the cell span was 60.1 μm in the low cell density, 67.7 μm in the medium cell density and 82.2 μm in the high cell density. A smaller change occurred in higher stiffness matrices, 46.7 μm in the low cell density, 50.3 μm in the medium cell density and 56.4 μm in the high cell density, though not significantly different. A significant difference was observed between the low and high matrix stiffness at the high cell density group ($p < 0.0491$), see Figure 3-5C.

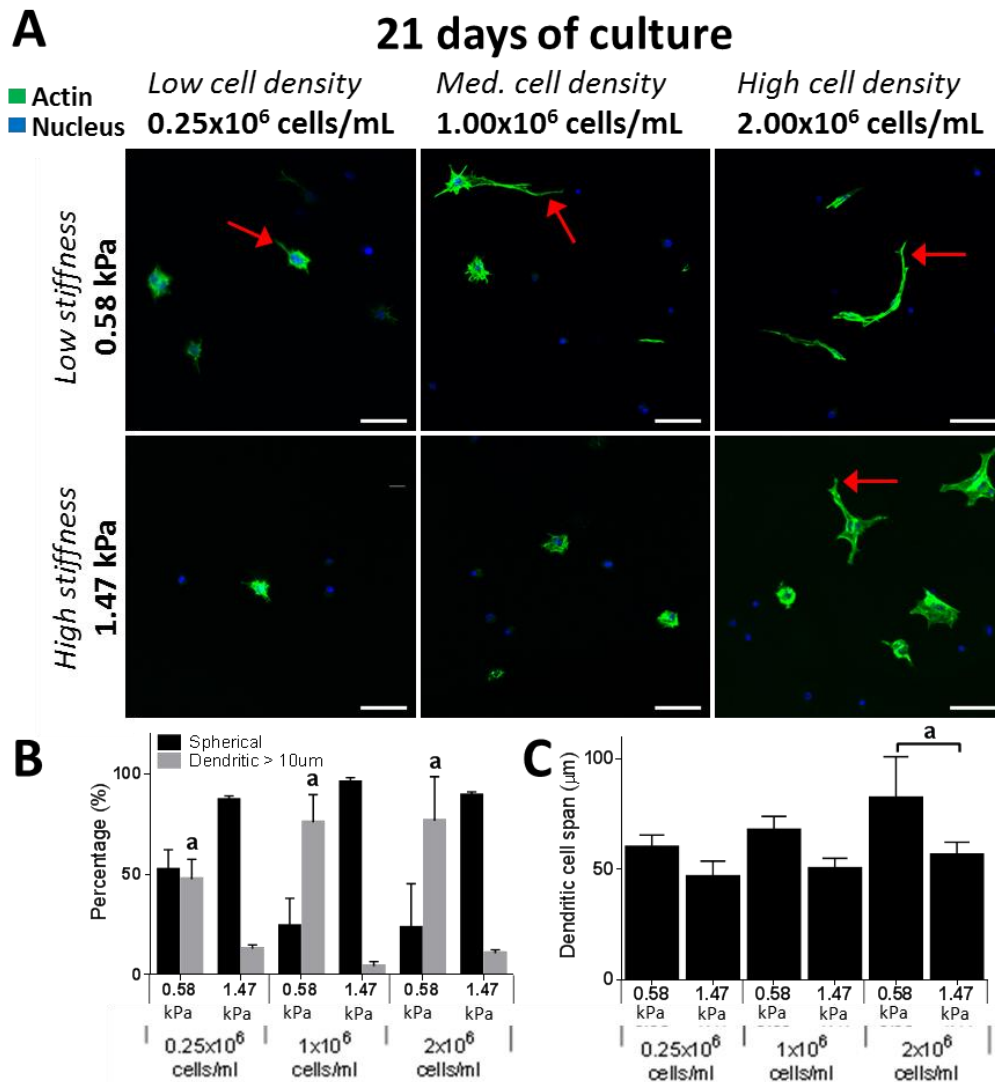


Figure 3-5: Actin staining of cell morphology after 21 hours of culture comparing spherical vs dendritic (Red arrows) morphology (A). Also shown is the percentage of spherical vs dendritic cells (B) and average dendritic cell span (C) within low (0.58 kPa) and high (1.47 kPa) stiffness matrices. ^a $p < 0.05$ representing a statistical difference between low (0.58 kPa) and high (1.47 kPa) stiffness at the same density group. Scale bar = 50 µm, same for all images.

3.3.3.3 MC3T3-E1 morphology, dendritic cell length and interconnections after 56 days

By 56 days, in all hydrogel groups, cells formed a confluent layer at the surface of the hydrogels, see Figure 3-6 and Figure. 3-7. Below the surface, at low and medium cell densities within a low stiffness matrix, cells had a similar morphology patterns with approximately 24 % spherical and 76 % dendritic ($p < 0.0001$). However, cells cultured within a high stiffness matrix at a low and

medium cell density were classified to be approximately 60 % spherical and 40 % dendritic, though not significantly different. For a high cell density and a low stiffness matrix, 14.6 % were classed as spherical, while 85.4 % were dendritic ($p < 0.0001$). In contrast, cells within a high stiffness matrix were 64.6 % spherical and 34.4 % dendritic ($p < 0.0148$). Similarly to day 21, a larger percentage of dendritic cells were observed in the low stiffness matrices compared to the high stiffness in all cell density groups ($p < 0.0093$), see Figure 3-8A for representative images and Figure 3-8B for summarised results.

At 56 days, average individual dendrite length within the low stiffness matrices was 46.2 μm in the low cell density, 53.9 μm in the medium cell density and 67.2 μm in the high cell density. Dendrite length in higher stiffness matrices was 35.7 μm in the low cell density, 36.9 μm in the medium cell density and 29.3 μm in the high cell density. Furthermore, a significant difference was observed between the low and high matrix stiffness at the high cell density group ($p < 0.0095$), see Figure 3-8C.

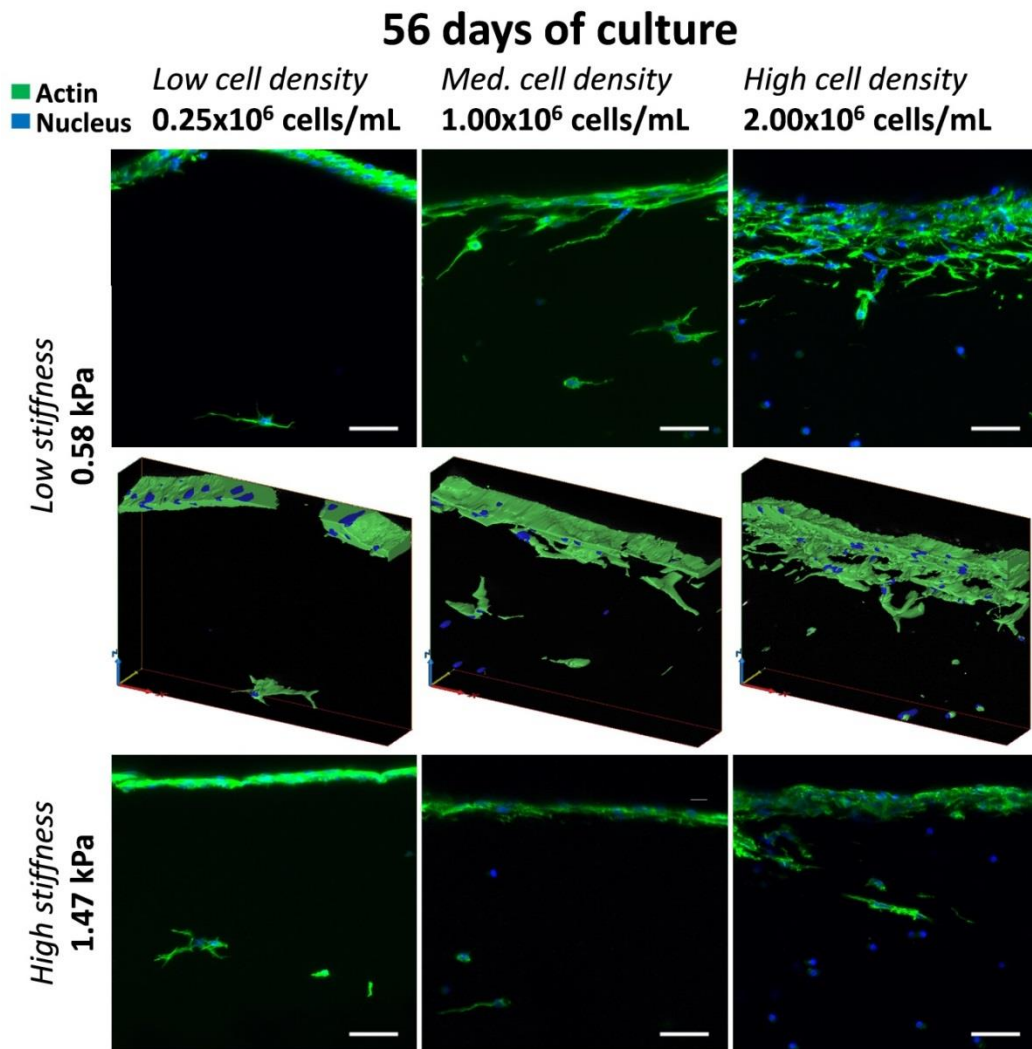


Figure 3-6: Section views of cell morphologies and interconnections at 56 days. Fluorescent images represented as 3D stacks in low stiffness matrix group. Scale bar = 50 μ m.

3.3.3.4 Cell interconnections after 56 days

Cells at a high cell density within a low stiffness matrix had the highest amount of interconnections between neighbouring dendritic cells compared to the high stiffness matrix at the same density ($p < 0.037$). Cells were classified as 38.8 % interconnected, whereas 30.9 % were unconnected and 30.3 % connected as dividing cells. For the higher stiffness matrix at the same cell density 4.6 % of cells were interconnected, 89.1 % were unconnected and 6.3 % connected as dividing cells. At a medium cell density within a low stiffness matrix cells were approximately classified as 16.5 % interconnected, while 32 % were unconnected and 51.5 % connected as dividing cells. For the higher stiffness matrix at the same

cell density 2.8 % of cells were interconnected, 71.9 % were unconnected and 25.3 % connected as dividing cells. For the low cell density within a low stiffness matrix 6.9 % of cells were interconnected, while 36.5 % were unconnected and 56.6 % connected as dividing cells. For the higher stiffness matrix at the same cell density 4.6 % of cells were interconnected, 89.1 % were unconnected and 6.3 % connected as dividing cells, see Figure 3-8D. It was found that the percentage of dendritic cells does not vary as a function of seeding density independently, only when compared with stiffness.

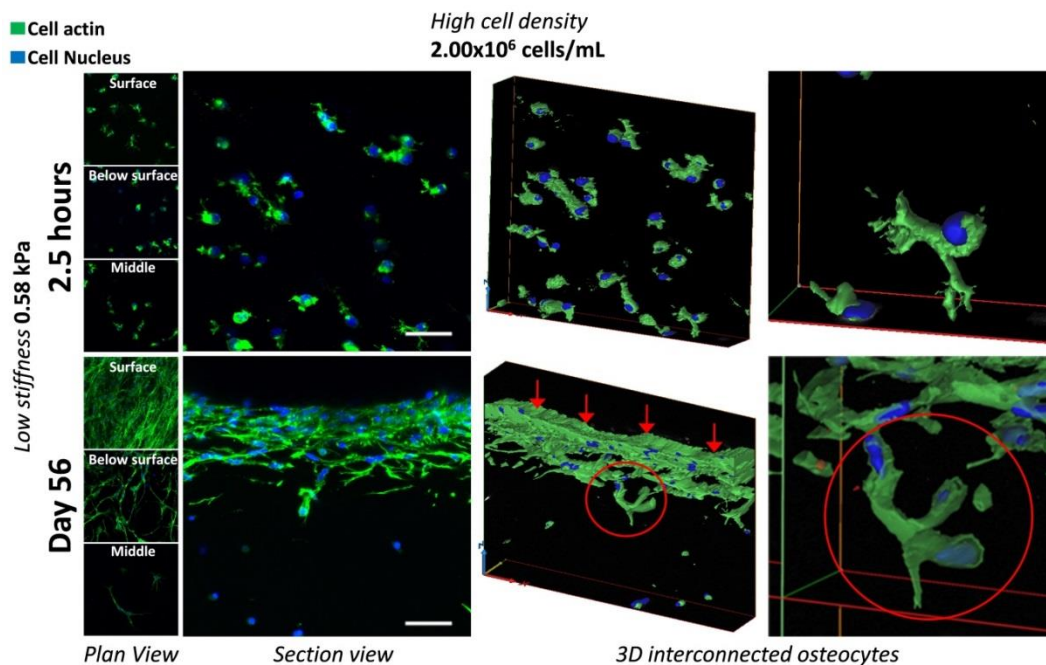


Figure. 3-7: Section view images of low stiffness matrix and high cell density comparing cell morphologies and interconnections at 2.5 hours and 56 days. After 2.5 hours cells form dendrites throughout the hydrogel. By 56 days, cells proliferate on surface, exhibiting a spread and confluent morphology (red arrows), progressing from the hydrogel surface cells become dendritic and forming interconnections (red circle). Scale bar = 50 μm .

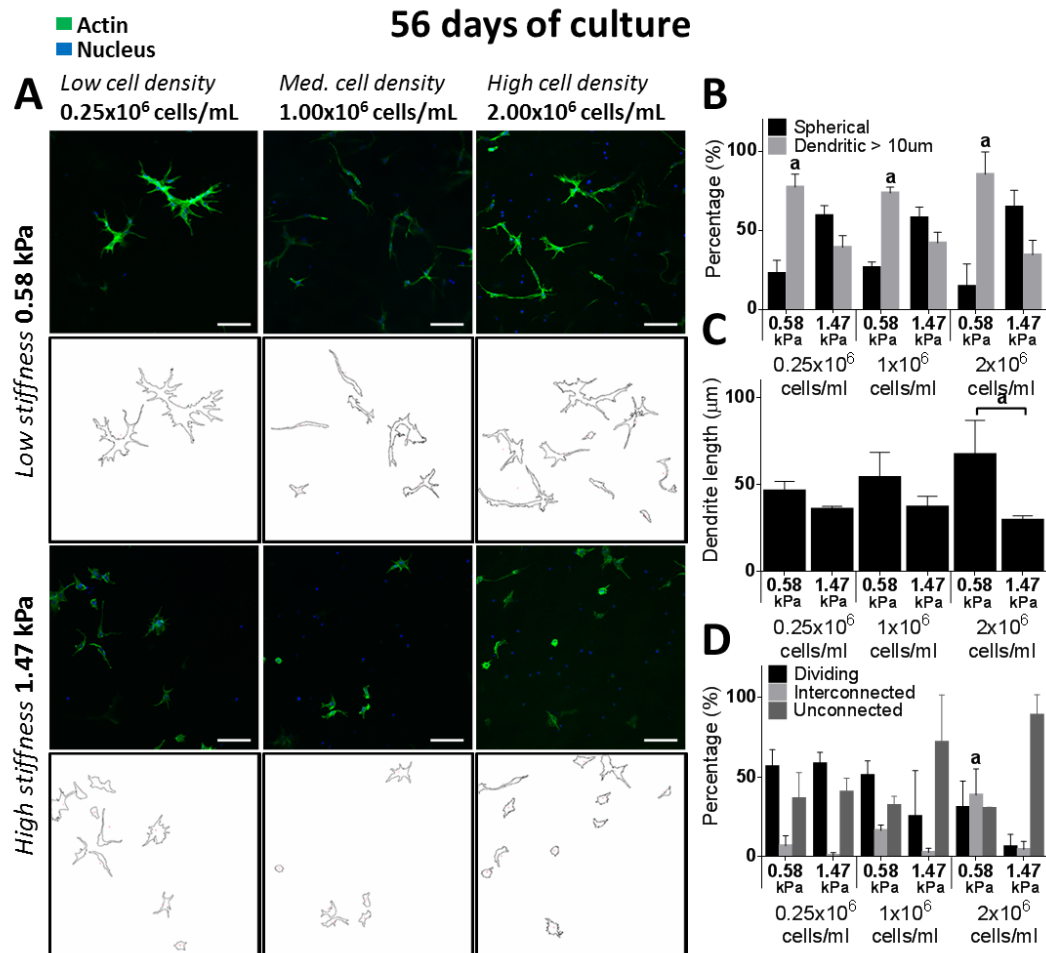


Figure 3-8: Actin staining and particle analysis illustrations of cell morphology after 56 days of culture comparing spherical vs dendritic morphology (A) within low (0.58 kPa) and high (1.47 kPa) stiffness matrices. Also shown is the percentage of spherical vs dendritic cells (B), average cell dendrite length (C) and percentage of interconnections formed between cells (D). ^ap<0.05 representing a statistical difference between low (0.58 kPa) and high (1.47 kPa) stiffness at the same density group. Scale bar = 100 μm.

3.3.3.5 Exploratory dendrites live cell imaging

Cell dendrite formation was observed after 1 hour of incubation within the lowest stiffness hydrogel. Dendrite formation was observed to increase with time. Dendrites were observed to be highly dynamic as cells repeatedly formed interconnections, extended and retracted their dendrites over the culture period. It was also observed that individual cells were active and viable throughout the entire 56 days culture period without proliferating, see Figure 3-9 A, 9B. However, it was also observed that an individual cell that initially exhibited a dendritic morphology, could become balled up, reduce in size and remain in the

hydrogel for the 56 day culture period (Figure 3-9 A, black arrows). These cells were referred to as “dormant” due to showing no normal cell activity (proliferating, motile, change in cell morphology, etc) throughout the culture period.

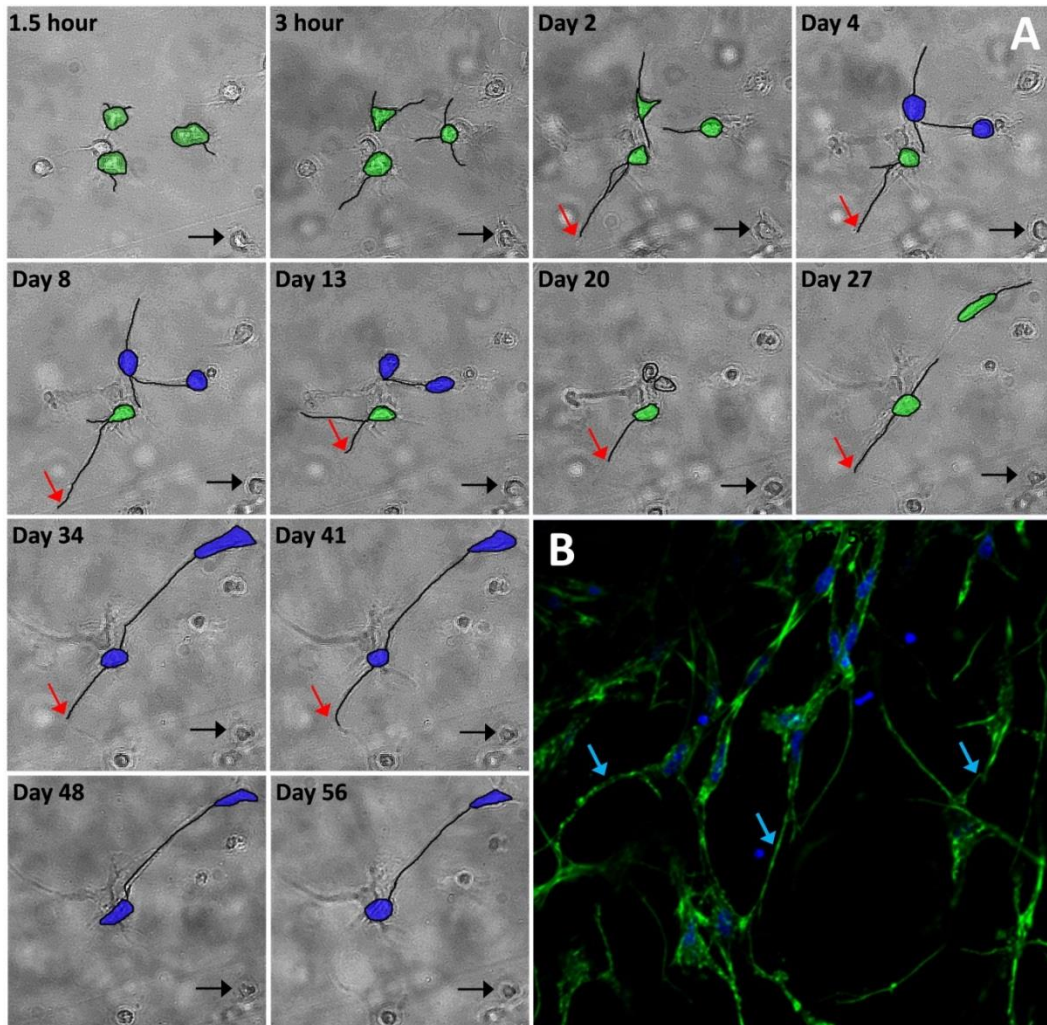


Figure 3-9: (A) Live cell imaging of a low stiffness matrix at a high cell density show cells (green cells) to be highly dynamic and constantly sending out exploratory dendrites (red arrow) throughout the study, while at the later timepoints the same cells formed interconnections with neighbouring cells (blue cells). Furthermore cells that became balled up and encapsulated (Black arrows), were observed to remain balled up within the hydrogel throughout the 56 days culture period and were classified as dormant. (B) Fluorescent imaging at day 56 show interconnections formed between cells (blue arrow).

3.3.4 DMP-1 immunofluorescent staining

Immunofluorescent staining for DMP-1 showed positive expression of DMP-1 within the proximity of cells encapsulated within the soft stiffness matrix (0.58

kPa), see Figure 3-10. At 10x magnification, DMP-1 staining was observed within the proximity of dendritic and interconnected cells at a medium cell density, see Figure 3-10B. At 40x magnification, at a low and high cell density, DMP-1 staining was observed within matrices at day 21 and 56 (Figure 3-10 C-F). DMP-1 staining, at the high cell density was observed as dispersed nodules within the surrounding matrix of dendritic and interconnected cells (Blue arrows) (Figure 3-10 E,F). DMP-1 staining was not observed in the negative control, where the primary antibody was omitted Figure 3-10 (A).

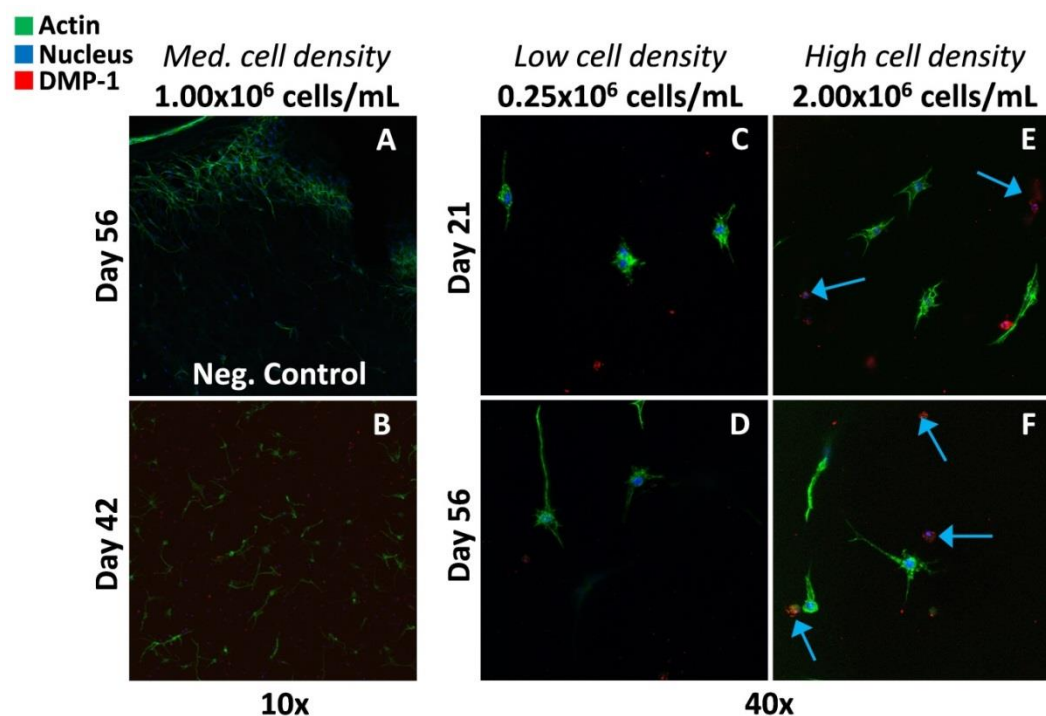


Figure 3-10: Immunofluorescent images of DMP-1 from cells encapsulated in a hydrogel at a low matrix stiffness (0.58 kPa). (A) Negative controls were performed by omitting the primary antibody and no DMP-1 staining was observed. (B) DMP-1 staining was observed within the proximity of dendritic and interconnected cells at a medium cell density (10x magnification). At a low (C, D) and high (E, F) cell density, DMP-1 staining was observed within matrices at day 21 and 56 (40x magnification). DMP-1 staining, at the high cell density (E, F) was observed as dispersed nodules within the surrounding matrix of dendritic and interconnected cells (Blue arrows, 40x magnification). Images were taken at approximately 50 μm below the hydrogel surface. Scale bar for 10x (A, B) = 120 μm ; 40x (C, D, E, F) = 50 μm .

3.3.5 ALP activity of cells

Extracellular alkaline phosphatase activity by day 3 showed a significant increase for the low cell density group within both the low and high stiffness matrices

compared to all other groups at the same timepoint ($p < 0.0001$). Furthermore, at a low cell density a significant increase in ALP activity was also observed in the high stiffness matrix compared to the low stiffness matrices (15.18 ± 2.1 nmol/ μ g vs. 12.31 ± 1.22 nmol/ μ g, $p < 0.0002$). Similarly by day 21 significantly higher ALP activity was observed within the low cell density groups for both the low and high stiffness matrices compared to the other groups at the same timepoint ($p < 0.0002$). By day 56, ALP activity was downregulated in all groups with no significant difference between groups, see Figure 3-11.

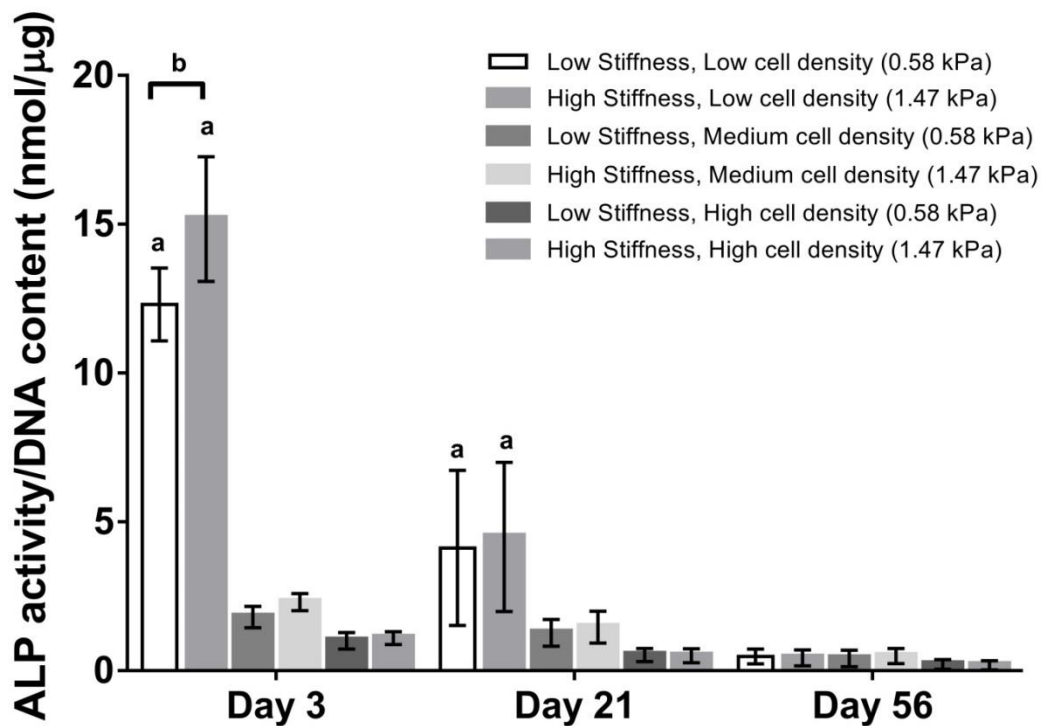


Figure 3-11: Extracellular ALP activity of each group at day 3, 21 and 56 ($n = 6$ samples per group per time-point). ^a $p < 0.05$ relative to the other cell density groups at the same timepoint and ^b $p < 0.05$ representing a statistical difference between low and high stiffness. Error bars denote standard deviation.

3.3.6 Mineralisation

Calcium content in the high cell density group within a low and high stiffness matrix showed a significant increase in mineralisation from day 21 to 56 ($p < 0.05$). By day 56, significantly higher calcium content was observed in the high cell density group within both the low and high stiffness matrix compared to the other groups at the same timepoint ($p < 0.05$). Furthermore, a significant difference

($p < 0.0287$) in calcium content was observed between the low and high matrix stiffness ($29.23 \pm 7.38 \mu\text{g}$ versus $20.3 \pm 10.06 \mu\text{g}$), see Figure 3-12.

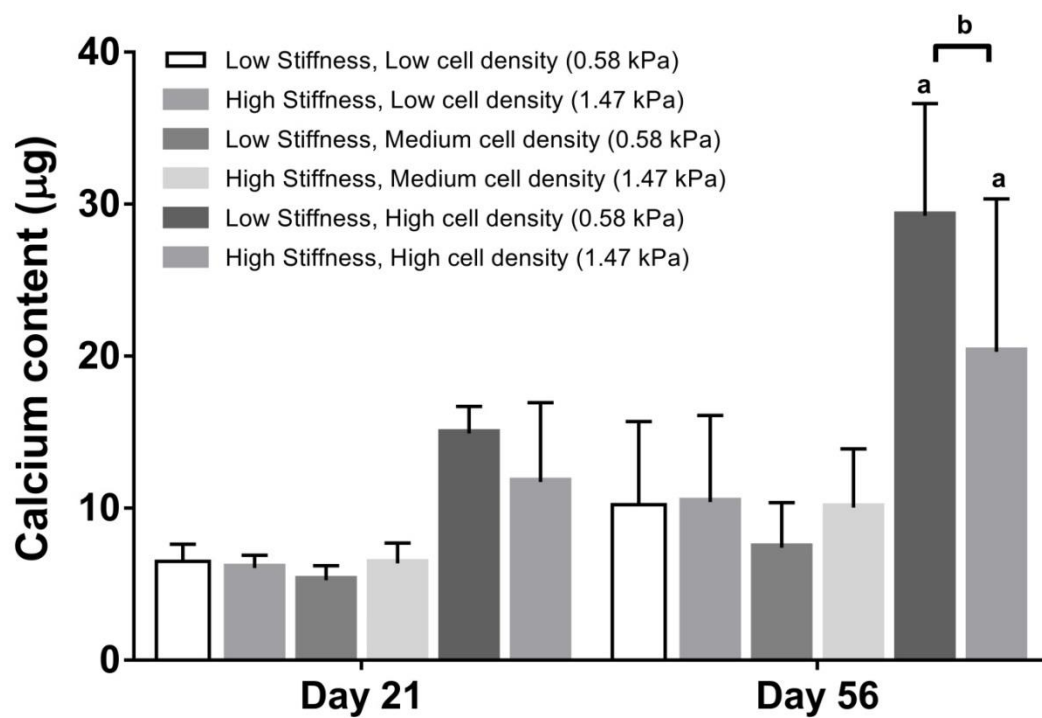


Figure 3-12: Calcium content of each group at days 21 and 56 ($n = 6$ samples per group per time-point). ^a $p < 0.05$ relative to the other cell density groups at the same timepoint. ^b $p < 0.05$ relative to the other matrix stiffness groups at the same timepoint. Error bars denote standard deviation.

3.4 Discussion

The results of this study show for the first time that osteocyte differentiation of MC3T3-E1 cells is regulated within a 3D cell environment by ECM stiffness and cell density. Specifically it was shown that the highest extent of osteoblast-osteocyte differentiation occurred within a soft 3D matrix (0.58 kPa) at high cell density (2×10^6 cells/mL). Interestingly after 56 days of culture these conditions led to the formation of an osteocyte-like network within the 3D matrix, characterised by long dendrites interconnecting with neighbouring osteocytic cells. DMP-1, a secreted protein that is upregulated during osteoblast to osteocyte differentiation, was identified within the matrix by immunohistochemistry. At the surface of this matrix cells formed a confluent layer, characteristic of osteoblast-like cells, which was also interconnected with the osteocyte-like network. Bone has a similar structure *in vivo*, wherein osteocytes form a complex interconnected network allowing for communicating with their neighbours and with osteoblasts cells on bone surfaces via long cellular processes. Within a stiffer matrix (1.47 kPa) at a low cell density, dendrite formation occurred but these dendrites were shorter and a reduced interconnecting network was established. These findings reveal that both the mechanical properties of ECM and the ability for cells to establish a communication network within a 3D environment, play a significant role in osteocyte differentiation and the formation an interconnected network.

Cell migration, proliferation and differentiation have all been shown to be influenced by substrate (2D) or matrix (3D) stiffness (Tan et al. 2014; Lo et al. 2000; Mullen et al. 2013; Engler et al. 2004; Hadjipanayi et al. 2009; Zaman & Trapani 2006). In particular, a soft 2D substrate (0.3 kPa) was shown to lead to osteocyte differentiation (Mullen et al. 2013), whereas more rigid 2D substrates (40 kPa) favour osteoblast differentiation (Engler et al. 2004). Osteoblast to osteocyte differentiation has been previously elicited in human primary osteoblast-like cells within 3D collagen gels, with 10% of cells becoming dendritic and expressing osteocyte-specific gene E11 after 28 days (Gerald J Atkins et al. 2009). Primary mouse calvarial and MC3T3-E1 cells formed dendrites and expressed osteocyte-specific genes (DMP1, Sost, Phex) after 35 days on type I collagen gels with osteogenic supplements (β -glycerophosphate and ascorbic acid) (Uchihashi *et al.*, 2013). The mouse clonal cell line (IDG-

SW3) developed dendrites and expressed osteocytic markers (DMP1, Sost) after 30 days on 3D collagen sponges (Woo *et al.*, 2011). Osteoblast-osteocyte differentiation, has been induced in human osteoblasts cultured in 3D with hydroxyapatite/tricalcium phosphate biphasic calcium phosphate ceramic particles (Boukhechba & Balaguer 2009). However, these studies did not characterise the mechanical properties of the 3D matrix and could not uncover the role of the mechanical environment for eliciting osteocyte differentiation. The hydrogel stiffness used here (0.58/1.47 kPa) are within the range of gelatin-mtgase hydrogels (1.58/32.32 kPa) used to elicit differentiation of mouse myoblast cells towards osteoblasts (Tan *et al.*, 2014), which showed osteoblast-like cells became elongated at stiffnesses of 1.58 kPa, but were spherical at higher stiffnesses (32.32 kPa) (Tan *et al.*, 2014). In the current study it was shown for the first time that osteocyte differentiation and the formation of interconnections is governed by soft 3D matrices (0.58 kPa). In contrast to previous studies, these results were achieved without addition of osteogenic growth factors.

In TE scaffolds crosslinking represents the main method of changing the ECM mechanical properties. However, as well as changing the mechanical properties, crosslinks also influence the matrix ligand density and hence the availability of binding sites (Trappmann *et al.* 2012). Therefore, matrix stiffness alone may not be entirely responsible in cell differentiation, but changes in the availability of binding sites due to increased cross-linking could also play an important role (Huebsch *et al.* 2010; Huebsch *et al.* 2015; Baker *et al.* 2015). A study by Huebsch *et al.* demonstrated that matrix stiffness controlled integrin binding as well as reorganisation of adhesion ligands, promoting osteogenic commitment of mesenchymal stem-cell populations. Results showed that cells interpret changes in the physical properties of adhesion substrates as changes in adhesion-ligand presentation (Huebsch *et al.* 2010). Matrix stiffness and the physical density of crosslinks formed have also been shown to influence scaffold degradation, requiring cell-mediated degradation of the crosslinked matrix (Khetan *et al.* 2013). Khetan *et al.* studied the effect of hMSCs encapsulated within HA hydrogels of the same stiffness (23.5 kPa), that either allowed for or restricted cell-mediated degradation. Hydrogels that allowed cell-mediated degradation, displayed high degrees of cell spreading and tractions, favouring

osteogenesis, compared to restricted cell-mediated degradation, exhibiting low degrees of cell spreading and tractions, favouring adipogenesis (Khetan et al. 2013). In this study the mechanism of matrix stiffness and its effects on cell differentiation was only focused on. However, it is worth noting the ease of matrix degradation and/or the density of crosslinks are also inextricably linked to matrix stiffness and all represent important aspects in cell differentiation.

In vivo, osteocytes are formed when osteoblasts become embedded within soft secreted osteoid and undergo a dramatic phenotypic transition to a dendritic shape (Knothe Tate et al. 2004; Palumbo et al. 2004), secrete DMP-1 protein, and form interconnections with neighbouring and surface cells to establish the osteocyte network. Interestingly the same traits of a dramatic phenotypic transition to a dendritic shape, DMP-1 expression and formation of an osteocyte network in cells cultured within a soft matrix was observed. It is proposed that the mechanical properties of the hydrogel matrix might provide similar extracellular mechanical cues to that of osteoid, which is a crucial component required for the embedding of an osteoblast and stimulating osteocyte differentiation *in vivo*. The compressive moduli 0.58 kPa was the lowest achievable stiffness in this 3D environment, while a higher matrix stiffness (1.47 kPa) was selected from the gels that were crosslinked at different densities, see Figure 3-2, on the basis that it was statistically significantly higher matrix stiffness (1.47 kPa) compared to the low matrix stiffness.

Previous *in vitro* studies have shown the significance of cell density on osteogenic cell differentiation. Rat bone marrow stromal cells (BMSC) grown at low density (7.5×10^4 cells/cm²) for 8 days on 2D poly(propylene fumarate), expressed higher amounts of ALP activity compared to cells at a high density (14.9×10^4 cells/cm²) (Kim et al. 2009). It was previously reported that MC3T3-E1 cells cultured at low density (0.1×10^4 cells/cm²) had higher ALP activity compared to those at high density (1×10^4 cells/cm²), albeit that higher amounts of mineralisation were reported for the low seeding density (Mullen et al. 2013). Human marrow-derived MSC cells and MG-63 osteosarcoma cells encapsulated at low densities ($2 \times 10^6/3 \times 10^6$ cells/mL) within 3D collagen/alginate gels had higher ALP activity than cells seeded at higher densities ($1 \times 10^8/15 \times 10^6$ cells/mL) (Bitar et al. 2008; Maia et al. 2014). Here it was shown that a low density (0.4×10^4

cells/cm² ~ 0.25x10⁶ cells/mL) lead to higher ALP production after 3 days compared to cells seeded at a high density (1.6x10⁴ cells/cm² ~ 2x10⁶ cells/mL). Furthermore, an increase in calcium content in the high cell density (1.6x10⁴ cells/cm² ~ 2x10⁶ cells/mL) group within a low and high stiffness matrix compared to the other groups by 56 days was observed.

The osteocyte network is analogous to the neuronal network, whereby neurons extend long interconnected dendrites. Neural differentiation has been shown on soft 2D substrates or 3D hydrogels with stiffnesses ranging from 100-1000 Pa (Leipzig & Shoichet 2009; Ali et al. 2015). Studies have shown an increase in the percentage of neurons on 2D substrates (0.25 - 7 kPa) (Georges et al. 2006; Previtiera et al. 2010), while in soft 3D agarose gels (~0.002 kPa) increased elongation rates of neurites relative to stiff gels (~0.13 kPa) have been observed (Balgude *et al.*, 2001). Interestingly, DMP-1 expression has also been observed within the brain, suggesting strong ties with dendrite formation in neuron cells (Kalajzic et al. 2004). Therefore, it is proposed that the formation of a dendritic interconnected network within both neurons and osteocytes is driven by ECM stiffness and cell density.

Results show that cells within a soft 3D matrix are dispersed throughout long-term culture and form interconnections with neighbouring cells (Figure 3-4A & Figure 3-5A), whereas those near the surface proliferate and form a confluent layer on the surface of the hydrogel, see Figure 3-7. Similarly, HepG2 cells proliferate more when grown on 2D collagen substrates than when encapsulated within a 3D alginate gels (Lan et al. 2010). It is intriguing to speculate on the potential mechanisms by which embedded cells form dendrites and interconnected networks inside gelatin hydrogels. Our live cell results (Figure 3-9 A) and other studies (Shahar & Dean 2013; Dallas et al. 2013; Dallas & Bonewald 2010; Webster et al. 2013; Balgude et al. 2001) have shown that osteocytes and neurites are highly dynamic and repeatedly extend and retract their dendrites, and can establish connections with neighbouring cells through gap junctions (Palumbo et al. 2004; Doty 1981) to form interconnected networks. Osteocyte dendrite formation is highly dependent on continuous cleavage of collagen through enzymes known as matrix metalloproteinases (MMPs) (Holmbeck et al. 2005), which are expressed by osteocytes (Hatori et al. 2004). Interestingly, matrix

degradation through MMP activity has been shown in gelatin gels (d'Ortho et al. 1998). Therefore, it's proposed that osteoblastic cells encapsulated with softer matrices form dendrites and express MMPs to degrade the matrix macromolecules, allowing for the dendrite to perforate through the matrix. The higher degree of crosslinking between matrix macromolecules in the high stiffness group might present a matrix that is more difficult to degrade and thus explain the lower proportion of dendritic cells in these matrices.

The use of osteoblast-like MC3T3-E1 cell-line is a possible limitation of this study. However, isolating primary osteoblasts can produce inhomogeneous cell populations and osteoblast-specific features can be lost upon subcultivation (Quarles et al. 1992; Leis et al. 1997). The MC3T3-E1 osteoblast cell line represents a uniformly defined cell population, which have similar traits to primary cells and can be readily expanded (Czekanska et al. 2012) and differentiated (Keogh, O'Brien, et al. 2010; Przybylowski et al. 2012; Partap et al. 2010; St-Pierre et al. 2005; Chatterjee et al. 2010; Uchihashi et al. 2013; Krishnan et al. 2010; Mullen et al. 2013), making the cell line a good representative of pre-osteoblasts (Grigoriadis et al. 1985; Quarles et al. 1992; Sudo et al. 1983; Wang et al. 1999). It should be noted that ALP activity was only assessed from extracellular ALP in the media at specific timepoints and thus might not be a reflection of the total ALP activity. *In vivo* mineralisation is observed in both osteoblast and osteocytes (Bonewald 2011; Dallas & Bonewald 2010). However, in this study mineral content was assessed in both osteoblast and osteocytes within the same constructs and therefore is a possible limitation for demonstrating which cells type or both produced the mineral. DMP-1 staining for higher stiffness hydrogels and DMP-1 quantification of hydrogels was not explored, representing a limitation in this study. Finally, the mechanical environment that arises during osteocyte differentiation *in vivo* or the mechanical environment known to elicit osteoblast-osteocyte differentiation in 2D (~0.3 kPa) was not investigate precisely (Mullen et al. 2013). However, the mechanical properties of osteoid are unknown, as newly laid down osteoid tissue represents a thin layer approximately 350 nm deep, which has made the extraction of samples for mechanical testing unfeasible. Moreover, maintaining a homogeneous cell distribution in a low stiffness 3D matrix (~0.3 kPa) proved challenging as the cells settled at the bottom of the well

before gelling occurred, whereas 0.58 kPa was found to be the lowest achievable matrix stiffness to avoid settling from occurring. Nonetheless the results of this study showed that osteocyte differentiation of MC3T3-E1 cells was indeed regulated within a 3D cell environment by ECM stiffness and cell density.

Various *in vitro* bone TE approaches, including porous biomaterial scaffolds (Keogh, O'Brien, et al. 2010; Gleeson et al. 2010; Curtin et al. 2012; Correia et al. 2012), cellular aggregates (Freeman et al. 2015; Fuchs et al. 2007; Rouwkema et al. 2006) and cell encapsulation within hydrogels (Castillo Diaz et al. 2014; Tan et al. 2014; Chatterjee et al. 2010; Shin et al. 2014), have shown potential for bone regeneration, as indicated by osteogenic protein and mineral production. However, none of these have reported substantial osteocyte differentiation, dendrite formation or interconnected osteocyte networks within the constructs. The approach developed here may be a promising tool to reproduce bone constructs with an osteocyte network in place, which is an essential component in the formation of bone and the treatment of large bone defects.

3.5 Conclusion

The results of this study show that external biophysical and biochemical cues, such as matrix stiffness and cell density, control the phenotypic shift from osteoblasts to osteocytes in a 3D environment. For the first time MC3T3-E1 osteoblast cells, at a seeding density of 2×10^6 cells/mL within a soft 3D matrix (0.58 kPa), have been induced to undergo osteocyte differentiation and form an interconnected network by 56 days of culture. On the matrix surface a confluent layer, representative of osteoblastic differentiation, was established. These results were achieved without the addition of growth factors. It is proposed that the encapsulation of cells within a soft matrix simulates the *in vivo* environment, wherein osteoblasts start to differentiate towards osteocytes after they have become embedded within osteoid, a soft unmineralised bone matrix. Future TE approaches could apply this method to develop bone constructs with an osteocyte network in place.

Chapter 4. An *in vitro* model for trabecular bone, recapitulating both osteoblast and osteocyte differentiation in porous TE scaffolds

4.1 Introduction

Biomaterial scaffolds act as an artificial extracellular matrix that strives to mimic *in vivo* properties of bone. In particular recent studies have sought to recreate the physical architecture of trabecular bone and its natural extracellular matrix, with the goal of facilitating cell adhesion, proliferation, differentiation and elicit new tissue formation (Wu et al. 2014; O'Brien 2011; Sopyan et al. 2007).

Long term *in vitro* cultivation of bone cells on porous biomaterials (Gleeson et al. 2010; Keogh et al. 2011; Keogh, O'Brien, et al. 2010; Curtin et al. 2012; Correia et al. 2012; Kim et al. 2007; O'Brien 2011) and hydrogel biomaterial scaffolds (Castillo Diaz et al. 2014; Chatterjee et al. 2010; Tan et al. 2014; Shin et al. 2014) can sustain substantial cell numbers, viability and mineral content, and thereby enhance osteogenic differentiation and mechanical properties (Keogh, O'Brien, et al. 2010; Sittichokechaiwut et al. 2009; Kim et al. 2007; Correia et al. 2012; Naito & Dohi 2011). Such scaffolds offer enhanced biocompatibility and bioactivity for faster host bone formation after *in vivo* implantation compared to tissue regeneration from native cells (Eniwumide et al. 2007; Matassi et al. 2011; Gleeson et al. 2010). *In vivo*, trabecular bone is a highly porous complex 3D structure, consisting of trabeculae, identified as “struts” and marrow-filled cavities, known as “pores”, which allow for the supply of nutrients and removal of waste generated by the activities of bone cells (Rho et al. 1998). Matrix producing osteoblasts typically spread out over the surface of trabecular struts, while also connecting with 3D embedded osteocytes interconnected throughout the bone tissue (Rho et al. 1998; Franz-Odenaal et al. 2006; Burger & Klein-Nulend 1999). *In vivo* new tissue formation is directed by osteocytes cells, which play a vital role in maintaining bone

health by monitoring physical cues arising during load-bearing activity and directing the activity of osteoblasts and osteoclasts to initiate bone formation and resorption (Burger & Klein-Nulend 1999).

Biomaterials have been shown to promote *in vitro* osteoblast to osteocyte differentiation (Mc Garrigle et al. 2016; Gerald J Atkins et al. 2009; Uchihashi et al. 2013). In chapter 3 of this PhD thesis the formation of an osteocyte-like network, characterised by DMP-1 expression and the development of long dendrites interconnecting with neighbouring osteocytic cells (Mc Garrigle et al. 2016), within a 3D gelatin-mtgase hydrogel of 0.58 kPa stiffness was reported. Similarly, osteoblast to osteocyte differentiation in human primary osteoblast-like cells was encouraged within 3D collagen gels, with 10% of these cells becoming dendritic and expressing the osteocyte-specific gene E11 (Gerald J Atkins et al. 2009). It has also been shown that primary mouse calvarial and MC3T3-E1 osteoblast cells, seeded on the surface of a 2D type I collagen gel layer, migrated into the gel, formed dendrites and expressed osteocyte-specific genes (DMP-1, Sost, Phex) after 35 days (Uchihashi *et al.*, 2013).

Currently in bone tissue engineering, cells can either be seeded in a porous or hydrogel environment. Porous scaffolds seeded with cells contain a similar structure to trabecular bone, providing a surface area for cells to attach, spread and proliferate over the surface of the pores, promoting new tissue formation, enhancing nutrients and waste exchange and allowing for host vessel infiltration (A.R. Amini et al. 2012; Wu et al. 2014; Barbetta et al. 2010; Duffy et al. 2011). While encapsulating scaffolds, such as “hydrogels” combined with cells, generates a nanoscale mesh around the cell and therefore “encapsulates” the cell inside a 3D matrix (Nicodemus & Bryant 2008; Zisch et al. 2003; Chiu et al. 2011; Sutter et al. 2007).

While both approaches have potential as a bone regeneration strategy, it has been shown that newly formed tissue in the scaffold acts as a barrier to remodelling and osseointegration with the host tissue (Lyons et al. 2010; Alhag et al. 2012). During *in vitro* culture of such scaffolds prior to implantation, tissue formation has been reported to be denser at the periphery of the scaffold (Sikavitsas et al. 2005),

effecting cell viability in scaffold cores, overall bulk mechanical properties (Keogh et al. 2011), which at the stage of *in vivo* culture restricts integration with the host tissue (Alhag et al. 2012; Anselme 2000). In trabecular bone osteoblasts typically spread out in a cuboidal morphology over the surface, forming connections with the 3D embedded osteocyte network (Rho et al. 1998; Franz-Odenaal et al. 2006; Burger & Klein-Nulend 1999). However, current biomaterial scaffolds have not simultaneously recapitulated these necessary, but distinctly different cell phenotypes within porous scaffolds (Mc Garrigle et al. 2016; Gerald J Atkins et al. 2009; Uchihashi et al. 2013; Keogh et al. 2011; McCoy et al. 2012; Murphy et al. 2010).

It has been reported that the consistency of the newly formed tissue is related to the initial cell distribution throughout the scaffold (Wendt et al. 2003; Holy et al. 2000; Kim et al. 2000; Ishaug-Riley et al. 1998), whereby scaffolds with a dispersed cell population have consistent tissue formation throughout the construct, whereas partial cellular infiltration can lead to localised tissue formation, particularly at the periphery of the scaffold (Keogh et al. 2011). Encapsulating hydrogels and porous scaffolds have shown potential for separately mimicking osteoblast and osteocyte environments, with porous scaffolds recapitulating the flat spread morphology of osteoblasts (Keogh et al. 2011; McCoy et al. 2012; Murphy et al. 2010) whereas hydrogel scaffolds promote osteoblast-osteocyte differentiation within a 3D matrix (Mc Garrigle et al. 2016; Gerald J Atkins et al. 2009; Uchihashi et al. 2013).

For bone tissue engineering, the combination of cells with biomaterial scaffolds is mainly achieved through peripheral seeding or cell encapsulation, with both methods determining initial cell distribution. Peripheral seeding involves covering each side of a pre-fabricated scaffold with cells, and hence relies on cellular migration into the scaffold interior from the periphery to populate the construct (Haugh et al. 2011). For such approaches, fabricating the scaffold prior to cell seeding allows for the formation of complex scaffold features with high mechanical properties from biomaterials, such as ceramic, silk or natural polymers (Correia et al. 2012; Curtin et al. 2012; Duffy et al. 2011; Harley & Gibson 2008; Keogh, O'Brien, et al. 2010; Kim et al. 2007; Sabree et al. 2015; Murphy et al. 2010). However,

peripheral seeding techniques are inadequate for large scale constructs, due to the time required for cells to proliferate throughout the construct (Arano et al. 2010; Gardel et al. 2013) and the occurrence of cell proliferation and differentiation around the periphery, which ultimately leads to core necrosis (Gardel et al. 2013; Holy et al. 2000; Arano et al. 2010; Ishaug-Riley et al. 1998; Keogh et al. 2011). Furthermore, within peripheral seeded scaffolds the timing of delivering osteogenic cues to facilitate cell differentiation is also important, as the cells will no longer proliferate or migrate after differentiation occurs (Ichida et al. 2011). Moreover the cells remain attached on the surface of the porous material, rather than becoming embedded within it, and rely on new tissue formation to provide cues for differentiation. Cellular encapsulation within a polymer solution allows the formation of a scaffold at the same time as integrating cells (Nichol et al. 2010; Amini & Nair 2012). Such approaches provide a more homogenous distribution of cells throughout the scaffolds, whereby cells are suspended in a 3D environment (Rana & Kumar, T.S. Sampath Ramalingam 2014). Large scaffolds with high cell seeding efficiencies and homogenous cell distribution can be achieved through this technique (Chen et al. 2013). Moreover, encapsulation provides an immediate 3D environment, akin to that existing *in vivo*, and might ultimately enhance cell differentiation.

Substrate stiffness is an important physical factor for regulation of cell distribution, due to the fact that it governs migration (Zaman & Trapani 2006), proliferation (Hadjipanayi et al. 2009), and differentiation (Tan et al. 2014; Lo et al. 2000; Mullen et al. 2013; Engler et al. 2004; Mc Garrigle et al. 2016). In peripherally seeded scaffolds, high stiffness collagen-glycosaminoglycan (CG) scaffolds (1.4 and 1.8 KPa) increased cell number and enhanced cellular distribution by 7 days, compared to those on low stiffness (~0.5 kPa) scaffolds (Haugh et al. 2011). However, low stiffness (0.48 kPa) promoted increased mineralisation and mechanical properties, compared to high stiffness scaffolds (1.17 and 1.37 kPa) (Keogh, O'Brien, et al. 2010). For encapsulation approaches, a low stiffness (1.3 kPa) alginate-fibrin matrix allowed primary fibroblasts cells to spread and proliferate within the alginate-fibrin hydrogel up to 7 days, compared to those encapsulated in a higher stiffness fibrin hydrogels (9.14 kPa) (Hwang et al. 2013). In a separate study,

a high matrix stiffness (225 kPa) promoted increased osteogenic protein and mineral production compared to low stiffness matrix (10 kPa) (Chatterjee et al. 2010). In chapter 3, it was reported that low stiffness substrates allowed for encapsulated MC3T3-E1 cells to migrate and form long dendrites and interconnections with neighbouring cells along with increased mineralisation, whereas those encapsulated in high stiffness hydrogels formed shorter dendrites and a less interconnected network and mineral (Mc Garrigle et al. 2016). While such studies provide evidence of the beneficial effects of peripheral seeding and simultaneous cell encapsulation, to date the optimum mechanical properties required for uniform cell distribution and differentiation within TE scaffolds have not been defined.

This study tests the hypothesis that initial cell distribution and stiffness in 3D will promote uniform cell distribution and subsequent tissue formation throughout TE scaffolds. Furthermore, combining porous and cell-encapsulating scaffolds may recapitulate the *in vivo* environment of trabecular bone priming constructs towards both osteoblast and osteocyte development. The first objective was to explore whether delaying the addition of differentiation cues until the scaffold has been fully populated, can enhance MC3T3-E1 pre-osteoblasts cell distribution and osteogenic differentiation in peripheral seeded GG scaffolds. The second objective was to investigate MC3T3-E1 cell distribution in gelatin scaffolds with varied scaffold stiffness; (1) peripheral seeded porous gelatin glycosaminoglycan (GG) scaffolds (0.5, 0.8 and 1.4 kPa), (2) cells encapsulated in hydrogels (15.98 and 19.33 kPa) and (3) porous mtgase-gelatin hydrogels (0.58 and 0.7 kPa). The third objective was to investigate whether combining cells with porous and cell-encapsulating scaffolds enhances cell distribution, tissue formation and the promotion of both osteoblasts and osteocyte within the same construct. Cell number and distribution was examined by DNA content and histological staining of cell nuclei and cytoskeleton actin. Osteogenic differentiation and tissue formation was examined by ALP activity, calcium content and distribution. Osteoblast-osteocyte differentiation was examined by DMP-1 expression, cell morphology and matrix mineralisation.

4.2 Methods

4.2.1 Cell culture

MC3T3-E1 pre-osteoblastic cells (Sigma–Aldrich) were cultured under standard conditions (5 % CO₂, 37 °C). Cells were routinely grown to 70-80% confluency in T175 culture flasks (Sarstedt Ltd, Wexford, Ireland) containing supplemented alpha minimum essential medium (α MEM) culture medium (Sigma–Aldrich), 10 % FBS (Sigma–Aldrich), 100 U/mL penicillin (Sigma-Aldrich), 100 g/mL streptomycin (Sigma Aldrich) and 2 mM L-glutamine (Sigma-Aldrich). Before peripheral seeding and encapsulating, MC3T3-E1 cells (Passage 14-16) were detached using trypsin–ethylenediaminetetraacetic acid (EDTA, Sigma-Aldrich).

4.2.2 Mechanical testing

Unconfined compressive testing was used to determine the mechanical properties of the crosslinked GG scaffold, encapsulated and porous encapsulated hydrogels. Mechanical testing of scaffold samples was carried out using a biaxial tensile tester (Z009; Zwick/Roell) fitted with a 10-N load cell. Samples were hydrated and held in a bath of PBS during testing. Unconfined compression testing was conducted at a strain rate of 10%/min with an impermeable, un-lubricated platen. The modulus was defined as the slope of a linear fit to the stress–strain curve over 2%–5% strain (Harley et al. 2007).

4.2.3 Cell number

Cell number was evaluated using the Hoechst 33258 DNA assay, which fluorescently labels double-stranded DNA (Sigma-Aldrich), as previously described (Haugh et al. 2011). Cell-seeded GG scaffolds and cell encapsulated gelatin-mtgase hydrogels were washed twice with PBS, frozen and stored at -80 °C. Samples were then thawed and digested overnight in papain digest (100 mM Sodium Phosphate Buffer containing 10 mM L-cysteine, 125 μ g/mL Papain and 5 mM Na₂EDTA (all from Sigma Aldrich) in ddH₂O at pH 6.5 and 60 °C). Once the samples were digested the biochemical assays were performed straight away or stored at – 80 °C until the assays could be performed. Briefly, 200 μ L of Hoechst dye solution was

added to 20 μL of digested samples / standards in a 96-well plate in triplicate. Fluorescence was then measured (excitation: 355 nm; emission: 460 nm) using a fluorescence spectrophotometer (Synergy HT Multi-mode microplate reader). Readings were converted to cell number using a standard curve, according to the manufacturer's protocol. The background fluorescent was accounted for by subtracting a blank sample containing no cells.

4.2.4 Peripheral seeding

4.2.4.1 GG freeze dried scaffold fabrication

Scaffolds were produced by freeze-drying a gelatin glycosaminoglycan (GG) suspension. Briefly, a suspension containing 1% (w/v) gelatin (Sigma-Aldrich) and 0.1% (w/v) chondroitin-4-sulfate (Sigma-Aldrich) was prepared in 0.05M acetic acid. This slurry was then freeze-dried using a freezing temperature of $-40\text{ }^{\circ}\text{C}$, as previously described (Haugh et al. 2011). After freeze-drying, cylindrical samples of diameter 12.7 mm and 4 mm height were cut from the scaffold sheet, see Figure 4-1. To produce scaffolds of different stiffness, samples were crosslinked in a solution of 1-Ethyl-3-(3-dimethylaminopropyl) carbodiimide (EDAC) (Sigma-Aldrich) and N-Hydroxysuccinimide (NHS) (Sigma-Aldrich) at concentrations of EDAC (3, 6, 12, 24 and 48mM per gram GG scaffold) (Haugh et al. 2011). Crosslinked GG Scaffolds were sterilised through ethanol washes, rinsed with phosphate buffer saline (PBS) and stored at $4\text{ }^{\circ}\text{C}$ till cell culture was carried out.

4.2.4.2 Scanning electron microscopy (SEM)

Scanning electron microscopy (SEM) images were captured of the GG scaffold pore structure. Briefly, dry scaffolds were fixed to an adhesive carbon stub and their surface sputter coated with gold and then observed through SEM (Hitachi S-4700).

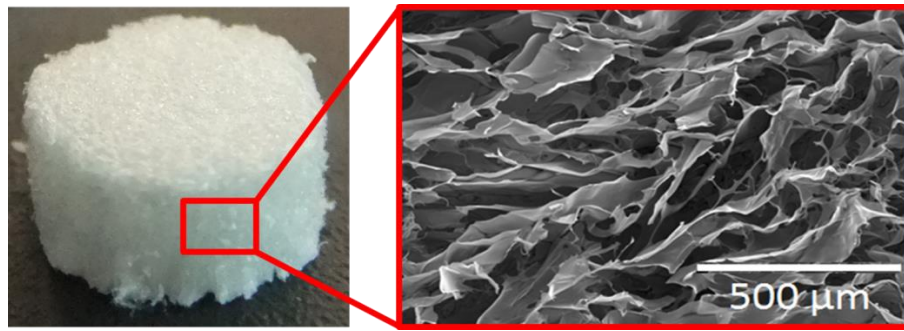


Figure 4-1: Scanning electron microscope (SEM) image of a dry porous GG scaffold

4.2.4.3 *Peripheral seeding*

GG scaffolds were seeded with 1×10^6 MC3T3 cells on one side for 15 mins, to allow cellular infiltration and attachment, before scaffolds were turned over and the other side was seeded with a further 1×10^6 cells and incubated for another 15 mins, thus a total 2×10^6 cells were seeded per construct. After the second incubation seeded scaffolds were either (a) allowed to differentiate immediately (Osteo group), through addition of osteogenic growth factors (100 nM dexamethasone, $50 \mu\text{g/ml}$ ascorbic acid, 10 mM β -glycerol phosphate) (Sigma-Aldrich) to cell culture media, or (b) cell differentiation was delayed (Delayed group) for 7 days, during which time cells proliferated in expansion media (10% foetal bovine serum, 2% penicillin/streptomycin and 1% L-glutamine). Both groups were cultured from day 7 in osteogenic media up to 28 days.

4.2.4.4 *Peripheral seeded cell distribution*

Cell distribution within GG scaffolds and hydrogels was assessed at 2 hours, 7, 21 and 28 days. Constructs were fixed in 10% formalin for 1 hour, dehydrated and paraffin embedded using an automated tissue processor (Leica ASP300; Leica). All constructs were sectioned with a thickness of $10 \mu\text{m}$ using a rotary microtome (Leica microtome, Leica). Construct sections were stained with 4', 6-Diamidino-2-Phenylindole (DAPI) dilactate (diluted 1:2000, Sigma Aldrich) to stain the nucleus.

GG scaffold particle analysis method:

Construct sections were imaged as a grid, containing overlapping areas. Images were captured at 4x magnification using an Olympus IX50 inverted fluorescence microscope. NIH ImageJ software was used to generate stitched images of the sectioned construct. Images were thresholded between 80-255 and converted to binary in preparation for particle analysis, see Figure 4-2 (A). Particle analysis was performed, with a particle size of 20–500, providing an x, y coordinate for each particle throughout the entire scaffold cross section, Figure 4-2 (B). Coordinate points (x, y) from particles were plotted to illustrate cell distribution in the scaffold cross-section, see Figure 4-2 (C).

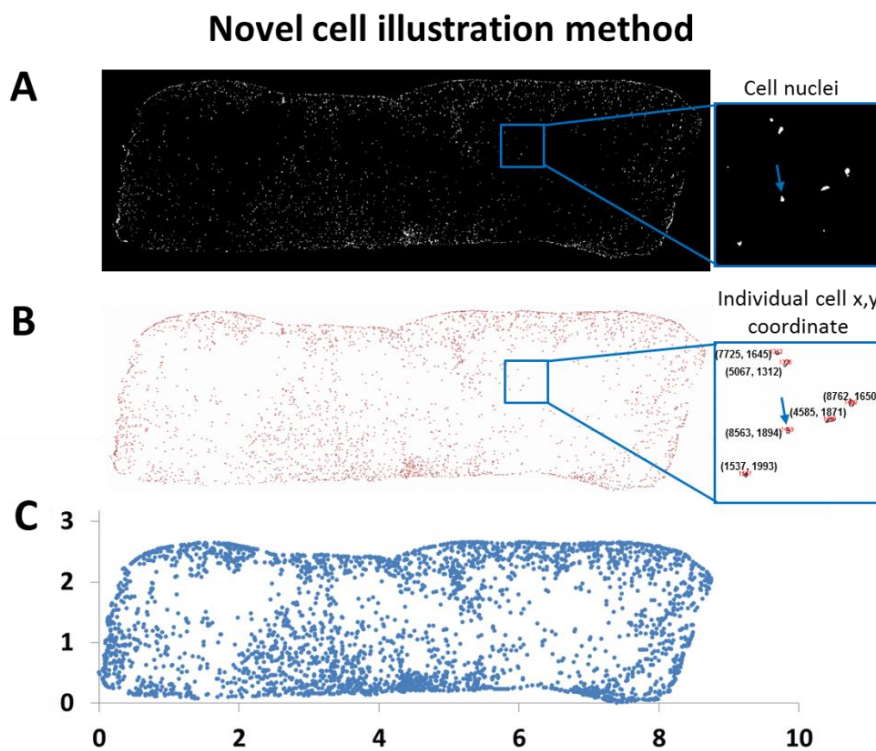


Figure 4-2: Cell nuclei distribution within a scaffold section (A). ImageJ software was used to threshold and perform particle analysis to determine coordinates of individual cell nuclei (B), allowing for a graph of cell distribution to be created (C).

4.2.4.5 Extracellular ALP activity

Extracellular alkaline phosphatase (ALP) activity was determined using a colorimetric assay of enzyme activity (SIGMAFAST *p*-NPP Kit, Sigma Aldrich), which uses *p*-nitrophenyl phosphate (*p*NPP) (nmol) as a phosphatase substrate, with

ALP enzyme (Sigma Aldrich) as a standard. Prior to media change, media was removed from samples at each timepoint, frozen and stored at $-80\text{ }^{\circ}\text{C}$. $40\text{ }\mu\text{L}$ of the medium was added to a 96-well plate in triplicate with a $50\text{ }\mu\text{L}$ of *p*NPP solution, which contains both *p*NPP and assay buffer. The samples were shielded from direct light at room temperature for one hour. After this, $20\text{ }\mu\text{L}$ of Stop Solution (3 M NaOH) was added to the wells and the plate was read at 405 nm in a Synergy HT Multi-mode microplate reader. Results were then normalised to cell number (μg) as determined through the Hoechst assay outlined above and expressed as nmol/ μg .

4.2.4.6 Calcium content

Calcium content within GG scaffold constructs was determined using a Calcium Liquicolour kit (Stanbio Laboratories, Syntec, Ireland) according to the manufacturer's protocol. After 21 and 28 days of incubation, GG scaffolds were washed twice with PBS, frozen and stored at $-80\text{ }^{\circ}\text{C}$. GG scaffolds were then thawed and digested by adding 1 mL of 0.5 M hydrochloric acid (HCL) (Sigma-Aldrich) to each sample and storing the solution at $4\text{ }^{\circ}\text{C}$. $10\text{ }\mu\text{L}$ each of the digested samples and assay standard was added to a 96-well plate and $200\text{ }\mu\text{L}$ of the working solution. The plate was read on a synergy HT Multi-mode microplate reader at an absorbance of 550 nm, as previously described (Freeman 2013).

4.2.4.7 Mineral distribution

Mineral distribution within scaffolds were assessed at days 0, 7, 21 and 28. Constructs ($n=2$) were fixed in 10% formalin for 30 mins, dehydrated and embedded in paraffin using an automated tissue processor (Leica ASP300, Leica). All samples were sectioned with a thickness of $10\text{ }\mu\text{m}$ using a rotary microtome (Leica microtome, Leica). Fixed sections were stained with 2% Alizarin red to determine calcium distribution throughout the scaffold as previously described (Haugh et al. 2011). Images were captured using an Olympus IX50 inverted microscope.

4.2.5 Cell encapsulation

4.2.5.1 Encapsulated and porous encapsulated gelatin-mtgase hydrogel fabrication

Encapsulated and porous encapsulated gelatin–mtgase hydrogels were fabricated with a final concentration of 6 % w/v gelatin. Hydrogels were prepared by mixing gelatin (type A, 175 Bloom, Sigma–Aldrich) at 80 °C in supplemented (α MEM) culture medium to obtain a liquid consistency for easier mixing. Gelatin suspensions were sterile filtered through a 0.22 μ m filter (Millipore, Cork, Ireland). Microbial transglutaminase (mtgase) (Activa WM; containing 1 % mtgase; Ajinomoto foods Europe S.A.S., Mesnil-Saint-Nicaise, France) crosslinking was carried out by mixing the gelatin suspension with 0.03 % and 0.08% mtgase per gram of gelatin. Moulds were fabricated in house and inserted into 24 well-plates with a plastic coverslip placed at the bottom to allow for easy removal of the gelatin hydrogels, see Figure 4-3. Cell free hydrogels suspensions were allowed to gel at 4 °C for 8 min within the moulds.

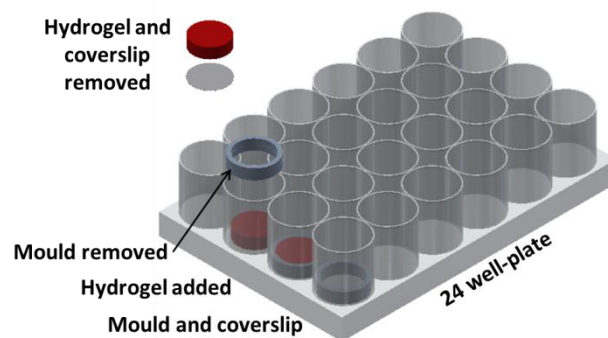


Figure 4-3: Illustrates the fabrication method of gelatin-mtgase hydrogels (diameter 12.7 x 4 mm). A coverslip and custom made moulds were inserted within the 24 well-plate and the hydrogel solution added. The moulds were removed and media added. The hydrogel could then be removed by lifting the coverslip.

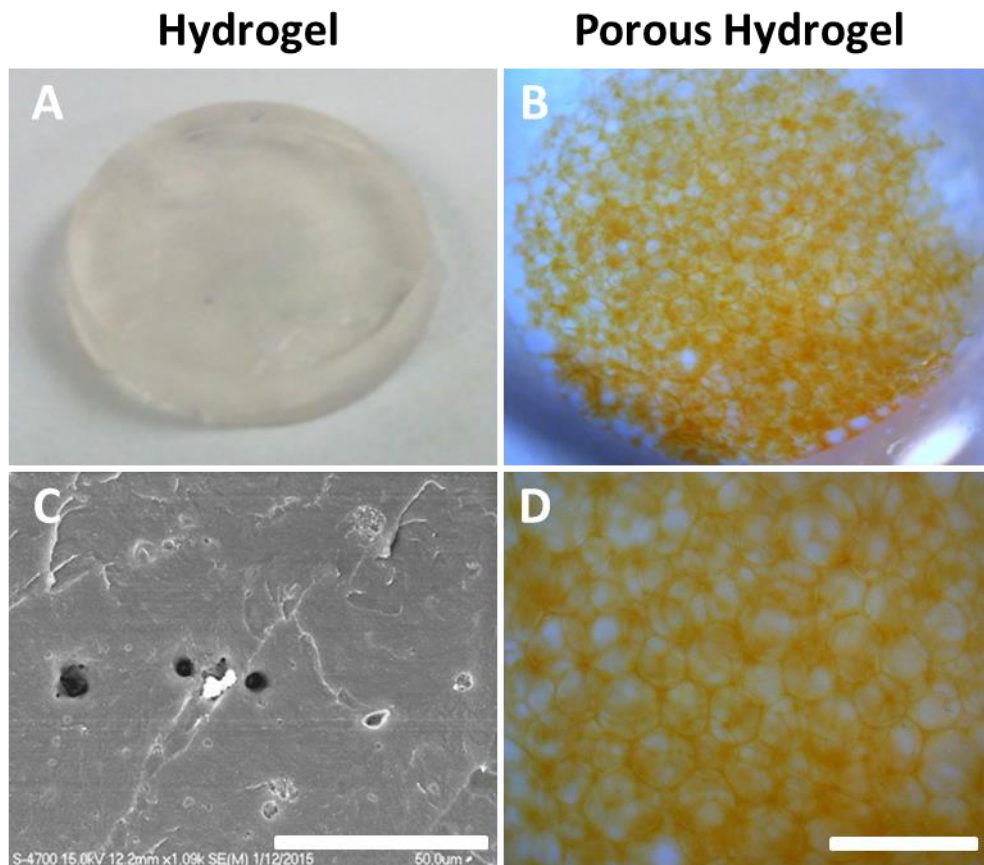


Figure 4-4: Illustrates a hydrogel (A) and a porous hydrogel (B). Scanning electron microscope (SEM) image of a hydrogel (C) and brightfield image of a porous hydrogel (D). Scale bars 50 μm (C) and 2 mm (D).

4.2.5.2 Cell encapsulation in hydrogels

Cell encapsulated hydrogels were produced by mixing cells with the mtgase-gelatin suspension at a ratio of 5:4:1 (v:v:v) and pipetting 500 μL of the solution into moulds within 24 well-plates. Hydrogels were produced with a final concentration of 6 % w/v gelatin, 2×10^6 cells per construct and a bulk overall volume of 500 μL .

4.2.5.3 Cell encapsulation in porous hydrogels

Porous cell encapsulated hydrogels were fabricated using the same solution of gelatin, but at a cell density of 8×10^6 cells/mL, to take into account the porous void volume, ensuring a total of 2×10^6 cells per construct. Micro-pores were introduced into the gelatin/mtgase/cell solution by forming micro-bubbles in the solution. Briefly, 125 μL of solution was pipetted into a thin liquid film. The pipette was set to

aspirate a controlled volume of 250 μL . During aspiration the pipette tip was immersed within the solution at approximately at 45° , allowing for a mixture of the solution (125 μL) and micro-bubbles (125 μL) to be introduced into the pipette tip, forming a close array of bubbles within the hydrogel. This was repeated forming the final 500 μL volume. Overall, the hydrogel solution comprised 250 μL , while the porous void consisted of 250 μL , giving a porosity of $\sim 50\%$. All hydrogel constructs had a diameter of 12.7 mm and height of 4 mm and were allowed to gel at 4°C for 6 min before media was added. Porous hydrogels were left in the incubator to stabilise for 30 mins before micro-bubbles were removed by vacuuming at ~ 60 Torr, replacing porous void volume with media and leaving behind an interconnected porous scaffold architecture. Samples were placed again in the incubator. Media was renewed every 2-3 days.

Encapsulated and porous encapsulated hydrogels were cultured for 2 hours and 7 days.

4.2.5.4 Encapsulated cell distribution

Porous cell encapsulated hydrogel constructs were fixed using 4 % (w/v) paraformaldehyde (Sigma-Aldrich) after 2 hours and 7 days of culture, for 1 hour. Cells within the hydrogels were permeabilised with 0.5 % Triton-X100 in PBS (Sigma-Aldrich) for 10 minutes at 4°C under rotation and washed with PBS three times. Hydrogels were then stained with phalloidin-Fluorescein Isothiocyanate (phalloidin-FITC) solution at $1.25\mu\text{g}/\text{mL}$ (diluted 1:400, Sigma Aldrich), to stain the actin cytoskeleton, and DAPI dilactate (diluted 1:2000, Sigma Aldrich), to stain the nucleus, and were finally rinsed again with PBS solution. All images were captured using an Olympus IX50 inverted fluorescence microscope.

4.2.5.5 DMP-1 immunofluorescent staining

The low stiffness porous hydrogel group was selected for cell morphology and osteoblast-osteocyte differentiation. Hydrogel constructs were fixed using 4% paraformaldehyde (Sigma-Aldrich) after 32 days of culture for 1 hour under rotation. Cells within the hydrogels were permeabilised with 2mM Sodium Chloride (NaCl), 1.5 mM Magnesium Chloride (MgCl_2), 16 mM Sucrose and 0.5% Triton-X100 in

PBS (all from Sigma-Aldrich) for 10 mins at 4°C under rotation and washed in PBS 3 times. Hydrogel constructs were covered with a 10% bovine serum albumin (BSA) / 3% normal goat serum (NGS) (Jackson Immuno research) blocking solution for 1 hour under rotation before incubation with monoclonal anti-DMP1 antibody at a dilution of 1:100 at 4°C overnight (Clone 8G10.3, Millipore). After washing 3 times with 1% BSA/PBS solution, samples were then treated with a Dylight™ 549 conjugate goat anti-mouse secondary antibody at a dilution of 1:100 (Jackson Immunoresearch) for 1 hour under rotation at room temperature. After secondary staining, samples were rinsed 3 times with 1% BSA/PBS solution. Hydrogels were then further counterstained with phalloidin-FITC at 1.25µg/mL (diluted 1:400, Sigma Aldrich) to stain the actin cytoskeleton and DAPI dilactate (diluted 1:2000, Sigma Aldrich) to stain the nucleus and rinsed again with 1% BSA/PBS solution. Confocal scans were taken using a confocal microscope (Olympus fluoview) at 20x, 40x and 60x magnification. Maximum intensity images were generated from z-stacks taken at 20x magnification with a distance of 5µm between each slice for a thickness of 25µm, while 40x and 60x magnification z-stacks were taken at a distance of 2.5µm between each slice for a thickness of 10µm.

4.2.5.6 Mineral distribution

Staining for calcium deposits was carried by incubating samples within 1% Alizarin red (pH 4.3) solution for 30 minutes at 22 °C on an orbital rocker, as previously described (Tan et al. 2014). Samples were imaged on an Olympus IX50 inverted microscope.

4.3 Statistical Analysis

Results are expressed as mean \pm standard deviation. For DNA content analysis two-way analysis of variance (ANOVA) was conducted, followed by pair-wise multiple comparison procedure (Tukey's HSD test). All analyses were performed with GraphPad Prism 6 (GraphPad software, San Diego, USA). For all comparisons, the level of significance was $p \leq 0.05$.

4.4 Results

4.4.1 Peripheral seeding

4.4.1.1 Mechanical testing of GG scaffolds

Compressive testing of varied GG scaffold stiffness showed an increase in stiffness with varied cross-linking concentration, see Figure 4-5. GG scaffolds containing 3, 6, 12, 24, 48 mM EDAC / g scaffold mtgase had compressive moduli of 0.6 ± 0.1 , 0.8 ± 0.2 , 0.98 ± 0.2 , 1.09 ± 0.2 and 1.4 ± 0.2 kPa, respectively. Three GG scaffold stiffnesses (0.5, 0.8, 1.4 kPa) were selected for further cell culture analysis. The compressive moduli 0.5 kPa was the lowest achievable stiffness with GG scaffolds, while the higher GG scaffold stiffnesses (0.8 and 1.4 kPa) was selected from the scaffolds that were crosslinked at different densities, on the basis that it was a significantly higher substrate stiffness compared to the low matrix stiffness.

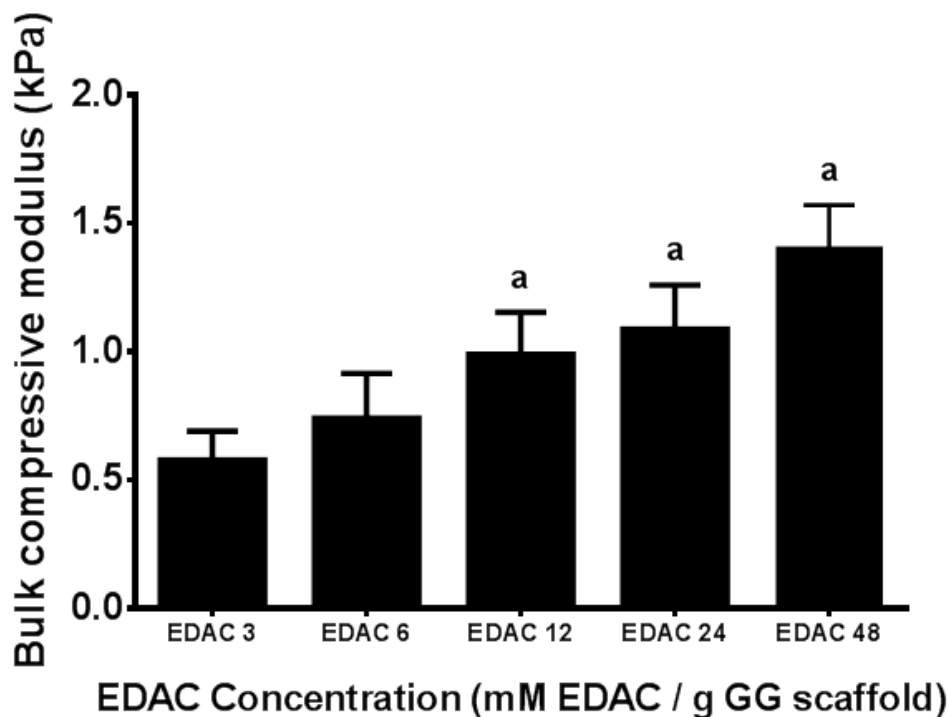


Figure 4-5: Concentration of EDAC crosslinking and mechanical properties of GG scaffolds. $n=8$ per group. ^a $p<0.05$ relative to EDAC 3 crosslinked GG scaffold.

4.4.1.2 Cell number

For peripherally seeded GG scaffolds, a significant increase in cell number from day 0 to 28 was observed in all groups, except the 0.5 kPa immediate osteogenic group ($p < 0.05$). Furthermore, at day 28, in the delayed osteogenic group, cell number was significantly higher in the high substrate stiffness (1.4 kPa) group compared to the low stiffness (0.5 kPa) group ($4.4 \times 10^6 \pm 0.61 \times 10^6$ vs. $2.9 \times 10^6 \pm 1.65 \times 10^6$, $p < 0.0012$). Similarly, at day 28 cell number was significantly higher in the 0.8 and 1.4 kPa immediate osteogenic group, compared to the 0.5 kPa group ($2.22 \times 10^6 \pm 0.47 \times 10^6$ and $3.4 \times 10^6 \pm 1.14 \times 10^6$ vs. $3.75 \times 10^6 \pm 0.62 \times 10^6$, $p < 0.04$), see Figure 4-6 ($p < 0.05$). No significant difference was observed between corresponding substrate stiffness groups for immediate and delayed osteogenic groups for any timepoint.

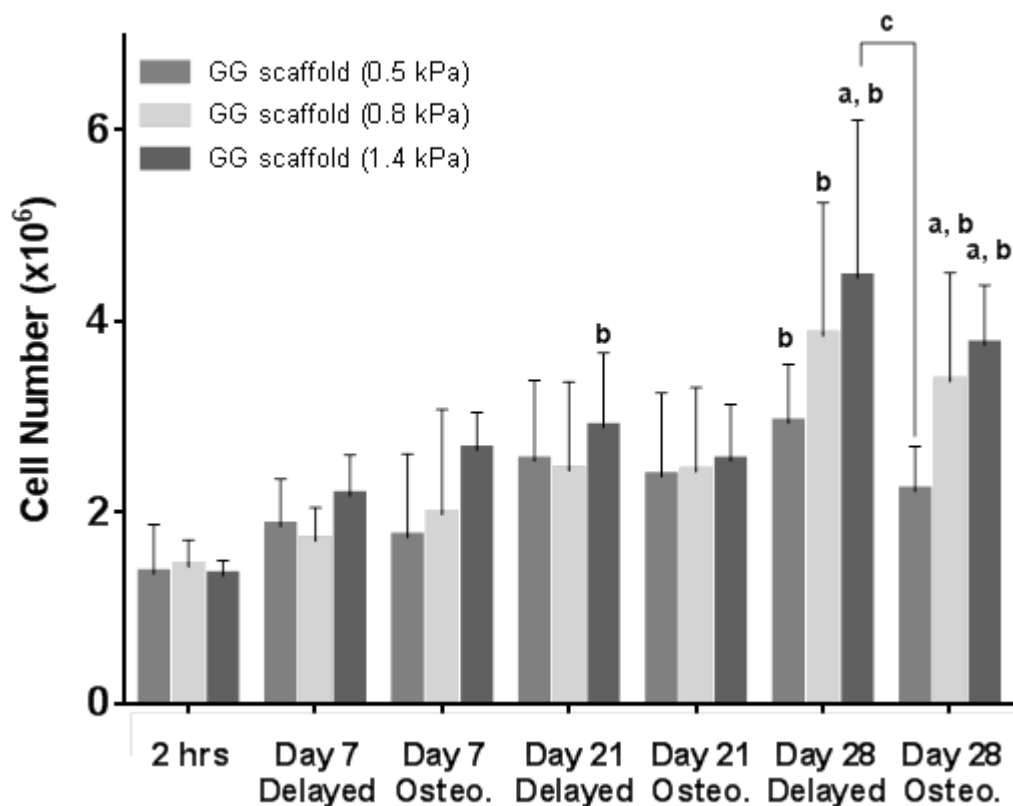


Figure 4-6: Cell number within GG scaffolds at 2 hrs, 7, 21 and 28 days. ^a $p < 0.05$ versus corresponding 0.5 kPa stiffness group at the same time point, ^b $p < 0.05$ versus corresponding stiffness group at 2 hrs and ^c $p < 0.05$ ($n = 6$ samples per group per time-point). Error bars denote the standard deviation.

4.4.1.3 Peripherally seeded cell distribution

After 2 hours, for all peripherally seeded GG scaffolds, it was observed that cell distribution was concentrated predominately around the scaffold periphery, with partial infiltration towards the scaffold centre. By day 7, increased cell infiltration towards the scaffold centre was observed for all groups, along with increased cell proliferation around the scaffold periphery. By day 21 and 28, no difference in distribution was observed between delayed and osteogenic groups, see Figure 4-7. In low stiffness GG scaffolds (0.5 & 0.8 kPa) over the culture period, it was visually observed that a reduction in the construct size occurred compared to the high stiffness scaffolds (1.4 kPa), which retained their structure, see Figure 4-7.

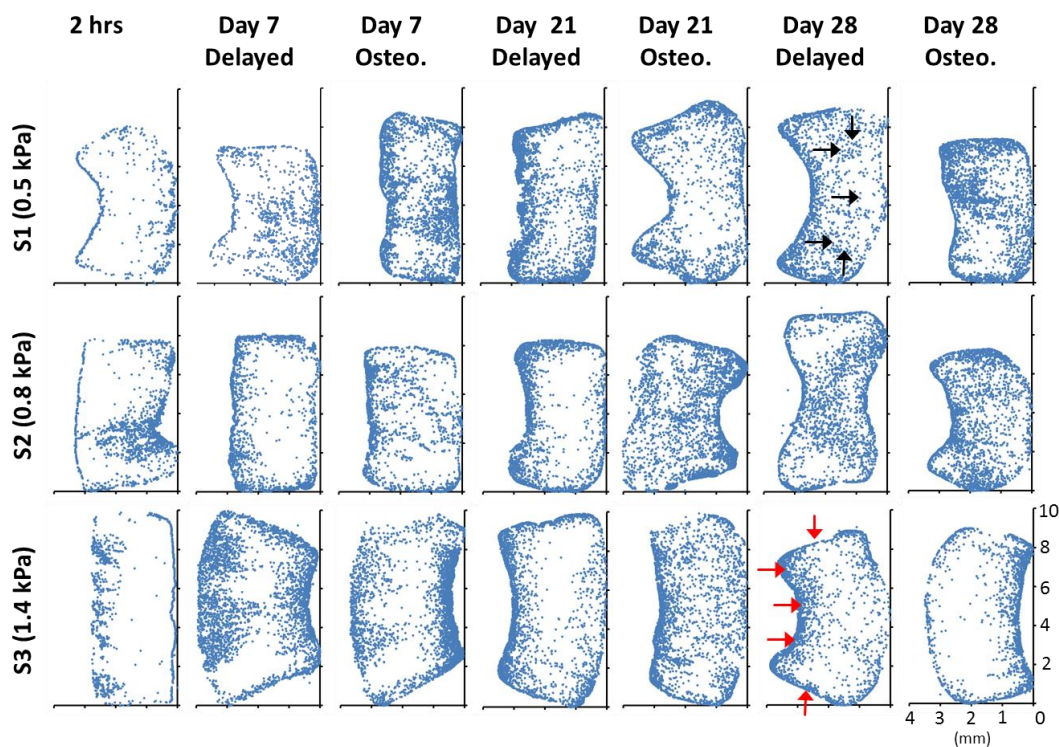


Figure 4-7: Cell distribution in GG scaffolds after 2 hours, 7, 21 and 28 days illustrating cell attachment around the periphery (Red arrows) of the scaffolds with migration towards the centre (Black arrows) over the course of 28 days ($n=2$).

4.4.1.4 Extracellular ALP activity

At day 21, ALP activity in the 0.5 and 0.8 kPa in delayed osteogenic groups was significantly higher than the respective 1.4 kPa group (0.76 ± 0.2 nmol/ μ g and

0.75±0.18 nmol/μg vs. 0.47±0.12 nmol/μg, $p < 0.006$), see Figure 4-8. For the delayed osteogenic group there was a significant increase in ALP activity compared to the immediate osteogenic group at substrate stiffness of 0.5 and 0.8 kPa ($p < 0.02$). By day 28, the 0.5 kPa stiffness group had significantly higher ALP activity than the 0.8 and 1.4 kPa stiffness groups, for both the delayed and immediate osteogenic groups ($p < 0.008$).

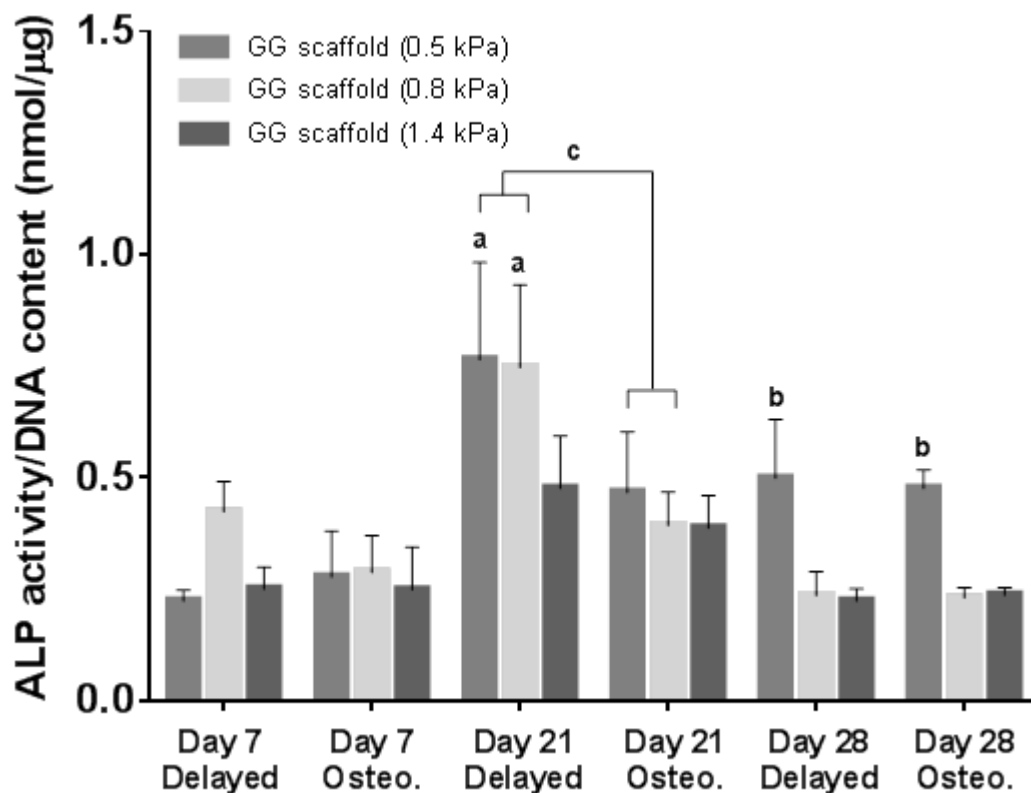


Figure 4-8: Extracellular ALP activity at day 7, 21 and 28. ^a $p < 0.05$ versus corresponding 1.4 kPa stiffness group at the same time point. ^b $p < 0.05$ versus corresponding stiffness groups at the same time point. ^c $p < 0.05$. Error bars denote the standard deviation ($n = 3$).

4.4.1.5 Calcium Content

All groups showed a significant increase in mineral content throughout the time course of the experiment, see Figure 4-9. A significant difference in calcium content was observed between the high stiffness scaffolds (1.4 kPa) in the delayed and immediate osteogenic groups by day 21 ($3.47 \pm 1.32 \mu\text{g}$ versus $7.3 \pm 0.81 \mu\text{g}$, $p <$

0.017). Delayed osteogenic groups showed a significant increase in calcium content from day 21 to 28, while no difference was observed in the immediate osteogenic groups. No significant difference was observed between groups at day 28.

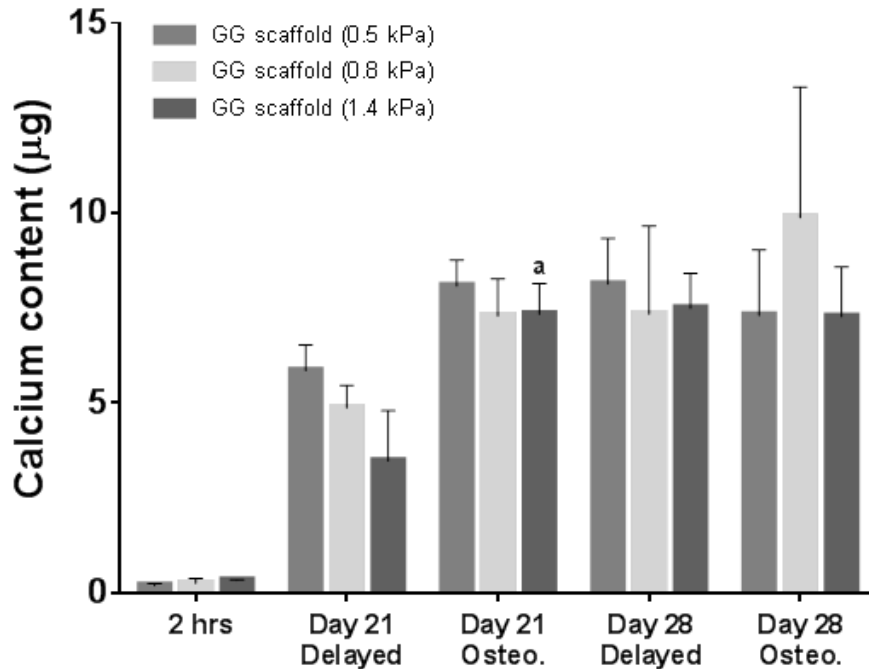


Figure 4-9: Calcium content at 2 hours, 21 and 28 days. ^a $p < 0.05$ versus corresponding stiffness at the same timepoint. Error bars denote the standard deviation ($n = 3$).

4.4.1.6 Mineralisation

Alizarin red staining for mineral distribution showed positive calcium staining in all groups at day 21 and 28, see Figure 4-10. Interestingly, consistent mineralisation was observed throughout the high stiffness GG scaffold (1.4 kPa), whereas in the lower stiffness scaffolds (0.5 kPa, 0.8 kPa) mineral formation was localized in discrete areas within the constructs, see Figure 4-10.

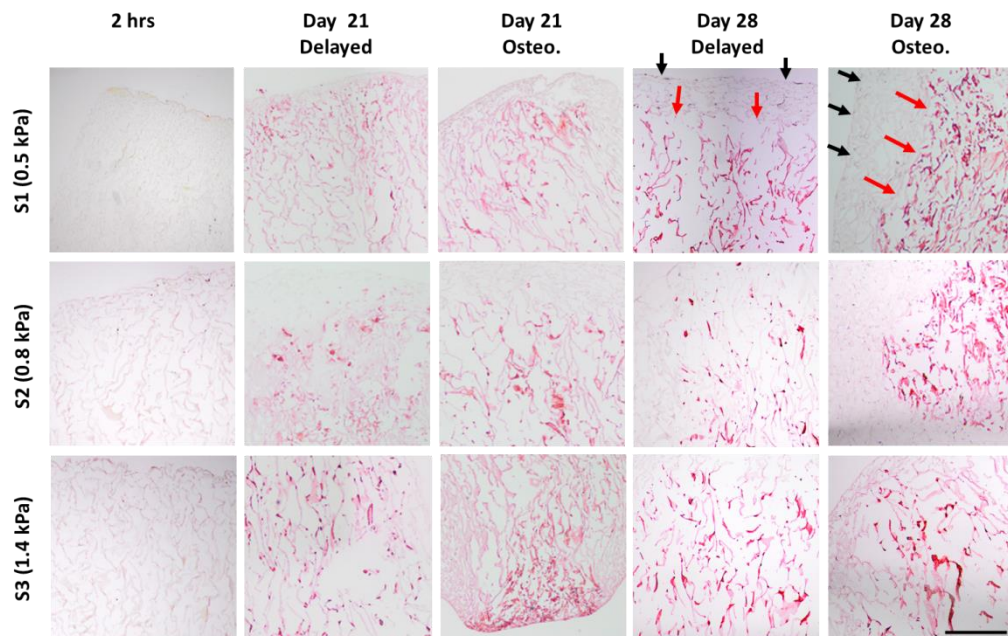


Figure 4-10: Alizarin red stain showing mineral distribution at 2 hours, 21 and 28 days ($n = 2$), with black arrows denoting the periphery of the scaffold and red arrows the start location of mineral. Scale bar 300 μm .

4.4.2 Cell encapsulation

4.4.2.1 Mechanical testing of encapsulated and porous encapsulated gelatin-mtgase hydrogels

Compressive testing of hydrogels showed a significant difference between a low (15.98 ± 2.5 kPa) and high (19.33 ± 1.23 kPa) crosslinking concentration ($p < 0.05$), Figure 4-11. However, no difference was observed between porous hydrogels at a low (0.58 ± 0.42 kPa) and high (0.7 ± 0.35 kPa) crosslinking density, see Figure 4-11.

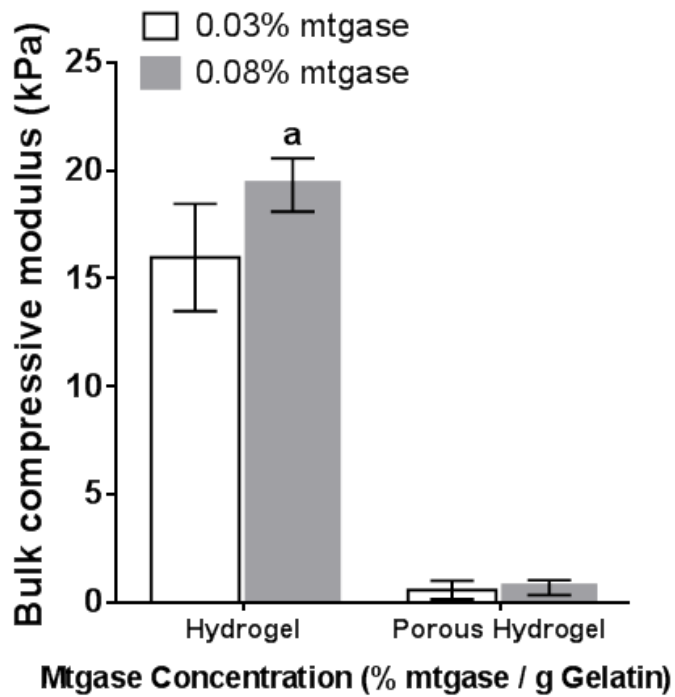


Figure 4-11: Compressive properties of 6 % gelatin encapsulated and porous encapsulated hydrogels crosslinked with 0.03% and 0.08% mtgase. ^a $p < 0.05$ relative to 0.03 % mtgase hydrogel (n = 8). Error bars denote the standard deviation.

4.4.2.2 Cell number

After 2 hours, similar cell numbers were observed between the encapsulated and porous encapsulated hydrogel groups, see Figure 4-12. After 7 days, no significant difference in cell number was observed between all groups.

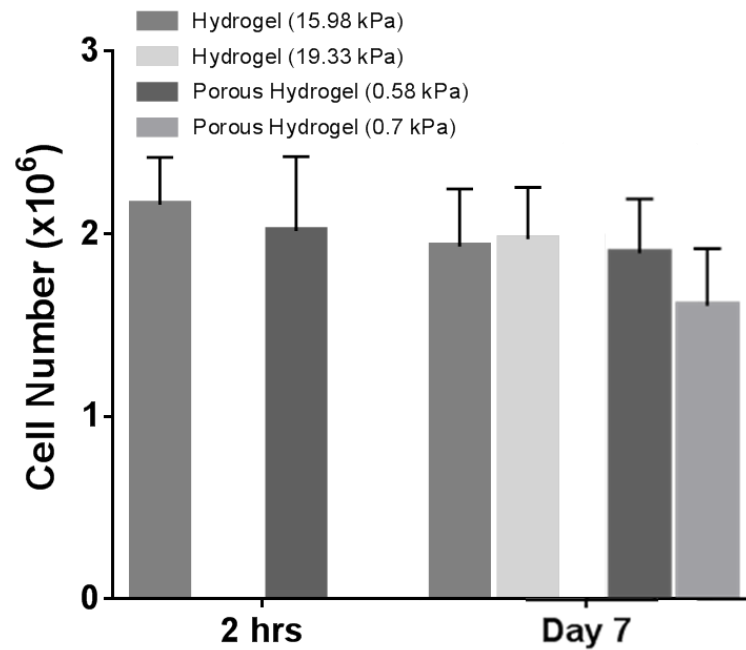


Figure 4-12: Cell number within encapsulated and porous encapsulated hydrogels at 2 hours and 7 days (B) ($n = 6$). Error bars denote the standard deviation.

4.4.2.3 Encapsulated cell distribution

After 2 hours, in the low stiffness encapsulated hydrogel group, cells were homogeneously distributed throughout the hydrogel. Similarly, cells were homogeneously distributed throughout the high stiffness porous encapsulated hydrogel, and were encapsulated in the struts of the scaffold structure, see Figure 4-13.

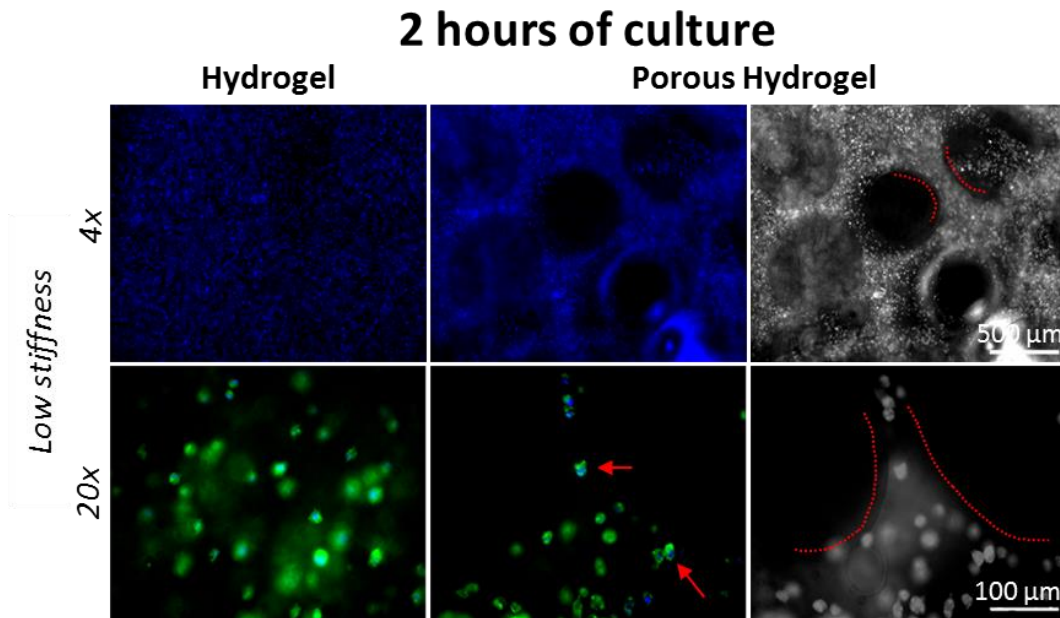


Figure 4-13: Actin (Green) and dapi (Blue) staining of cell nuclei and cytoskeleton illustrating cell distribution ($n = 4$) after 2 hours within low stiffness encapsulated and porous encapsulated hydrogels. Encapsulated hydrogels had a homogenous distribution of cells throughout the construct. Porous encapsulated hydrogels groups showing homogenous distribution of cells throughout pores/struts of construct (Red dashed lines). Scale bar is 500 & 100 μm for 4 and 20 x magnifications respectively.

After 7 days, cells within the low and high stiffness encapsulated hydrogel groups remained homogeneously distributed throughout the hydrogel, see Figure 4-14. Similarly, cells were homogeneously distributed throughout the structure of both porous encapsulated hydrogel stiffness groups, see Figure 4-14. Furthermore, cells were observed to spread over the surface of the pores/struts forming interconnections with neighbouring cells, whereas cells within the struts remained encapsulated within the 3D hydrogel matrix, in a similar fashion to cells within the encapsulated hydrogels.

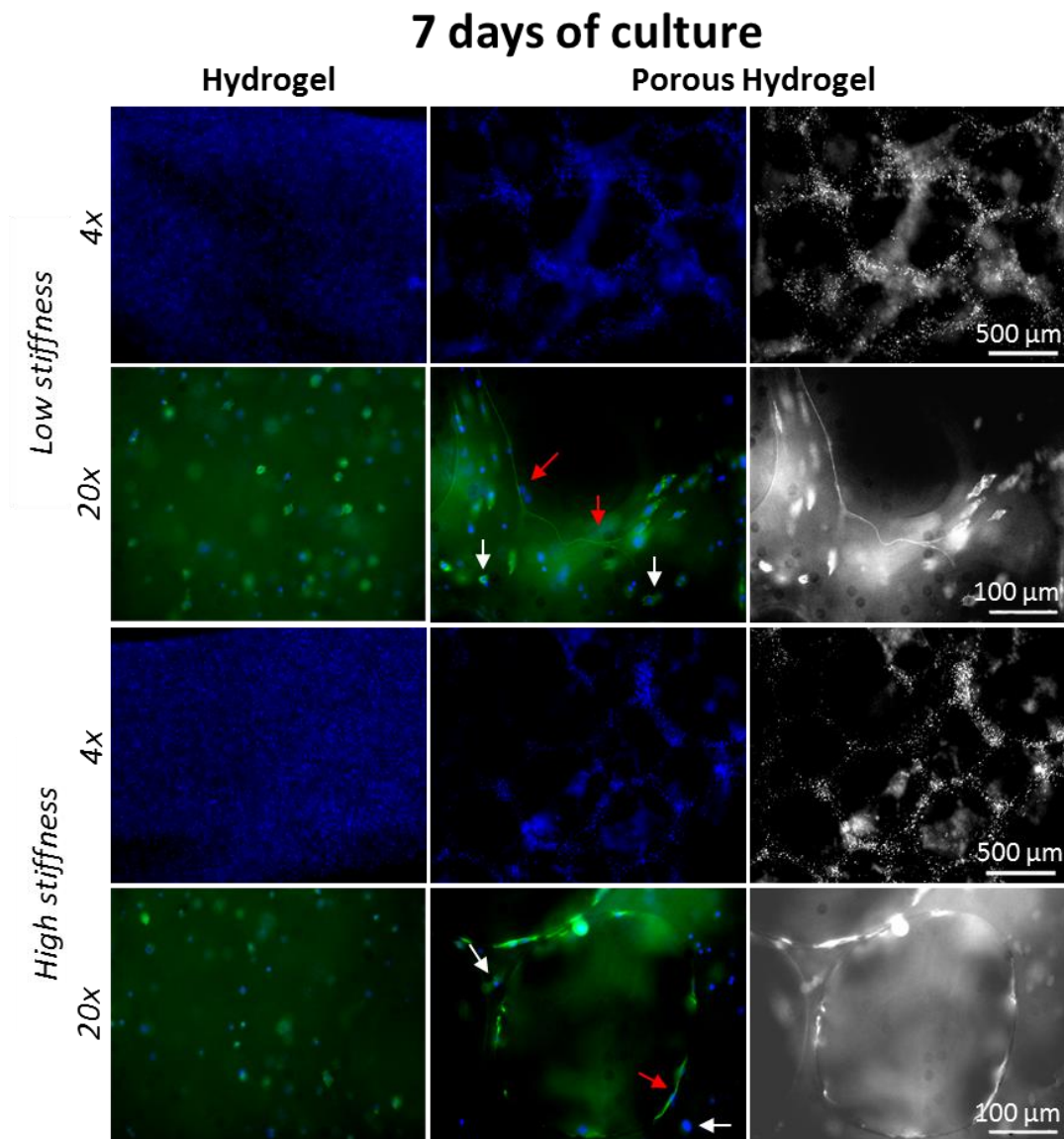


Figure 4-14: Actin (Green) and DAPI (Blue) staining of cell nuclei and cytoskeleton illustrating cell distribution and morphology after 7 days in encapsulated and porous encapsulated hydrogels at low and high hydrogel stiffnesses. Cells within all hydrogels groups remained homogenously distribution throughout constructs. In low stiffness porous hydrogels after 7 days of culture, cells were observed to spread over the pore surface along with expressing a bipolar morphology (Red arrows), while cells within the struts (white arrows) remained surrounded by the 3D hydrogel matrix. Scale bar is 500 & 100 μ m for 4 and 20 x magnifications respectively.

4.4.2.4 DMP-1 immunofluorescent staining

By 32 days, in a low stiffness (0.58 kPa) porous encapsulated hydrogel, cells were observed to proliferate and spread over the surface of pores, while cells within hydrogels remained encapsulated in the 3D hydrogel matrix, see Figure 4-15 for representative images. Immunofluorescent staining for DMP-1 was observed within the proximity of cells spread over the surface of pores and encapsulated within the hydrogel at day 32, see Figure 4-15.

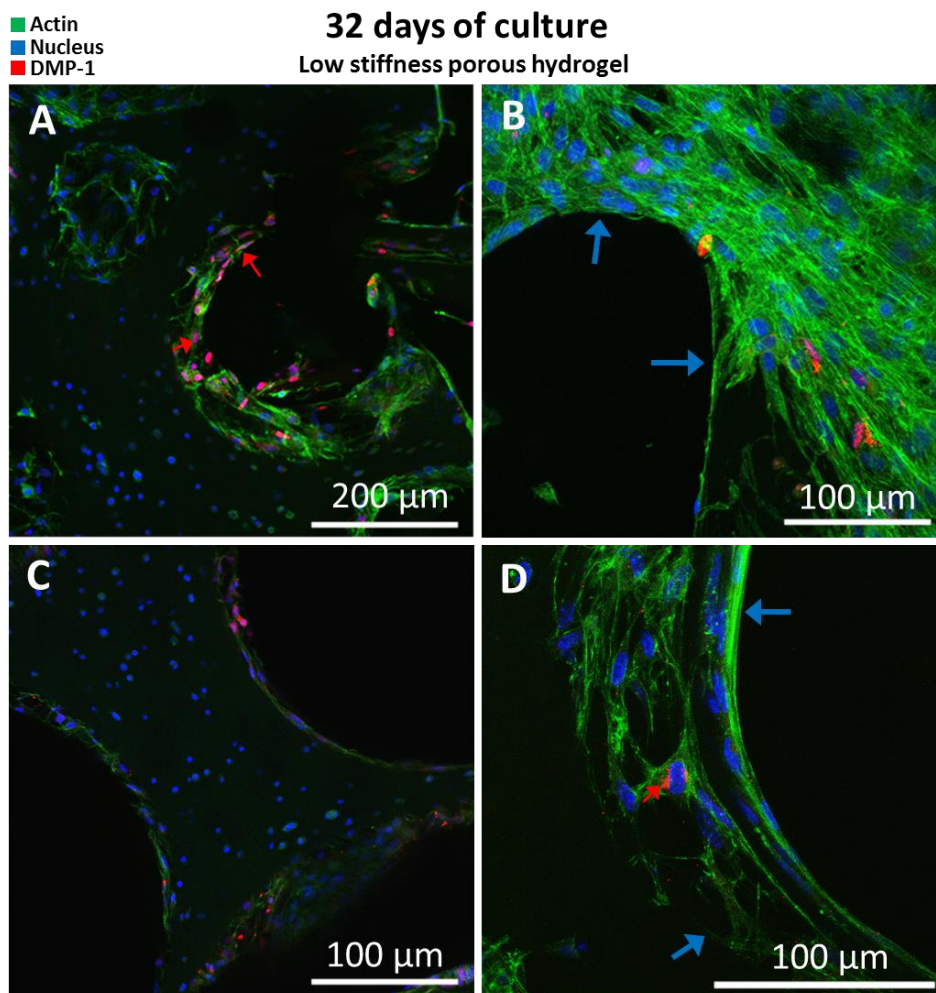


Figure 4-15: After 32 days, immunofluorescent images of DMP-1 (Red arrows) from cells spread over pore surface (Blue arrow) and encapsulated in the porous hydrogel at 20x (A), 40x (B, C) and 60x (D) magnifications. Scale bar for 20x = 200 μm ; 40x = 100 μm ; 60x = 100 μm .

4.4.2.5 Mineral distribution

Alizarin red staining for mineral distribution showed positive calcium staining in low stiffness porous hydrogels at day 32, see Figure 4-16. Dark patches arise from alizarin red staining of calcium deposits/nodules.

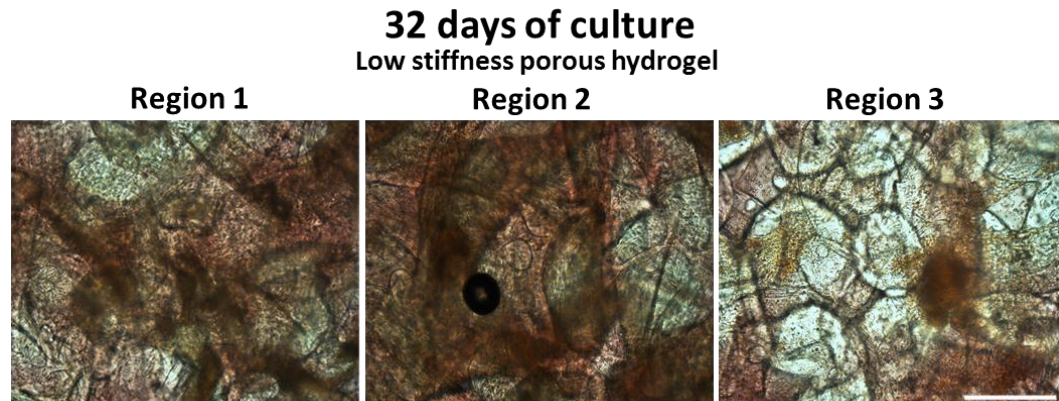


Figure 4-16: Representative images of alizarin red stain in a low stiffness (0.58 kPa) porous hydrogel showing mineral distribution at 32 days in low stiffness porous hydrogels at magnifications of 20x (A) and 40x (B) (n = 2). Scale bar for 20x = 200 μ m; 40x = 100 μ m

4.5 Discussion

This chapter investigates whether a tissue engineering approach that enhanced cell distribution and stiffness within 3D cell environments contributed to a consistent cell distribution throughout TE scaffolds. Furthermore, this chapter investigated whether combining porous scaffolds and cell encapsulation may recapitulate trabecular geometries and thereby support both osteoblast cells at the strut surfaces and osteocyte development within the matrix. The results of this study showed that cellular encapsulation within a hydrogel lead to a homogenous distribution of cells, with cells surrounded by a 3D matrix. In a porous hydrogel cells were found to spread and proliferate at the surface, but also allowed for cells to be evenly distributed in 3D within the gel and cell number to remain at the same population. After 32 days, osteoblast cells within the porous hydrogels stained positively for mineralisation and DMP-1, a secreted protein that is upregulated during osteoblast to osteocyte differentiation. Therefore, these findings reveal porous hydrogels

containing encapsulated MC3T3-E1 cells promotes both osteoblast and osteocyte development and mineralisation that might ultimately represent trabecular bone. These results were achieved without the addition of osteogenic supplements.

In chapter 3 the candidate reported that, during long term culture, encapsulated cells that migrate from hydrogels to a flat 2D surface, form a confluent layer over the surface, characteristic of osteoblast-like cells, which also interconnected with osteocyte-like cells within the hydrogel. Trabecular bone has a similar structure *in vivo*, wherein osteoblasts typically spread out in a cuboidal morphology over the trabecular surfaces, forming connections with osteocytes embedded within the 3D bone matrix. The results of this Chapter reveal that the addition of porosity to hydrogels containing encapsulated cells, allows for the homogenous distribution of cells in a 3D environment, but also allows for cells to spread at the surface of the pores, thereby creating an environment appropriate for both osteoblast and osteocyte development, similar to trabecular bone. Furthermore, encapsulated osteoblasts within porous hydrogels were shown to induce osteoblast-osteocyte differentiation as indicated by DMP-1 expression, cell morphology and mineralisation.

The use of osteoblast-like MC3T3-E1 cell-line is a possible limitation of this study. However, isolating primary osteoblasts can produce inhomogeneous cell populations and osteoblast-specific features can be lost upon subcultivation (Quarles et al. 1992; Leis et al. 1997). The MC3T3-E1 osteoblast cell line represents a uniformly defined cell population, which have similar traits to primary cells and can be readily expanded (Czekanska et al. 2012) and differentiated (Keogh, O'Brien, et al. 2010; Przybylowski et al. 2012; Partap et al. 2010; St-Pierre et al. 2005; Chatterjee et al. 2010; Uchihashi et al. 2013; Krishnan et al. 2010; Mullen et al. 2013), making the cell line a good representative of pre-osteoblasts (Grigoriadis et al. 1985; Quarles et al. 1992; Sudo et al. 1983; Wang et al. 1999). A higher matrix stiffness was used in this study (compared to chapter 3), which was necessitated by the fact that the porous hydrogels have weak mechanical properties, which rendered handling of these scaffolds extremely difficult. Nonetheless the results of this study showed that for porous hydrogels of 0.58 kPa stiffness, cells were able to spread at

the surface of the pores and also remain surrounded by a 3D matrix. Based on chapter 3, long term culturing (56 days) of osteoblasts within a low stiffness 3D matrix promoted osteoblast-osteocyte differentiation and mineral formation. Therefore, in this chapter osteoblast-osteocyte differentiation, DMP-1 expression and mineralisation was investigated in the low stiffness porous hydrogel. Furthermore, the porous hydrogel was only investigated for long term culture (32 days), as day 7 results indicated that both spread and 3D encapsulated cells geometries could be achieved throughout the construct, compared to the hydrogel, which only retained encapsulated cells or the peripherally seeded GG scaffold, which had an uneven cell distribution. Finally, no significant difference in bulk compressive modulus was observed between low and high stiffness porous hydrogels groups. This is likely due to the addition of porosity reducing the overall difference in bulk compressive modulus between groups, requiring a higher resolution of testing to detect a change in force between groups. However, at the local hydrogel material level a significant difference in matrix stiffness is still present, as determined from the testing of the low and high stiffness hydrogels.

Peripheral seeding has allowed researchers to fashion complex bone TE scaffold structures from a variety of biomaterials such as ceramic, silk or natural polymers (Correia et al. 2012; Curtin et al. 2012; Duffy et al. 2011; Harley & Gibson 2008; Keogh, O'Brien, et al. 2010; Kim et al. 2007; Sabree et al. 2015; Murphy et al. 2010). However, peripheral seeding onto the scaffold's external surface and relying on cell infiltration throughout, restricts a homogenous cell distribution throughout scaffolds (Arano et al. 2010; Keogh et al. 2011; Gardel et al. 2013). The results from the current study confirm this, by showing that peripheral seeding of GG scaffolds lead to cell proliferation around the periphery of the scaffold with partial infiltration towards the scaffold centre over 28 days. Studies have shown that a homogenous distribution of cells can be achieved by cell encapsulation, along with the advantage of suspending cells in a 3D environment (Nichol et al. 2010; Amini & Nair 2012). In this study osteoblast cells were homogeneous distribution throughout hydrogels after 2 hours and 7 days. Furthermore, suspending bone cells, such as MSCs and osteoblasts in a 3D matrix has been shown to promote osteoblast and osteocyte

differentiation (Castillo Diaz et al. 2014; Chatterjee et al. 2010; Amini & Nair 2012; Mc Garrigle et al. 2016; Gerald J Atkins et al. 2009; Uchihashi et al. 2013; Hwang et al. 2011; Maia et al. 2014). Although, peripheral seeding is advantageous for creating complex bone TE scaffold structures and cell encapsulation provides a homogenous cell distribution within a 3D matrix, these approaches do not recapitulate the environments of osteoblasts and osteocytes in native trabecular bone.

In vivo, osteoblasts typically spread out in a cuboidal morphology over bone surface, while osteocytes form a complex interconnected 3D network allowing for communicating with their neighbours. In peripherally seeded porous scaffolds, the internal struts act as a flat surface to which cells attach by either bridging pores or spreading along the scaffold surfaces (McCoy et al. 2012). This initial environment might delay osteocyte formation until tissue formation within the pores surrounds the osteoblasts and hence induces differentiation towards osteocytes (Boukhechba & Balaguer 2009). Encapsulating osteoblasts cells within hydrogels leads to the surrounding of the cell in a 3D matrix, mimicking the *in vivo* approach of osteoid embedding, and has been shown to promote the formation of an osteocyte-like network, characterised by long dendrites interconnecting with neighbouring osteocytic cells (Mc Garrigle et al. 2016; Uchihashi et al. 2013; Gerald J Atkins et al. 2009). This 3D geometry is relevant for osteoblast-osteocyte differentiation, but is unnatural for bone matrix-secreting osteoblasts, which typically spread out in a cuboidal morphology over the surface of bone, in particular trabecular bone (Franz-Odendaal et al. 2006). In the current study the addition of porosity to hydrogels provides a surface area for cells near the surface to migrate out of the gel and to spread over the surface, while also maintaining cells surrounded by a 3D matrix within the gel that ultimately differentiate into osteocytes.

For both cell-seeded scaffolds and cell encapsulated hydrogels, studies have shown that matrix stiffness is an important physical factor in regulating cell behaviours such as migration, proliferation, and differentiation promoting osteogenic protein and mineral production (Castillo Diaz et al. 2014; Tan et al. 2014; Chatterjee et al. 2010; Shin et al. 2014; Haugh et al. 2011; Keogh, O'Brien, et al. 2010; Zaman

& Trapani 2006; Hadjipanayi et al. 2009; Lo et al. 2000; Mullen et al. 2013). In this study peripherally seeded GG scaffolds at a low stiffness (0.5 kPa) showed enhanced cell migration towards the centre, however at the expense of the construct contracting in size and containing a lower cell population by day 28, compared to higher stiffness scaffolds (0.8 and 1.4 kPa). It is proposed the peripheral pores undergo collapse under cell-mediated contraction due to the low substrate stiffness. Studies have shown that cell contraction can positively increase osteoblast differentiation and decrease cell proliferation (Keogh, O'Brien, et al. 2010; Murphy et al. 2015; Keogh, O'Brien, et al. 2010). Therefore, pore contraction may contribute to regions containing increased levels of differentiated osteoblasts and hence localising mineralisation to certain areas within the scaffold. Alternatively, high stiffness (0.8 and 1.4 kPa) peripherally seeded GG scaffolds were more effective in inducing cell proliferation compared to low stiffness scaffolds (0.5 kPa), however cell distribution was mainly restricted to the periphery. It is proposed that these scaffolds retained their overall structure, providing a larger surface area for initial cell proliferation around the scaffold periphery before infiltrating towards the centre. This might promote higher nutrient and waste exchange compared to the lower stiffness scaffolds, and thereby promote consistent tissue formation. For cell encapsulation, similar cell distribution results were observed between low and high matrix stiffness within encapsulated and porous encapsulated hydrogels. However, the matrix used in this study was a higher stiffness (15.98, 19.33 kPa) compared to chapter 3, where osteocyte formation was observed at a matrix stiffness of 0.58 kPa after 56 days. It is proposed that the higher matrix stiffnesses used in this study initially restricts cells from degrading their surroundings, hence delaying osteocyte differentiation.

In vitro bone TE has shown potential as an approach for bone regeneration, as indicated by the production of osteogenic protein and mineral in biomaterial scaffolds combined with bone cells (Keogh, O'Brien, et al. 2010; Gleeson et al. 2010; Curtin et al. 2012; Correia et al. 2012; Castillo Diaz et al. 2014; Tan et al. 2014; Chatterjee et al. 2010; Shin et al. 2014). However, *in vivo* these approaches are limited due to newly formed tissue in the scaffold acting as a barrier to remodelling

and osseointegration with the host tissue (Lyons et al. 2010; Alhag et al. 2012). Furthermore, current biomaterial scaffolds do not recapitulate the trabecular bone cell environments within TE constructs. The approach developed here provides a homogenous cell distribution in 3D environments, but also provides a porous structure on which osteoblasts attach and spread. Furthermore, after 32 days, osteoblast-osteocyte differentiation was observed within the porous hydrogels as indicated by DMP-1 and mineralisation. Future TE approaches could apply this method to develop bone constructs containing both osteoblasts and osteocytes within a porous environment similar to trabecular bone, directing faster host integration, tissue formation and vessel infiltration. Such cellular networks are crucial in the development of functional bone tissue substitutes for the treatment of large bone defects.

4.6 Conclusion

The results of this study show that the addition of porosity to hydrogels containing encapsulated cells, allowed for the homogenous distribution of cells in 3D environments, but also cell attachment and spreading at the surface, which is representative of the trabecular bone environment *in vivo*. For the first time, it has been shown that porous gelatin-mtgase hydrogels provide a surface area for MC3T3-E1 cells to migrate out of the gel and spread over a flat 2D surface while also maintaining cells surrounding by a 3D matrix within a porous structure. Furthermore, the development of osteocytes was observed within the porous hydrogels as indicated by DMP-1 expression and the production of mineral. It is proposed that the homogenous distribution of osteoblasts cells over the scaffold surface while, also maintaining cells surrounding by a 3D matrix, may lead to matrix producing osteoblasts and osteocytes and hence consistent tissue formation throughout TE scaffolds. This approach is further tested in chapter 6 with combined stimulus applied to constructs.

Chapter 5: Design, fabrication and validation of a perfusion-compression bioreactor integrated with microscopy for TE scaffolds

5.1 Introduction

Musculoskeletal conditions are responsible for severe long term pain and disability in 20-30% of adults in Europe who are affected by long-term muscle, bone and joint diseases such as osteoporosis, rheumatism and arthritis (Woolf 2007). Clinical treatment to re-establish function in musculoskeletal tissues requires transplanting tissue grafts from another part of the patient or a donor. However, accessing viable tissue within the patient is challenging and there is also a scarcity of suitable donors. As such there is a strong rationale for the development of functional substitutes for damaged or diseased musculoskeletal tissues. Tissue engineering (TE) is a promising scientific field with significant potential for generating tissue substitutes, using a combination of biomaterials and the natural capacity for biological cells to grow and produce tissue constituents under conditions that emulate the body's biochemical and physical environment. Significant advances have been made in the development of *in vitro* bone graft substitutes through the association of novel biomaterials with cells (Gleeson et al. 2010; Alhag et al. 2012; Schubert et al. 2013; Kim et al. 2014; Matsumoto et al. 2012; Yamada et al. 2013; Dumas et al. 2012; Thorpe et al. 2013; C. C. Wang et al. 2012; R. Zheng et al. 2013; Ando et al. 2007). However, fully functional and mechanically suitable tissue grafts that can be used for clinical applications are not yet widely available (Keogh et al. 2011; Lyons et al. 2010; Arano et al. 2010).

Bioreactors, are engineering devices that influence biological processes, which have shown great potential to control process parameters, such as fluid flow velocity and mechanical compression, and thereby regulate culture conditions for new tissue development (Keogh et al. 2011; Gardel et al. 2013; Thorpe et al. 2010;

Schulz et al. 2008). Moreover, existing bioreactors are also widely applicable for large scale drug screening for pharmaceutical applications (Gupta et al. 2010; Jang et al. 2008; Lozito et al. 2013) and experimental testing under microgravity conditions experienced in space (Walther et al. 2013). Bioreactor operation can be achieved through the integration of mechanical systems with specialised equipment. As an example, hydrostatic bioreactors are able to recreate cyclic hydrostatic pressure up to 10 MPa through the use of servo-hydraulic mechanical testing systems (Wagner et al. 2008). Perfusion bioreactors use syringe pumps to create flow profiles such as oscillatory flow within TE scaffolds (Jaasma et al. 2008), whereas bioreactors can apply compressive or vibration loading by integrating with dynamic mechanical tensile testers, such as a ELF3200 mechanical testing machine (ElectroForce Systems, Bose) allowing for precise control over loads and displacements applied to scaffolds (Sittichockechaiwut et al. 2009).

Bioreactor systems need to be highly flexible in design, meet the wide range of stimuli required for different tissue types and their biomaterials, and also maintain operation during long term culture periods for tissue formation to occur. However, commercially available bioreactors, such as the TC-3 Cell Culture Bioreactor from EBERS Medical Technology S.L., BioTense Perfusion Bioreactor from ADMET and Flexcell® FX-5000™ Compression System from Flexcell require a lot of space due to their large design and/or the requirement for additional equipment, such as fluid pumps or a compressed air supply, to fully operate, restricting the portability within a laboratory environment. Furthermore, due to complicated setup procedures, restricted sample numbers and visualisation of constructs, these systems require the knowledge of specialised users, such as engineers or qualified technicians with a practical understanding of fundamental engineering concepts, such as programming and mechanical device control, assembly and operation. This is limiting for potential users, such as biomedical scientists, pharmacologists and microbiologists, who may not have the appropriate background, but could greatly benefit from bioreactor technology. Moreover, existing systems do not accurately mimic the mechanical stimulation experienced in the *in vivo* environment (e.g. fluid shear stress, mechanical strain (Keogh et al. 2011; Sittichockechaiwut et al. 2009)). Multiphysics computational modelling has been applied to predict the fluid perfusion and mechanical compression necessary to ensure the desired level of mechanical

stimulation within 3D TE scaffolds containing different properties and structure (Zhao et al. 2015; Zhao et al. 2014). Furthermore, Zhao et al found that the applied fluid flow played a more significant role in dictating the magnitude of resulting WSS within scaffolds, while dynamic compression determined the patterns (i.e. frequency) of resulted WSS in a combined loading system. Interestingly, the WSS was amplified under the combined loading, compared to the WSS generated from isolated fluid perfusion and mechanical compression systems (Zhao et al. 2015). Also, Zhao et al predicted that combined loading (perfusion and compression) could enhance stimulation on cells with different morphologies, which attached on the struts surface and bridged across the scaffold pores (Zhao et al. 2014). To some extent, this was supported by previous experimental study, which showed that a combination of fluid perfusion (inlet flow rate = 10mL/min) and compression (compressive strain=10%) could stimulate the bone cells to produce larger amount of osteocalcin and higher Runx2 expression after 3-week culture (Jagodzinski et al. 2008). However, to date a system, which can achieve real-time monitoring of cells/scaffold and apply combined stimuli to biomaterial scaffold has not been designed or validated yet.

The objective of this chapter was to design and fabricate a compression perfusion bioreactor system capable of applying controlled stimulation in the form of compression and perfusion to TE scaffolds. The system design is based on the predictions of computational models that determined a combination of perfusion and compressive loading at appropriate experimental conditions enhances tissue formation in 3D TE scaffolds (Zhao et al. 2014; Zhao et al. 2015). This chapter focuses on the development, fabrication and validation of the combined perfusion-compression bioreactor system. The development of the bioreactor involved identifying parameters, such as design criteria, component selection and analysis, while also allowing for design reiteration due to fabrication requirements and hence, after bioreactor fabrication, carrying out validation tests of the compression and perfusion system.

5.2 Materials & Methods

5.2.1 Bioreactor design criteria, component selection and analysis

This section focuses on the identification of design criteria, component selection, analysis and defining the constraints in the design of a perfusion-compression bioreactor system.

5.2.1.1 Sample holding, perfusion and compression concurrently

The first stage in designing a bioreactor required the identification of boundary conditions surrounding the TE scaffold under loading and also a method to concurrently compress and perfuse media through the TE scaffold. It was decided to apply uni-axial perfusion and compression stimulus to the scaffold top with the bottom side fixed, while the four other sides were confined on all sides, preventing perfusion from occurring around the scaffold periphery, see Figure 5-1 (A). A previous study applied uni-axial compression-perfusion loading to agarose hydrogels seeded with chondrocytes, through a plate containing holes to allow for direct compression and perfusion simultaneously (Schulz et al. 2008). However, porous scaffolds are commonly used in bone TE (Keogh, O'Brien, et al. 2010; Sittichokechaiwut et al. 2009; Curtin et al. 2012), with scaffolds such as collagen GAG scaffolds consist of pore sizes ranging from 85-325 μm (Murphy et al. 2010). To achieve homogenous compression over a porous scaffold surface requires the selection of appropriate sized holes within the platen. Holes larger than the scaffold pores would result in partial compression of the scaffold surface area, while too small of a hole would restrict flow through the platen affecting platen porosity and hence pressure changes. Therefore, a small pore size platen $<85 \mu\text{m}$ with a high porosity $> 50\%$ was desired. Furthermore, the platen mechanical/material properties were selected so that the scaffold maintained its structure when under loading and also its biocompatibility with cells in a cell culture environment.

Stainless steel sintered filtered disks are commonly found in industry for applications such as plastic extruding and compress air regulation, see Figure 5-1 (B,C). Sintered filter disks are formed by compressing particles under high heat and pressure until the particles bond together without reaching the point of liquefaction. The grade 306 stainless steel has shown a high biocompatibility with cells, while

also been a high rigidity material that can be autoclaved. Furthermore, excess material within the pores of platen can be easily removed through chemical cleaning. A stainless steel filter disk (SIKA-R 200 AX, GKN) with an average porosity of 51%, permeability coefficient of $78 \times 10^{-12} \text{ m}^2$) and pore size of $70 \mu\text{m}$ was selected.

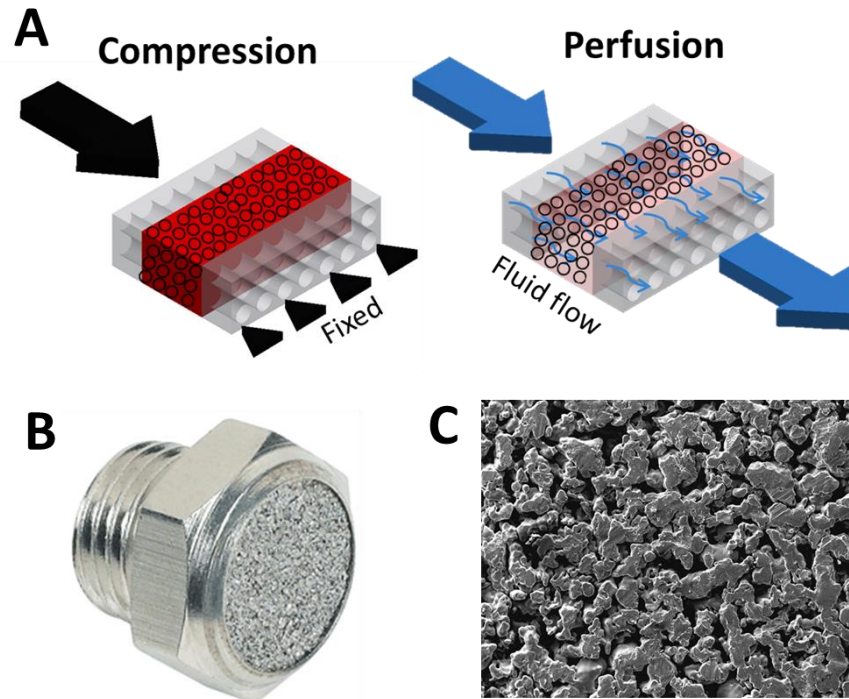


Figure 5-1: Porous platens allow for direct homogenous compression of a TE scaffold (Red porous block) confined on 5 sides, while also allowing for fluid perfusion (Blue arrows) to occur through the TE scaffold (A). A sintered filter element (B) contains a porous structure allowing for fluid to pass through while providing a rigid structure for compressive loading (C).

5.2.1.2 Defining biomaterial scaffolds suitable for use in the bioreactor

Biomaterial scaffolds are widely used in tissue engineering applications, and depending on the tissue phenotype/clinical target the mechanical properties of these vary widely. Hydrogels and polymers are widely used, and have elastic moduli in the range of 1.8-306 kPa (Castillo Diaz et al. 2014; Chatterjee et al. 2010; Haugh et al. 2011), while composites, ceramics and metallic scaffolds range from 700-25,000 kPa (Sabree et al. 2015; Tiainen et al. 2013; Tiainen et al. 2010). However, the most successful TE scaffolds for bone repair have moduli in the kPa range (Haugh et al. 2011; Cunniffe et al. 2010) with scaffolds such as collagen-GAG and hydroxyapatite

scaffolds showing bone tissue formation and vascularisation *in vitro* (Curtin et al. 2012; Duffy et al. 2011; Harley & Gibson 2008; Keogh, O'Brien, et al. 2010) along with favourable host integration *in vivo* (Lyons et al. 2010; Gleeson et al. 2010). Furthermore, studies have shown that scaffold stiffness within the kPa range is an important physical factor in regulating osteogenic differentiation (Engler et al. 2006; Mullen et al. 2013; Tan et al. 2014; Mc Garrigle et al. 2016) and differentiation (Tan et al. 2014; Lo et al. 2000). Therefore, a bioreactor designed to apply mechanical stimulus to scaffolds with low compressive moduli is widely appropriate for testing and hence enhancing tissue formation. As a prototype bioreactor design and due to previously developed hydrogels within the kPa range (Mc Garrigle et al. 2016), the bioreactor design will be limited to testing scaffolds up to the MPa range (ie. 1000 kPa).

5.2.1.3 Determining incremental displacement and controlled fluid velocities to apply to TE scaffolds

The bioreactor system was required to mechanically stimulate cells within porous scaffolds towards osteogenic differentiation and hence tissue formation. Therefore, the prediction of the level of mechanical loading to apply to cells within TE scaffolds represented an important aspect for determining the resolution and operation parameters of the compression and perfusion system. Computational modelling has been used to predicted the physical environment within TE scaffolds under fluid perfusion and mechanical compression loading, using computational fluid dynamics (CFD) and fluid structure interaction (FSI) approaches (Zhao et al. 2014; Zhao et al. 2015). The computational approach was capable of predicting the cellular level stress arising in mechanical stimulated TE scaffolds, with the aim of identifying and applying specific loading regimes that could stimulate bone formation within the scaffold. For these models a porous hydrogel with a porosity of ~50% and average pore size of ~500 μ m was investigated to inform the design and operating conditions of the bioreactor system, see Figure 5-2. In the computational model, the pores of the porous hydrogel were idealised with a spherical geometry with a diameter of 500 μ m. It was determined that for a fluid perfusion system, a constant inlet flow rate of 0.3 mL/min (fluid velocity $v = 250 \mu\text{m/s}$) was required to achieve the applicable wall shear stress at the cell level that would entice bone formation. While, in the

mechanical compression system, a compressive strain of 0.5% on the top surface of the scaffold was required to achieve the desired mechanical strain at the cellular level to induce osteogenic differentiation and hence bone formation. To prevent cell desensitization from mechanical stimulation, a rest period (no stimulus) was required (Jaasma & O'Brien 2008; Jaasma et al. 2008; Plunkett et al. 2010). However, to ensure nutrients and waste exchange a low flow rate of 0.05 mL/min below the effective mechanical stimulus of cells was determined. In the case of a 4 mm wide sample, 0.5% strain would correspond to 20 μm displacement, required from the compression system. Therefore, 10 μm was selected as the minimum displacement resolution and a minimum flow rate of 0.01 mL/min.

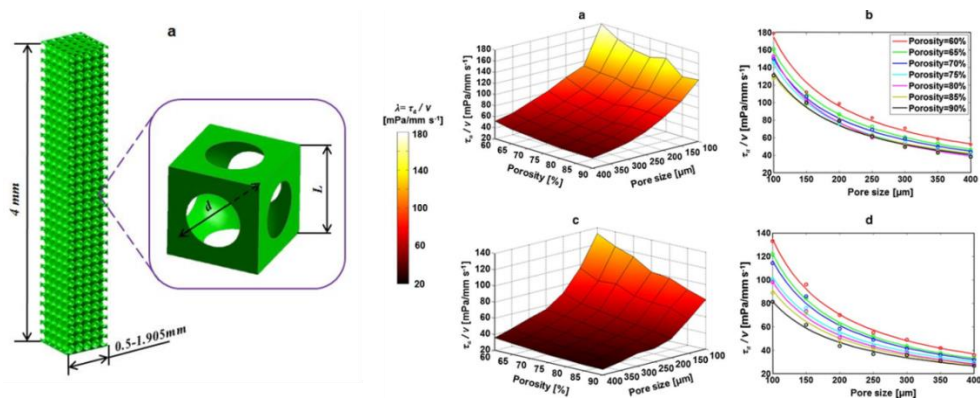


Figure 5-2: Computational models predicted for a porous hydrogel with a porosity of $\sim 50\%$ and idealised pore size of $\sim 500 \mu\text{m}$ a peak flow rate of 0.3 mL/min (fluid velocity $v = 250 \mu\text{m/s}$) and a compressive strain of 0.5% at 1 Hz was required for osteogenic differentiation to occur through mechanical stimulus (Zhao et al. 2014; Zhao et al. 2015). Furthermore, a low flow rate of 0.05 mL/min was determined for nutrients and waste exchange (Zhao et al. 2014; Zhao et al. 2015).

5.2.1.4 Controlled displacement

To apply precise displacement to the porous platen a ball screw and geared stepper motor transmission system was employed. Ball screws consist of a screw shaft and nut that translate turning motion into linear motion and force, with linear distance controlled by the degree of screw revolutions. The screw shaft and nut consist of threads formed into a helical structure, containing precisely ground ball bearing to deliver low frictional resistance during loading and increasing accuracy. To achieve the desired mechanical compression, the ball screw was required to displace at a minimum incremental resolution of 10 μm , while also been able to load scaffolds

with compressive moduli up to 1000 kPa. Moreover, after applying linear motion, it was desired for the transmission system to remain self-locking, negating the effect of the ballscrew reverting to the original position after the motor power is turned off.

A ballscrew with a pitch size of 0.5 mm and an accuracy grading of C5 was selected, allowing for an axial play of ± 5 microns and hence meeting the 10 μm range of displacing. This corresponds to the ballscrew shaft rotating by 14.4° to linearly travel a distance of 20 μm . The ballscrew (model FBS0400.5A-36R110 C5) has a basic dynamic load rating of 160 N.

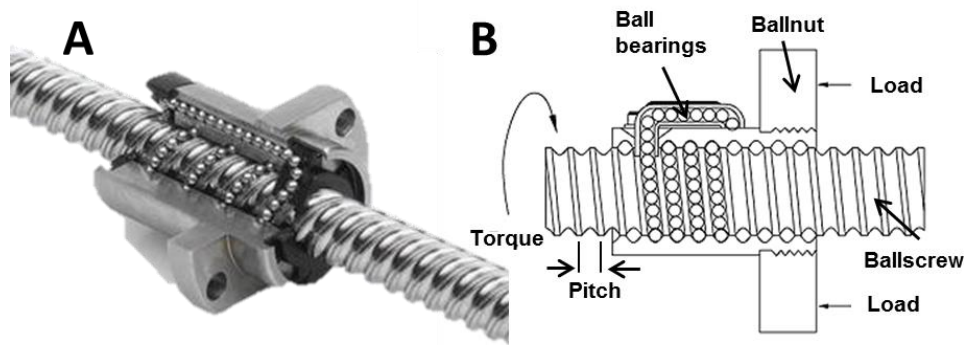


Figure 5-3: Illustration of a Ballscrew (A). During rotation the ball bearings circulate along threaded slots in the ballscrew and ballnut, allowing low friction and high accuracies during high loads.

After identifying a suitable ballscrew, mechanical analysis was performed to determine the motor torque requirements to rotate the ballscrew under its max rated load of 160 N. The torque required to raise or lower load can be determined by Equation 2.1 (Budynas & Nisbett 2006).

$$T_R = \frac{F d_m}{2} \left(\frac{l + \pi f d_m}{\pi d_m - f l} \right) \quad (2.1)$$

$$d_m = d - \frac{p}{2} \quad l = np$$

F = Force (N), np = (No. of treads) x (pitch), d = major diameter, Coefficient of friction (f) = 0.8, d_c = mean collar diameter

As calculated from equation 2.1, a load rating of 160 N requires a 26.2 Ncm torque to rotate the screw against the load and 21.98 Ncm to overcome friction during unloading. Both results show positive values meaning friction remains higher than the load, indicating that the ballscrew remains self-locking when the power to the motor is turn off.

Applying controlled rotation to the ballscrew, required identifying a motor with an output transmission shaft capable of accurate rotations and speeds that would meet the 14.4 degree rotation at a torque rating greater than 26.2 Ncm. Furthermore, to meet the microscopy requirements, the motor height was limited to 30 mm. Stepper motors integrated with planetary gearing permit precise control of output transmission. Stepper motors operate by dividing a full 360° rotation into a large number of steps (e.g. 200 steps, 1.8° per step) with precisely controlled rotation to a step or between steps. Planetary gearing significantly reduces output speed, increasing torque, while also providing a compact design meeting space requirements, see Figure 5-4. Research identified a suitable high-torque stepper motor (Nanotec, ST2018S0604) that could be combined with planetary gearing (Nanotec, GPLL22-90), allowing for a max torque output of 86 Ncm, meeting the max torque (26.2Ncm) required to rotate the ballscrew. Finally, a motor couple was used as a method of providing transmission between the geared stepper motor and the ballscrew shafts. This takes into account any misalignment between the motor and the ballscrew shaft, through a flexible coupling. See Figure 5-4 for overall assembly.

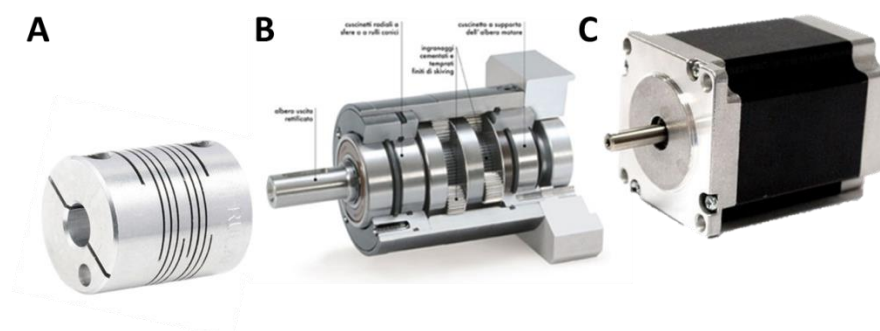


Figure 5-4: Stepper motor (C) combined with planetary gearing (B) and flexible motor couple (A) forming connection with ballscrew shaft.

5.2.1.5 *Controlled fluid velocities*

To achieve the desired levels of perfusion stimulation of cells within TE scaffolds, a peak fluid velocity of 300 $\mu\text{m/s}$, corresponding to a peak flow rate of 0.3 mL/min was required. Furthermore, a minimum flow rate of 0.05 mL/min was required for nutrient and waste exchange. Syringe pumps are capable of low flow rates and complicated loading profiles, such as oscillatory flow at high frequencies. Syringe pumps precisely infuse and withdraw media by applying a positive and negative pressure to a syringe. The max volume of media that can be pumped in one direction is determined by the size of the syringe. In the case of a bioreactor system a large volume of media was desired for perfusion over long term culture. Based on these requirements a syringe pump (NE-1600) was selected. The pump is capable low flow rates (0.454 $\mu\text{L/hr}$), can hold large volumes of media (100 mL) and perform complicated flow profiles, such as oscillatory fluid flow. Furthermore, the pump is capable of applying up to 160 LBS force to six 120 mL syringes, corresponding to ~ 3800 Pa of pressure per syringe and allows for communication with a laptop through a USB connection and hence to the operating software (Syringepump pro).

5.2.1.6 *Cell culture requirements, material selection, sealing and sterilisation*

Culturing of cells requires maintaining an appropriate temperature and gas mixture (37 $^{\circ}\text{C}$, 5% CO_2) through an incubator system, negating the risks of outside contamination and continuous support of cell growth through culture media. Effective bioreactor integration with cell culture requires the capability of either recreating this environment or integrating the device into an existing incubator system. Furthermore, maintaining cell growth and health for a prolonged culture period requires a system capable of media renewal, while also keeping a sterile environment. To ensure system sterility, the bioreactor was designed to be fully assembled prior to sterilisation, ruling out the possibility of contamination during re-assembly. Furthermore, the bioreactor was designed to operate within a standard incubator environment requiring full media changes every 7 days.

Material selection for constructing the bioreactor parts required identification of a cell culture friendly material, which also had favourable machining and mechanical properties. General cell culture plastics, such as 24 well plates and flasks are made from polycarbonate, as it has excellent cell biocompatibility, machining

and fabrication capabilities. Furthermore, TE scaffolds testing would be carried out on low stiffness scaffolds within the kPa range compared to polycarbonate contain material properties in the GPa. Therefore, polycarbonate was selected as the main material for constructing the bioreactor. Aluminium was used as high load bearing parts, such as transmission mounts and transferring compression loads.

Many commercial bioreactors systems are fabricated from multiple parts and components, requiring continuous disassembly, reassembly and maintaining a seal under static or dynamic conditions. Common static sealing methods can be achieved by compressing gaskets within specific sized glands/grooves. Therefore, static parts sealing was carried out using 1 mm Viton gaskets (Abbeyseals) allowing for autoclave ability and cell culture biocompatibility. Sealing was achieved between two surfaces by placing the gasket within a 1.4 x 0.7mm gland on one part, according to manufacture specification, and using the second surface to compress the gasket forming a seal. Sealing of dynamic parts require specialised methods, such as multiple o-rings and sealing oils to ensure full sealing has been accomplished. However, these methods are difficult to fully seal when used with low viscosity liquids such as water and cell culture media, leading to complications with leaks and contamination. In the case of applying compression stimulus to TE constructs, maximum strains are not expected to exceed 40%, as these would damage cells and the construct. Therefore, a flexible diaphragm membrane was incorporated into the bioreactor design for full system sealing during compression with the max scaffold displacement limited to ~4mm, after which failure will occur. The membrane is in the shape of a washer with both ends held in place forming a seal, while still allowing for movement between the ends, see Figure 5-5. A high shore hardness silicon (60A) (SilexSiliconesLTD) was selected allowing for sealing at the ends while still allowing for flexibility between the interfaces. The internal and external diameter of the diaphragm washer was influenced by the 4 mm compression distance. It was estimated for a 5 mm displacement the membrane would experience a 15% strain, while sealing would require 30% compression.

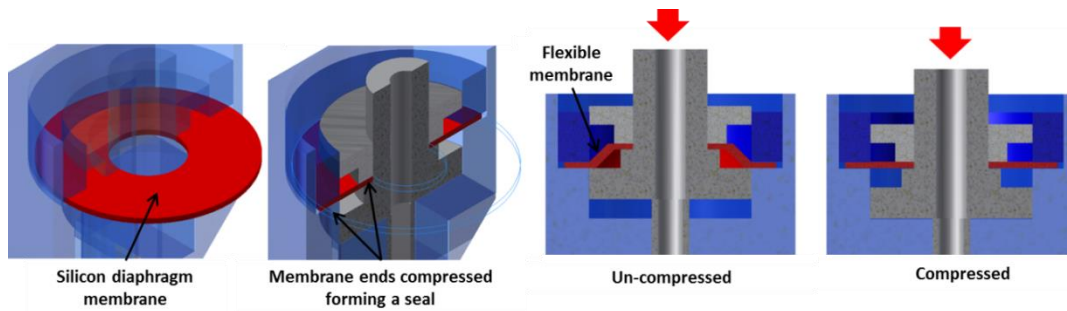


Figure 5-5: Diaphragm sealing method to prevent leaking during compressive loading. Membrane in the shape of a washer (Red) with both ends held in place forming a seal, while still allowing for movement between the two sealed ends during compression.

The bioreactor was designed to be sterilised by gamma sterilisation, a fully assembled bioreactor could be sterilised entirely and hence remain sterile after removal. The fully assembled bioreactor chamber was designed to fit within a gamma irradiator system with a diameter of 110 mm and height of 180 mm.

5.2.1.7 Real time imaging in the Bioreactor

The high cost of bioreactor components, along with loading time and space requirements, limits the number of potential samples that can be loaded within bioreactors. Therefore, gathering as much information on the same sample during the culture period and at the end represents an important approach in saving time and costs. Previous studies have shown the advantages of real time imaging for quickly identifying specific features, such as cell viability, morphology and gene expression through fluorescent staining. Furthermore, a low and high range of imaging magnifications provides a global and local picture of events occurring within the sample been tested, such as real time tissue formation at the structure level and cellular responses at the cell level. Additionally, real time imaging allows for direct visualisation of stimulus status and hence calibration and evaluation over long term culture. Therefore, the bioreactor was designed to allow for real time imaging of mechanical stimulus at low and high magnifications. Standard Olympus inverted microscopes contain an insert disk within the stage, which can be easily removed, recreating a 107 mm diameter opening, see Figure 5-6 (A). The opening within the table was used as a template for the base of the bioreactor, allowing for easy

installation and fixation into the microscope during loading. A glass microscopy slide (~1 mm thick), allowing for transparent imaging and providing a rigid surface during testing, was incorporated into the design as the main objective viewing window. Furthermore, an upper observation window was included into the design allowing for light to pass through the sample and hence to the objective. Additionally, to determine specific features on the global scale (whole construct), a standard microscopy endoscope was also incorporated in the bioreactor design providing an overall magnification of constructs, see Figure 5-6 (B).

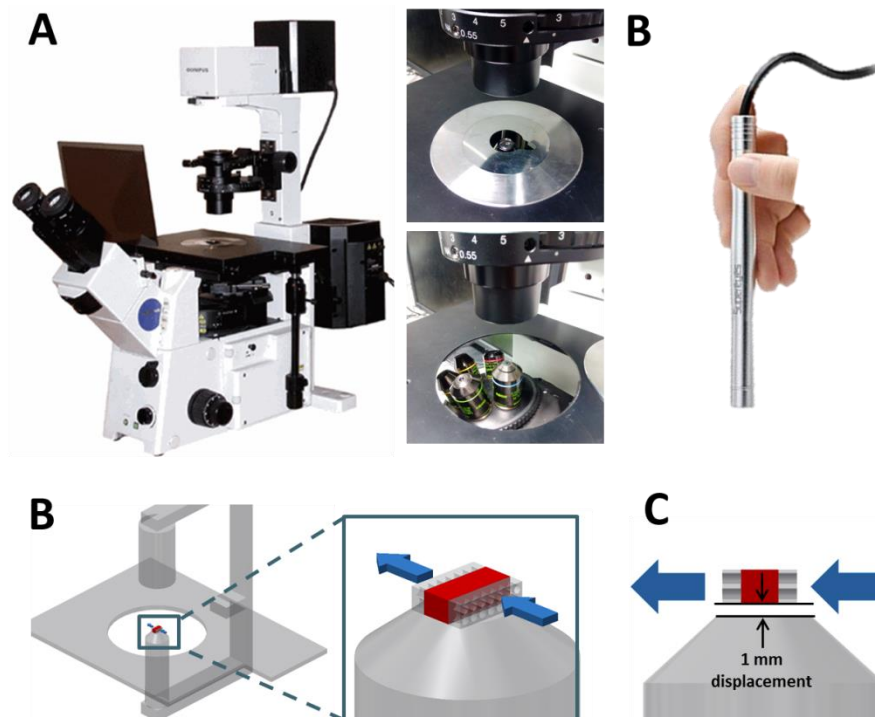


Figure 5-6: Olympus inverted microscope, containing a removable disk from the stage, leaving behind a circular opening which acted as template for the bioreactor base (A). Standard microscope endoscope allowing for low magnification of scaffolds at the global level (B). A 3D model of the microscope stage was created to determine the bioreactor size restrictions (B), such as the TE constructed limited to 1 mm above the objective (C).

5.2.1.8 Sample size, number and max compressive moduli of samples testable

Based on the design criteria and selected components a max sample width of 6 mm was determined, allowing for an adjustable sample width of 2-6 mm. Sample height was restricted to 3 mm to accommodate imaging under a microscope and based on TE scaffolds used in literature a max width of 13 mm was selected (Curtin et al.

2012; Duffy et al. 2011; Harley & Gibson 2008; Keogh, O'Brien, et al. 2010). A total of 4 samples were determined to fit within the bioreactor allowing for simultaneous compression and perfusion loading to be applied to samples. Furthermore, based on the sample size (3 x 4 x 13 mm), ball screw load rating (160 N) and at a 15% strain the bioreactor transmission system was rated to apply loads to TE scaffolds with compressive moduli up to ~2000 kPa.

5.2.1.9 Summary

In summary, based on the design criteria and selected components, the bioreactor system was required to hold and fully confine four TE scaffold, with combined compression and perfusion applied homogenously to the scaffold surface through a porous platen. The bioreactor compression system is rated to displace at a resolution of ~10 μm , allowing for compression of 4 mm wide samples at 0.5% strain. While, the perfusion system is capable of low flow rates (0.454 $\mu\text{L/hr}$), meeting the desired range required for nutrients/waste exchange (0.05 mL/min), mechanical stimulus (0.3 mL/min) and also perfusing large volumes of media (100 mL). The bioreactor was required to maintain an appropriate temperature and gas mixture (37 °C, 5% CO₂), negating the risks of outside contamination and continuous support of cell growth. Furthermore, sealing of bioreactor static and dynamic parts required the integration of gaskets and a diaphragm sealing membrane mechanism. Polycarbonate was selected as the material for construction of bioreactor parts. The bioreactor was designed to operate on TE scaffolds up to 1 MPa. Finally, real time imaging was integrated into the bioreactor design, requiring a specialised design to meet microscopy requirements.

5.2.2 Bioreactor design

5.2.2.1 Combined bioreactor design and assembly

After selecting the main components and parts, a fully functional bioreactor concept was developed using CAD software (Autodesk Inventor Professional 2016), allowing for combined compression and perfusion stimulation of four TE scaffolds (3 x 4 x 13 mm). The full bioreactor system consists of two main parts, the bioreactor chamber and the compression rig. The bioreactor chamber holds the four samples, maintaining a closed sealed system during combined perfusion flow and

compression stimuli. A top and bottom viewing window permits direct observation of TE scaffold morphology under loading at high magnification at the global and cellular level under microscopy. Controlled compressive loading is applied by slotting the bioreactor chamber into a compression rig, see Figure 5-7. The compression rig consists of the full transmission system for applying compression to the bioreactor chamber. A stepper motor and gearing provided transmission to a precision ball power screw, and thus applies microscale displacements to the bioreactor chamber compression shaft. Direct communication is established with the running software through a mounted connector. The main bioreactor chamber can be easily removed from the compression rig and maintain a fixed or adjustable scaffold compression state, see Figure 5-7.

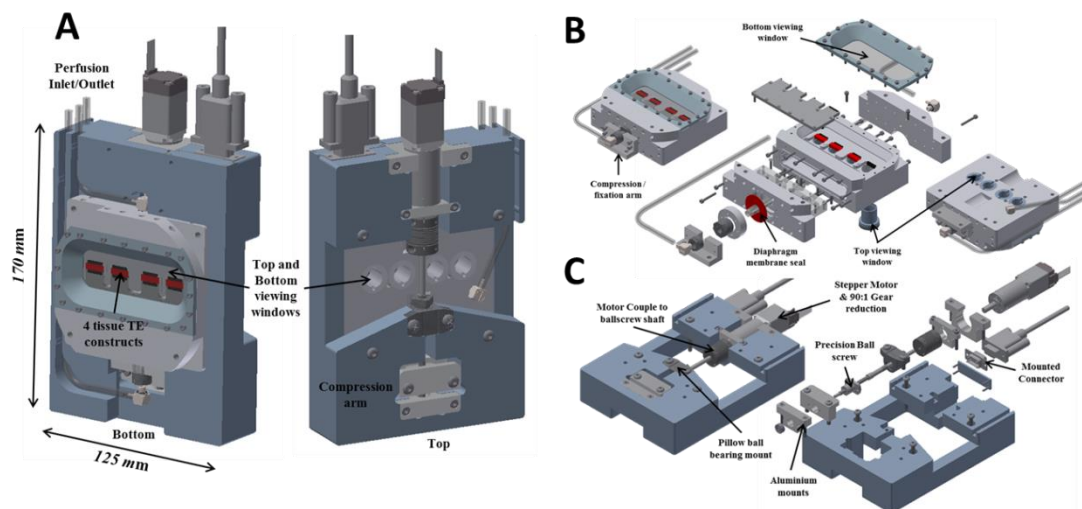


Figure 5-7: The full bioreactor system (170 x 125 mm) consists of two main parts, the bioreactor chamber and the compression rig (A). An exploded illustration of all parts within the bioreactor perfusion chamber (B) and compression rig (C). The bioreactor chamber holds four samples with full sealing achieved through the diaphragm membrane and gaskets during loading. Direct observation of samples can be achieved at low and high magnification. Compression rig provides the main compression power transmission system. Aluminium mounts were used for holding the transmission system.

5.2.2.2 Bioreactor operation

Perfusion stimulus is applied to scaffolds by infusing media through an inlet port and hence into four channels containing the porous platens and scaffolds at the centre. Media perfuses through the porous platens and hence into the scaffold, before exiting

through the opposite porous platen. The four channels re-converge before exiting the bioreactor through an outlet port. Moreover, the perfusion stimulus can be reversed without effecting fluid velocities, see Figure 5-8. The compression stimulus is externally applied to a compression shaft at the bottom of the bioreactor and is internally applied to the four compression arms containing the perfusion channels and hence to the scaffolds through the porous platen in contact with the scaffold surface. The opposite platen is fixed restricting movement of the scaffold during loading, see Figure 5-8.

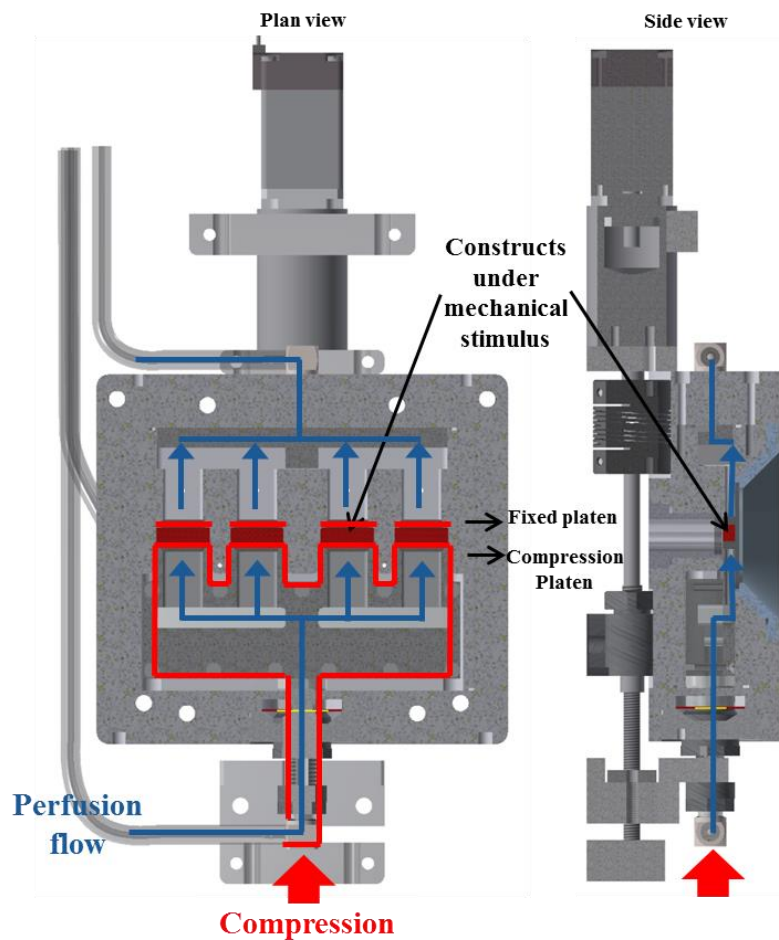


Figure 5-8: Plan and end view of bioreactor stimuli operation. Homogenous perfusion (Blue) is applied through an inlet port and hence diverges in the 4 channels with the compression arm before entering the porous platens and scaffolds. Fluid perfuses out through the scaffold and the fixed platen before re-converging and exiting the bioreactor. Perfusion flow can be fully reversed. Homogenous compression applied externally to samples through a compression shaft (Red) and internally applied to samples by four compression arms containing platens. Fixed platens on the opposite side of the sample restrict movement during compression.

5.2.3 *Bioreactor in-house fabrication and construction*

5.2.3.1 *Porous platen cleaning and passivation treatment*

Porous platens machining was outsourced to a company (Spectrum tooling, Galway) specialised in wire electrical discharge machining (EDM). The platen geometry was precisely cut with a thin single-strand metal wire (100 μm) by inducing a series of electrical discharges (sparks) between the wire and the platen resulting in the removal of material. This method allows for reduced material removal and creating a smooth finish cut, while also preventing blockage of platen pores due to material build up and material overheating effect, see Figure 5-9. After machining, a degreasing and passivation process was carried out in-house, removing grease or residues from the machining process and also forming a new oxide layer on the cut surfaces. Platens were degreased and cleaned by placing in 100% ethanol and carrying out Ultra Sonication cleaning for 15 mins. After cleaning platens, passivation treatment was carried out by submerging in a 20% solution of Nitric acid diluted in dH²O at 50 °C for 20 mins. After passivation samples were rinsed in dH²O and placed in the Ultra sonic cleaner for 15 mins two times.



Figure 5-9: Two porous platens after degreasing and passivation

Assembly of the transmission system (Ballscrew and motor) was carried out in-house. To reduce friction and axial loads on the ballscrew shaft during compression suitable support bearings were selected. A thrust bearing within a pillow mount was selected as the main support unit for the fixed side of the ballscrew ball nut, while a standard bearing was used on the support side. This

required the design of a custom ballscrew shaft, with machining out-sourced to ABSAAC, see Figure 5-10 (A). The custom shaft allowed for direct mounting and fixation of bearings and motor couple, see Figure 5-10 (B). According to the manufactures specification the thrust bearing was assembled and tightened in position on the ball screw shaft to a torque rating of 190 Ncm.

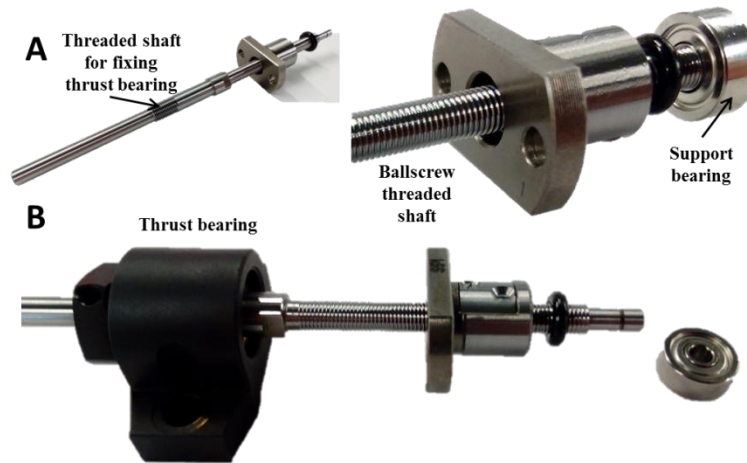


Figure 5-10: Custom machined ballscrew (A) with thrust and support bearing axially fixed to the ballscrew shaft (B).

5.2.3.2 Bioreactor fabrication

Bioreactor fabrication and construction was performed in-house at NUI Galway Engineering Building. The main components of the bioreactor, such as the bioreactor chamber, motor mounts, bearing holders and frames were fabricated using computer numeric control (CNC) machining. Specialised cutters to machine the bioreactor geometry were identified, along with appropriate spindle speeds and feed rates to achieve a clean finished surface. G-codes to operate the CNC were developed, involving machining profiles “toolpaths” such as thread milling, pocket milling, contour milling and slot milling allowing for the formation of geometries, including threaded shafts, gasket gland channels (1.4 x 0.7 mm) and 2mm fluid flow Channels, see Figure 5-11. Manual machining was performed to finishes off parts, such as tapping, cutting and drilling. A detailed overview of the fabrication is described in appendix 1.



Figure 5-11: CNC machining carried out on four sides of the bioreactor chamber stock block. Bioreactor windows were machined and thread milling performed (A-C). Machining of side 2 formed a slot for the compression chamber (D-F). Machining of side 3 formed 2 mm channels for fluid flow (G-I). Finally machining of side 4 preformed for observation window and scaffold holding slots (J-K).

5.2.3.3 *Hardware, electronics and software for compression rig*

After selecting the geared motor suitable hardware and software were identified for controlling the stepper motor through a laptop. A hardware kit consisting of a micro controller (SCMI12, Nanotec), relevant connections and cables was selected. Power was supplied to the micro controller through a 60 Watt external AC-DC power adapter at 24V and between 1-3 Amps. Establishing communication between the laptop and micro controller was achieved through a RS485 driver and hence through a USB connection. Housing was designed to hold all electronics and connectors, allowing for complete disconnection of the stepper motor away from the housing, see Figure 5-12. Assembly was carried out in-house requiring the machining of slots to hold the connectors and wire soldering. The stepper motor software (Nanopro

1.70) allowed for different operating profiles, full adjustment of speeds, distance and direction, see Figure 5-12. Oscillatory compression was achieved by reversing motor under timed repetition, see Figure 5-12.

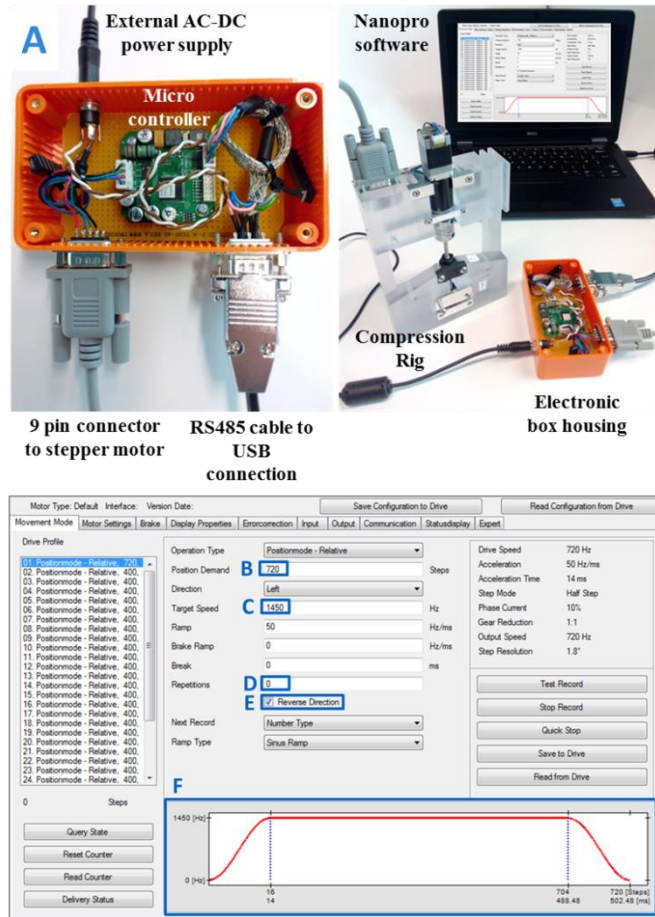


Figure 5-12: Compression rig control box (A). The microcontroller is connected to external AC-DC power supply, with a 9 pin connector connected from the micro controller to stepper motor. The micro controller connects to laptop through RS485 cable and hence through USB connections. Nanopro software allows for full control over the stepper motor travel distance by the number of steps (B), motor speed (C) and repetitions of the same motion. Reversing motor direction (D) allows for oscillatory compression profile. While, a graph (E) shows real time feedback of motor position during operation

5.2.3.4 *Assembled fabricated bioreactor*

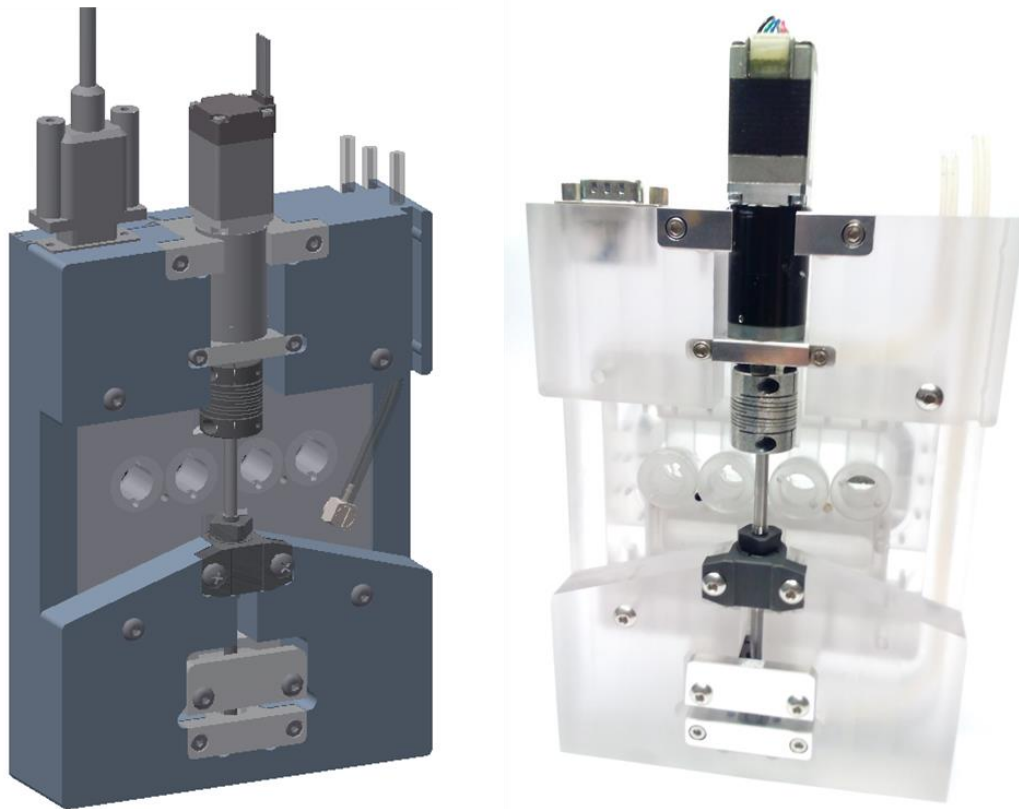


Figure 5-13: 3D CAD illustration of bioreactor versus assembled fabricated bioreactor.

5.2.4 *Design changes and final bioreactor design*

The bioreactor system was further adapted to contain four additional samples within the compression rig. This was achieved by adding an adaptor to the compression rig, allowing for a second bioreactor chamber to be slotted onto the opposite side of the compression rig, see Figure 5-14. This permitted the loading of 8 samples concurrently within one compression rig by loading two bioreactor chambers concurrently.

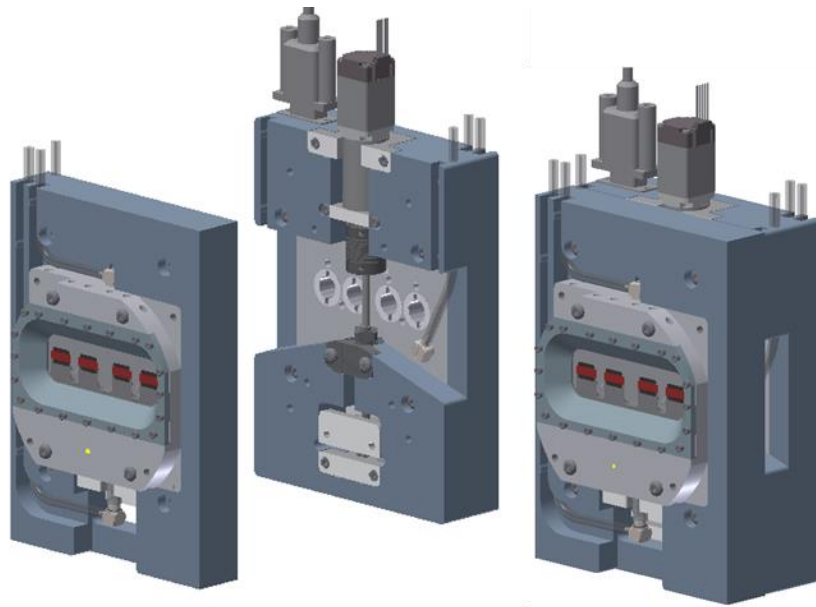


Figure 5-14: Bioreactor compression rig redesigned to accommodate a second bioreactor chamber system that can be attached, compressive loading 8 samples concurrently.

5.3 Bioreactor Validation

After developing a full cell culture bioreactor system, validation testing was carried out to determine the bioreactor compression and perfusion system overall performance. Validation tests included compressive and perfusion testing at the global level and local cellular level. Compressive and perfusion validation tests were carried out using a porous sponge test sample, mimicking the structural properties of a porous scaffold. The sample allowed for easy installation and removal from the bioreactor.

5.3.1 *Microscopy and live cell imaging setup*

The bioreactor system was setup within an Olympus live cell microscope, allowing for visualisation of the porous cell laden hydrogels under mechanical and perfusion stimulus in real time, see Figure 5-15. The microscope objectives (4x, 10x, 20x and 40x) allowed for the capturing of high magnification cell images, while the endoscope positioned in a separate window allowed for low magnification images of the global scaffold geometry.

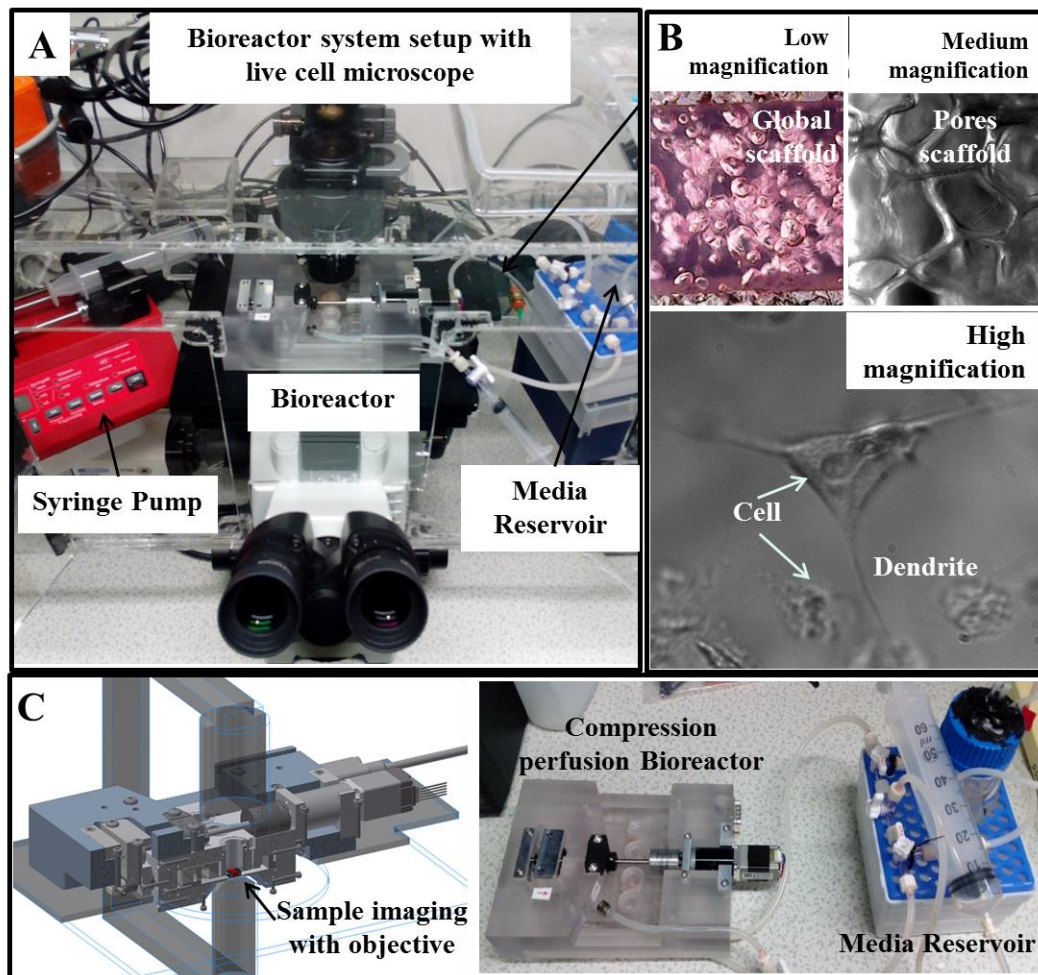


Figure 5-15: Bioreactor setup within the live cell microscope (A), imaging at low, medium and high magnification, identifying the global scaffold geometry, pore structure and individual cells (B). Microscope objective capable of moving between samples, while endoscope allows for low magnification images (C). Bioreactor system remains fixed in place during loading.

5.3.2 Compression Validation

Compression validation was experimentally quantified at different stages in the transmission system, from stepper motor rotation to platen displacement. Applying 0.5% compression to a 4 mm high scaffold required a minimum linear displacement of 20 μm , corresponding to a ballscrew shaft rotation of 14.4 degrees, and a motor shaft rotation of 720 steps. To verify this, the degree of rotation from the geared stepper motor output shaft was manually measured, resulting in a corresponding ~ 14.4 degree rotation, see Figure 5-16 (A). To validate displacement applied to the platens and hence to the scaffold, precise calibration scale bars of known distance

were incorporated into the bioreactor design, see Figure 5-16 (B). The calibration bars were machined at the interface between the sample and the loading platen, allowing for visualisation from the microscope in real time. After applying the 20 μm displacement to the ballscrew, no corresponding displacement was observed at the porous platen. However, after continued motor operation for a further 100 μm , a displacement of 20 μm displacement was observed. After determining the initial loading conditions, a global oscillatory loading profile with a peak displacement of 20 μm at 1 Hz was developed and applied to samples, see Figure 5-16 (C).

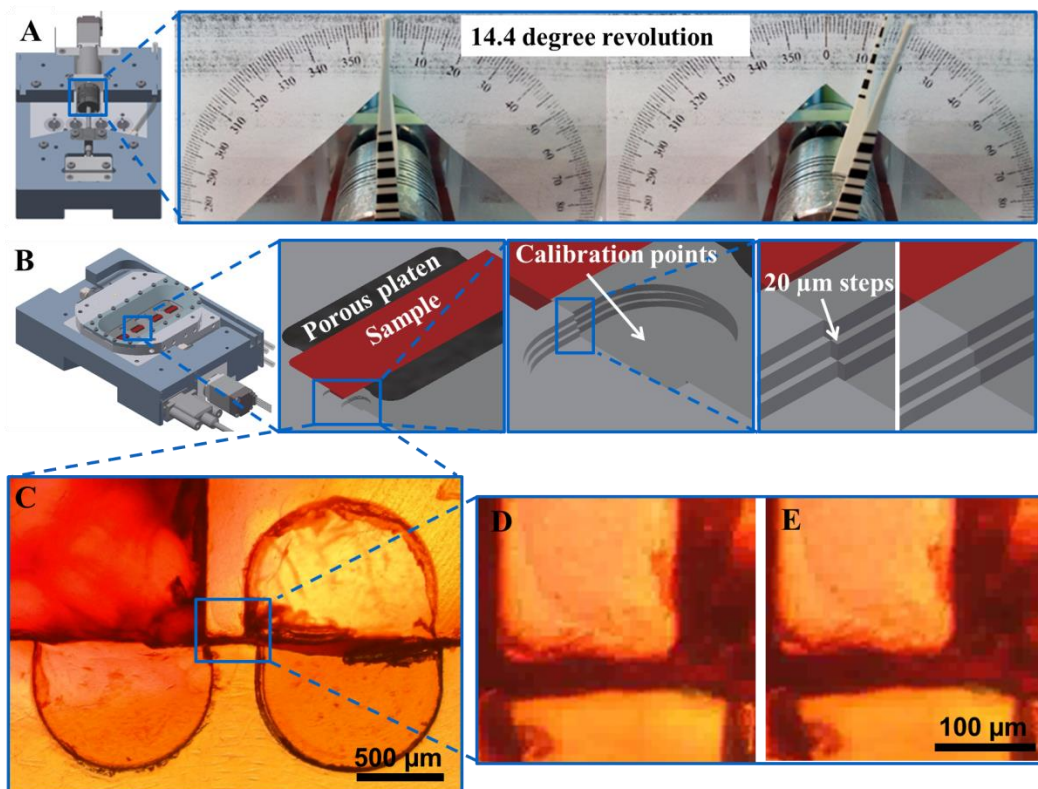


Figure 5-16: After programming the geared stepper motor to revolve 720 steps a corresponding output of 14.4 degree was observed (A). Calibration points machined in bioreactor chamber objective window, allowing for visualisation of 20 μm displacement applied to the porous platen (B). Compressive loading was calibrated to the correct displacement by microscopy imaging allowing for the visualisation of platen displacement during loading (C, D, E)

After validating global displacements applied to the scaffold, local strains were determined within the scaffold struts. Controlled displacements were applied to the sample porous scaffold and recorded under high magnification. In collaboration with

Dr. Stefaan Verbruggen, strain distribution was experimentally determined at the local cellular level using a digital image correlation (DIC) technique (Verbruggen et al. 2015). Figure 5-17 shows real time video frames acquired of strut deformation within a test sample when subjected to controlled displacement. Images were acquired of a sample deformed by $278.47\ \mu\text{m}$ and digital image correlation techniques were applied to determine ensuing tensile and compressive strains within sample struts along with average tensile (17.52%) and compressive (16.45%) strains throughout the sample, see Figure 5-17. Hence, for 3D scaffold containing cells, this information will determine what proportion of cells are experiencing high levels of strain compared to cells experiencing low level strains and hence subsequent adjustment of loading to achieve physiologically relevant average strain in cells throughout.

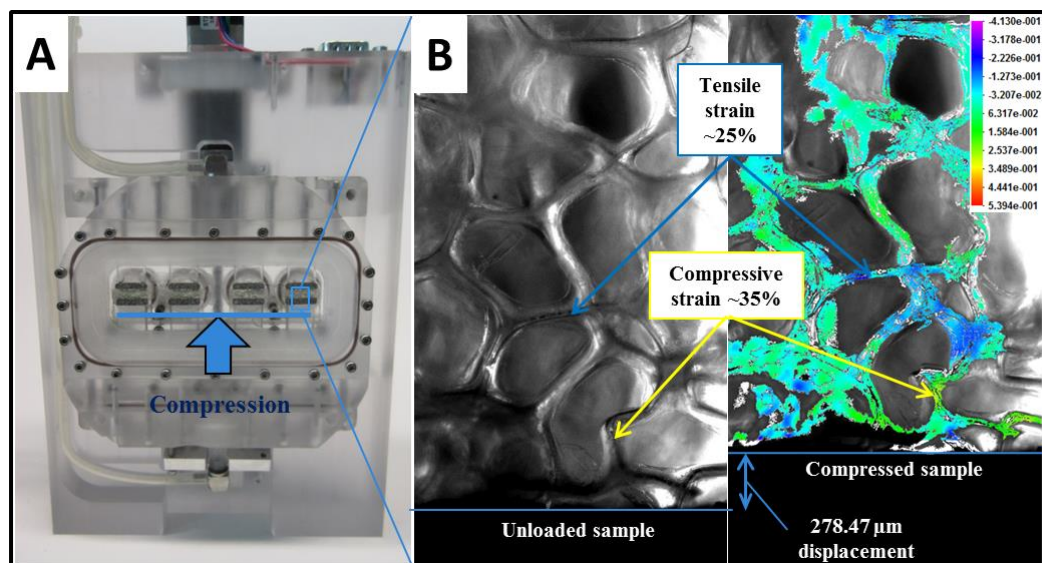


Figure 5-17: Illustrates controlled displacement applied to the porous platen and hence to the porous test sample (Blue arrows) (A). Real time videos were acquired of the strut deformation under controlled displacement (B).

5.3.3 Perfusion Validation

The bioreactor perfusion system was fully assembled, sealed, and tested for leaks when subject to an increase in pressure. Visual inspection observed no leaks in the static or dynamic seals during manual operation of the compression arm. Perfusion validation was carried out at the global level to determine the symmetry of fluid

velocities across the four channels. This was first performed without the addition of the porous platens and scaffolds within the bioreactor chamber. Red dye was perfused through the bioreactor chamber at a peak steady flow rate of 1.2 mL/min (0.3 mL/min per channel) and recorded in real time. It was observed that red dye infused at higher velocities through the side channels, compared to the centre channels, resulting in an initial uneven flow profile and hence fluid velocities across the four channels, see Figure 5-18.

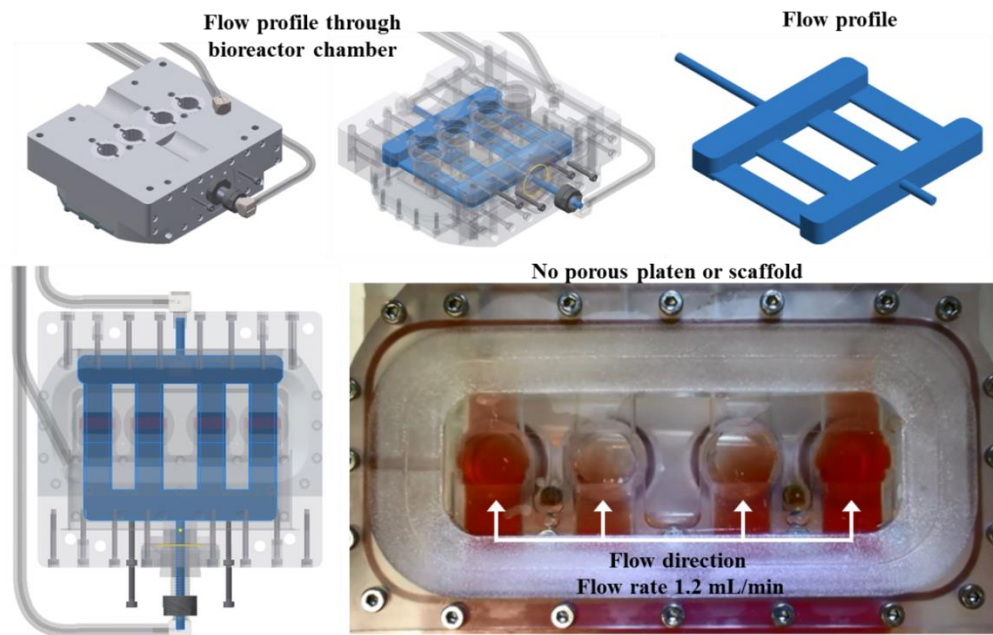


Figure 5-18: Validation of first bioreactor design showed an uneven flow profile across the 4 channels in the bioreactor chamber at peak flow rate of 1.2 mL/min.

In collaboration with Dr. Feihu Zhao, computational modelling was employed to optimise the flow profile geometry design towards a symmetric flow profile with homogenous fluid velocities through each of the four channels. Computational modelling was carried out by Zhao et al under dynamic conditions, modelling oscillatory flow at peak flow rate of 1.2 mL/min at a frequency of 1 Hz. Computational fluid dynamics (CFD) was performed using ANSYS CFD software. It was desired to have a uniform flow across the four channels, however, the first flow chamber design resulted in an irregular flow profile, see Figure 5-19 (First design). This occurred due to the inlet flow entering the four channels through an irregular geometry that was not in symmetry with the four channels. A number of

reiterations of the bioreactor flow chamber design were performed in developing the symmetric flow geometry, before a final profile was selected and computationally compared with the original version.

Computational results showed a homogenous flow profile in the final design compared the first design, see Figure 5-19 (Final design). The final flow profile design was implemented into the overall bioreactor design and a new prototype manufactured containing the flow profile geometry. Experimental perfusion validation was carried out again by infusing red dye into the final bioreactor design. A homogenous flow profile was visually observed across the 4 channels, see Figure 5-19.

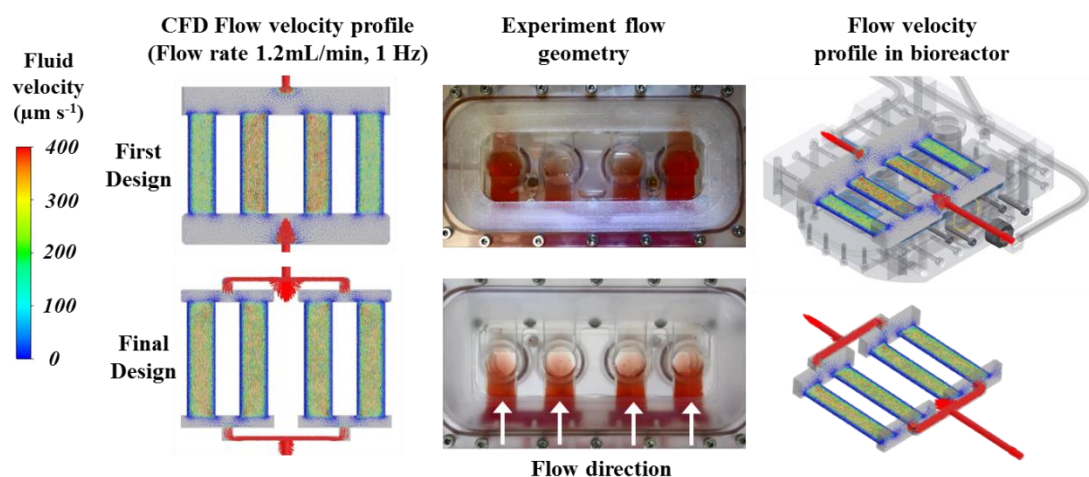


Figure 5-19: Computational and experimental testing of the old and new bioreactor flow profile. Fluid (stain with red dye) enters through the bottom of the four channels and permeates through the channels before re-converging and exiting the bioreactor chamber. A homogenous flow profile was observed across the 4 channels in the final design compared to the first design.

After experimentally and computationally validating a homogenous flow profile across the four channels, validation of fluid flow through porous platens and porous test scaffolds was carried out. Red dye was infused at flow rate of 1.2 mL/min through the four channels. The addition of the porous platens had a small effect on the symmetry of the flow profile with red dye perfusion occurring quicker through certain platens, see Figure 5-20 (A). It is believed this occurred due to small differences in the porous platen and scaffold structure/porosities, leading to changes

in pressures between each channels and hence fluid velocities. These differences in flow profile were assumed to have negligible effect on the average flow velocities through the scaffold under fully established flow. Local fluid velocity profiles, representative of the cellular level were visually observed experimentally by injecting a concentrated dye stream at the entrance to the porous platen. Real time imaging at low and high magnification showed the fluid profile through the porous platen and scaffold. Concentrated red dye enters through the compressive porous platens and permeates through the test sample, exiting through the top porous platen, see Figure 5-20 (B&C).

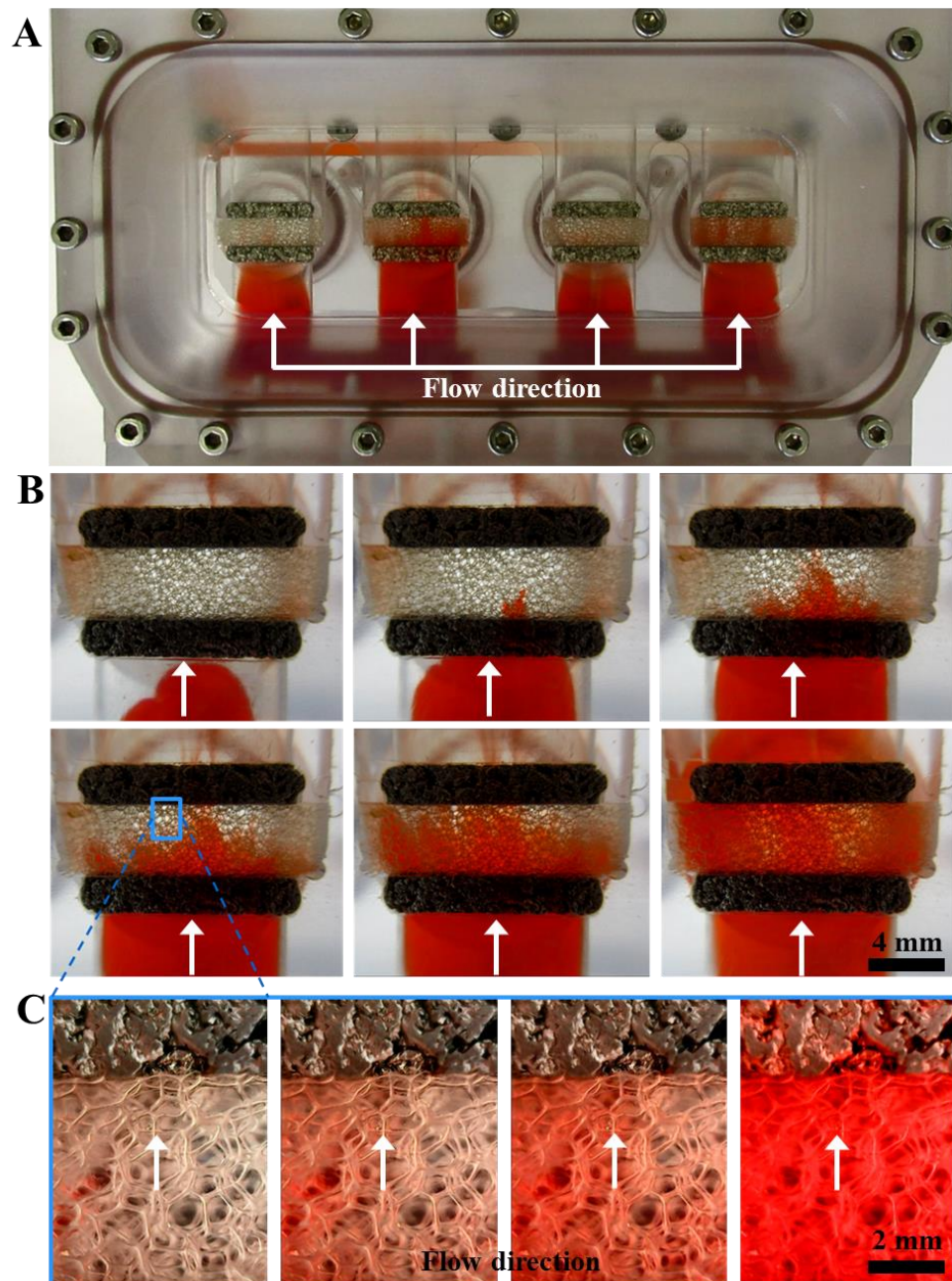


Figure 5-20: Real time video frames shows red dye being perfused through the bioreactor chamber under a steady flow rate of 1.2mL/min. Small changes in flow profiles were observed between the 4 channels containing porous platens and scaffolds (A). Global fluid perfusion was observed through the compressive porous platens and hence through the test sample before exiting through the fixed porous platen (B). Magnified of the scaffold structure shows red dye perfusing through pores and out through the porous platens (White arrows) (C).

5.4 Bioreactor evaluation (Results and conclusion)

A custom perfusion-compression bioreactor was designed to apply physiologically relevant levels of mechanical loading to tissue engineered (TE) scaffolds. Compressive loading is guided by a high-torque stepper motor with a 90:1 gear reduction connected to a custom designed high precision ballscrew, allowing for precise displacement (axial play of 5 μm) of porous platens. The applied loading is displacement-controlled with speeds and magnitudes controlled using commercial software (Nanopro 1.70). Custom designed interconnected porous (51 %) platens, with a Young's modulus of 200 GPa and Poisson's ratio of 0.26, were cut from 316 stainless steel filters allowing for homogenous compression of bone constructs, but also facilitates fluid flow to the porous sample when under flow perfusion. Fluid perfusion is applied by a programmable syringe pump (NE-1600) with flow rates ($>0.454 \mu\text{L/hr}$) and profiles controlled by commercial software (Syringe Pump Pro). Furthermore, a diaphragm sealing method allows for the application of compression movement, preventing leaking when under fluid perfusion and thereby ensuring system sterility. Moreover, the bioreactor is compatible with inverted microscopes, such as fluorescent, confocal and light microscopes, thus allowing for live cell imaging during the application of mechanical stimulus. This system may provide a valuable tool in generating fully functional and mechanically suitable tissue grafts that can be used for clinical applications and hence the treatment of musculoskeletal conditions.

Existing bioreactor systems do not accurately mimic the mechanical stimulation experienced in the *in vivo* environment, such as fluid shear stress and mechanical strain (Keogh et al. 2011; Sittichokechaiwut et al. 2009)). However, computational models have predicted that a combination of perfusion and compressive loading at appropriate experimental conditions enhances tissue formation in 3D TE scaffolds (Zhao et al. 2014; Zhao et al. 2015). This system is capable of applying combined fluid shear stress and mechanical strain at resolution applicable to strains experienced by bone cells at levels that are analogous to *in vivo* environment. Furthermore, current commercially available bioreactors, such as the TC-3 Cell Culture Bioreactor from EBERS Medical Technology S.L. require a lot of

space, to fully operate, restricting the portability within a laboratory environment. The system presented in this Chapter is flexible in design, allowing for a wide range of stimuli to be applied to different tissue types and their biomaterials with compressive moduli up to 1 MPa, and also maintain operation during long term culture periods for tissue formation to occur. Finally, existing bioreactor systems have restricted capability in visualisation of samples at the cellular level. The capability of real time imaging, provides a global and local level picture of events occurring within samples been tested, such as determining cell viability, morphology and gene expression. Additionally, real time imaging provides direct visualisation of stimulus/status and hence calibration and evaluation over long term culture. The bioreactor system designed here allows for sample visualisation at low and high magnification, representing real time imaging of the overall scaffold geometry and at the cellular level, while under mechanical stimuli.

The lengthy time involved in the assembly and full sterilisation of the bioreactor system is a possible limitation. This is mainly due to a large number of bolts required in the assembly and sealing of parts. Also, if connected to the syringe pump, the bioreactors overall portability is restricted, requiring the disconnection of the syringe for easy portability. Though the compression system is capable of applying appropriate displacements after adjustment, the deflections occurring between the Ballscrew and compression arm is a possible limitation as calibration is required. The microscope observation window incorporated into the design allows for imaging with all objectives. However, when the bioreactor is positioned within the stage, changing of image magnification is restricted, requiring the sacrifice of the current image position to change image magnification. This occurs due to objective window design restricting the rotation between microscope objectives when positioned in the stage, requiring the removal of the bioreactor from the stage to allow for changing of microscope objective. The bioreactor system loads 8 samples, however samples are not independently loaded within a closed media system. This was deemed unfeasible due to the requirement of 8 separate syringes and hence pumps. Finally, experimental perfusion validation was carried out using a steady flow rate compared to the dynamic flow profiles used in experiments.

Future work would further develop the compression-perfusion bioreactor to stage that it is easy to use, portable and requires no extra equipment, with associated software. This bioreactor would be designed to allow for real time imaging of tissue samples with a variety of different research microscopes. Moreover, the design will be evolved to incorporate a load cell to monitor changes in mechanical properties due to tissue formation in the constructs over time as tissue constructs evolve. Control software would be developed to encompass control of complicated loading profiles, while also allowing for visualisation and monitoring of displacement, fluid velocities, real time images and mechanical properties from a single graphical interface. Finally, perfusion validation would be carried out using micro particle image velocimetry (PIV) techniques, allowing for visualisation and predictions of fluid velocities and wall shear stresses within scaffold pores.

In summary, a “proof of concept” model for applying *in vivo* levels of fluid perfusion and mechanical compression to bone constructs, with the capability of real time monitoring of cell behaviour and tissue formation was developed. This novel system was a small perfusion-compression bioreactor that allowed for precise control of fluid velocities and strains applied to cells within TE scaffolds. The system holds a fully confined TE scaffold, while also applying combined uni-axial compression at 0.5% strain with fluid perfusion at a peak rate of 0.3 mL/min and a minimum of 0.05 mL/min. Compression and perfusion is applied homogenously to the scaffold surface through a porous platen. The bioreactor maintains an appropriate temperature and gas mixture (37 °C, 5% CO₂), negating the risks of outside contamination and continuous support of cell growth. Furthermore, bioreactor parts are constructed from polycarbonate and are sealed through the integration of gaskets and a custom designed diaphragm sealing membrane mechanism. The bioreactor was designed to operate on TE scaffolds with compressive moduli up to 1MPa. Finally, real time imaging was integrated into the bioreactor design, thus allowing for live cell imaging during the application of mechanical stimulus. In collaboration with Dr Feihu Zhao, computational results have provided a theoretical prediction of the appropriate fluid perfusion and mechanical compression to be applied to a porous hydrogel. The next study in this thesis will focus on applying these computational results to a cell-laden porous hydrogel to generate both cellular level stress and mechanical stimulation

regimes comparable to the physical environment experienced *in vivo* over long term culture. Furthermore, as a novel device that provides *in vivo* levels of mechanical stimulus to tissue constructs, along with the capability of real time imaging, future directions will also focus on the commercial potential of this device.

Chapter 6: Combined compression and perfusion stimulus promotes osteocyte differentiation.

6.1 Introduction

In vitro approaches have shown success in the use of biomaterial scaffolds to promote osteoblast-osteocyte differentiation (Mc Garrigle et al. 2016; Gerald J Atkins et al. 2009; Uchihashi et al. 2013) and mineralisation within biomaterial scaffolds (Gleeson et al. 2010; Keogh et al. 2011; Keogh, O'Brien, et al. 2010; Curtin et al. 2012; Correia et al. 2012; Castillo Diaz et al. 2014; Tan et al. 2014; Chatterjee et al. 2010; Shin et al. 2014; Kim et al. 2007; O'Brien 2011). Chapter 3 of this thesis showed that osteocyte differentiation of MC3T3-E1 cells is regulated within a 3D cell environment by ECM stiffness and cell density. In chapter 4 the addition of porosity to hydrogels, containing encapsulated osteoblasts, provided an environment for both osteoblast and osteocyte development. Chapter 5 designed and developed a custom perfusion-compression bioreactor to apply physiologically relevant levels of mechanical loading to tissue engineered (TE) scaffolds. In this chapter, strategies from the previous three studies were combined to provide an experimental model to study the combined effect of matrix stiffness, compression and perfusion stimulus on osteoblast-osteocyte differentiation in porous hydrogels containing encapsulated osteoblasts.

In vivo, bone is mechanically loaded experiencing pressurisation and deformation, generating oscillatory fluid flow and matrix strain throughout its structure (Wittkowske et al. 2016; Du et al. 2009; Jacobs et al. 1998). Osteocytes *in vivo* experience mechanical stimulation in the form of extracellular matrix strain and fluid shear stress within the fluid-filled lacunar-canalicular network, while osteoblasts experience wall shear stress due to fluid flow of the bone marrow (Chan et al. 2009; Wittkowske et al. 2016; Keogh et al. 2011; Jaasma et al. 2008; Ban et al. 2011; Owan et al. 1997; You et al. 2001; Smalt et al. 1997; Gomes et al. 2003;

Zhang et al. 2006; Klein-Nulend et al. 2012; Saunders et al. 2006; Bacabac et al. 2004; Metzger et al. 2015; Birmingham et al. 2014; Vaughan 2013). In bone tissue the stiff calcified osteoid surrounding the osteocyte acts a mediator of mechanical stimulation through cell-ECM interactions (Wittkowske et al. 2016; Chan et al. 2009; Wang et al. 2007). Deformation of the pericellular space in the ECM matrix generates interstitial fluid flow within the lacunar-canalicular system, thereby applying a fluid shear stress on osteocyte cell processes and pericellular matrix fibers that tether the cells to the ECM. Together these stimuli act as physical cues on osteocytes during load-bearing activity (McNamara et al. 2009; Wang et al. 2007). *In vitro*, such stimuli can be applied to bone cells through direct fluid perfusion within flow chambers, creating a fluid shear stress, and also indirectly through compression of the matrix in which they are seeded, thereby creating matrix strain (Vazquez et al. 2014; Sittichokechaiwut et al. 2009). Bioreactor technology can apply dynamic culture such as fluid perfusion or compressive strain to porous TE constructs, supporting the expansion of a cell population and promoting tissue formation (Sladkova & de Peppo 2014; Jaasma et al. 2008; Sittichokechaiwut et al. 2009).

In vitro, studies have shown bone cells are sensitive to flow-induced shear stress as observed in osteoblasts (Keogh et al. 2011; Jaasma et al. 2008; Ban et al. 2011), osteocytes (Owan et al. 1997; You et al. 2001; Smalt et al. 1997) and bone marrow cells (Gomes et al. 2003; Sikavitsas et al. 2005). Fluid flow is known to induce a shear stress on osteoblast and osteocyte cells, inducing osteogenic differentiation, the production of matrix and also providing waste and nutrients exchange, negating problems associated cell death in scaffold cores (Keogh et al. 2011; Jaasma et al. 2008; Ban et al. 2011; Gomes et al. 2003; Bancroft et al. 2002; Cartmell & Porter 2003; Grayson et al. 2011). MC3T3-E1 osteoblast cells seeded on a flat 2D polylysine-coated glass slide expressed increased levels of nitric oxide (NO) when subjected to fluid shear stress for 15 mins at peak range of 39.6 Pa-Hz (Bacabac et al. 2004). Grayson et al, revealed that steady flow velocities, ranging from 400 to 800 $\mu\text{m/s}$, produced the best overall osteogenic responses of human MSCs seeded in decellularized trabecular bone cores (Grayson et al. 2011). While, Zhang et al, showed that MLO-Y4 osteocytes-like cells subject to fluid flow in the

form of shear stress (16 dynes/cm²) had longer dendrites and increased expression of E11, compared to cells receiving no flow (Zhang et al. 2006).

Static culturing of constructs can lead to the newly produced tissue in the scaffold acting as a barrier to remodelling and osseointegration within the host tissue (Lyons et al. 2010; Alhag et al. 2012; Anselme 2000), which can result in cell death within scaffold cores (Sikavitsas et al. 2005; Keogh et al. 2011; Lyons et al. 2010; Alhag et al. 2012). Mechanical loading is important in TE construct development, and has been shown to enhance cell distribution, osteogenic differentiation, nutrient and waste transport and hence influence the consistency of tissue formation and overall mechanical properties (Bacabac et al. 2004; Saunders et al. 2006; Sittichokechaiwut et al. 2009; Matziolis et al. 2011; Verbruggen et al. 2012; Nicoletta 2006; Stern & Nicoletta 2013; Klein-Nulend et al. 2012; Zhang et al. 2006; Nicoletta et al. 2006). Cyclic mechanical loading (0.05 Hz, 4 kPa) enhanced osteogenic pre-differentiation of human bone marrow-derived stem cells in 3D fibrin-DMEM constructs improving osteogenic differentiation and host osseous integration (Matziolis et al. 2011). Additionally, cyclic compressive loading (5% strain, 1 Hz) in polyurethane scaffolds seeded with fully differentiated osteoblastic (MLO-A5) cells led to an upregulation of type 1 collagen, osteopontin, osteocalcin and calcium deposition (Sittichokechaiwut et al. 2009). A study showed that *in vivo* mechanical loading (compressive load -3.5 N @ 2Hz, 30 secs) promoted increased levels of E11 in osteocytes near the surface and embedded within the matrix of three month old wild-type and heterozygotic mice (Zhang et al. 2006). Furthermore, cyclic compressive loading (5 min, 10 Hz, 2.5 N) applied to type I collagen gels containing osteoblasts (MC3T3-E1) on the surface and embedded osteocytes (MLO-Y4) maintained their morphology, phenotype and demonstrated increase levels of PGE₂ expression (Vazquez et al. 2014). However, even though many bioreactor-based bone regeneration approaches have been widely explored (Keogh et al. 2011; Gardel et al. 2013; Vazquez et al. 2014; Sittichokechaiwut et al. 2009; Jaasma et al. 2008; Ban et al. 2011), the primary focus has been to use fluid perfusion to enhance nutrient exchange and waste removal and thereby maintain cell viability throughout TE constructs. Moreover, bioreactor systems that apply combined mechanical stimulation (perfusion and compression), have not sought to mimic the *in vivo*

physical environment that is appropriate for both osteoblast and osteocyte differentiation to enhance tissue formation (Keogh et al. 2011; Sittichockechaiwut et al. 2009).

Applying physiologically relevant stimulus, such as oscillatory compression and perfusion loading to TE constructs, may enhance osteoblast and osteocyte differentiation, cell viability, tissue formation and the constructs overall osteogenic potential (Keogh et al. 2011; Gardel et al. 2013; Vazquez et al. 2014; Sittichockechaiwut et al. 2009; Jaasma et al. 2008; Ban et al. 2011). Computational models have predicted the levels of mechanical stimulation, such as fluid flow or strain, that can enhance osteogenic differentiation within tissue engineered scaffolds (Stops, Heraty, et al. 2010; Stops, Harrison, et al. 2010; Jungreuthmayer et al. 2009; McCoy et al. 2012; Olivares et al. 2009; Milan et al. 2009; Zhao et al. 2015; Zhao et al. 2014). In particular, a multiphysics computational model was developed to predict the desired mechanical stimulation to apply to a porous 3D TE scaffolds for bone regeneration (Zhao et al. 2015; Zhao et al. 2014). These models showed that a combination of perfusion and compression loading amplified mechanical stimulus in cell seeded TE scaffolds, and predicted that this could drive osteogenic differentiation (Zhao et al. 2015; Zhao et al. 2014). Furthermore, experimental studies have also demonstrated that combined compression and perfusion stimulus promoted increased osteoblast differentiation, matrix mineralisation and the functional properties of constructs (Bouet et al. 2015; Liu et al. 2012). While such studies provide evidence of the beneficial effects of applying compression or fluid flow to TE scaffolds, to date simultaneously applying combined mechanical cues, akin to that existing *in vivo* (i.e. both matrix-derived stimuli and extrinsically applied stimuli) to porous scaffolds containing encapsulated osteoblasts has not been achieved.

In this study it is hypothesised that a combination of mechanical stimuli, (compression and fluid perfusion) will promote enhanced differentiation of both osteoblasts and osteocytes in a porous trabecular-like biomaterial scaffold. The overall objective of this chapter was to investigate the effect of combined compression and perfusion stimulation on MC3T3-E1 cells encapsulated within porous gelatin-mtgase hydrogels using a custom compression-perfusion bioreactor

system designed in Chapter 5. Cell viability was examined by Live/Dead fluorescent staining of cells within constructs after 32 days. Osteoblast-osteocyte differentiation was confirmed by examining DMP-1 expression, cell morphology and matrix mineralisation. Osteogenic differentiation and tissue formation was examined by ALP activity, calcium content (micro-CT) and distribution (micro-CT and Alizarin red staining). The mechanical properties of the constructs after 32 days of culture were examined by testing the bulk compressive modulus.

6.2 Materials and Methods

6.2.1 Combined perfusion-compression bioreactor and moulds

The custom perfusion-compression bioreactor designed in chapter 5 was used to apply physiologically relevant levels of mechanical loading to porous gelatin-mtgase hydrogels, see Figure 6-1. Constructs in the static groups were fabricated in moulds containing the same dimensions as the bioreactor constructs (3 x 4 x 13 mm), see Figure 6-1.

In preparation for cell culture, all bioreactor parts were cleaned in an ultrasonic bath containing deionized water and detergent for 20 mins at 50 °C and rinsed with deionized water. A hydrophobic layer (Sigmacote, Sigma-Aldrich) was coated onto bioreactor parts to prevent constructs sticking during loading, which were then rinsed with deionized water. Subsequently, the bioreactor chamber was fully assembled, sealed and sterilised through gamma irradiation at a dose of 33 kGy. The perfusion system parts, such as tubing and connectors, were autoclaved for 15 minutes at 120 °C and hence assembled under a biosafety cabinet forming a sealed sterile unit.

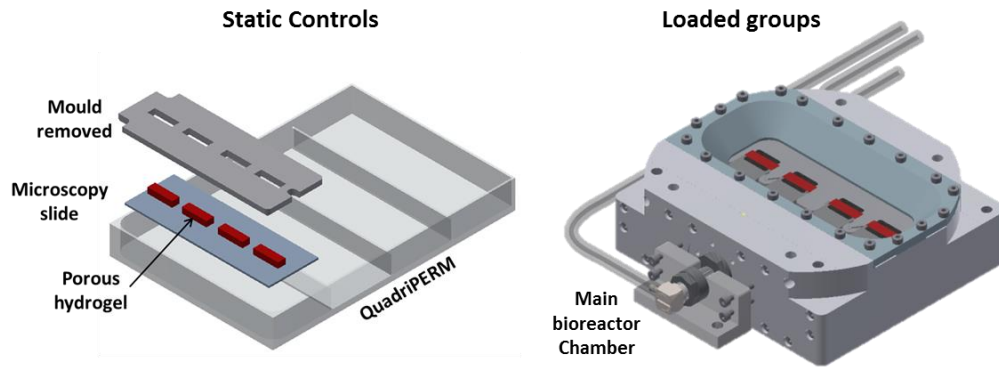


Figure 6-1: Custom design moulds for static and osteogenic constructs. Constructs receiving mechanical stimulus were moulded in the bioreactor chamber

6.2.2 Cell culture and porous cell-laden gelatin-mtgase hydrogels fabrication

Porous gelatin–mtgase hydrogels were fabricated with a final concentration of 6 % w/v gelatin. Hydrogels were prepared by mixing gelatin (type A, 175 Bloom, Sigma–Aldrich) at 80 °C in supplemented alpha minimum essential medium (α MEM) to obtain a liquid consistency for easier mixing. Gelatin suspensions were sterile filtered through a 0.22 μ m filter (Millipore, Cork, Ireland). MC3T3-E1 pre-osteoblastic cells (Sigma–Aldrich) were cultured under standard conditions (5 % CO₂, 37 °C). Cells were routinely grown to 70–80% confluency in T175 culture flasks (Sarstedt Ltd, Wexford, Ireland) containing supplemented (α MEM) (Sigma–Aldrich), 10 % FBS (Sigma–Aldrich), 1% antimycotic antibiotic (100 U/mL penicillin (Sigma-Aldrich), 100 μ g/mL streptomycin) (Sigma Aldrich) and 2 mM L-glutamine (Sigma-Aldrich). Before encapsulating, MC3T3-E1 cells (Passage 14-16) were detached using trypsin–ethylenediaminetetraacetic acid (EDTA, Sigma-Aldrich) and suspended in supplemented medium at 8×10^6 cells/mL. Cell suspensions were mixed with the gelatin solution and a 0.03% mtgase at a ratio of 5:4:1 (v:v:v). The final concentration of the mixture was 6 % w/v gelatin, 8×10^6 cells/mL and an mtgase concentration of 0.03 % per gram of gelatin. Micro-pores were introduced into the gelatin/mtgase/cell solution by forming micro-bubbles in the solution. During aspiration the pipette tip was immersed within the solution and held approximately at 45°, allowing for a mixture of solution and micro-bubbles to be introduced into the pipette tip. The pipette was set to aspirate a controlled volume

of 500 μL , hence when aspirating the 250 μL solution an additional 250 μL of micro bubbles was introduced into the solution, forming a close array of bubbles within the hydrogel. The hydrogel solution consisted of 78 μL , while the porous void consisted of 78 μL , giving a porosity of $\sim 50\%$. Hydrogels were allowed to gel at 4 $^{\circ}\text{C}$ for 6 min before αMEM culture medium was added to static and loaded groups, while osteogenic growth factors (100 nM dexamethasone, 50 $\mu\text{g}/\text{ml}$ ascorbic acid, 10 mM β -glycerol phosphate) (Sigma-Aldrich) were added to the osteogenic group. Porous hydrogels were left in the incubator to stabilise for 30 mins before micro-bubbles were removed through vacuuming at ~ 60 Torr, replacing the porous void volume with media and leaving behind an interconnected porous scaffold architecture. Samples were placed again in the incubator. All hydrogel constructs had a 4 mm width, 3 mm height and 13 mm length.

6.2.3 Mechanical stimulation procedure

Constructs were separated into five groups: (1) Static control Group 1, which received regular culture medium, and (2) Static control group 2, which was cultured in osteogenic media. Three groups were mechanically loaded by subjected to either (3) oscillatory flow, (4) oscillatory compression or (5) combined oscillatory flow and compression. The following list outlines the five groups:

1. Static (Culture Media)
2. Static osteo. (Osteogenic media)
3. Perfusion (Oscillatory flow; 1.2 mL/min flow rate at 1 Hz, 1 hr/day)
4. Compression (Oscillatory compression; 0.5% strain at 0.5 Hz, 1 hr/day)
5. Combined (Combined oscillatory flow and compression groups, 1 hr/day)

In the perfusion group, oscillatory fluid flow was applied at 1Hz with a peak flow rate of 1.2 mL/min. While, in the compression group, oscillatory compression was applied at 0.5 Hz at 0.5% strain. The combined group consisted of applying perfusion and compression stimulus at the same time. In all loaded groups stimulus was applied for 1 hour per day. To prevent osteoblast desensitization to mechanical stimulation a rest period (no stimulus) for 1 hour was included after applying stimulus (Jaasma & O'Brien 2008; Jaasma et al. 2008; Plunkett et al. 2010). For all stimulus groups, loading/rest sessions were separated by ~ 22 hours, during which a

low flow rate of 0.05 mL/min was applied. The high mechanical stimulus conditions were designed to mechanically stimulate the osteoblasts, and the low-flow condition were designed to provide nutrient delivery to the cells, along with providing a window for cells to recover from desensitization (Jaasma & O'Brien 2008). Media was infused and withdrawn every 17 mL, with approximately half of the total media (60 mL) within the bioreactor system fully renewed every 7 days. On day 32, constructs were removed from bioreactor and placed in 24-well plates for analysis.

6.2.4 Cell viability

Cell viability within constructs was assessed by carrying out LIVE/DEAD staining. Samples (n=2 per group) were transferred to a 24-well plate and washed with phosphate buffer saline (PBS) before staining. A staining solution containing 500 μ l of PBS, 2 μ M calcein AM (Life Technologies) and 4 μ M ethidium homodimer-1 (Eth-1) (Life Technologies) was added to samples for 40 minutes at 37 °C (Chen et al. 2013). All images were captured using an Olympus IX50 inverted fluorescence microscope. Images were examined at 4x magnification with five images obtain per construct.

6.2.5 Cell morphology and DMP-1 immunofluorescent staining

Static, Static Osteo and Combined groups were stained for cell morphology and DMP-1 to determine osteoblast-osteocyte differentiation. Hydrogel constructs were fixed using 4% paraformaldehyde (Sigma-Aldrich) after 32 days of culture for 1 hour under rotation. Cells within the hydrogels were permeabilised with 2mM Sodium Chloride (NaCl), 1.5 mM Magnesium Chloride (MgCl₂), 16 mM Sucrose and 0.5% Triton-X100 in PBS (all from Sigma-Aldrich) for 10 mins at 4°C under rotation and washed in PBS 3 times. Hydrogel constructs were covered with a 10% bovine serum albumin (BSA) / 3% normal goat serum (NGS) (Jackson Immunoresearch) blocking solution for 1 hour under rotation before incubation with monoclonal anti-DMP1 antibody at a dilution of 1:100 at 4°C overnight (Clone 8G10.3, Millipore). After washing 3 times with 1% BSA/PBS solution, samples were then treated with a Dylight™ 549 conjugate goat anti-mouse secondary antibody at a dilution of 1:100 (Jackson Immunoresearch) for 1 hour under rotation at room temperature. After secondary staining, samples were rinsed 3 times with 1%

BSA/PBS solution. Hydrogels were then further counterstained with phalloidin-FITC at 1.25 μ g/mL (diluted 1:400, Sigma Aldrich) to stain the actin cytoskeleton and DAPI dilactate (diluted 1:2000, Sigma Aldrich) to stain the nucleus and rinsed again with 1% BSA/PBS solution. Confocal scans were taken using a confocal microscope (Olympus Fluoview) at 20x, 40x and 60x magnification. Maximum intensity images were generated from z-stacks taken at 20x magnification with a distance of 5 μ m between each slice for a thickness of 25 μ m, while 40x and 60x magnification z-stacks were taken at a distance of 2.5 μ m between each slice for a thickness of 10 μ m. All stacks were obtained at the same intensity setting between groups.

As a control a demineralised bovine core was stained for DMP-1. Briefly, slides were dewaxed overnight at 60°C and then in Xylenes (Sigma Aldrich), three times for 5 min each. Slides were then rehydrated in decreasing grades of ethanol (100, 90, 70, 50, 30%; Fisher Scientific), twice for 2 min each, and rinsed in deionised water. Antigen retrieval was performed using proteinase K (20 μ g/mL, Sigma Aldrich), in Tris EDTA buffer (TE; 50 mM Tris base (Sigma Aldrich), 1 mM EDTA, 0.5% TritonX-100 (Sigma Aldrich), pH = 7.5), for 10 min at 37°C, followed by 10 min cooling and rinsing twice for 2 min each in PBS-Tween (Sigma Aldrich) 0.5% v/v. DMP-1 staining was carried out using the method described above. NIH ImageJ software was used to quantify DMP-1 staining of images. Images were thresholded between 40-255 and converted to binary to determine the area of staining within a 1024 x 1024 pixel image. Percentage area of staining was determined.

6.2.6 Extracellular ALP activity

Extracellular alkaline phosphatase (ALP) activity was determined using a colorimetric assay of enzyme activity (SIGMAFAST *p*-NPP Kit, Sigma Aldrich), which uses *p*-nitrophenyl phosphate (*p*NPP) (nmol) as a phosphatase substrate, with ALP enzyme (Sigma Aldrich) as a standard. After 32 days constructs were removed from bioreactors and placed in 24-well plates containing culture media. Constructs were left for 2 hours to incubate before media was removed, frozen and stored at -80 °C, after which 40 μ L of the medium was added to a 96-well plate in triplicate with a

50 μL of *p*NPP solution, which contains both *p*NPP and assay buffer. The samples were shielded from direct light at room temperature for one hour. After this, 20 μL of Stop Solution (3 M NaOH) was added to the wells and the plate was read at 405 nm in a Synergy HT Multi-mode microplate reader.

6.2.7 *Micro-CT*

Mineral distribution and volume after 32 days was analysed within the construct by micro-computed tomography ($\mu\text{-CT}$). Custom design holders were fabricated to hold the samples in position during scanning. Samples were immersed in PBS to prevent dehydration during scanning. Three volumes (11.40 mm^3 / section) within the construct were selected to save on scanning time. Thresholding was carried out to distinguish the porous hydrogel from the calcium produced. Below the lower thresholding limit it was found that the micro-CT was scanning the hydrogel material and therefore mineral was defined as a density threshold greater than 3089 Hounsfield units. The threshold limits were kept consistent across all samples. A Scanco Medical μCT 100 system (beam energy 45 kVp; beam intensity 200 μA , spatial resolution 5 μm) was used for evaluation.

6.2.8 *Mineralisation*

Staining for calcium deposits was carried by incubating samples within 1% Alizarin red (pH 4.3) solution for 30 minutes at 22 $^{\circ}\text{C}$ on an orbital rocker, as previously described (Tan et al. 2014). Samples were rinsed three times in deionized water and imaged on an Olympus IX50 inverted microscope.

6.2.9 *Mechanical testing*

Unconfined compressive testing was used to determine the mechanical properties of the constructs after 32 days. Mechanical testing was carried out using a biaxial tensile tester (Z009; Zwick/Roell) fitted with a 10-N load cell. Samples were held in a bath of phosphate buffered saline (PBS) during testing. Unconfined compression testing was conducted at a strain rate of 10%/min with impermeable, un-lubricated platens. The modulus was defined as the slope of a linear fit to the stress–strain curve over 2–5% strain (Harley et al. 2007). Samples were measured using Vernier callipers and cross-sectional area determined. After mechanical testing, samples

were fixed using 4% paraformaldehyde (PFA) for micro-computed tomography (μ -CT) analysis.

6.3 Results

6.3.1 Cell viability

Viability of MC3T3-E1 cells in the porous hydrogels was assessed after 32 days. Live/dead images illustrate viable cells (Green) in all groups, along with dead cells (Red), see Figure 6-2. Viable cells were observed along the surface of the pores and also encapsulated within the hydrogel. Dead cells were also observed encapsulated within the hydrogel and at the surfaces of constructs.

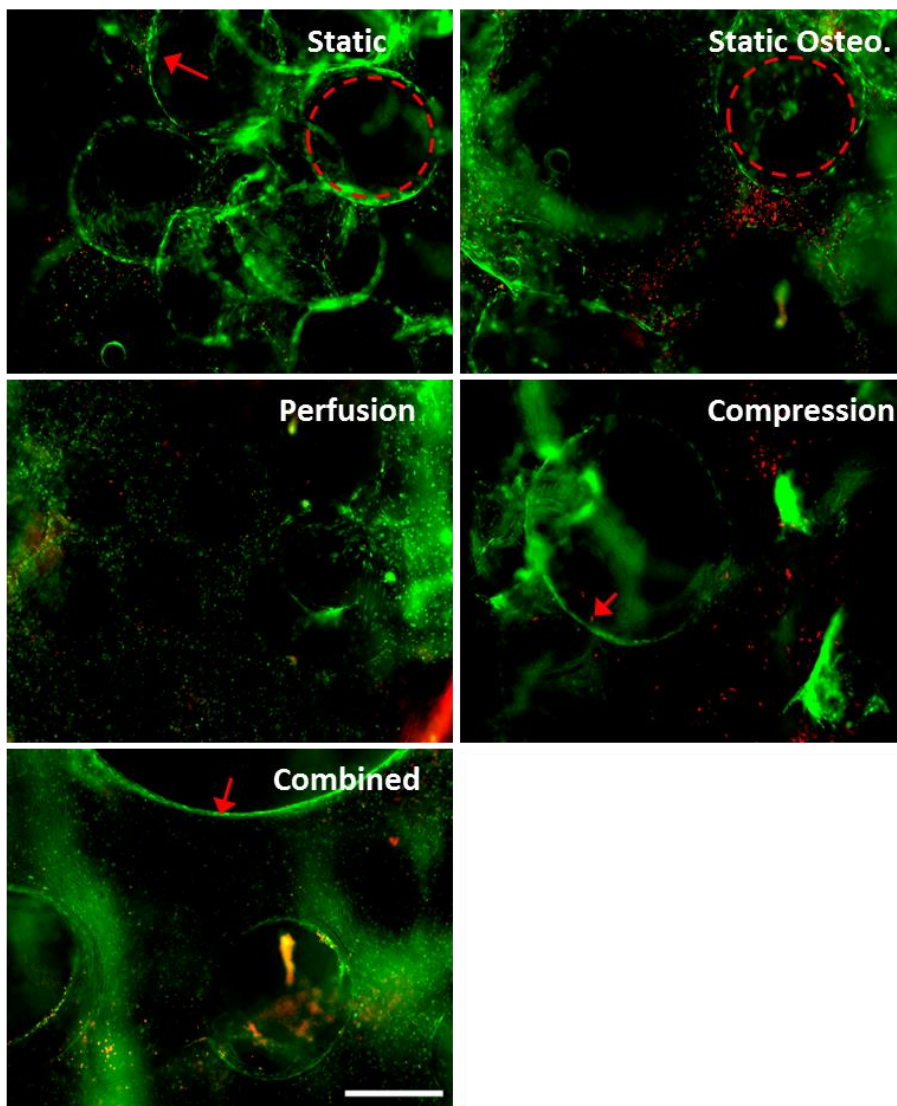


Figure 6-2: Live/dead staining showed viable cells within all groups after 32 days. Viable cells (Red arrows) were observed encapsulated in the hydrogel and on the

surface of pores (Red circle). Dead cells were observed encapsulated in the hydrogel. Calcein AM, staining live cells (Green) and Eth-1 staining dead cells (Red) (n=2). Scale bar is 500 μm

6.3.2 Cell morphology and DMP-1 immunofluorescent staining

By 32 days, for the static, static osteo. and combined groups, cells were observed to proliferate and spread over the surface of pores, while cells within hydrogels remained encapsulated in 3D hydrogel matrix, containing dendritic and spherical morphology, see Figure 6-3 and Figure 6-4 for representative images.

Immunofluorescent staining for DMP-1 showed positive expression of DMP-1 in the static, static osteo. and combined groups. However, it was observed that the intensity and distribution was increased in the combined compression-perfusion group compared to the static and osteo groups, see Figure 6-3 and Figure 6-4 (B-D). DMP-1 staining was observed within the proximity of dendritic, Figure 6-4 (B), and also around the nucleus and along dendrites, see Figure 6-4 (D). Furthermore, results for the percentage area of DMP-1 staining showed a significant difference between the static and combined groups at low and high magnifications.

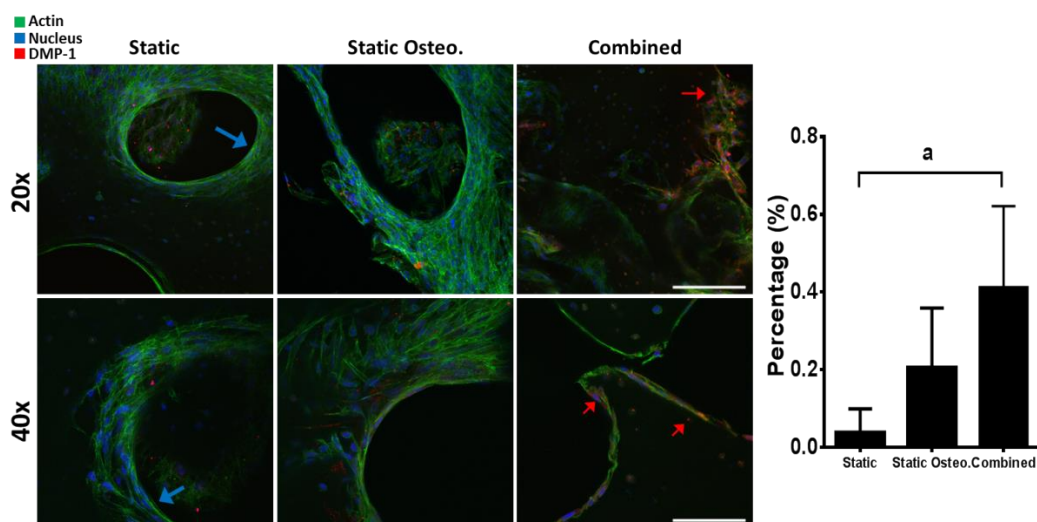


Figure 6-3: Cells within porous hydrogels were observed to proliferate and spread over the surface of pores (Blue arrows), while cells within hydrogels remained encapsulated in 3D hydrogel matrix. DMP-1 expression from cells was observed as dispersed nodules within the surrounding matrix of spread and encapsulated cells. DMP-1 staining in all groups, however a higher intensity of staining was observed in the combined group (Red arrows). Scale bar for 20x = 200 μm ; 40x = 100 μm . Quantification of DMP-1 staining.

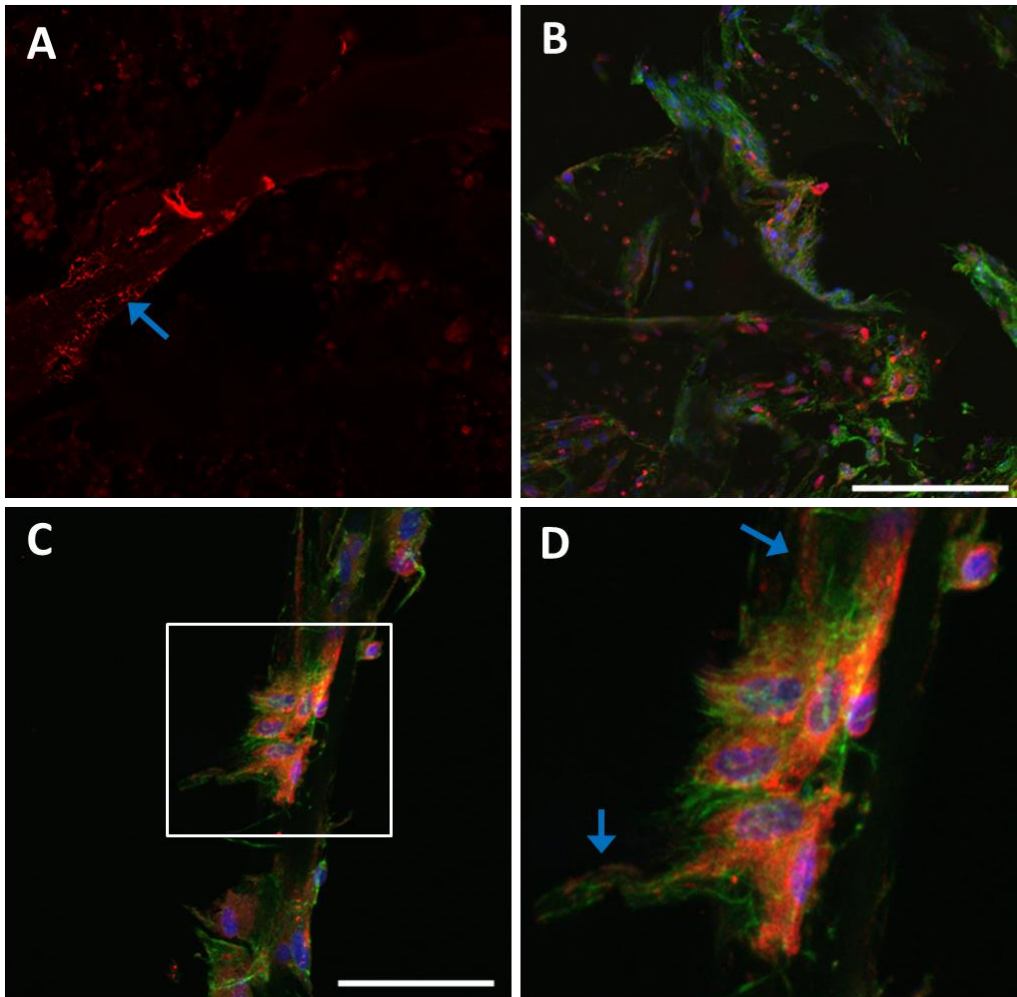


Figure 6-4: Positive control bovine sample stained for DMP-1 (A). DMP-1 expression observed in cells encapsulated in porous hydrogels subject to combined compression and perfusion stimulus, at 20x magnification (B). DMP-1 staining was observed within the proximity of dendritic cells, 40x magnification (C). DMP-1 was observed to be secret from cell nucleus and along dendrites (Blue arrows) (D). Scale bar for 20x = 200 μm ; 40x = 100 μm

6.3.3 Extracellular ALP activity

Extracellular alkaline phosphatase activity showed no significant difference between groups, see Figure 6-5.

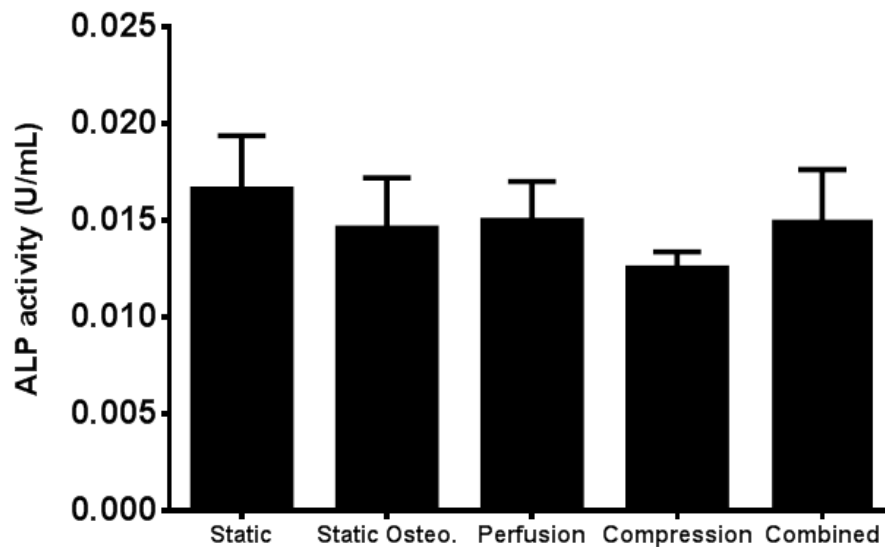


Figure 6-5: Extracellular alkaline phosphatase activity of each group (n = 6) after 32 days. No significant differences were observed between groups

6.3.4 Micro-CT

Micro-CT analysis of constructs illustrated qualitatively and quantitatively mineral content. Average mineral volume was determined within an 11.4 mm^3 section from a construct after 32 days of culture in each group, see Figure 6-6. No statistical difference observed between groups, see Figure 6-6. Quantitative values for static, static osteo, perfusion, compression and combined had average mineral volumes of 0.000056 ± 0.0001 , 0.00011 ± 0.000225 , 0.00016 ± 0.00046 , 0.00011 ± 0.00021 and $0.00011 \pm 0.00008 \text{ mm}^3$ respectively, see Figure 6-6.

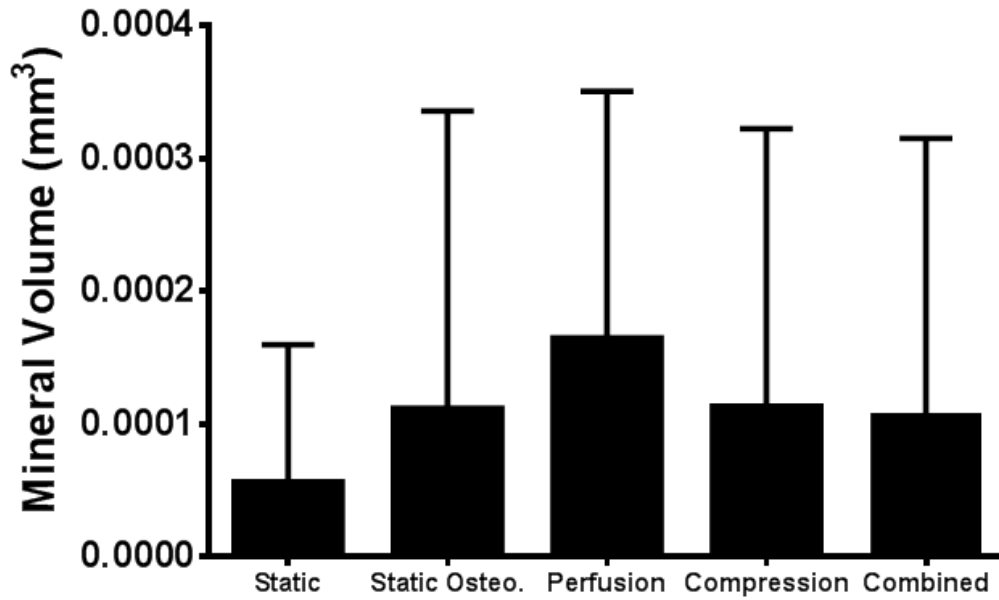


Figure 6-6: Average mineral volume within an 11.4 mm³ section from a construct after 32 days in each group determined from Micro CT scans.

Mineral distribution was observed as small particles randomly distributed throughout the 11.4 mm³ sections, see Figure 6-7. No difference was observed in mineral distribution between groups.

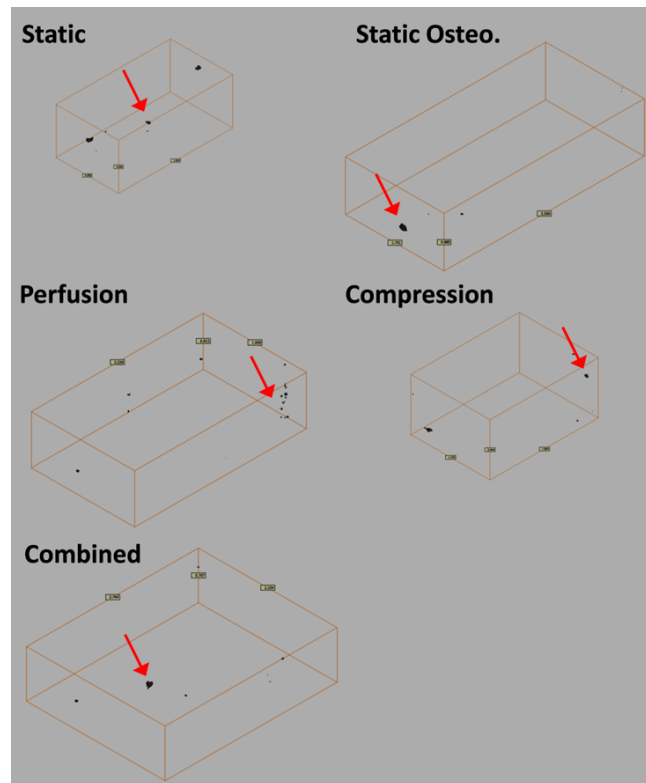


Figure 6-7: Representative micro-CT images of mineral distribution (red arrows) in an 11.4 mm³ sections after 32 days of culture in each group.

6.3.5 Mineralisation

Alizarin red staining for mineral distribution in static, static osteo, perfusion, compression and combined groups showed positive calcium staining at day 32, see Figure 6-8. Dark red patches arise from alizarin red staining of calcium deposits/nodules. Increased alizarin red staining intensity was observed in combined stimulus group compare to perfusion and compression groups. While, similar staining was observed between static, osteogenic and combined stimulus groups.

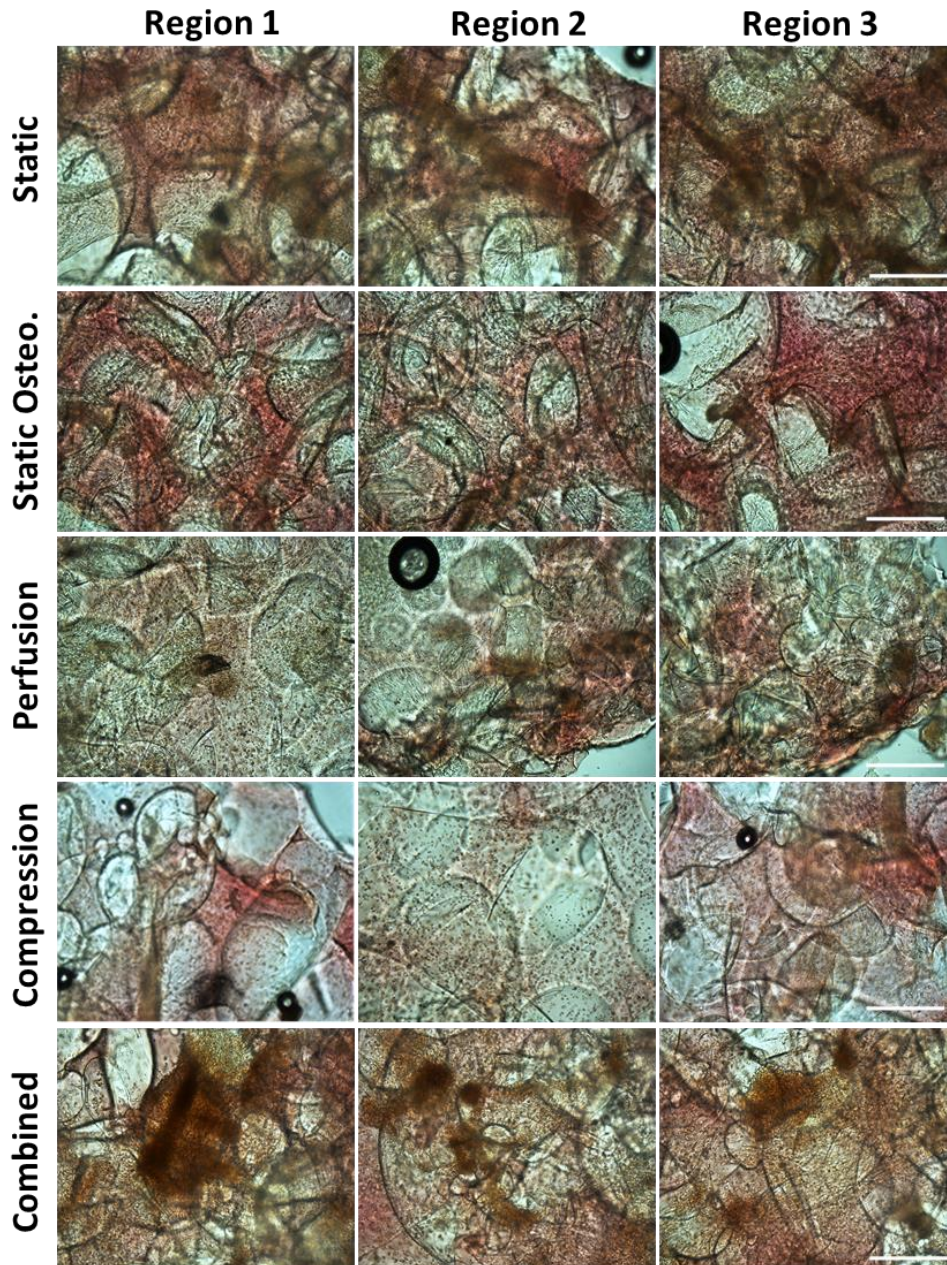


Figure 6-8: Alizarin red stain showing mineral distribution at 32 days in all groups at 20x magnification ($n = 2$). Dark red patches arise from Alizarin red staining of calcium deposits/nodules. Scale bar 200 μm .

6.3.6 Mechanical testing

Compressive testing of constructs after 32 days. No statistical difference was observed between loaded groups. However, a significant difference was observed between the combined and control groups ($p < 0.05$). Constructs cultured under static, static osteogenic, perfusion, compression and combined had compressive moduli of

0.28±0.03, 0.48±0.1, 0.4±0.08, 0.43±0.04, 0.55±0.48 and 0.51±0.16 kPa respectively, see Figure 6-9.

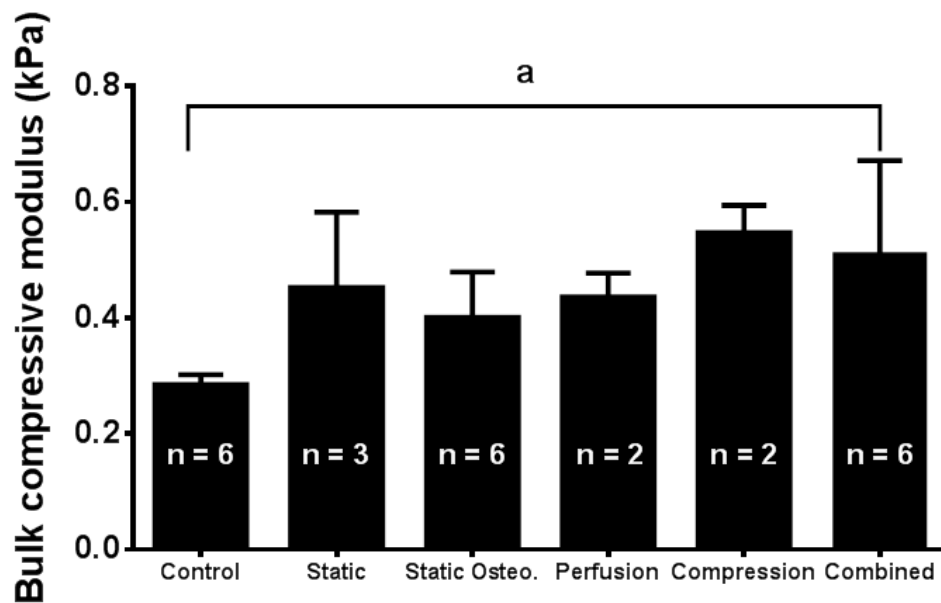


Figure 6-9: Bulk compressive modulus of control sample containing no cells and constructs in all groups after 32 days of culture. ^ap<0.05 relative to control

6.4 Discussion

This chapter investigates the effect of combined matrix stiffness, compression and perfusion stimulation on MC3T3-E1 cells encapsulated within porous gelatin-mtgate hydrogels using a custom compression-perfusion bioreactor system. The results of this study showed that applying combined compression-perfusion stimulus, specifically oscillatory cyclic fluid flow (250 $\mu\text{m/s}$) and strain (0.5%), to porous hydrogels containing encapsulated osteoblasts, promoted differentiation towards the osteocyte phenotype as indicated by DMP-1 and cell morphology. Results for DMP-1 expression in the combined stimulus group showed increased staining, compared to static constructs. Furthermore, a significant increase in mechanical properties was only observed in the combined stimulus group (0.51 kPa) compared to unseeded hydrogel samples (0.28 kPa), whereas no difference in mechanical properties was observed between unseeded, static, osteogenic, perfusion and compression groups. These findings reveal that the addition of combined stimulus to porous hydrogels

containing encapsulated MC3T3-E1 cells, promotes osteocyte development within an environment similar to trabecular bone. In contrast to other studies these results were achieved without the addition of osteogenic supplements.

As a limitation the static osteogenic group received continuous osteogenic growth factors (100 nM dexamethasone, 50 μ g/ml ascorbic acid, 10 mM β -glycerol phosphate) compared to the perfusion, compression and combined groups, which only received 1 hour of stimulus a day in standard α MEM culture medium over the 32 day culture period. Furthermore, constructs in stimulus groups (perfusion, compression and combined) were partially exposed to small air bubbles during bioreactor culture as a result of air initially trapped in the perfusion system released during system movement and entering the porous constructs. This resulted in a period of time in which the constructs contained air bubbles until dissolving at a later stage during the experiment compared to static groups, which were continuously submerged in media. This may have affected nutrients and waste exchange and also the distribution of compression and perfusion stimulus to the global construct during the early stage of the experiment. Furthermore, DMP-1 staining was carried out on the combined stimulus constructs due to the significant increase in compressive modulus compared to the unseeded hydrogel samples, while static and static osteogenic groups were selected as controls. There were low sample numbers ($n = 2$) for mechanical testing of two groups, the perfusion and compression groups, due to the loss of samples as a result of an infection during culture. However, these groups are not of particular interest, as they were included as controls to compare to the combined stimulus group, while the low sample number still allowed for comparison between groups. Additionally, static controls were not cultured under the same conditions as stimulated samples loaded within the bioreactor environment, due to the requirement of extra bioreactors. Also, two different oscillatory frequencies were selected for perfusion (1 Hz) and compression (0.5 Hz), due to an operation limitation of the bioreactor system. This may affected the distribution of stimulus to cells within the constructs. Finally, quantification of alizarin red staining for mineralisation was deemed impractical due to the large amount of diffuse staining of the label in images. Nonetheless, the results of this study showed that osteoblast and

osteocyte differentiation was promoted within a porous construct subject to combined perfusion and compression stimulus.

In vivo, the dynamic relationship between fluid flow and matrix strain in porous trabecular-like bone, plays an important role in osteogenic differentiation and directing osteocyte activity (Chan et al. 2009; Vazquez et al. 2014; You et al. 2001; Bacabac et al. 2004; Owan et al. 1997; Smalt et al. 1997; Keogh et al. 2011; Jaasma et al. 2008; Ban et al. 2011; Gomes et al. 2003; Bancroft et al. 2002; Cartmell & Porter 2003; Grayson et al. 2011). Studies have previously shown the significance of fluid flow (shear stress) in osteoblast activation (Bacabac et al. 2004), osteogenic response (Grayson et al. 2011) and differentiation towards the osteocyte phenotype (Zhang et al. 2006). Similarly, matrix strain applied to osteoblast cells has been shown to promote osteogenic differentiation (Matziolis et al. 2011), matrix formation (Sittichockechaiwut et al. 2009) and also maintaining the osteocyte phenotype (Vazquez et al. 2014). However, few studies have provided evidence of the beneficial effects of applying combined compression and fluid flow to TE scaffolds. Bouet et al revealed by combining perfusion (2 $\mu\text{L}/\text{min}$) and compression (4 μm amplitude, at 3 Hz) stimulus to ceramic scaffolds seeded with mouse calvarial cells, promoted osteoblast differentiation and the formation of a mineralised matrix (Bouet et al. 2015). While, Liu et al applied compression (10% strain, 0.5 Hz, 4 times/day, 2 h/time with 4 h of rest thereafter) and perfusion (10 ml/min) loading to polyurethane-based meniscus scaffolds seeded with human bone mesenchymal stromal cells (Liu et al. 2012). It was found that combined stimulus enhanced the functional properties (equilibrium modulus, tensile modulus and type III collagen) of constructs (Liu et al. 2012). However, none of these studies demonstrated osteoblast-osteocyte differentiation using combined matrix stiffness and compression-perfusion stimulus. In the current study it was shown that combined oscillatory compression-perfusion stimulus applied to porous gelatin-mtgase hydrogels, containing encapsulated osteoblasts, promoted osteocyte differentiation, as indicated by DMP-1 expression and cell morphology after 32 days. Furthermore, results for compressive modulus showed that any of the individual stimuli on their own (matrix stiffness, perfusion or compression) did not result in a significant change in mechanical properties compared to un-seeded samples. However, it was only by combining the three

stimuli that a significant difference in mechanical properties was achieved compared to un-seeded samples.

In vivo, osteoblast-osteocyte differentiation is a complex process induced during the early stage of bone remodelling (Takano-Yamamoto 2014; van Oers et al. 2015). During the laying down of new tissue some of the mature osteoblasts become embedded in the collagen matrix (osteoid) (Landis et al. 1996; Barragan-Adjemian et al. 2006; Dallas & Bonewald 2010). The combination of biophysical cues from the newly generated ECM and the extrinsically applied mechanical loading promotes the osteoblast to undergo a dramatic phenotypic transition to a dendritic shape, expressing DMP-1 and mineral (Dallas & Bonewald 2010; Barragan-Adjemian et al. 2006; Cowin 1989; Knothe Tate et al. 2004; Palumbo et al. 2004). In the present study, oscillatory compression-perfusion loading applied to the scaffold structure creates load-induced fluid flow and strain within the porous hydrogel containing encapsulated osteoblasts. It is proposed that the mechanical properties of the hydrogel matrix and the addition of combined oscillatory stimulus provide similar extracellular mechanical cues, both matrix-derived and extrinsically applied, promoting osteoblast-osteocyte differentiation.

Bioreactor technology provides a method of applying dynamic stimulus, such as perfusion or compressive loading to 3D bone scaffolds combined with cells (Liu et al. 2012; Bouet et al. 2015; Sittichockechaiwut et al. 2009; Matziolis et al. 2011; Keogh et al. 2011; Jaasma et al. 2008; Ban et al. 2011; Owan et al. 1997; You et al. 2001; Smalt et al. 1997; Gomes et al. 2003). However, existing systems do not precisely translate the *in vivo* physical environment to the appropriate range of stimulus (shear stress and strain) required in TE porous scaffolds to promote osteogenic differentiation and tissue formation (Keogh et al. 2011; Sittichockechaiwut et al. 2009). But, through multiphysics modelling a combination of perfusion (250 $\mu\text{m/s}$) and compression (0.5%) was determined to ensure the desired level of mechanical stimulus was applied to cells within porous scaffolds (Zhao et al. 2015; Zhao et al. 2014). For the first time the bioreactor system used in this study allows for combined stimulus (fluid flow (0.03 mL/min) and matrix strain (0.5%)) to be applied simultaneously each day to porous constructs containing encapsulated osteoblast cells. Furthermore, after 32 days cell viability within

constructs was maintained at a low flow rate of 0.05 mL/min in all groups, as indicated by Live/Dead staining.

It proposed that the approach developed here provides physiologically relevant stimulus to both spread osteoblasts and 3D embedded osteocyte-like cells, while maintaining cell viability and uniform cell distribution over 32 days. Although combined stimulus constructs showed low mechanical properties (0.51 kPa) for use in tissue engineering application, to create a bone tissue graft requires the accommodation of osteocytes within constructs. It is postulated that, with a longer culturing time, tissue formation and mineralisation would further increase the constructs overall mechanical properties. Future TE approaches could apply this method to develop bone constructs containing osteocytes within a porous environment similar to trabecular bone, directing faster host integration, tissue formation and vessel infiltration. This represents an opportunity for the development of functional bone tissue substitutes and the treatment of bone diseases such as osteoporosis.

6.5 Conclusion

In this study, compression and perfusion mechanical stimuli was experimentally applied to cell-encapsulated porous hydrogels using a custom made bioreactor. Computational models developed by Zhao et al, determined that combined perfusion (250 $\mu\text{m/s}$) and compression (0.5%) was required to mechanical stimulate cells within porous scaffolds. The results of this study showed that applying combined compression-perfusion stimulus under oscillatory fluid flow (0.03 mL/min) and strain (0.5%) to porous hydrogels containing encapsulated osteoblasts promoted differentiation towards the osteocyte phenotype as indicated by DMP-1 expression and cell morphology. Furthermore, the combined stimulus constructs showed increase mechanical properties (0.51 kPa) compared to unseeded hydrogel samples (0.28 kPa). These findings reveal that the addition of combined stimulus to porous hydrogels containing encapsulated MC3T3-E1 cells promotes osteocyte development, along with mineralisation and enhanced mechanical properties, within an environment similar to trabecular bone. These results were achieved without the addition of osteogenic supplements. In summary, this study has potential for the

development of porous constructs containing osteocytes, essential regulators of long-term bone maintenance and consequently the availability of treatments for bone diseases such as osteoporosis.

Chapter 7: Discussion and Conclusion

7.1 Introduction

This chapter summarises the main findings of this thesis, bringing together the insight acquired from the *in vitro* studies performed and the bioreactor based approaches implemented. The relationship amongst the separate chapters of this thesis and previous important publications are graphically represented in a flow chart in Figure 7-1 and are further discussed in Section 7.2. Finally, recommendations are made for future work in bone mechanobiology and the field of tissue engineering.

7.2 Main findings of the thesis

The research conducted in this PhD Thesis has sought to identify whether an *in vitro* bone tissue approach that promotes osteoblast development within a porous trabecular-like structure, can enhance osteocyte differentiation, tissue formation and mechanical properties. In particular the results from this Thesis sought to determine the effect of a 3D cell environment, extracellular matrix (ECM) stiffness and cell density on osteoblast-osteocyte differentiation *in vitro*. Furthermore, the effect of delayed osteogenic differentiation, scaffold stiffness and 3D scaffold porosity on cell distribution, mineralisation and the formation of an osteoblast-osteocyte network were investigated. *In vitro* experimental approaches were conducted to develop porous TE constructs containing 3D environments for both osteoblasts and osteocytes. Finally, to examine the effect of combined matrix stiffness, compression and perfusion mechanical stimuli on osteoblast and osteocyte differentiation within a porous TE scaffold. This required the design and fabrication of a compression-perfusion bioreactor system capable of applying combined compression and perfusion stimulus to TE scaffolds. The key contributions of each hypothesis are summarised below.

Hypothesis 1: Osteocyte differentiation is regulated by ECM stiffness and cell density within a 3D environment (Chapter 3).

The first study, presented in Chapter 3 of this Thesis, demonstrated that both the mechanical properties of the ECM and the ability for cells to establish a communication network within a 3D environment, play a significant role in osteocyte differentiation and the formation an interconnected network. It was found that osteocyte differentiation and the formation of an interconnected network between dendritic cells was significantly increased within low stiffness 3D matrices at high cell densities, compared to cells within high stiffness matrices at a low cell densities. Moreover, this network was interconnected, expressed DMP-1 and also connected with osteoblast-like cells at the matrix surface. As such, the results confirm the Hypothesis that osteocyte differentiation is regulated by ECM stiffness and cell density within a 3D environment.

Hypothesis 2: Initial cell distribution and stiffness in 3D will promote uniform cell distribution and subsequent tissue formation throughout TE scaffolds

Hypothesis 3: Porous gelatin scaffolds represent the structurally different mechanical environments of trabecular bone in vivo (pores and struts), promoting both osteoblast and osteocyte development

The second study, presented in chapter 4 of this thesis, demonstrated that the addition of porosity to hydrogels containing encapsulated cells, allowed for the homogenous distribution of osteoblast and osteocytes cells in 3D environments. It was found that porous gelatin-mtgase hydrogels provided a surface area for MC3T3-E1 cells to migrate out of the gel and spread over a flat 2D surface, while also maintaining cells surrounded by a 3D matrix, representing both osteoblast and osteocyte cells, as indicated by DMP-1 expression and mineralisation. The results of this chapter support the hypothesis that porous gelatin scaffolds can promote both osteoblast and osteocyte differentiation within a trabecular-like scaffold.

Hypothesis 4: Combined compression and perfusion mechanical stimuli will promote both osteoblast and osteocyte differentiation

The final study of this Thesis, investigated whether applying combined matrix stiffness, compression and perfusion stimulus to cell-seeded scaffolds may generate osteocytes in a porous trabecular-like scaffold. The results of this study showed that applying combined oscillatory compression-perfusion stimulus to porous hydrogels containing encapsulated osteoblasts, led to osteocyte differentiation as indicated by cell morphology, DMP-1 expression and mineralisation. Furthermore, combined stimulus constructs showed increased mechanical properties, compared to unseeded hydrogel constructs, whereas no difference in mechanical properties was observed between unseeded, static, osteogenic, perfusion and compression groups. Together, these results indicate that combined stimulus promotes osteocyte development and as such corroborated Hypothesis 4.

These findings are further considered in the context of the current understanding of bone tissue engineering, and the optimum conditions needed to design a construct that will rapidly heal bone defects.

7.3 Implications for the fields of bone mechanobiology and bone tissue engineering

The findings of this thesis have important implications for the field of bone mechanobiology and tissue engineering to reproduce bone constructs with an osteoblast and osteocyte network in place, within a trabecular-like structure, representing an essential component in the treatment of diseases such as osteoporosis. To date, various *in vitro* bone TE approaches, including porous biomaterial scaffolds (Keogh, O'Brien, et al. 2010; Gleeson et al. 2010; Curtin et al. 2012; Correia et al. 2012), cellular aggregates (Freeman et al. 2015; Fuchs et al. 2007; Rouwkema et al. 2006), cell encapsulation within hydrogels (Castillo Diaz et al. 2014; Tan et al. 2014; Chatterjee et al. 2010; Shin et al. 2014), and bioreactor based approaches (Matziolis et al. 2011; Sittichokechaiwut et al. 2009; Bouet et al. 2015; Chunqiu et al. 2008; Liu et al. 2012; Keogh et al. 2011; Jaasma et al. 2008; Ban et al. 2011) have shown potential for bone regeneration. Recently researchers have sought to promote osteoblast and osteocyte differentiation using biomaterial approaches (Mullen et al. 2013; Gerald J Atkins et al. 2009; Uchihashi et al. 2013; Woo et al. 2011; Boukhechba & Balaguer 2009; Keogh, O'Brien, et al. 2010;

Gleeson et al. 2010; Curtin et al. 2012; Correia et al. 2012; Tan et al. 2014) or through the application of mechanical stimulus (Keogh et al. 2011; Jaasma et al. 2008; Ban et al. 2011; Owan et al. 1997; You et al. 2001; Smalt et al. 1997; Gomes et al. 2003; Sikavitsas et al. 2005; Bancroft et al. 2002; Cartmell & Porter 2003; Grayson et al. 2011; Bacabac et al. 2004; Zhang et al. 2006; Matziolis et al. 2011; Sittichokechaiwut et al. 2009; Vazquez et al. 2014; Bouet et al. 2015; Chunqiu et al. 2008; Liu et al. 2012). Each of these studies have progressed the understanding of *in vitro* factors that can govern osteoblasts and osteocyte development in TE scaffolds, and key studies that preceded this thesis are summarised in the context of the studies from this thesis in Figure 7-1.

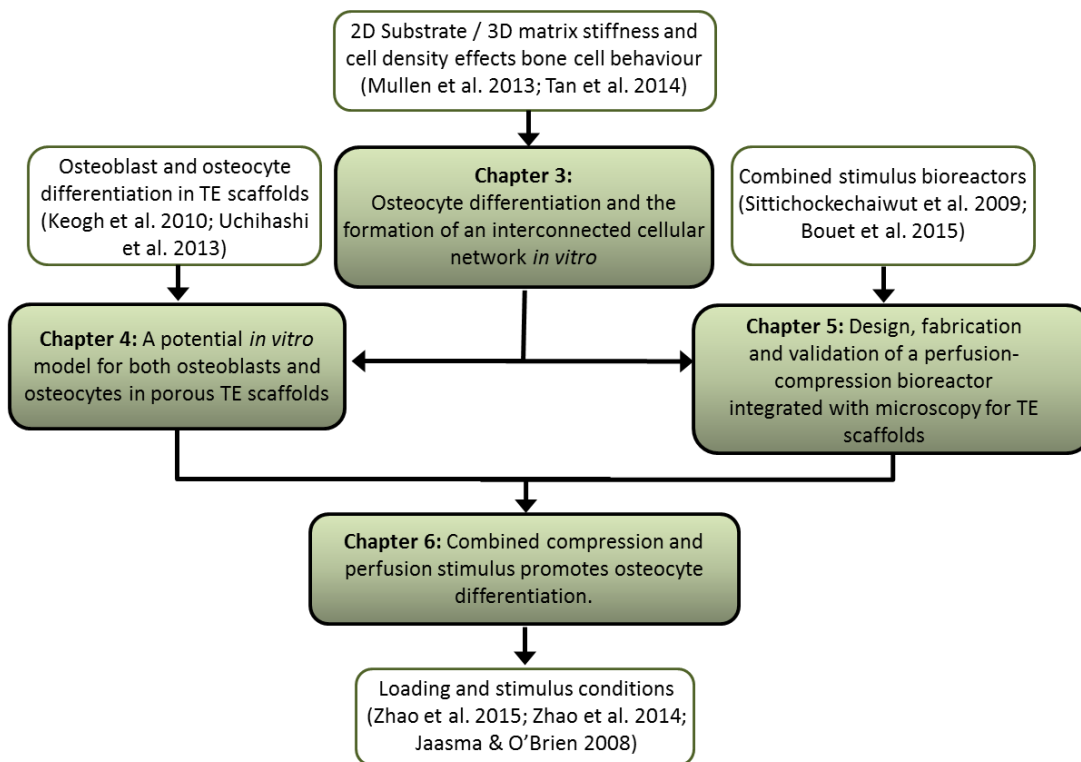


Figure 7-1: Graphical illustration of the work conducted as part of this thesis with respect to key studies used in hypotheses formation.

Prior to this thesis, a study investigated the importance of 2D substrate stiffness in regulating pre-osteoblast to early osteocyte transition (Mullen et al. 2013). It was reported that 2D culture of pre-osteoblastic cells seeded on relatively soft collagen substrates was shown to favour osteocyte differentiation (0.286 kPa) (Mullen et al. 2013), whereas a separate study reported that culturing on a more rigid substrate (20-

40 kPa) led to osteogenic differentiation (Engler et al. 2004). Additionally, the important role of cell separation density in osteocyte formation was highlighted previously (Mullen et al. 2013; Mc Garrigle et al. 2016). A low cell seeding density increases dendrite formation and osteocytic phenotype compared to a high cell density encouraging the osteoblastic phenotype (Mullen et al. 2013). Tan et al, demonstrated that 3D matrix stiffness was an essential physical factor to prompt a phenotypic shift towards osteogenic differentiation, while also providing a method to encapsulate cells at varied matrix stiffness within a 3D environment (Tan et al. 2014). Mouse myoblast cells encapsulated within gelatin-mtgase hydrogels (1.58/32.32 kPa) were elicited to differentiate towards osteoblasts (Tan *et al.*, 2014). While varying matrix stiffnesses resulted in osteoblast-like cells extending in length at stiffnesses of 1.58 kPa, but were spherical at higher stiffnesses (32.32 kPa) (Tan *et al.*, 2014). The results of chapter 3 demonstrated for the first time osteoblast-osteocyte differentiation is controlled by external biophysical and biochemical cues, such as matrix stiffness and cell density in a 3D environment. After 56 days osteoblast cells within a soft 3D matrix were induced to undergo osteocyte differentiation and form an interconnected network, along with the establishment of a confluent osteoblast layer over the surface. Future TE approaches could apply this method to develop bone constructs with an osteocyte network in place.

Bone cells can either be seeded in porous scaffolds (A.R. Amini et al. 2012; Wu et al. 2014; Barbetta et al. 2010; Duffy et al. 2011) or encapsulated in a 3D matrix (hydrogels) (Nicodemus & Bryant 2008; Zisch et al. 2003; Chiu et al. 2011; Sutter et al. 2007). Peripheral seeding or cell encapsulation represents the two methods of combining cells with scaffolds, with both methods determining initial cell distribution and morphology. However, in peripheral seeding as the construct size increases, the ability to achieve a fully cell populated and uniform construct is impaired. This is due to the time required for cells to proliferate throughout the construct (Arano et al. 2010; Gardel et al. 2013) and also the occurrence of higher cell proliferation around the periphery where nutrients are readily available (Gardel et al. 2013; Holy et al. 2000; Arano et al. 2010; Ishaug-Riley et al. 1998; Keogh et al. 2011). Others have shown that encapsulating cells within hydrogels leads to the surrounding of the cells within in a 3D matrix (Nicodemus & Bryant 2008; Zisch et al. 2003; Chiu et al. 2011; Sutter et al. 2007). *In vivo*, this 3D geometry is relevant

for osteoblast-osteocyte differentiation, but is unnatural for bone matrix-secreting osteoblasts, which spread out over the surface of bone (Franz-Odenaal et al. 2006). Despite gaining an understanding of the role of matrix stiffness and seeding density, from the PhD studies in chapter 3 and other important studies (G J Atkins et al. 2009; Uchihashi et al. 2013; Castillo Diaz et al. 2014; Chatterjee et al. 2010; Amini & Nair 2012; Mc Garrigle et al. 2016; Gerald J Atkins et al. 2009; Hwang et al. 2011; Maia et al. 2014) an approach was needed to promote 3D cell environments, but also to allow for cells to spread on the surfaces of porous scaffolds, thereby creating an appropriate environment for both osteoblast and osteocyte development. Chapter 4 investigated different methods to achieve these goals and address the deficit of knowledge. This study demonstrated for the first time that cellular encapsulation within a porous gelatin-mtgate hydrogels provided a surface area for MC3T3-E1 cells to migrate out of the hydrogel, forming a confluent layer over the surface, while also maintaining cells surrounded by a 3D matrix within a porous trabecular-like structure. Through this method future bone constructs containing both osteoblasts and osteocytes within a porous trabecular-like environment, could be developed.

Osteocytes play a key role in bone remodelling process by directing the activity of osteoblasts and osteoclasts to regulate bone resorption and formation (Rauh & Milan 2011; Wittkowske et al. 2016; Stops, Heraty, et al. 2010; McNamara 2011; Burger & Klein-Nulend 1999; Schaffler et al. 2014; J. Klein-Nulend et al. 1995; J Klein-Nulend et al. 1995). Studies have shown that *in vivo* osteoblasts and osteocytes experience wall shear stress and matrix strain (Chan et al. 2009; Wittkowske et al. 2016; Keogh et al. 2011; Jaasma et al. 2008; Ban et al. 2011; Owan et al. 1997; You et al. 2001; Smalt et al. 1997; Gomes et al. 2003; Zhang et al. 2006; Klein-Nulend et al. 2012; Saunders et al. 2006; Bacabac et al. 2004). The dynamic relationship between matrix strain and fluid flow in porous trabecular-like bone, plays an important relationship in both osteoblast and osteocyte development and hence bone formation and resorption (Chan et al. 2009; Vazquez et al. 2014; You et al. 2001). However, approaches in TE have not simultaneously replicated these loading conditions within porous scaffolds containing osteogenic cells (Mc Garrigle et al. 2016; Gerald J Atkins et al. 2009; Uchihashi et al. 2013; Franz-Odenaal et al. 2006; Keogh et al. 2011; Sittichockechaiwut et al. 2009). Studies

have implemented bioreactor technology as a method to apply dynamic compression or perfusion stimulus to porous TE constructs (Sladkova & de Peppo 2014; Jaasma et al. 2008; Sittichokechaiwut et al. 2009). The experimental work from Chapters 4, 5 and 6 aimed to develop an experimental model to recapitulate combined strain and shear stress stimulus and apply this stimulus range to the porous constructs developed in chapter 4, addressing this deficit in knowledge. As part of chapter 5, a bioreactor system capable of applying *in vivo* levels of fluid perfusion and mechanical compression to bone constructs, with the capability of real time monitoring of cell behaviour and tissue formation was fabricated and tested. The results from Chapter 6 indicated that applying combined oscillatory compression-perfusion to porous hydrogels containing encapsulated osteoblasts led to osteoblast-osteocyte differentiation, as indicated by DMP-1 and mineralisation. Furthermore, compressive modulus results showed that any of the individual stimuli on their own (matrix stiffness, perfusion or compression) did not lead to a significant change in mechanical properties compared to un-seeded samples. Yet, by combining the three stimuli a significant difference in mechanical properties was achieved compared to un-seeded samples. Taken together, the results of this Thesis found that combining matrix stiffness and cell density promotes both osteoblast and osteocyte development within porous trabecular-like constructs.

Osteoblasts and osteocytes play a key role in the regulation of bone resorption and formation (Matassi et al. 2011). Currently, a large number of bone tissue engineering studies have been carried out using TE scaffolds combined with cells in clinical applications (Marcacci et al. 2007; Quarto et al. 2001; Springer et al. 2006; Schimming & Schmelzeisen 2004; Shayesteh et al. 2008; Pradel et al. 2006; Meijer et al. 2007; Meijer et al. 2008; d'Aquino et al. 2009; Vacanti 2001). However, no study has succeeded in tissue engineering a bone construct containing both osteoblast and osteocyte within a porous trabecular-like structure. The separate studies reported in this Thesis built upon these previous studies and provided a novel insight into the effect of different 3D environments (e.g. porous and hydrogel scaffolds), matrix stiffness, cell density, distribution and mechanical stimulus on osteoblast and osteocyte development. Furthermore, a bioreactor system was designed and fabricated to apply combined perfusion and compression stimulus to

TE constructs. When examined collectively, the findings of this thesis provide a novel understanding into integrating osteoblast and osteocytes into future porous constructs, see Figure 7-2 for a graphical representation.

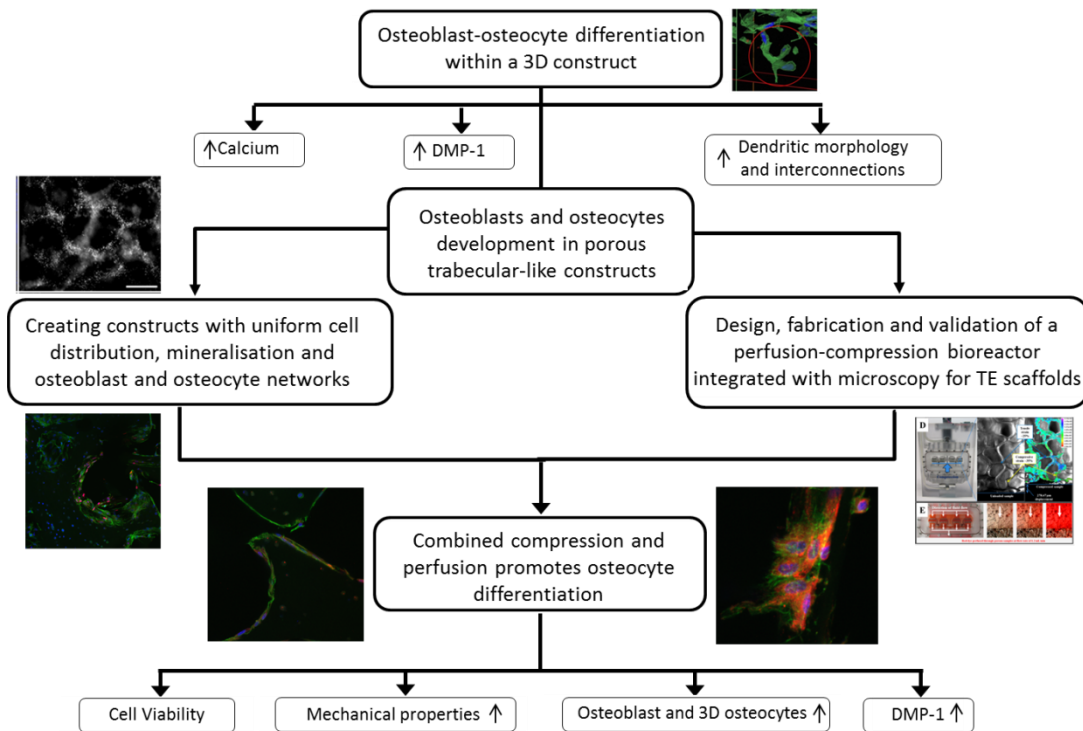


Figure 7-2: Graphical representation of thesis findings, which developed osteoblast-osteocyte networks in 3D constructs and applied mechanical stimulus to porous trabecular-like constructs, ultimately promoting both osteoblast and osteocyte differentiation as determined from chapters 3, 4, 5 and 6.

7.4 Future Work

These studies provide a novel insight into the mechanobiology of osteoblast-osteocyte differentiation and the optimum conditions needed to promote osteoblast and osteocyte development in bone TE scaffolds. Furthermore, the bioreactor system may provide an experimental model to apply physiologically relevant compression and perfusion stimulus to constructs *in vitro*. Based on the findings of this Thesis the following recommendations are made for future research;

7.4.1 Combine low and high matrix stiffness in cell encapsulated hydrogels

As discussed in chapter 3, osteoblast-osteocyte differentiation is increased within a low stiffness hydrogel (0.58 kPa) at a high cell density (2×10^6 cells/mL). While,

chapter 4 illustrated a method of recreating a homogenous distribution of spread osteoblasts and 3D embedded osteocytes within porous hydrogels. However, at low matrix stiffness, hydrogels have weak mechanical properties, making them difficult to handle. Future approaches could focus on improving the overall bulk mechanical properties of constructs by combining the low stiffness gelatin-mtase hydrogels (0.58 kPa) used in this study with high stiffness hydrogels such as poly(ethylene glycol) dimethacrylate (PEGDM) (300 kPa) (Chatterjee et al. 2010). This could be achieved through 3D printing of multiple hydrogels stiffnesses containing encapsulated cells (You et al. 2016; Kolesky et al. 2014). Kolesky et al, illustrated by using multiple printable heads and different crosslinking concentrations of gelatin metacrylate hydrogels containing encapsulated fibroblasts and Human umbilical vein endothelial cells allowed for the printing of different matrix stiffnesses and cell types into a porous scaffold structure (Kolesky et al. 2014).

7.4.2 Improvement of bioreactor operating design, usability and a larger range of tissue testing

Chapter 5 demonstrated a novel bioreactor design capable of precise control over mechanical stimulation (both fluid velocity and compression) applied to cells within 3D biomaterial scaffolds/matrices and thereby closely mimicking the *in vivo* physical environment. Furthermore, it facilitates long-term monitoring of tissue development in real time by integrating live-cell microscopy. However, further improvements and adjustments are required to make the systems more feasible within a lab environment. Future work could further develop the compression-perfusion bioreactor to a stage that it is easy to use, portable and capable of providing user feedback on construct development, mechanical properties and adjustment of operating parameters over long term culture periods. This requires focus on specific areas in the bioreactor design. The first main aspect is the improvement of the system towards faster sterilisation of parts and assembly time. This could be achieved by implementing one-off disposable sterile parts that can be incorporated into an overall system. While improved portability could be achieved through replacing the current perfusion system with a compact geared micro-pump. Furthermore, removal of air from the system during construct loading is important to avoid air bubbles been introduced into constructs during applying stimulus.

Therefore, future approaches could create an internal vacuum using the perfusion system to quickly remove air from the systems. Furthermore, monitoring changes in mechanical properties due to tissue formation in the constructs over time as tissue constructs evolve is important. This requires the development of a user feedback to facilitate long-term monitoring of tissue development in real-time, determining features such as changes in pore structure as new tissue fills the pores. This could be achieved by real-time monitoring and visualisation of samples under loading, using load cells to monitor changes in mechanical properties of constructs over time and cameras for visual inspection of the system during operation.

7.4.3 Adjustment of stimulus in conjunction with new tissue formation in scaffolds

Long term culturing of constructs results in the formation of tissue within the pores of the scaffolds. The addition of new tissue to the construct pores results in a decrease in their size and hence affects fluid velocities throughout constructs if maintained at the same flowrate. Thus, after initial tissue formation, cells might be subjected to higher stimulus outside the threshold required for osteogenic differentiation. Multiphysics computational modelling has shown this problem in 3D TE scaffolds containing different properties and structure, where adjustment of fluid perfusion and mechanical compressive was necessary to ensure the desired level of mechanical stimulation is maintained to optimise bone formation (Zhao et al. 2015; Zhao et al. 2014). Theoretical adaptive algorithms have allowed for the prediction of bone formation under mechanical stimuli and inform appropriate experimental conditions for long-term culture and bone TE applications. Future *in vitro* studies using the bioreactor designed here could investigate the predictions of the computational models and determine the required adjustment of stimulus over long term culture in TE constructs.

7.4.4 Bioreactor technology in the pharmaceutical industry

Bioreactor technology still requires further development before constructs can be used in human trials. The pharmaceutical industry represents a potentially interesting field for early stage bioreactor technology. TE constructs developed through bioreactor technology could be used for the testing of new drug treatments, large

scale drug screening, particularly to accelerate drug discovery and decrease drug development costs (Gupta et al. 2010; Jang et al. 2008; Lozito et al. 2013). Currently, the pharmaceutical industry is facing significant challenges owing to rising costs associated with existing methods of drug research and development, such as high-throughput screening of specific physiological responses in cell-based or animal models (Bhatia & Ingber 2014; W. Zheng et al. 2013). Cell-based models for drug development typically involve culturing immortalized cell lines on 2D multiwell plates (W. Zheng et al. 2013; Zang et al. 2012; Aiken et al. 2004; Quintavalle et al. 2011), which poorly represent the complex *in vivo* environment and can result in errors in predicting tissue-specific responses due to the loss of native morphology and limited cell-cell and cell-matrix interactions (Zang et al. 2012; Baker & Chen 2012; Baharvand et al. 2006; Pampaloni et al. 2007). Single-use disposable bioreactors, such as the Wave Bioreactor (GE Healthcare Life Sciences, Chicago, America), are the main technologies currently used in large scale cell growth in biopharmaceutical manufacturing (Shukla & Gottschalk 2013), representing a basic design that use rocking motion for mixing and gas transfer in cell growth. However, these devices often represent over-simplified tissue surrogates, in particular limiting the cell environment to 2D monolayers, thus restricting their potential for advanced stage testing in drug development. Bioreactor technology will enable the development of more complex tissues, which represent physiological conditions and thus can be used as surrogates for the *in vivo* environment to assess the viability of new drug treatments and accelerate drug discovery before proceeding to costly animal models or clinical trials.

7.5 Conclusion

To conclude, this Thesis has presented experimental studies throughout the course of the author's PhD studies to investigate whether an *in vitro* tissue engineering approach that applied physiologically relevant stimulus in porous trabecular-like constructs containing encapsulated pre-osteoblast cells, promoted both osteoblast and osteocyte differentiation in TE scaffolds. *In vitro* cell culture methods were used to examine the effect of EXM matrix stiffness and cell density on osteocyte differentiation of MC3T3-E1 cells within a 3D cell environment. The results from

these studies demonstrated that both the mechanical properties of ECM and the ability for cells to establish a communication network within a 3D environment, play a significant role in osteocyte differentiation and the formation of an interconnected network. Moreover, *in vitro* tissue engineering approaches were used to investigate the effect of delaying osteogenic differentiation and combining cells with hydrogels and porous 3D scaffolds on cell distribution and the promotion of both osteoblasts and osteocytes within the same construct. The results showed that porous gelatin-mtase hydrogels provide a surface area for cells to migrate out of the matrix and spread over a flat 2D surface while also maintaining cells surrounded by a 3D matrix within a porous trabecular-like structure. Finally, using a custom designed perfusion-compression bioreactor system, mechanical stimulation in the form of shear stress and strain was applied to porous hydrogels containing encapsulated osteoblasts. The results show that applying combined oscillatory compression-perfusion led to cell differentiation towards the osteocyte phenotypes and increased mechanical properties within an environment similar to trabecular bone. The results from this thesis provide a novel understanding of the conditions, environments and stimulus needed to generate porous constructs containing both osteoblast and osteocytes cells. In summary, this study has significant potential for the development of porous TE bone grafts containing osteocytes networks, essential regulators of long-term bone maintenance and consequently the availability of treatments for bone diseases such as osteoporosis.

References

- Aiken, C.T., Tobin, A.J. & Schweitzer, E.S., 2004. A cell-based screen for drugs to treat Huntington's disease. *Neurobiology of Disease*, 16(3), pp.546–555.
- Akita, S. et al., 2004. Capillary Vessel Network Integration by Inserting a Vascular Pedicle Enhances Bone Formation in Tissue-Engineered Bone. , 10(5).
- Alhag, M. et al., 2012. Evaluation of the ability of collagen-glycosaminoglycan scaffolds with or without mesenchymal stem cells to heal bone defects in Wistar rats. *Oral and maxillofacial surgery*, 16(1), pp.47–55. Available at: <http://www.ncbi.nlm.nih.gov/pubmed/21968608> [Accessed August 21, 2013].
- Ali, S. et al., 2015. The effect of Young's modulus on the neuronal differentiation of mouse embryonic stem cells. *Acta Biomaterialia*, 25, pp.253–267.
- Alsberg, E. et al., 2001. Cell-interactive alginate hydrogels for bone tissue engineering. *Journal of dental research*, 80(11), pp.2025–2029. Available at: <http://jdr.sagepub.com/cgi/doi/10.1177/00220345010800111501>.
- Amini, A.R. et al., 2012. Optimally Porous and Biomechanically Compatible Scaffolds for Large-Area Bone Regeneration. *Tissue Engineering Part A*, 18(13–14), pp.1376–1388. Available at: <http://online.liebertpub.com/doi/abs/10.1089/ten.TEA.2011.0076> [Accessed November 13, 2013].
- Amini, A.R., Laurencin, C.T. & Nukavarapu, S.P., 2012. Bone tissue engineering: recent advances and challenges. *Critical reviews in biomedical engineering*, 40(5), pp.363–408. Available at: <http://www.ncbi.nlm.nih.gov/pubmed/23339648> <http://www.pubmedcentral.nih.gov/articlerender.fcgi?artid=PMC3766369>.
- Amini, a. a. & Nair, L.S., 2012. Enzymatically cross-linked injectable gelatin gel as osteoblast delivery vehicle. *Journal of Bioactive and Compatible Polymers*, 27(4), pp.342–355. Available at: <http://jbc.sagepub.com/cgi/doi/10.1177/0883911512444713> [Accessed December 5, 2013].
- Anderson, E.J. & Knothe Tate, M.L., 2008. Idealization of pericellular fluid space geometry and dimension results in a profound underprediction of nano-microscale stresses imparted by fluid drag on osteocytes. *Journal of Biomechanics*, 41(8), pp.1736–1746.
- Anderson, J.M., 2001. Biological Responses To Materials. *Annu. Rev. Mater. Res*, 31, pp.81–110.
- Ando, W. et al., 2007. Cartilage repair using an in vitro generated scaffold-free tissue-engineered construct derived from porcine synovial mesenchymal stem cells. *Biomaterials*, 28(36), pp.5462–5470. Available at: <http://www.ncbi.nlm.nih.gov/pubmed/17854887>.
- Anselme, K., 2000. Osteoblast adhesion on biomaterials. *Biomaterials*, 21(7), pp.667–81. Available at: <http://www.ncbi.nlm.nih.gov/pubmed/10711964>.
- Arano, T., Sato, T. & Matsuzaka, K., 2010. Osteoblastic cell proliferation with uniform distribution in a large scaffold using radial-flow bioreactor. ... *Engineering Part C: ...*, 16(6), pp.1387–1398. Available at: <http://online.liebertpub.com/doi/abs/10.1089/ten.tec.2009.0377> [Accessed October 19,

2013].

- Arrington, E.D. et al., 1996. Complications of iliac crest bone graft harvesting. *Clinical orthopaedics and related research*, 329(329), pp.300–9. Available at: <http://www.ncbi.nlm.nih.gov/pubmed/21704997>.
- Atkins, G.J. et al., 2009. Strontium ranelate treatment of human primary osteoblasts promotes an osteocyte-like phenotype while eliciting an osteoprotegerin response. *Osteoporosis international : a journal established as result of cooperation between the European Foundation for Osteoporosis and the National Osteoporosis Foundation of the USA*, 20(4), pp.653–64. Available at: <http://www.ncbi.nlm.nih.gov/pubmed/18763010> [Accessed August 25, 2014].
- Atkins, G.J. et al., 2009. Vitamin K promotes mineralization, osteoblast-to-osteocyte transition, and an anticatabolic phenotype by γ -carboxylation-dependent and -independent mechanisms. *American journal of physiology. Cell physiology*, 297(6), pp.C1358–C1367. Available at: <http://www.ncbi.nlm.nih.gov/pubmed/19675304>.
- Bacabac, R.G. et al., 2004. Nitric oxide production by bone cells is fluid shear stress rate dependent. *Biochemical and Biophysical Research Communications*, 315(4), pp.823–829.
- Baharvand, H. et al., 2006. Differentiation of human embryonic stem cells into hepatocytes in 2D and 3D culture systems in vitro. *The International journal of developmental biology*, 50(7), pp.645–652.
- Baker, B.M. et al., 2015. Cell-mediated fibre recruitment drives extracellular matrix mechanosensing in engineered fibrillar microenvironments. *Nature Materials*, 14(12), pp.1262–1268. Available at: <http://www.nature.com/doi/10.1038/nmat4444>.
- Baker, B.M. & Chen, C.S., 2012. Deconstructing the third dimension: how 3D culture microenvironments alter cellular cues. *Journal of cell science*, 125(Pt 13), pp.3015–24. Available at: <http://www.pubmedcentral.nih.gov/articlerender.fcgi?artid=3434846&tool=pmcentrez&rendertype=abstract> [Accessed March 21, 2014].
- Balgude, a. P. et al., 2001. Agarose gel stiffness determines rate of DRG neurite extension in 3D cultures. *Biomaterials*, 22, pp.1077–1084.
- Ban, Y. et al., 2011. Response of osteoblasts to low fluid shear stress is time dependent. *Tissue and Cell*, 43(5), pp.311–317. Available at: <http://dx.doi.org/10.1016/j.tice.2011.06.003>.
- Bancroft, G.N. et al., 2002. Fluid flow increases mineralized matrix deposition in 3D perfusion culture of marrow stromal osteoblasts in a dose-dependent manner. *Proceedings of the National Academy of Sciences of the United States of America*, 99(20), pp.12600–5. Available at: <http://www.pubmedcentral.nih.gov/articlerender.fcgi?artid=130506&tool=pmcentrez&rendertype=abstract>.
- Barbetta, A. et al., 2010. Porous gelatin hydrogels by gas-in-liquid foam templating. *Soft Matter*, 6(8), p.1785.
- Barragan-Adjemian, C. et al., 2006. Mechanism by which MLO-A5 late osteoblasts/early osteocytes mineralize in culture: similarities with mineralization of lamellar bone.

- Calcified tissue international*, 79(5), pp.340–53. Available at: <http://www.pubmedcentral.nih.gov/articlerender.fcgi?artid=1802097&tool=pmcentrez&rendertype=abstract> [Accessed August 14, 2014].
- Behrens, B.-A. et al., 2009. Numerical investigations on the strain-adaptive bone remodelling in the periprosthetic femur: Influence of the boundary conditions. *BioMedical Engineering OnLine*, 8(1), p.7. Available at: <http://www.biomedical-engineering-online.com/content/8/1/7>.
- Bertoni, F. et al., 2006. Transglutaminase reactivity with gelatine: perspective applications in tissue engineering. *Biotechnology letters*, 28(10), pp.697–702. Available at: <http://www.ncbi.nlm.nih.gov/pubmed/16791723> [Accessed December 1, 2013].
- Bhatia, S.N. & Ingber, D.E., 2014. Microfluidic organs-on-chips. *Nature Biotechnology*, 32(8), pp.760–772. Available at: <http://www.nature.com/doi/10.1038/nbt.2989>.
- Birmingham, E. et al., 2014. Mechanical Stimulation of Bone Marrow In Situ Induces Bone Formation in Trabecular Explants. *Annals of Biomedical Engineering*. Available at: <http://link.springer.com/10.1007/s10439-014-1135-0>.
- Bitar, M. et al., 2008. Effect of cell density on osteoblastic differentiation and matrix degradation of biomimetic dense collagen scaffolds. *Biomacromolecules*, 9(1), pp.129–135. Available at: <http://www.ncbi.nlm.nih.gov/pubmed/18095652>.
- Bonewald, L.F., 2011. The amazing osteocyte. *Journal of bone and mineral research : the official journal of the American Society for Bone and Mineral Research*, 26(2), pp.229–38. Available at: <http://www.pubmedcentral.nih.gov/articlerender.fcgi?artid=3179345&tool=pmcentrez&rendertype=abstract> [Accessed July 15, 2014].
- Botchwey, 2001. Bone tissue engineering in a rotating bioreactor using a microcarrier matrix system. *Journal of Biomedical Materials Research*, 55(2), pp.242–253.
- Bouet, G. et al., 2015. Validation of an in Vitro 3D Bone Culture Model With Perfused and Mechanically Stressed Ceramic Scaffold. , 29, pp.250–267.
- Boukhechba, F. & Balaguer, T., 2009. Human primary osteocyte differentiation in a 3D culture system. *Journal of bone and mineral research*, 24(11), pp.1927–1935. Available at: <http://onlinelibrary.wiley.com/doi/10.1359/jbmr.090517/full> [Accessed October 13, 2014].
- Braccini, A. et al., 2005. Three-Dimensional Perfusion Culture of Human Bone Marrow Cells and Generation of Osteoinductive Grafts. *Stem Cells*, 23(8), pp.1066–1072. Available at: <http://dx.doi.org/10.1634/stemcells.2005-0002>.
- Brydone, a S., Meek, D. & Maclaine, S., 2010. Bone grafting, orthopaedic biomaterials, and the clinical need for bone engineering. *Proceedings of the Institution of Mechanical Engineers. Part H, Journal of engineering in medicine*, 224(12), pp.1329–1343.
- Budynas, R. & Nisbett, K., 2006. *Shigley's Mechanical Engineering Design (Mcgraw-Hill Series in Mechanical Engineering)*, McGraw-Hill Science/Engineering/Math. Available at: citeulike-article-id:2997357.
- Burger, E.H. & Klein-Nulend, J., 1999. Mechanotransduction in bone-role of the lacuno-canalicular network. *FASEB journal: official publication of the Federation of American Societies for Experimental Biology*, 13, pp.S101-12. Available at:

- <http://www.ncbi.nlm.nih.gov/pubmed/10352151>.
- Cartmell, S. & Porter, B., 2003. Effects of medium perfusion rate on cell-seeded three-dimensional bone constructs in vitro. *Tissue ...*, 9(6), pp.1197–1203. Available at: <http://online.liebertpub.com/doi/abs/10.1089/10763270360728107> [Accessed October 31, 2013].
- Castillo Diaz, L.A. et al., 2014. Human osteoblasts within soft peptide hydrogels promote mineralisation in vitro. *Journal of Tissue Engineering*, 5. Available at: <http://tej.sagepub.com/lookup/doi/10.1177/2041731414539344>.
- Chan, M.E. et al., 2009. A trabecular bone explant model of osteocyte-osteoblast co-culture for bone mechanobiology. *Cellular and Molecular Bioengineering*, 2(3), pp.405–415.
- Chao, E.Y.S. & Inoue, N., 2003. Biophysical stimulation of bone fracture repair, regeneration and remodelling. *European cells & materials*, 6(1979), pp.72-84–5. Available at: <http://www.ncbi.nlm.nih.gov/pubmed/14722904>.
- Chatterjee, K. et al., 2010. The effect of 3D hydrogel scaffold modulus on osteoblast differentiation and mineralization revealed by combinatorial screening. *Biomaterials*, 31(19), pp.5051–5062. Available at: <http://www.sciencedirect.com/science/article/pii/S0142961210003807> [Accessed October 17, 2013].
- Chen, P.-Y. et al., 2013. Fabrication of Large Perfusable Macro-Porous Cell-Laden Hydrogel Scaffolds Using Microbial Transglutaminase. *Acta biomaterialia*, (November). Available at: <http://www.ncbi.nlm.nih.gov/pubmed/24262131> [Accessed November 25, 2013].
- Chen, S. et al., 2015. Mesenchymal stem cell-laden anti-inflammatory hydrogel enhances diabetic wound healing. *Scientific Reports*, 5, p.18104. Available at: <http://www.nature.com/articles/srep18104>.
- Chiu, Y.C. et al., 2011. The role of pore size on vascularization and tissue remodeling in PEG hydrogels. *Biomaterials*, 32(26), pp.6045–6051. Available at: <http://dx.doi.org/10.1016/j.biomaterials.2011.04.066>.
- Choi, K. et al., 1990. The elastic moduli of human subchondral, trabecular, and cortical bone tissue and the size-dependency of cortical bone modulus. *Journal of Biomechanics*, 23(11), pp.1103–1113.
- Chunqiu, Z. et al., 2008. Perfusion–compression bioreactor as the optimum choice for growing large-sized engineered bone constructs in vitro. *Bioscience Hypotheses*, 1(6), pp.319–323. Available at: <http://linkinghub.elsevier.com/retrieve/pii/S1756239208001298> [Accessed July 27, 2012].
- Correia, C. et al., 2012. Development of silk-based scaffolds for tissue engineering of bone from human adipose-derived stem cells. *Acta biomaterialia*, 8(7), pp.2483–92. Available at: <http://www.pubmedcentral.nih.gov/articlerender.fcgi?artid=3367114&tool=pmcentrez&rendertype=abstract> [Accessed September 8, 2013].
- Cowin, S., 1989. *Bone Mechanics Handbook*, Available at: <http://www.getcited.org/pub/102636188> [Accessed July 3, 2012].

- Cunniffe, G.M. et al., 2010. Development and characterisation of a collagen nano-hydroxyapatite composite scaffold for bone tissue engineering. *Journal of materials science. Materials in medicine*, 21(8), pp.2293–8. Available at: <http://www.ncbi.nlm.nih.gov/pubmed/20091099> [Accessed June 28, 2013].
- Cunniffe, G.M. et al., 2015. Porous decellularized tissue engineered hypertrophic cartilage as a scaffold for large bone defect healing. *Acta Biomaterialia*, 23, pp.82–90.
- Curtin, C.M. et al., 2012. Innovative collagen nano-hydroxyapatite scaffolds offer a highly efficient non-viral gene delivery platform for stem cell-mediated bone formation. *Advanced materials (Deerfield Beach, Fla.)*, 24(6), pp.749–54. Available at: <http://www.ncbi.nlm.nih.gov/pubmed/22213347> [Accessed March 30, 2013].
- Czekanska, E.M. et al., 2012. In search of an osteoblast cell model for in vitro research. *European Cells and Materials*, 24, pp.1–17.
- d'Aquino, R. et al., 2009. Human mandible bone defect repair by the grafting of dental pulp stem/progenitor cells and collagen sponge biocomplexes. *European cells & materials*, 18, pp.75–83. Available at: <http://www.ncbi.nlm.nih.gov/pubmed/19908196>.
- d'Ortho, M.P. et al., 1998. MT1-MMP on the cell surface causes focal degradation of gelatin films. *FEBS letters*, 421(2), pp.159–64. Available at: <http://www.ncbi.nlm.nih.gov/pubmed/9468298>.
- D'Souza, R.N. et al., 1997. Gene expression patterns of murine dentin matrix protein 1 (Dmp1) and dentin sialophosphoprotein (DSPP) suggest distinct developmental functions in vivo. *J Bone Miner Res*, 12(12), pp.2040–2049. Available at: <http://www.ncbi.nlm.nih.gov/pubmed/9421236>.
- Dallas, S.L. & Bonewald, L.F., 2010. Dynamics of the transition from osteoblast to osteocyte. *Annals of the New York Academy of Sciences*, 1192, pp.437–43. Available at: <http://www.pubmedcentral.nih.gov/articlerender.fcgi?artid=2981593&tool=pmcentrez&rendertype=abstract> [Accessed August 29, 2014].
- Dallas, S.L., Prideaux, M. & Bonewald, L.F., 2013. The osteocyte: an endocrine cell and more. *Endocrine reviews*, 34(5), pp.658–90. Available at: <http://www.ncbi.nlm.nih.gov/pubmed/23612223> [Accessed August 25, 2014].
- Davies, C.M. et al., 2006. Mechanically loaded ex vivo bone culture system “Zetos”: systems and culture preparation. *European cells & materials*, 11(0), p.57–75; discussion 75. Available at: <http://www.ncbi.nlm.nih.gov/pubmed/16612792>.
- Dick, H.M. & Strauch, R.J., 1994. Infection of massive bone allografts. *Clinical orthopaedics and related research*, pp.46–53.
- Dimitriou, R. et al., 2011. Bone regeneration: current concepts and future directions. *BMC medicine*, 9(1), p.66. Available at: <http://www.pubmedcentral.nih.gov/articlerender.fcgi?artid=3123714&tool=pmcentrez&rendertype=abstract> [Accessed July 26, 2012].
- Doty, S., 1981. Morphological evidence of gap junctions between bone cells. *Calcified Tissue International*, 33(1), pp.509–512. Available at: <http://dx.doi.org/10.1007/BF02409482>.
- Du, D., Furukawa, K.S. & Ushida, T., 2009. 3D culture of osteoblast-like cells by

- unidirectional or oscillatory flow for bone tissue engineering. *Biotechnology and Bioengineering*, 102(6), pp.1670–1678.
- Ducy, P. et al., 1997. Osf2/Cbfa1: a transcriptional activator of osteoblast differentiation. *Cell*, 89(5), pp.747–54. Available at: <http://www.ncbi.nlm.nih.gov/pubmed/9182762>.
- Duffy, G.P. et al., 2011. Towards in vitro vascularisation of collagen-GAG scaffolds. *European cells & materials*, 21(1), pp.15–30. Available at: <http://www.ncbi.nlm.nih.gov/pubmed/21225592>.
- Dumas, J.E. et al., 2012. Injectable reactive biocomposites for bone healing in critical-size rabbit calvarial defects. *Biomedical materials (Bristol, England)*, 7(2), p.24112. Available at: <http://www.ncbi.nlm.nih.gov/pubmed/22456057> [Accessed November 1, 2013].
- Ebraheim, N. a, Elgafy, H. & Xu, R., 2001. Bone-graft harvesting from iliac and fibular donor sites: techniques and complications. *The Journal of the American Academy of Orthopaedic Surgeons*, 9(3), pp.210–218.
- Engler, A. et al., 2004. Substrate compliance versus ligand density in cell on gel responses. *Biophysical journal*, 86(1 Pt 1), pp.617–28. Available at: <http://www.pubmedcentral.nih.gov/articlerender.fcgi?artid=1303831&tool=pmcentrez&rendertype=abstract>.
- Engler, A.J. et al., 2006. Matrix elasticity directs stem cell lineage specification. *Cell*, 126(4), pp.677–89. Available at: <http://www.ncbi.nlm.nih.gov/pubmed/16923388> [Accessed May 23, 2013].
- Eniwumide, J.O. et al., 2007. Ectopic Bone Formation in Bone Marrow Stem Cell Seeded Calcium Phosphate Scaffolds As Compared To Autograft and (Cell Seeded). *Eerials Maturopean Cells and*, 14, pp.30–39.
- EUMUSC, 2014. Musculoskeletal Health in Europe Report v5.0. *European Musculoskeletal Health Surveillance and Infromation Network*, pp.1–13. Available at: <http://www.eumusc.net/myUploadData/files/Musculoskeletal Health in Europe Report v5.pdf>.
- Evans, N.D. et al., 2009. Substrate stiffness affects early differentiation events in embryonic stem cells. *European cells & materials*, 18, pp.1–13.
- Feng, J.Q. et al., 2002. Dentin matrix protein 1, a target molecule for Cbfa1 in bone, is a unique bone marker gene. *Journal of bone and mineral research : the official journal of the American Society for Bone and Mineral Research*, 17(10), pp.1822–31. Available at: <http://www.ncbi.nlm.nih.gov/pubmed/12369786>.
- Ferreira, J. & Padilla, R., 2013. Titanium-Enriched Hydroxyapatite – Gelatin Scaffolds with Osteogenically Differentiated Progenitor Cell Aggregates for Calvaria Bone Regeneration. ... *Engineering Part A*, 19. Available at: <http://online.liebertpub.com/doi/abs/10.1089/ten.TEA.2012.0520> [Accessed January 23, 2014].
- Frank, E.H. et al., 2000. A versatile shear and compression apparatus for mechanical stimulation of tissue culture explants. *Journal of Biomechanics*, 33(11), pp.1523–1527.
- Franz-Odendaal, T. a, Hall, B.K. & Witten, P.E., 2006. Buried alive: how osteoblasts become osteocytes. *Developmental dynamics : an official publication of the American*

- Association of Anatomists*, 235(1), pp.176–90. Available at: <http://www.ncbi.nlm.nih.gov/pubmed/16258960> [Accessed July 17, 2014].
- Freeman, F., 2013. Investigation of the optimal timing for chondrogenic priming of MSCs to enhance osteogenic differentiation in vitro as a bone tissue engineering strategy. ... *of tissue engineering* Available at: <http://onlinelibrary.wiley.com/doi/10.1002/term.1793/full> [Accessed November 26, 2013].
- Freeman, F.E., Haugh, M.G. & McNamara, L.M., 2015. An In Vitro Bone Tissue Regeneration Strategy Combining Chondrogenic and Vascular Priming Enhances the Mineralization Potential of Mesenchymal Stem Cells In Vitro While Also Allowing for Vessel Formation. *Tissue Engineering Part A*, 21(7–8), pp.1320–1332. Available at: <http://online.liebertpub.com/doi/10.1089/ten.tea.2014.0249>.
- Fröhlich, M. & Grayson, W., 2009. Bone grafts engineered from human adipose-derived stem cells in perfusion bioreactor culture. ... *Engineering Part A*, 16(1). Available at: <http://online.liebertpub.com/doi/abs/10.1089/ten.TEA.2009.0164> [Accessed February 6, 2013].
- Frost, H.M., 1990. Skeletal structural adaptations to mechanical usage (SATMU): 3. The hyaline cartilage modeling problem. *The Anatomical Record*, 226(4), pp.423–432.
- Fuchs, S., Hofmann, A. & Kirkpatrick, C.J., 2007. Microvessel-like structures from outgrowth endothelial cells from human peripheral blood in 2-dimensional and 3-dimensional co-cultures with osteoblastic lineage cells. *Tissue engineering*, 13(10), pp.2577–2588.
- Gardel, L.S. et al., 2013. A novel bidirectional continuous perfusion bioreactor for the culture of large-sized bone tissue-engineered constructs. *Journal of biomedical materials research. Part B, Applied biomaterials*, pp.1–10. Available at: <http://www.ncbi.nlm.nih.gov/pubmed/23681695>.
- Gaspar, D.A., Gomide, V. & Monteiro, F.J., 2012. The role of perfusion bioreactors in bone tissue engineering. *Biomatter*, 2(4), pp.167–175. Available at: <http://www.ncbi.nlm.nih.gov/pmc/articles/PMC3568103/>.
- Georges, P.C. et al., 2006. Matrices with compliance comparable to that of brain tissue select neuronal over glial growth in mixed cortical cultures. *Biophysical journal*, 90(April), pp.3012–3018.
- Gerhardt, L.-C. & Boccaccini, A.R., 2010. Bioactive Glass and Glass-Ceramic Scaffolds for Bone Tissue Engineering. *Materials*, 3(7), pp.3867–3910. Available at: <http://www.mdpi.com/1996-1944/3/7/3867/> [Accessed March 11, 2013].
- Gibson, L.J. & Ashby, M.F., 1990. *Cellular solids: Structure and properties*,
- Gleeson, J.P., Plunkett, N.A. & O'Brien, F.J., 2010. Addition of hydroxyapatite improves stiffness, interconnectivity and osteogenic potential of a highly porous collagen-based scaffold for bone tissue regeneration. *European cells & materials*, 20(0), pp.218–30. Available at: <http://www.ncbi.nlm.nih.gov/pubmed/20922667>.
- Gomes, M.E. et al., 2003. Effect of flow perfusion on the osteogenic differentiation of bone marrow stromal cells cultured on starch-based three-dimensional scaffolds. *Journal of biomedical materials research. Part A*, 67(1), pp.87–95. Available at:

- <http://www.ncbi.nlm.nih.gov/pubmed/14517865>.
- Grayson, W.L. et al., 2010. Engineering anatomically shaped human bone grafts. *Proceedings of the National Academy of Sciences of the United States of America*, 107(8), pp.3299–304. Available at: <http://www.pubmedcentral.nih.gov/articlerender.fcgi?artid=2840502&tool=pmcentrez&rendertype=abstract> [Accessed July 27, 2012].
- Grayson, W.L. et al., 2011. Optimizing the medium perfusion rate in bone tissue engineering bioreactors. *Biotechnology and bioengineering*, 108(5), pp.1159–70. Available at: <http://www.pubmedcentral.nih.gov/articlerender.fcgi?artid=3077473&tool=pmcentrez&rendertype=abstract> [Accessed July 27, 2012].
- Grayson, W.L. et al., 2010. Spatial regulation of human mesenchymal stem cell differentiation in engineered osteochondral constructs: effects of pre-differentiation, soluble factors and medium perfusion. *Osteoarthritis and cartilage / OARS, Osteoarthritis Research Society*, 18(5), pp.714–23. Available at: <http://www.pubmedcentral.nih.gov/articlerender.fcgi?artid=2862865&tool=pmcentrez&rendertype=abstract> [Accessed July 27, 2012].
- Grayson, W.L.W. et al., 2008. Effects of initial seeding density and fluid perfusion rate on formation of tissue-engineered bone. ... *Engineering Part A*, 14(11), pp.1809–1820. Available at: <http://www.pubmedcentral.nih.gov/articlerender.fcgi?artid=2773295&tool=pmcentrez&rendertype=abstract> [Accessed July 26, 2012].
- Grigoriadis, A.E. et al., 1985. Subclone heterogeneity in a clonally-derived osteoblast-like cell line. *Bone*, 6(4), pp.249–256. Available at: <http://www.sciencedirect.com/science/article/pii/8756328285900080>.
- Grover, C.N. et al., 2012. Crosslinking and composition influence the surface properties, mechanical stiffness and cell reactivity of collagen-based films. *Acta biomaterialia*, 8(8), pp.3080–90. Available at: <http://www.pubmedcentral.nih.gov/articlerender.fcgi?artid=3396844&tool=pmcentrez&rendertype=abstract> [Accessed March 25, 2013].
- Gunatillake, P. a & Adhikari, R., 2003. Biodegradable synthetic polymers for tissue engineering. *European cells & materials*, 5, p.1–16; discussion 16. Available at: <http://www.ncbi.nlm.nih.gov/pubmed/14562275>.
- Gupta, K. et al., 2010. Lab-on-a-chip devices as an emerging platform for stem cell biology. *Lab on a chip*, 10(16), pp.2019–2031. Available at: <http://www.ncbi.nlm.nih.gov/pubmed/20556297>.
- Hadjipanayi, E., Mudera, V. & Brown, R.A., 2009. Close dependence of fibroblast proliferation on collagen scaffold matrix stiffness. *Journal of tissue engineering and regenerative medicine*, 3(2), pp.77–84. Available at: <http://www.ncbi.nlm.nih.gov/pubmed/19051218>.
- Han, Y. et al., 2004. Mechanotransduction and strain amplification in osteocyte cell processes. *Proceedings of the National Academy of Sciences of the United States of America*, 101(47), pp.16689–94. Available at: <http://www.pubmedcentral.nih.gov/articlerender.fcgi?artid=534548&tool=pmcentrez&rendertype=abstract>.

- Hannah, K.M. et al., 2010. Bimodal distribution of osteocyte lacunar size in the human femoral cortex as revealed by micro-CT. *Bone*, 47(5), pp.866–871.
- Hansmann, J. et al., 2013. Bioreactors in tissue engineering-principles, applications and commercial constraints. *Biotechnology Journal*, 8(3), pp.298–307.
- Harley, B. et al., 2007. Mechanical characterization of collagen–glycosaminoglycan scaffolds. *Acta biomaterialia*, 3(4), pp.463–74. Available at: <http://www.sciencedirect.com/science/article/pii/S1742706107000025> [Accessed November 13, 2013].
- Harley, B. a. C. & Gibson, L.J., 2008. In vivo and in vitro applications of collagen-GAG scaffolds. *Chemical Engineering Journal*, 137(1), pp.102–121. Available at: <http://linkinghub.elsevier.com/retrieve/pii/S1385894707006055> [Accessed March 24, 2013].
- Hatori, K. et al., 2004. Osteoblasts and osteocytes express MMP2 and -8 and TIMP1, -2, and -3 along with extracellular matrix molecules during appositional bone formation. *The anatomical record. Part A, Discoveries in molecular, cellular, and evolutionary biology*, 277(October 2003), pp.262–271.
- Haug, M.G. et al., 2011. Crosslinking and mechanical properties significantly influence cell attachment, proliferation, and migration within collagen glycosaminoglycan scaffolds. *Tissue Engineering Part A*, 17. Available at: <http://online.liebertpub.com/doi/abs/10.1089/ten.tea.2010.0590> [Accessed March 19, 2013].
- Haug, M.G., 2009. *The Development of Novel Scaffolds for Tissue Engineering with a Range of Structural and Mechanical Properties*.
- Haug, M.G., Murphy, C.M. & O'Brien, F.J., 2010. Novel freeze-drying methods to produce a range of collagen-glycosaminoglycan scaffolds with tailored mean pore sizes. *Tissue engineering. Part C, Methods*, 16(5), pp.887–94. Available at: <http://www.ncbi.nlm.nih.gov/pubmed/19903089>.
- Haug, M.G., Vaughan, T.J. & McNamara, L.M., 2015. The role of integrin $\alpha V\beta 3$ in osteocyte mechanotransduction. *Journal of the mechanical behavior of biomedical materials*, 42, pp.67–75. Available at: <http://www.sciencedirect.com/science/article/pii/S1751616114003403> [Accessed January 16, 2015].
- Holmbeck, K., Bianco, P. & Pidoux, I., 2005. The metalloproteinase MT1-MMP is required for normal development and maintenance of osteocyte processes in bone. *Journal of cell ...*. Available at: <http://jcs.biologists.org/content/118/1/147.short> [Accessed August 22, 2014].
- Holy, C.E., Shoichet, M.S. & Davies, J.E., 2000. Engineering three-dimensional bone tissue in vitro using biodegradable scaffolds: investigating initial cell-seeding density and culture period. *Journal of biomedical materials research*, 51(3), pp.376–82. Available at: <http://www.ncbi.nlm.nih.gov/pubmed/10880079>.
- Home, W.C., 1995. Toward a more complete molecular description of the osteoclast. *Bone*, 17(2), pp.107–109.
- Hou, Q., Grijpma, D.W. & Feijen, J., 2003. Preparation of interconnected highly porous

- polymeric structures by a replication and freeze-drying process. *Journal of biomedical materials research. Part B, Applied biomaterials*, 67(2), pp.732–40. Available at: <http://www.ncbi.nlm.nih.gov/pubmed/14598400>.
- Huang, A.H. et al., 2010. Long-term dynamic loading improves the mechanical properties of chondrogenic mesenchymal stem cell-laden hydrogels. *European cells & materials*, 19(215), pp.72–85. Available at: <http://www.ncbi.nlm.nih.gov/pmc/articles/PMC3486923/> [Accessed November 21, 2013].
- Huebsch, N. et al., 2010. Harnessing traction-mediated manipulation of the cell/matrix interface to control stem-cell fate. *Nature materials*, 9(6), pp.518–26. Available at: <http://www.pubmedcentral.nih.gov/articlerender.fcgi?artid=2919753&tool=pmcentrez&rendertype=abstract> [Accessed December 13, 2013].
- Huebsch, N. et al., 2015. Matrix elasticity of void-forming hydrogels controls transplanted-stem-cell-mediated bone formation. *Nature Materials*, 14(12), pp.1269–1277. Available at: <http://www.nature.com/doi/10.1038/nmat4407>.
- Hwang, C.M. et al., 2013. Assessments of injectable alginate particle-embedded fibrin hydrogels for soft tissue reconstruction. *Biomedical materials (Bristol, England)*, 8(1), p.14105. Available at: <http://www.ncbi.nlm.nih.gov/pubmed/23353697>.
- Hwang, C.M. et al., 2010. Fabrication of three-dimensional porous cell-laden hydrogel for tissue engineering. *Biofabrication*, 2(3), p.35003.
- Hwang, N.S. et al., 2011. Regulation of osteogenic and chondrogenic differentiation of mesenchymal stem cells in PEG-ECM hydrogels. *Cell and tissue research*, 344(3), pp.499–509. Available at: <http://www.ncbi.nlm.nih.gov/pubmed/21503601> [Accessed May 15, 2014].
- Ichida, M. et al., 2011. Changes in cell migration of mesenchymal cells during osteogenic differentiation. *FEBS Letters*, 585(24), pp.4018–4024. Available at: <http://dx.doi.org/10.1016/j.febslet.2011.11.014>.
- Ishaug-Riley, S.L. et al., 1998. Three-dimensional culture of rat calvarial osteoblasts in porous biodegradable polymers. *Biomaterials*, 19(15), pp.1405–1412.
- Jaasma, M.J. & O'Brien, F.J., 2008. Mechanical Stimulation of Osteoblasts Using Steady and Dynamic Fluid Flow. *Tissue Engineering Part A*, 14(7), pp.1213–1223. Available at: <http://www.liebertonline.com/doi/abs/10.1089/ten.tea.2007.0321> [Accessed February 6, 2013].
- Jaasma, M.J., Plunkett, N. a & O'Brien, F.J., 2008. Design and validation of a dynamic flow perfusion bioreactor for use with compliant tissue engineering scaffolds. *Journal of biotechnology*, 133(4), pp.490–6. Available at: <http://www.ncbi.nlm.nih.gov/pubmed/18221813> [Accessed November 28, 2012].
- Jacobs, C.R. et al., 1998. Differential effect of steady versus oscillating flow on bone cells. *Journal of Biomechanics*, 31(11), pp.969–976. Available at: <http://www.sciencedirect.com/science/article/pii/S0021929098001146> [Accessed April 7, 2013].
- Jagodzinski, M. et al., 2008. Influence of perfusion and cyclic compression on proliferation and differentiation of bone marrow stromal cells in 3-dimensional culture. *Journal of*

- Biomechanics*, 41(9), pp.1885–1891.
- Jahangir, B.A.A. et al., 2008. Bone-graft substitutes in orthopaedic surgery. *AAOS Now*, pp.5–9.
- Jang, K. et al., 2008. Development of an osteoblast-based 3D continuous-perfusion microfluidic system for drug screening. *Analytical and Bioanalytical Chemistry*, 390(3), pp.825–832.
- Janssen, F.W. et al., 2010. Human tissue-engineered bone produced in clinically relevant amounts using a semi-automated perfusion bioreactor system : a preliminary study. , (October 2009), pp.12–24.
- Jee, W.S., 2001. Integrated Bone Tissue Physiology. In *Bone Mechanics Handbook, Second Edition*. CRC Press, pp. 1–68. Available at: <http://dx.doi.org/10.1201/b14263-3>.
- Jiang, Y. et al., 2002. Pluripotency of mesenchymal stem cells derived from adult marrow. *Nature*, 447(7146), pp.880–881. Available at: <http://www.nature.com/doi/10.1038/nature05812>.
- Johnell, O. et al., 2004. Mortality after osteoporotic fractures. *Osteoporosis international : a journal established as result of cooperation between the European Foundation for Osteoporosis and the National Osteoporosis Foundation of the USA*, 15(1), pp.38–42. Available at: <http://www.ncbi.nlm.nih.gov/pubmed/14593451> [Accessed April 6, 2013].
- Jungreuthmayer, C. et al., 2009. A comparative study of shear stresses in collagen-glycosaminoglycan and calcium phosphate scaffolds in bone tissue-engineering bioreactors. *Tissue engineering. Part A*, 15(5), pp.1141–1149.
- Kalajzic, I. et al., 2004. Dentin matrix protein 1 expression during osteoblastic differentiation, generation of an osteocyte GFP-transgene. *Bone*, 35(1), pp.74–82. Available at: <http://linkinghub.elsevier.com/retrieve/pii/S8756328204001097>.
- Kasper, C. et al., A Newly Developed Rotating Bed Bioreactor for Bone Tissue Engineering. , 3.
- Keogh, M.B. et al., 2011. Three hours of perfusion culture prior to 28 days of static culture, enhances osteogenesis by human cells in a collagen GAG scaffold. *Biotechnology and bioengineering*, 108(5), pp.1203–10. Available at: <http://www.ncbi.nlm.nih.gov/pubmed/21165906> [Accessed March 6, 2013].
- Keogh, M.B., O’ Brien, F.J. & Daly, J.S., 2010. A novel collagen scaffold supports human osteogenesis--applications for bone tissue engineering. *Cell and tissue research*, 340(1), pp.169–77. Available at: <http://www.ncbi.nlm.nih.gov/pubmed/20198386> [Accessed February 25, 2013].
- Keogh, M.B., O’Brien, F.J. & Daly, J.S., 2010. Substrate stiffness and contractile behaviour modulate the functional maturation of osteoblasts on a collagen-GAG scaffold. *Acta biomaterialia*, 6(11), pp.4305–13. Available at: <http://www.ncbi.nlm.nih.gov/pubmed/20570642> [Accessed March 30, 2013].
- Khetan, S. et al., 2013. Degradation-mediated cellular traction directs stem cell fate in covalently crosslinked three-dimensional hydrogels. *Nature materials*, 12(5), pp.458–65. Available at: <http://www.pubmedcentral.nih.gov/articlerender.fcgi?artid=3633615&tool=pmcentrez>

- &rendertype=abstract [Accessed December 12, 2013].
- Kim, H.J. et al., 2007. Bone regeneration on macroporous aqueous-derived silk 3-D scaffolds. *Macromolecular bioscience*, 7(5), pp.643–55. Available at: <http://www.ncbi.nlm.nih.gov/pubmed/17477447> [Accessed October 18, 2013].
- Kim, K. et al., 2009. Effect of initial cell seeding density on early osteogenic signal expression of rat bone marrow stromal cells cultured on cross-linked poly(propylene fumarate) disks. *Biomacromolecules*, 10(7), pp.1810–7. Available at: <http://www.pubmedcentral.nih.gov/articlerender.fcgi?artid=3655530&tool=pmcentrez&rendertype=abstract>.
- Kim, S.S. et al., 2000. Dynamic seeding and in vitro culture of hepatocytes in a flow perfusion system. *Tissue engineering*, 6(1), pp.39–44. Available at: <http://online.liebertpub.com/doi/abs/10.1089/107632700320874>.
- Kim, Y.-H., Furuya, H. & Tabata, Y., 2014. Enhancement of bone regeneration by dual release of a macrophage recruitment agent and platelet-rich plasma from gelatin hydrogels. *Biomaterials*, 35(1), pp.214–24. Available at: <http://www.ncbi.nlm.nih.gov/pubmed/24125774> [Accessed November 8, 2013].
- Klein-Nulend, J. et al., 1995. Pulsating fluid flow increases nitric oxide (NO) synthesis by osteocytes but not periosteal fibroblasts--correlation with prostaglandin upregulation. *Biochemical and biophysical research communications*, 217(2), pp.640–648.
- Klein-Nulend, J. et al., 1995. Sensitivity of osteocytes to biomechanical stress in vitro. *The FASEB journal: official publication of the Federation of American Societies for Experimental Biology*, 9(5), pp.441–445.
- Klein-Nulend, J., Bacabac, R.G. & Bakker, a D., 2012. Mechanical loading and how it affects bone cells: The role of the osteocyte cytoskeleton in maintaining our skeleton. *European cells & materials*, 24, pp.278–91. Available at: <http://www.ncbi.nlm.nih.gov/pubmed/23007912>.
- Knothe Tate, M.L. et al., 2000. In vivo demonstration of load-induced fluid flow in the rat tibia and its potential implications for processes associated with functional adaptation. *The Journal of experimental biology*, 203(Pt 18), pp.2737–2745.
- Knothe Tate, M.L. et al., 2004. The osteocyte. *The International Journal of Biochemistry & Cell Biology*, 36(1), pp.1–8. Available at: <http://www.sciencedirect.com/science/article/pii/S1357272503002413> [Accessed July 3, 2012].
- Knothe Tate, M.L. & Niederer, P., 1998. A theoretical FE-basemodel developed to predict the relative contribution of convective and diffusive transport mechanisms for the maintenance of local equilibria within cortical bone. In *Paper presented at the Advances in Heat and Mass Transfer in Biotechnology, Anaheim, California*.
- Knothe Tate, M.L., Niederer, P. & Knothe, U., 1998. In vivo tracer transport through the lacunocanalicular system of rat bone in an environment devoid of mechanical loading. *Bone*, 22(2), pp.107–117.
- Kolesky, D.B. et al., 2014. 3D bioprinting of vascularized, heterogeneous cell-laden tissue constructs. *Advanced Materials*, 26(19), pp.3124–3130.
- Krishnan, V. et al., 2010. Osteogenesis in vitro: from pre-osteoblasts to osteocytes. *In vitro*

- cellular & developmental biology. Animal*, 46(1), pp.28–35. Available at: <http://www.ncbi.nlm.nih.gov/pubmed/19826885> [Accessed October 6, 2014].
- Kuwahara, K. & Yang, Z., 2009. Cell delivery using an injectable and adhesive transglutaminase–gelatin gel. *Tissue Engineering Part C*, 16(4). Available at: <http://online.liebertpub.com/doi/abs/10.1089/ten.TEC.2009.0406> [Accessed December 3, 2013].
- de la Puente, P. & Ludeña, D., 2013. Cell culture in autologous fibrin scaffolds for applications in tissue engineering. *Experimental cell research*. Available at: <http://www.ncbi.nlm.nih.gov/pubmed/24378385> [Accessed January 9, 2014].
- Lan, S.F., Safiejko-Mroccka, B. & Starly, B., 2010. Long-term cultivation of HepG2 liver cells encapsulated in alginate hydrogels: A study of cell viability, morphology and drug metabolism. *Toxicology in Vitro*, 24(4), pp.1314–1323. Available at: <http://dx.doi.org/10.1016/j.tiv.2010.02.015>.
- Landis, W.J. et al., 1996. Mineralization of collagen may occur on fibril surfaces: evidence from conventional and high-voltage electron microscopy and three-dimensional imaging. *Journal of structural biology*, 117(1), pp.24–35. Available at: <http://www.ncbi.nlm.nih.gov/pubmed/8776885>.
- Langer, R. & Peppas, N. a., 2003. Advances in biomaterials, drug delivery, and bionanotechnology. *AICHE Journal*, 49(12), pp.2990–3006. Available at: <http://doi.wiley.com/10.1002/aic.690491202>.
- Langer, R. & Vacanti, J.P., 1993. Tissue engineering. *Science (New York, N.Y.)*, 260(5110), pp.920–6. Available at: <http://www.ncbi.nlm.nih.gov/pubmed/18613140>.
- Lee, C.R., Grodzinsky, a J. & Spector, M., 2001. The effects of cross-linking of collagen-glycosaminoglycan scaffolds on compressive stiffness, chondrocyte-mediated contraction, proliferation and biosynthesis. *Biomaterials*, 22(23), pp.3145–54. Available at: <http://www.ncbi.nlm.nih.gov/pubmed/11603587>.
- Lee, J.-W., Yamaguchi, A. & Iimura, T., 2014. Functional heterogeneity of osteocytes in FGF23 production: the possible involvement of DMP1 as a direct negative regulator. *BoneKEY reports*, 3(February), p.543. Available at: <http://www.ncbi.nlm.nih.gov/pubmed/24991406> [Accessed August 8, 2014].
- Legant, W., Miller, J. & Blakely, B., 2010. Measurement of mechanical tractions exerted by cells in three-dimensional matrices. *Nature methods*, 7(12). Available at: <http://www.nature.com/nmeth/journal/vaop/ncurrent/full/nmeth.1531.html> [Accessed May 27, 2014].
- Leipzig, N.D. & Shoichet, M.S., 2009. The effect of substrate stiffness on adult neural stem cell behavior. *Biomaterials*, 30(36), pp.6867–6878.
- Leis, H.J. et al., 1997. Phenotypic heterogeneity of osteoblast-like MC3T3-E1 cells: changes of bradykinin-induced prostaglandin E2 production during osteoblast maturation. *Journal of bone and mineral research : the official journal of the American Society for Bone and Mineral Research*, 12(4), pp.541–51. Available at: <http://www.ncbi.nlm.nih.gov/pubmed/9101365>.
- Levato, R. et al., 2014. Biofabrication of tissue constructs by 3D bioprinting of cell-laden microcarriers. *Biofabrication*, 6(3), p.35020. Available at:

- <http://www.ncbi.nlm.nih.gov/pubmed/25048797>.
- Li, R. et al., 2015. Mechanical strain regulates osteogenic and adipogenic differentiation of bone marrow mesenchymal stem cells. *BioMed Research International*, 2015.
- Liang, Y. et al., 2011. A cell-instructive hydrogel to regulate malignancy of 3D tumor spheroids with matrix rigidity. *Biomaterials*, 32(35), pp.9308–15. Available at: <http://www.ncbi.nlm.nih.gov/pubmed/21911252> [Accessed December 1, 2013].
- Liu, C. et al., 2012. Influence of perfusion and compression on the proliferation and differentiation of bone mesenchymal stromal cells seeded on polyurethane scaffolds. *Biomaterials*, 33(4), pp.1052–64. Available at: <http://www.ncbi.nlm.nih.gov/pubmed/22056755> [Accessed May 26, 2014].
- Liu, H., Slamovich, E.B. & Webster, T.J., 2006. Less harmful acidic degradation of poly(lactic-co-glycolic acid) bone tissue engineering scaffolds through titania nanoparticle addition. *International Journal of Nanomedicine*, 1(4), pp.541–545.
- Liu, X. et al., 2009. Biomimetic nanofibrous gelatin/apatite composite scaffolds for bone tissue engineering. *Biomaterials*, 30(12), pp.2252–8. Available at: <http://www.pubmedcentral.nih.gov/articlerender.fcgi?artid=2679864&tool=pmcentrez&rendertype=abstract> [Accessed December 4, 2013].
- Liu, Y. et al., 2009. Segmental bone regeneration using an rhBMP-2-loaded gelatin/nanohydroxyapatite/fibrin scaffold in a rabbit model. *Biomaterials*, 30(31), pp.6276–6285.
- Liu Tsang, V. et al., 2007. Fabrication of 3D hepatic tissues by additive photopatterning of cellular hydrogels. *FASEB journal : official publication of the Federation of American Societies for Experimental Biology*, 21(3), pp.790–801. Available at: <http://www.ncbi.nlm.nih.gov/pubmed/17197384> [Accessed November 7, 2013].
- Lo, C.M. et al., 2000. Cell movement is guided by the rigidity of the substrate. *Biophysical journal*, 79(1), pp.144–52. Available at: <http://www.pubmedcentral.nih.gov/articlerender.fcgi?artid=1300921&tool=pmcentrez&rendertype=abstract>.
- Lohberger, B. et al., 2014. Effect of cyclic mechanical stimulation on the expression of osteogenesis genes in human intraoral mesenchymal stromal and progenitor cells. *BioMed Research International*, 2014.
- Lozito, T.P. et al., 2013. Three-dimensional osteochondral microtissue to model pathogenesis of osteoarthritis. *Stem Cell Research & Therapy*, 4(Suppl 1), p.S6. Available at: <http://www.pubmedcentral.nih.gov/articlerender.fcgi?artid=4029306&tool=pmcentrez&rendertype=abstract>.
- Luger, N.M. et al., 2005. Bone cancer pain: from model to mechanism to therapy. *Journal of pain and symptom management*, 29(5 Suppl), pp.S32-46. Available at: <http://www.ncbi.nlm.nih.gov/pubmed/15907645> [Accessed April 6, 2013].
- Lyons, F.G. et al., 2010. The healing of bony defects by cell-free collagen-based scaffolds compared to stem cell-seeded tissue engineered constructs. *Biomaterials*, 31(35), pp.9232–43. Available at: <http://www.ncbi.nlm.nih.gov/pubmed/20863559> [Accessed May 28, 2013].

- Machado, C.B. et al., 2007. 3D chitosan-gelatin-chondroitin porous scaffold improves osteogenic differentiation of mesenchymal stem cells. *Biomedical materials (Bristol, England)*, 2(2), pp.124–31. Available at: <http://www.ncbi.nlm.nih.gov/pubmed/18458445> [Accessed March 27, 2013].
- Maia, F.R. et al., 2014. Effect of cell density on mesenchymal stem cells aggregation in RGD-alginate 3D matrices under osteoinductive conditions. *Macromolecular Bioscience*, 14, pp.759–771.
- Mankin, H.J., Hornicek, F.J. & Raskin, K. a, 2005. Infection in massive bone allografts. *Clinical orthopaedics and related research*, (432), pp.210–216.
- Marcacci, M. et al., 2007. Stem cells associated with macroporous bioceramics for long bone repair: 6- to 7-year outcome of a pilot clinical study. *Tissue engineering*, 13(5), pp.947–55. Available at: <http://www.ncbi.nlm.nih.gov/pubmed/17484701> [Accessed October 25, 2013].
- Martin, I., Wendt, D. & Heberer, M., 2004. The role of bioreactors in tissue engineering. *Trends in biotechnology*, 22(2), pp.80–6. Available at: <http://www.ncbi.nlm.nih.gov/pubmed/14757042> [Accessed March 3, 2013].
- Massari, K. V et al., 2015. Tissue reaction after subcutaneous implantation of a membrane composed of bacterial cellulose embedded with hydroxyapatite. *Dental, Oral and Craniofacial Research*, 1(2), pp.25–30.
- Matassi, F. et al., 2011. New biomaterials for bone regeneration. *Clinical cases in mineral and bone metabolism: the official journal of the Italian Society of Osteoporosis, Mineral Metabolism, and Skeletal Diseases*, 8(1), pp.21–4. Available at: <http://www.ncbi.nlm.nih.gov/pubmed/24147880>.
- Matsumoto, G. et al., 2012. Bone regeneration by polyhedral microcrystals from silkworm virus. *Scientific reports*, 2, p.935. Available at: <http://www.pubmedcentral.nih.gov/articlerender.fcgi?artid=3515804&tool=pmcentrez&rendertype=abstract> [Accessed November 1, 2013].
- Matziolis, D. et al., 2011. Osteogenic predifferentiation of human bone marrow-derived stem cells by short-term mechanical stimulation. *The open orthopaedics journal*, 5, pp.1–6. Available at: <http://www.pubmedcentral.nih.gov/articlerender.fcgi?artid=3027083&tool=pmcentrez&rendertype=abstract>.
- Mauck, R.L. et al., 2007. Regulation of cartilaginous ECM gene transcription by chondrocytes and MSCs in 3D culture in response to dynamic loading. *Biomechanics and modeling in mechanobiology*, 6(1–2), pp.113–25. Available at: <http://www.ncbi.nlm.nih.gov/pubmed/16691412> [Accessed November 8, 2013].
- Mc Garrigle, M.J. et al., 2016. Osteocyte Differentiation and the Formation of an Interconnected Cellular Network in Vitro. *European Cells and Materials*, 31(353), pp.323–340.
- McCoy, R.J., Jungreuthmayer, C. & O'Brien, F.J., 2012. Influence of flow rate and scaffold pore size on cell behavior during mechanical stimulation in a flow perfusion bioreactor. *Biotechnology and bioengineering*, 109(6), pp.1583–94. Available at: <http://www.ncbi.nlm.nih.gov/pubmed/22249971> [Accessed August 7, 2013].

- McNamara, L., 2011. 2.210 - Bone as a Material. In *Comprehensive Biomaterials*. pp. 169–186. Available at: <http://www.sciencedirect.com/science/article/pii/B9780080552941000684> [Accessed January 2, 2017].
- McNamara, L.M. et al., 2009. Attachment of osteocyte cell processes to the bone matrix. *Anatomical record (Hoboken, N.J.: 2007)*, 292(3), pp.355–63. Available at: <http://www.pubmedcentral.nih.gov/articlerender.fcgi?artid=2861341&tool=pmcentrez&rendertype=abstract> [Accessed May 28, 2013].
- McNamara, L.M., 2010. Perspective on post-menopausal osteoporosis: establishing an interdisciplinary understanding of the sequence of events from the molecular level to whole bone fractures. *Journal of the Royal Society, Interface / the Royal Society*, 7(44), pp.353–72. Available at: <http://www.pubmedcentral.nih.gov/articlerender.fcgi?artid=2842799&tool=pmcentrez&rendertype=abstract> [Accessed July 3, 2012].
- McNamara, L.M. et al., 2006. Stress-concentrating effect of resorption lacunae in trabecular bone. *Journal of biomechanics*, 39(4), pp.734–41. Available at: <http://www.ncbi.nlm.nih.gov/pubmed/16439243> [Accessed July 23, 2013].
- Meijer, G.J. et al., 2007. Cell-based bone tissue engineering. *PLoS Medicine*, 4(2), pp.0260–0264.
- Meijer, G.J. et al., 2008. Cell based bone tissue engineering in jaw defects. *Biomaterials*, 29(21), pp.3053–61. Available at: <http://www.ncbi.nlm.nih.gov/pubmed/18433864> [Accessed October 25, 2013].
- Metzger, T.A. et al., 2015. Pressure and shear stress in trabecular bone marrow during whole bone loading. *Journal of Biomechanics*, 48(12), pp.3035–3043. Available at: <http://dx.doi.org/10.1016/j.jbiomech.2015.07.028>.
- Mikuni-Takagaki, Y. et al., 1995. Matrix mineralization and the differentiation of osteocyte-like cells in culture. *Journal of Bone and Mineral Research*, 10(2), pp.231–242. Available at: <http://dx.doi.org/10.1002/jbmr.5650100209>.
- Milan, J.-L., Planell, J. a & Lacroix, D., 2009. Computational modelling of the mechanical environment of osteogenesis within a polylactic acid-calcium phosphate glass scaffold. *Biomaterials*, 30(25), pp.4219–26. Available at: <http://www.ncbi.nlm.nih.gov/pubmed/19477510> [Accessed March 11, 2013].
- Min, J.H. et al., 2014. The use of Matriderm and autologous skin graft in the treatment of full thickness skin defects. *Archives of Plastic Surgery*, 41(4), pp.330–336.
- Mitchell, G.R. & Tojeira, A., 2013. Role of Anisotropy in Tissue Engineering. *Procedia Engineering*, 59, pp.117–125. Available at: <http://linkinghub.elsevier.com/retrieve/pii/S187770581301014X> [Accessed July 18, 2013].
- Mullen, C.A. et al., 2014. Cell morphology and focal adhesion location alters internal cell stress. *Journal of The Royal Society Interface*, 11(101). Available at: <http://rsif.royalsocietypublishing.org/content/11/101/20140885.abstract>.
- Mullen, C.A. et al., 2013. Osteocyte differentiation is regulated by extracellular matrix stiffness and intercellular separation. *Journal of the mechanical behavior of biomedical*

- materials*, 28, pp.183–194. Available at: <http://www.ncbi.nlm.nih.gov/pubmed/23994943> [Accessed October 12, 2013].
- Murphy, C.M. et al., 2013. Cell-scaffold interactions in the bone tissue engineering triad. *European cells & materials*, 26, pp.120–32. Available at: <http://www.ncbi.nlm.nih.gov/pubmed/24052425>.
- Murphy, C.M. et al., 2015. Effect of collagen-glycosaminoglycan scaffold pore size on matrix mineralization and cellular behavior in different cell types. *Journal of Biomedical Materials Research Part A*, (SEPTEMBER), p.n/a-n/a. Available at: <http://doi.wiley.com/10.1002/jbm.a.35567>.
- Murphy, C.M. et al., 2012. Mesenchymal stem cell fate is regulated by the composition and mechanical properties of collagen-glycosaminoglycan scaffolds. *Journal of the mechanical behavior of biomedical materials*, 11, pp.53–62. Available at: <http://www.ncbi.nlm.nih.gov/pubmed/22658154> [Accessed February 6, 2013].
- Murphy, C.M., Haugh, M.G. & O'Brien, F.J., 2010. The effect of mean pore size on cell attachment, proliferation and migration in collagen-glycosaminoglycan scaffolds for bone tissue engineering. *Biomaterials*, 31(3), pp.461–6. Available at: <http://www.ncbi.nlm.nih.gov/pubmed/19819008> [Accessed August 4, 2012].
- Murshid, S.A. et al., 2007. Actin and microtubule cytoskeletons of the processes of 3D-cultured MC3T3-E1 cells and osteocytes. *Journal of bone and mineral metabolism*, 25(3), pp.151–8. Available at: <http://www.ncbi.nlm.nih.gov/pubmed/17447112> [Accessed November 19, 2014].
- Myeroff, C. & Archdeacon, M., 2011. Autogenous bone graft: donor sites and techniques. *The Journal of bone and joint surgery. American volume*, 93(23), pp.2227–36. Available at: <http://www.ncbi.nlm.nih.gov/pubmed/22159859>.
- Naito, H. & Dohi, Y., 2011. The effect of mesenchymal stem cell osteoblastic differentiation on the mechanical properties of engineered bone-like tissue. *Tissue ...*, 17. Available at: <http://online.liebertpub.com/doi/abs/10.1089/ten.tea.2011.0099> [Accessed November 13, 2013].
- Nakano, Y. et al., 2004. Site-specific localization of two distinct phosphatases along the osteoblast plasma membrane: tissue non-specific alkaline phosphatase and plasma membrane calcium ATPase. *Bone*, 35(5), pp.1077–1085. Available at: <http://linkinghub.elsevier.com/retrieve/pii/S8756328204003047>.
- Nam, Y.S., Yoon, J.J. & Park, T.G., 2000. A novel fabrication method of macroporous biodegradable polymer scaffolds using gas foaming salt as a porogen additive. *Journal of biomedical materials research*, 53(1), pp.1–7. Available at: <http://www.ncbi.nlm.nih.gov/pubmed/10634946>.
- Narayanan, K. et al., 2003. Dual functional roles of dentin matrix protein 1. Implications in biomineralization and gene transcription by activation of intracellular Ca²⁺ store. *Journal of Biological Chemistry*, 278(19), pp.17500–17508.
- Nichol, J.W. et al., 2010. Cell-laden microengineered gelatin methacrylate hydrogels. *Biomaterials*, 31(21), pp.5536–44. Available at: <http://www.pubmedcentral.nih.gov/articlerender.fcgi?artid=2878615&tool=pmcentrez&rendertype=abstract> [Accessed November 6, 2013].

Reference

- Nicodemus, G.D. & Bryant, S.J., 2008. Cell encapsulation in biodegradable hydrogels for tissue engineering applications. *Tissue engineering. Part B, Reviews*, 14(2), pp.149–65. Available at: <http://www.pubmedcentral.nih.gov/articlerender.fcgi?artid=2962861&tool=pmcentrez&rendertype=abstract> [Accessed December 11, 2013].
- Nicolella, D.P., 2006. Osteocyte lacunae tissue strain in cortical bone. *Journal of biomechanics*.
- Nicolella, D.P. et al., 2006. Osteocyte lacunae tissue strain in cortical bone. *Journal of biomechanics*, 39(9), pp.1735–43. Available at: <http://www.pubmedcentral.nih.gov/articlerender.fcgi?artid=1866263&tool=pmcentrez&rendertype=abstract> [Accessed July 27, 2012].
- Nishi, M. et al., 2012. Engineered bone tissue associated with vascularization utilizing a rotating wall vessel bioreactor. *Journal of biomedical materials research. Part A*, pp.1–7. Available at: <http://www.ncbi.nlm.nih.gov/pubmed/22865391> [Accessed August 8, 2012].
- O'Brien, F.J., 2011. Biomaterials & scaffolds for tissue engineering. *Materials Today*, 14(3), pp.88–95. Available at: <http://linkinghub.elsevier.com/retrieve/pii/S136970211170058X> [Accessed September 26, 2013].
- O'Brien, F.J. et al., 2005. The effect of pore size on cell adhesion in collagen-GAG scaffolds. *Biomaterials*, 26(4), pp.433–41. Available at: <http://www.ncbi.nlm.nih.gov/pubmed/15275817> [Accessed July 18, 2012].
- van Oers, R.F.M., Wang, H. & Bacabac, R.G., 2015. Osteocyte Shape and Mechanical Loading. *Current Osteoporosis Reports*, 13(2), pp.61–66.
- Olivares, A.L. et al., 2009. Finite element study of scaffold architecture design and culture conditions for tissue engineering. *Biomaterials*, 30(30), pp.6142–9. Available at: <http://www.ncbi.nlm.nih.gov/pubmed/19674779> [Accessed March 11, 2013].
- Olivares, A.L., Ph, D. & Lacroix, D., 2012. Simulation of Cell Seeding Within a Three-Dimensional Porous Scaffold : A Fluid-Particle Analysis. , 18(8), pp.624–631.
- Orban, J.M. et al., 2004. Crosslinking of collagen gels by transglutaminase. *Journal of biomedical materials research. Part A*, 68(4), pp.756–762.
- Owan, I. et al., 1997. Mechanotransduction in bone: osteoblasts are more responsive to fluid forces than mechanical strain. *Journal of Chemical Information and Modeling*, 53(9), pp.1689–1699.
- Paguirigan, a & Beebe, D.J., 2006. Gelatin based microfluidic devices for cell culture. *Lab on a chip*, 6(3), pp.407–13. Available at: <http://www.ncbi.nlm.nih.gov/pubmed/16511624> [Accessed November 19, 2013].
- Palazzini, S. et al., 1998. Stromal cell structure and relationships in perimedullary spaces of chick embryo shaft bones. *Anatomy and embryology*, 39, pp.349–357. Available at: <http://link.springer.com/article/10.1007/s004290050145> [Accessed October 13, 2014].
- Palumbo, C., 1986. A three-dimensional ultrastructural study of osteoid-osteocytes in the tibia of chick embryos. *Cell and tissue research*, 246, pp.125–131. Available at: <http://link.springer.com/article/10.1007/BF00219008> [Accessed August 18, 2014].

- Palumbo, C., Ferretti, M. & Marotti, G., 2004. Osteocyte dendrogenesis in static and dynamic bone formation: an ultrastructural study. *The anatomical record. Part A, Discoveries in molecular, cellular, and evolutionary biology*, 278(1), pp.474–80. Available at: <http://www.ncbi.nlm.nih.gov/pubmed/15103743> [Accessed August 18, 2014].
- Pampaloni, F., Reynaud, E.G. & Stelzer, E.H.K., 2007. The third dimension bridges the gap between cell culture and live tissue. *Nature reviews. Molecular cell biology*, 8(10), pp.839–45. Available at: <http://www.ncbi.nlm.nih.gov/pubmed/17684528>.
- Park, J.S. et al., 2011. The effect of matrix stiffness on the differentiation of mesenchymal stem cells in response to TGF- β . *Biomaterials*, 32(16), pp.3921–30. Available at: <http://www.pubmedcentral.nih.gov/articlerender.fcgi?artid=3073995&tool=pmcentrez&rendertype=abstract> [Accessed October 17, 2013].
- Park, S.-H. et al., 2006. An electromagnetic compressive force by cell exciter stimulates chondrogenic differentiation of bone marrow-derived mesenchymal stem cells. *Tissue engineering*, 12(11), pp.3107–17. Available at: <http://www.ncbi.nlm.nih.gov/pubmed/17518626>.
- Partap, S. et al., 2010. Stimulation of osteoblasts using rest periods during bioreactor culture on collagen-glycosaminoglycan scaffolds. *Journal of materials science. Materials in medicine*, 21(8), pp.2325–30. Available at: <http://www.ncbi.nlm.nih.gov/pubmed/20091098> [Accessed March 6, 2013].
- Peppas, N. a. et al., 2006. Hydrogels in Biology and Medicine: From Molecular Principles to Bionanotechnology. *Advanced Materials*, 18(11), pp.1345–1360. Available at: <http://doi.wiley.com/10.1002/adma.200501612> [Accessed November 8, 2013].
- de Peppo, G.M. et al., 2013. Engineering bone tissue substitutes from human induced pluripotent stem cells. *Proceedings of the National Academy of Sciences of the United States of America*, 110(21). Available at: <http://www.ncbi.nlm.nih.gov/pubmed/23653480> [Accessed May 22, 2013].
- Phinney, D.G. & Prockop, D.J., 2007. Concise Review: Mesenchymal Stem/Multipotent Stromal Cells: The State of Transdifferentiation and Modes of Tissue Repair-Current Views. *Stem Cells*, 25(11), pp.2896–2902. Available at: <http://doi.wiley.com/10.1634/stemcells.2007-0637>.
- Plunkett, N. a, Partap, S. & O'Brien, F.J., 2010. Osteoblast response to rest periods during bioreactor culture of collagen-glycosaminoglycan scaffolds. *Tissue engineering. Part A*, 16(3), pp.943–51. Available at: <http://www.ncbi.nlm.nih.gov/pubmed/19827912>.
- Plunkett, N. & O'Brien, F.J., 2010. IV.3. Bioreactors in tissue engineering. *Studies in health technology and informatics*, 152, pp.214–30. Available at: <http://www.ncbi.nlm.nih.gov/pubmed/20407197>.
- Polo-Corrales, L., Latorre-Esteves, M. & Ramirez-Vick, J.E., 2014. Scaffold design for bone regeneration. *Journal of nanoscience and nanotechnology*, 14(1), pp.15–56. Available at: <http://www.ncbi.nlm.nih.gov/pubmed/24730250> <http://www.pubmedcentral.nih.gov/articlerender.fcgi?artid=PMC3997175>.
- Pradel, W., Eckelt, U. & Lauer, G., 2006. Bone regeneration after enucleation of mandibular cysts: comparing autogenous grafts from tissue-engineered bone and iliac bone. *Oral*

- surgery, oral medicine, oral pathology, oral radiology, and endodontics*, 101(3), pp.285–90. Available at: <http://www.ncbi.nlm.nih.gov/pubmed/16504859> [Accessed October 25, 2013].
- Pradhan-Bhatt, S. et al., 2014. A novel in vivo model for evaluating functional restoration of a tissue-engineered salivary gland. *Laryngoscope*, 124(2), pp.456–461.
- Previtera, M.L., Langhammer, C.G. & Firestein, B.L., 2010. Effects of substrate stiffness and cell density on primary hippocampal cultures. *Journal of Bioscience and Bioengineering*, 110(4), pp.459–470. Available at: <http://dx.doi.org/10.1016/j.jbiosc.2010.04.004>.
- Prideaux, M. et al., 2012. Extracellular matrix mineralization promotes E11/gp38 glycoprotein expression and drives osteocytic differentiation. *PloS one*, 7(5), p.e36786. Available at: <http://www.pubmedcentral.nih.gov/articlerender.fcgi?artid=3346717&tool=pmcentrez&rendertype=abstract> [Accessed August 14, 2014].
- Priya, S.G., Jungvid, H. & Kumar, A., 2008. Skin tissue engineering for tissue repair and regeneration. *Tissue engineering. Part B, Reviews*, 14(1), pp.105–118.
- Przybylowski, C. et al., 2012. MC3T3 preosteoblast differentiation on bone morphogenetic protein-2 peptide ormosils. *Journal of Materials Chemistry*, 22(21), p.10672. Available at: <http://xlink.rsc.org/?DOI=c2jm16490f> [Accessed April 4, 2014].
- Quarles, L.D. et al., 1992. Distinct proliferative and differentiated stages of murine MC3T3-E1 cells in culture: an in vitro model of osteoblast development. *Journal of bone and mineral research : the official journal of the American Society for Bone and Mineral Research*, 7(6), pp.683–692.
- Quarto, R. et al., 2001. Repair of Large Bone Defects with the Use of Autologous Bone Marrow Stromal Cells. *New England Journal of Medicine*, 14(5), pp.663–70. Available at: <http://dx.doi.org/10.1056/NEJM200102013440516>.
- Quintavalle, M. et al., 2011. A cell-based high-content screening assay reveals activators and inhibitors of cancer cell invasion. *Sci. Signal.*, 4(183), p.ra49.
- Rana, D. & Kumar, T.S. Sampath Ramalingam, M., 2014. Cell-Laden Hydrogels for Tissue Engineering. *Journal of Biomaterials and Tissue Engineering*, 4(29), pp.507–535.
- Rauh, J. & Milan, F., 2011. Bioreactor systems for bone tissue engineering. *Tissue Engineering Part ...*, 17(4). Available at: <http://online.liebertpub.com/doi/abs/10.1089/ten.teb.2010.0612> [Accessed December 4, 2013].
- Reid, R.L., 1968. *Hernia through an iliac bone-graft donor site. A case report.*,
- Rho, J.-Y., Kuhn-Spearing, L. & Zioupos, P., 1998. Mechanical properties and the hierarchical structure of bone. *Medical Engineering & Physics*, 20(2), pp.92–102. Available at: <http://www.sciencedirect.com/science/article/pii/S1350453398000071>.
- Rho, J.Y., Ashman, R.B. & Turner, C.H., 1993. Young's modulus of trabecular and cortical bone material: Ultrasonic and microtensile measurements. *Journal of Biomechanics*, 26(2), pp.111–119.
- Rho, J.Y., Tsui, T.Y. & Pharr, G.M., 1997. Elastic properties of human cortical and

- trabecular lamellar bone measured by nanoindentation. *Biomaterials*, 18(20), pp.1325–1330.
- Rhodes, N., 2004. Biocompatibility testing of tissue engineered products. *Vox sanguinis*, 87 Suppl 2, pp.161–3. Available at: <http://www.ncbi.nlm.nih.gov/pubmed/15209906>.
- Rios, H.F. et al., 2005. DMP1 is essential for osteocyte formation and function. *Journal of musculoskeletal & neuronal interactions*, 5(4), pp.325–7. Available at: <http://www.ncbi.nlm.nih.gov/pubmed/16340123>.
- Rosser, J. & Bonewald, L.F., 2012. Studying Osteocyte Function Using the Cell Lines MLO-Y4 and MLO-A5 M. H. Helfrich & S. H. Ralston, eds. , 816. Available at: <http://www.springerlink.com/index/10.1007/978-1-61779-415-5> [Accessed July 24, 2012].
- Rouwkema, J., de Boer, J. & Van Blitterswijk, C.A., 2006. Endothelial cells assemble into a 3-dimensional prevascular network in a bone tissue engineering construct. *Tissue engineering*, 12(9), pp.2685–2693.
- Sabree, I., Gough, J.E. & Derby, B., 2015. Mechanical properties of porous ceramic scaffolds: Influence of internal dimensions. *Ceramics International*, 41(7), pp.8425–8432.
- Sachar, A. et al., 2012. Osteoblasts responses to three-dimensional nanofibrous gelatin scaffolds. *Journal of biomedical materials research. Part A*, 100(11), pp.3029–41. Available at: <http://www.pubmedcentral.nih.gov/articlerender.fcgi?artid=3455145&tool=pmcentrez&rendertype=abstract> [Accessed December 4, 2013].
- Salgado, A.J., Coutinho, O.P. & Reis, R.L., 2004. Bone tissue engineering: state of the art and future trends. *Macromolecular bioscience*, 4(8), pp.743–65. Available at: <http://www.ncbi.nlm.nih.gov/pubmed/15468269> [Accessed March 1, 2013].
- Sapir-Koren, R. & Livshits, G., 2011. Bone mineralization and regulation of phosphate homeostasis. *IBMS BoneKEy*, 8(6), pp.286–300. Available at: <http://www.nature.com/doi/10.1138/20110516> [Accessed August 14, 2014].
- Saunders, M.M. et al., 2006. Mechanical stimulation effects on functional end effectors in osteoblastic MG-63 cells. *Journal of biomechanics*, 39(8), pp.1419–27. Available at: <http://www.ncbi.nlm.nih.gov/pubmed/15953606> [Accessed November 28, 2012].
- Schaffler, M.B. et al., 2014. Osteocytes: Master orchestrators of bone. *Calcified Tissue International*, 94(1), pp.5–24.
- Schimming, R. & Schmelzeisen, R., 2004. Tissue-engineered bone for maxillary sinus augmentation. *Journal of Oral and Maxillofacial Surgery*, 62(6), pp.724–729. Available at: <http://linkinghub.elsevier.com/retrieve/pii/S0278239104001454> [Accessed October 25, 2013].
- Schliephake, H. et al., 2009. Bone formation in trabecular bone cell seeded scaffolds used for reconstruction of the rat mandible. *International Journal of Oral and Maxillofacial Surgery*, 38(2), pp.166–172.
- Schubert, T. et al., 2013. Critical size bone defect reconstruction by an autologous 3D osteogenic-like tissue derived from differentiated adipose MSCs. *Biomaterials*, 34(18), pp.4428–38. Available at: <http://www.ncbi.nlm.nih.gov/pubmed/23507085> [Accessed

April 1, 2013].

- Schulz, R.M. et al., 2008. Development and validation of a novel bioreactor system for load- and perfusion-controlled tissue engineering of chondrocyte-constructs. *Biotechnology and bioengineering*, 101(4), pp.714–28. Available at: <http://www.ncbi.nlm.nih.gov/pubmed/18814291> [Accessed March 21, 2013].
- Schwarz, R.P., Goodwin, T.J. & Wolf, D.A., 1992. Cell culture for three-dimensional modeling in rotating-wall vessels: An application of simulated microgravity. *Journal of Tissue Culture Methods*, 14(2), pp.51–57.
- Seiler, J.G. & Johnson, J., 2000. Iliac crest autogenous bone grafting: donor site complications. *Journal of the Southern Orthopaedic Association*, 9(2), pp.91–7. Available at: <http://www.ncbi.nlm.nih.gov/pubmed/10901646>.
- Shahar, R. & Dean, M.N., 2013. The enigmas of bone without osteocytes. *BoneKEy reports*, 2(January), p.343. Available at: <http://www.pubmedcentral.nih.gov/articlerender.fcgi?artid=3692265&tool=pmcentrez&rendertype=abstract>.
- Shayesteh, Y.S. et al., 2008. Sinus augmentation using human mesenchymal stem cells loaded into a Beta-tricalcium phosphate/hydroxyapatite scaffold. *Oral Surgery, Oral Medicine, Oral Pathology, Oral Radiology and Endodontology*, 106(2), pp.203–209.
- Shevchenko, R. V, James, S.L. & James, S.E., 2010. A review of tissue-engineered skin bioconstructs available for skin reconstruction. *Journal of the Royal Society, Interface / the Royal Society*, 7(43), pp.229–258.
- Shin, H., Olsen, B.D. & Khademhosseini, A., 2014. Gellan gum microgel-reinforced cell-laden gelatin hydrogels. *Journal of Materials Chemistry B*. Available at: <http://xlink.rsc.org/?DOI=c3tb20984a> [Accessed November 27, 2013].
- Shukla, A.A. & Gottschalk, U., 2013. Single-use disposable technologies for biopharmaceutical manufacturing. *Trends in Biotechnology*, 31(3), pp.147–154. Available at: <http://dx.doi.org/10.1016/j.tibtech.2012.10.004>.
- Sikavitsas, V.I. et al., 2005. Flow Perfusion Enhances the Calcified Matrix Deposition of Marrow Stromal Cells in Biodegradable Nonwoven Fiber Mesh Scaffolds. *Annals of Biomedical Engineering*, 33(1), pp.63–70. Available at: <http://www.springerlink.com/openurl.asp?id=doi:10.1007/s10439-005-8963-x> [Accessed January 28, 2013].
- Sikavitsas, V.I., Bancroft, G.N. & Mikos, A.G., 2002. Formation of three-dimensional cell/polymer constructs for bone tissue engineering in a spinner flask and a rotating wall vessel bioreactor. *Journal of biomedical materials research*, 62(1), pp.136–48. Available at: <http://www.ncbi.nlm.nih.gov/pubmed/12124795>.
- Sittichockechaiwut, A. et al., 2009. Use of rapidly mineralising osteoblasts and short periods of mechanical loading to accelerate matrix maturation in 3D scaffolds. *Bone*, 44(5), pp.822–9. Available at: <http://www.ncbi.nlm.nih.gov/pubmed/19442630> [Accessed February 6, 2013].
- Sladkova, M. & de Peppo, G., 2014. Bioreactor Systems for Human Bone Tissue Engineering. *Processes*, 2(2), pp.494–525. Available at: <http://www.mdpi.com/2227-9717/2/2/494/htm>.

- Smalt, R. et al., 1997. Induction of NO and prostaglandin E2 in osteoblasts by wall-shear stress but not mechanical strain. *The American journal of physiology*, 273(4 Pt 1), pp.E751-8. Available at: <http://www.ncbi.nlm.nih.gov/pubmed/9357805>.
- Smith, B.D. & Grande, D.A., 2015. The current state of scaffolds for musculoskeletal regenerative applications. *Nat Rev Rheumatol*, 11(4), pp.213–222. Available at: <http://www.ncbi.nlm.nih.gov/pubmed/25776947><http://www.nature.com/nrrheum/journal/v11/n4/pdf/nrrheum.2015.27.pdf>.
- Soares, C.P. et al., 2012. 2D and 3D-organized cardiac cells shows differences in cellular morphology, adhesion junctions, presence of myofibrils and protein expression. *PLoS ONE*, 7(5).
- Sokic, S. et al., 2014. In situ generation of cell-laden porous MMP-sensitive PEGDA hydrogels by gelatin leaching. *Macromolecular Bioscience*, 14(5), pp.731–739.
- Sopyan, I. et al., 2007. Porous hydroxyapatite for artificial bone applications. *Science and Technology of Advanced Materials*, 8(1–2), pp.116–123. Available at: <http://stacks.iop.org/1468-6996/8/i=1-2/a=A21?key=crossref.4412a0f22a4464474c8a5a963155a75c> [Accessed July 25, 2012].
- Springer, I.N. et al., 2006. Two techniques for the preparation of cell-scaffold constructs suitable for sinus augmentation: steps into clinical application. *Tissue engineering*, 12(9), pp.2649–56. Available at: <http://www.ncbi.nlm.nih.gov/pubmed/16995798>.
- St-Pierre, J.-P. et al., 2005. Three-dimensional growth of differentiating MC3T3-E1 pre-osteoblasts on porous titanium scaffolds. *Biomaterials*, 26(35), pp.7319–28. Available at: <http://www.ncbi.nlm.nih.gov/pubmed/16000220> [Accessed March 1, 2013].
- Stern, A.R. & Nicoletta, D.P., 2013. Measurement and estimation of osteocyte mechanical strain. *Bone*, pp.1–5. Available at: <http://www.ncbi.nlm.nih.gov/pubmed/23369990> [Accessed March 4, 2013].
- Stevens, M., 2008. Biomaterials for bone tissue engineering. *Materials today*, 11(5), pp.18–25. Available at: <http://www.sciencedirect.com/science/article/pii/S1369702108700865> [Accessed April 2, 2013].
- Stops, a J.F., Heraty, K.B., et al., 2010. A prediction of cell differentiation and proliferation within a collagen-glycosaminoglycan scaffold subjected to mechanical strain and perfusive fluid flow. *Journal of biomechanics*, 43(4), pp.618–26. Available at: <http://www.ncbi.nlm.nih.gov/pubmed/19939388> [Accessed September 2, 2012].
- Stops, a J.F., Harrison, N.M., et al., 2010. Local and regional mechanical characterisation of a collagen-glycosaminoglycan scaffold using high-resolution finite element analysis. *Journal of the mechanical behavior of biomedical materials*, 3(4), pp.292–302. Available at: <http://www.ncbi.nlm.nih.gov/pubmed/20346897> [Accessed August 24, 2012].
- Sudo, H. et al., 1983. In vitro differentiation and calcification in a new clonal osteogenic cell line derived from newborn mouse calvaria. *The Journal of cell biology*, 96(1), pp.191–8. Available at: <http://www.pubmedcentral.nih.gov/articlerender.fcgi?artid=2112252&tool=pmcentrez&rendertype=abstract>.

- Summers, K., Jinnett, K. & Bevan, S., 2015. Musculoskeletal Disorders , Workforce Health and Productivity in the United States. , (June), pp.1–41. Available at: <http://www.theworkfoundation.com/Reports/385/Musculoskeletal-Disorders-Workforce-Health-and-Productivity-in-the-United-States>.
- Sutter, M. et al., 2007. Recombinant gelatin hydrogels for the sustained release of proteins. *Journal of controlled release: official journal of the Controlled Release Society*, 119(3), pp.301–12. Available at: <http://www.ncbi.nlm.nih.gov/pubmed/17467099> [Accessed December 16, 2013].
- Suwandi, J.S. et al., 2015. Inducing tissue specific tolerance in autoimmune disease with tolerogenic dendritic cells. *Clinical and Experimental Rheumatology*, 33, pp.97–103.
- Takano-Yamamoto, T., 2014. Osteocyte function under compressive mechanical force. *Japanese Dental Science Review*, 50(2), pp.29–39. Available at: <http://dx.doi.org/10.1016/j.jdsr.2013.10.004>.
- Tan, S. et al., 2014. The synergetic effect of hydrogel stiffness and growth factor on osteogenic differentiation. *Biomaterials*, 35(20), pp.5294–5306. Available at: <http://linkinghub.elsevier.com/retrieve/pii/S0142961214001963> [Accessed April 7, 2014].
- Teo, J.C.M. et al., 2006. Determination of Bone Trabeculae Modulus—An Ultrasonic Scanning and MicroCT (μ CT) Imaging Combination Approach. *Experimental Mechanics*, 46(4), pp.453–461.
- Thorpe, S.D. et al., 2008. Dynamic compression can inhibit chondrogenesis of mesenchymal stem cells. *Biochemical and biophysical research communications*, 377(2), pp.458–62. Available at: <http://www.ncbi.nlm.nih.gov/pubmed/18851955> [Accessed August 13, 2013].
- Thorpe, S.D. et al., 2013. Modulating Gradients in Regulatory Signals within Mesenchymal Stem Cell Seeded Hydrogels: A Novel Strategy to Engineer Zonal Articular Cartilage. *PloS one*, 8(4), p.e60764. Available at: <http://www.pubmedcentral.nih.gov/articlerender.fcgi?artid=3628868&tool=pmcentrez&rendertype=abstract> [Accessed June 17, 2013].
- Thorpe, S.D. et al., 2010. The response of bone marrow-derived mesenchymal stem cells to dynamic compression following TGF-beta3 induced chondrogenic differentiation. *Annals of biomedical engineering*, 38(9), pp.2896–909. Available at: <http://www.ncbi.nlm.nih.gov/pubmed/20458627> [Accessed November 12, 2013].
- Tiainen, H. et al., 2010. Ultra-porous titanium oxide scaffold with high compressive strength. *Journal of Materials Science: Materials in Medicine*, 21(10), pp.2783–2792.
- Tiainen, H., Wiedmer, D. & Haugen, H.J., 2013. Processing of highly porous TiO₂ bone scaffolds with improved compressive strength. *Journal of the European Ceramic Society*, 33(1), pp.15–24. Available at: <http://linkinghub.elsevier.com/retrieve/pii/S0955221912004645> [Accessed April 12, 2013].
- Tierney, C.M., Jaasma, M.J. & O'Brien, F.J., 2009. Osteoblast activity on collagen-GAG scaffolds is affected by collagen and GAG concentrations. *Journal of biomedical materials research. Part A*, 91(1), pp.92–101. Available at: <http://www.ncbi.nlm.nih.gov/pubmed/18767061> [Accessed October 23, 2013].

- Townsend, P.R., Rose, R.M. & Radin, E.L., 1975. Buckling studies of single human trabeculae. *Journal of Biomechanics*, 8(3–4).
- Trappmann, B. et al., 2012. Extracellular-matrix tethering regulates stem-cell fate. *Nature Materials*, 11(7), pp.642–649. Available at: <http://www.nature.com/doi/10.1038/nmat3339> [Accessed July 31, 2013].
- Uchihashi, K. et al., 2013. Osteoblast migration into type I collagen gel and differentiation to osteocyte-like cells within a self-produced mineralized matrix: A novel system for analyzing differentiation from osteoblast to osteocyte. *Bone*, 52(1), pp.102–110. Available at: <http://dx.doi.org/10.1016/j.bone.2012.09.001>.
- Uemura, T. et al., 2003. Transplantation of cultured bone cells using combinations of scaffolds and culture techniques. *Biomaterials*, 24(13), pp.2277–2286.
- Undale, A.H. et al., 2009. Mesenchymal Stem Cells for Bone Repair and Metabolic Bone Diseases. *Mayo Clinic Proceedings*, 84(10), pp.893–902. Available at: <http://linkinghub.elsevier.com/retrieve/pii/S0025619611605065>.
- Vacanti, 2001. Replacement of an Avulsed phalanx with tissue-engineered bone. *The new england journal of medicine*, 344(20), pp.1511–1514.
- Vaughan, T., 2013. Are all osteocytes equal? Multiscale modelling of cortical bone to characterise the mechanical stimulation of osteocytes. *International journal for ...*. Available at: <http://onlinelibrary.wiley.com/doi/10.1002/cnm.2578/full> [Accessed November 29, 2013].
- Vaughan, T.J., McCarthy, C.T. & McNamara, L.M., 2012. A three-scale finite element investigation into the effects of tissue mineralisation and lamellar organisation in human cortical and trabecular bone. *Journal of the mechanical behavior of biomedical materials*, 12, pp.50–62. Available at: <http://www.ncbi.nlm.nih.gov/pubmed/22659366> [Accessed July 30, 2013].
- Vazquez, M. et al., 2014. A new method to investigate how mechanical loading of osteocytes controls osteoblasts. *Frontiers in Endocrinology*, 5(December), p.208. Available at: <http://www.pubmedcentral.nih.gov/articlerender.fcgi?artid=4260042&tool=pmcentrez&rendertype=abstract>.
- Verbruggen, S.W. et al., 2015. Altered Mechanical Environment of Bone Cells in an Animal Model of Short- and Long-Term Osteoporosis. *Biophysical Journal*, 108(7), pp.1587–1598. Available at: <http://linkinghub.elsevier.com/retrieve/pii/S0006349515002386>.
- Verbruggen, S.W., Vaughan, T.J. & McNamara, L.M., 2013. Fluid flow in the osteocyte mechanical environment: a fluid-structure interaction approach. *Biomechanics and modeling in mechanobiology*. Available at: <http://www.ncbi.nlm.nih.gov/pubmed/23567965> [Accessed July 23, 2013].
- Verbruggen, S.W., Vaughan, T.J. & McNamara, L.M., 2012. Strain amplification in bone mechanobiology: a computational investigation of the in vivo mechanics of osteocytes. *Journal of the Royal Society, Interface / the Royal Society*, 9(75), pp.2735–44. Available at: <http://www.pubmedcentral.nih.gov/articlerender.fcgi?artid=3427527&tool=pmcentrez&rendertype=abstract> [Accessed June 22, 2012].

Reference

- Wagner, D.R. et al., 2008. Hydrostatic pressure enhances chondrogenic differentiation of human bone marrow stromal cells in osteochondrogenic medium. *Annals of biomedical engineering*, 36(5), pp.813–20. Available at: <http://www.ncbi.nlm.nih.gov/pubmed/18266109> [Accessed May 22, 2013].
- Walther, I., Cogoli, M. & Egli, M., 2013. Microgravity Cell Culture Systems and Bioreactors: Current Status and Future Developments. *Current Biotechnology*, 2(3), pp.244–249. Available at: <http://www.ingentaconnect.com/content/ben/cbiot/2013/00000002/00000003/art00011>.
- Wang, C.C. et al., 2012. Cartilage regeneration in SCID mice using a highly organized three-dimensional alginate scaffold. *Biomaterials*, 33(1), pp.120–127. Available at: <http://dx.doi.org/10.1016/j.biomaterials.2011.09.042>.
- Wang, D. et al., 1999. Isolation and characterization of MC3T3-E1 preosteoblast subclones with distinct in vitro and in vivo differentiation/mineralization potential. *Journal of bone and mineral research : the official journal of the American Society for Bone and Mineral Research*, 14(6), pp.893–903. Available at: <http://www.ncbi.nlm.nih.gov/pubmed/10352097>.
- Wang, L. et al., 2005. In situ measurement of solute transport in the bone lacunar-canalicular system. *Proceedings of the National Academy of Sciences of the United States of America*, 102(33), pp.11911–11916.
- Wang, L. et al., 2000. Modeling tracer transport in an osteon under cyclic loading. *Annals of Biomedical Engineering*, 28(10), pp.1200–1209.
- Wang, L.S. et al., 2012. Enzymatically cross-linked gelatin-phenol hydrogels with a broader stiffness range for osteogenic differentiation of human mesenchymal stem cells. *Acta Biomaterialia*, 8(5), pp.1826–1837. Available at: <http://dx.doi.org/10.1016/j.actbio.2012.02.002>.
- Wang, Y. et al., 2007. A model for the role of integrins in flow induced mechanotransduction in osteocytes. *Proceedings of the National Academy of Sciences*, 104(40), pp.15941–15946. Available at: <http://www.pnas.org/content/104/40/15941.abstract>.
- Webster, D.J. et al., 2013. Studying osteocytes within their environment. *Bone*, 54(2), pp.285–295. Available at: <http://linkinghub.elsevier.com/retrieve/pii/S8756328213000100>.
- Weinbaum, S., Cowin, S.C. & Zeng, Y., 1994. A model for the excitation of osteocytes by mechanical loading-induced bone fluid shear stresses. *Journal of Biomechanics*, 27(3), pp.339–360.
- Wen, A. et al., 2016. Skin tissue engineering advances in severe burns: review and therapeutic applications. *Burns & Trauma*, pp.1–14. Available at: <http://dx.doi.org/10.1186/s41038-016-0027-y>.
- Wendt, D. et al., 2003. Oscillating perfusion of cell suspensions through three-dimensional scaffolds enhances cell seeding efficiency and uniformity. *Biotechnology and bioengineering*, 84(2), pp.205–14. Available at: <http://www.ncbi.nlm.nih.gov/pubmed/12966577> [Accessed August 6, 2012].
- Whyte, M.P., 2006. Paget's Disease of Bone. *New England Journal of Medicine*, 355(6),

- pp.593–600. Available at: <http://dx.doi.org/10.1056/NEJMcp060278>.
- Wittkowske, C. et al., 2016. In Vitro Bone Cell Models: Impact of Fluid Shear Stress on Bone Formation. *Frontiers in Bioengineering and Biotechnology*, 4(November). Available at: <http://journal.frontiersin.org/article/10.3389/fbioe.2016.00087/full>.
- Wolff, J., 1986. Concept of the Law of Bone Remodelling. In *The Law of Bone Remodelling*. Berlin, Heidelberg: Springer Berlin Heidelberg, p. 1. Available at: http://dx.doi.org/10.1007/978-3-642-71031-5_1.
- Woo, S.M. et al., 2011. Cell line IDG-SW3 replicates osteoblast-to-late-osteocyte differentiation in vitro and accelerates bone formation in vivo. *Journal of bone and mineral research : the official journal of the American Society for Bone and Mineral Research*, 26(11), pp.2634–46. Available at: <http://www.pubmedcentral.nih.gov/articlerender.fcgi?artid=3192242&tool=pmcentrez&rendertype=abstract> [Accessed April 29, 2014].
- Woolf, A.D., 2007. Healthcare services for those with musculoskeletal conditions: a rheumatology service. Recommendations of the European Union of Medical Specialists Section of Rheumatology/European Board of Rheumatology 2006. *Annals of the rheumatic diseases*, 66(3), pp.293–301. Available at: <http://www.pubmedcentral.nih.gov/articlerender.fcgi?artid=1856014&tool=pmcentrez&rendertype=abstract>.
- Wu, S. et al., 2014. Biomimetic porous scaffolds for bone tissue engineering. *Materials Science and Engineering R: Reports*, 80(1), pp.1–36. Available at: <http://dx.doi.org/10.1016/j.msere.2014.04.001>.
- Yamada, N., Kim, W. & Yoshida, T., 2013. Effect of Gelatin β -tricalcium Phosphate Sponge with Platelet-rich Plasma on Bone Regeneration in Massive Ulna Defects. *Journal of Medical ...*, 33(6), pp.545–551. Available at: <http://jmbe.bme.ncku.edu.tw/index.php/bme/article/viewArticle/2029> [Accessed January 15, 2014].
- Yan, L.-P. et al., 2016. Tumor Growth Suppression Induced by Biomimetic Silk Fibroin Hydrogels. *Scientific Reports*, 6(August), p.31037. Available at: <http://dx.doi.org/10.1038/srep31037%5Cnhttp://10.1038/srep31037%5Cnhttp://www.nature.com/articles/srep31037#supplementary-information>.
- Yarlagadda, P.K.D. V, Chandrasekharan, M. & Shyan, J.Y.M., 2005. Recent advances and current developments in tissue scaffolding. *Bio-medical materials and engineering*, 15(3), pp.159–77. Available at: <http://www.ncbi.nlm.nih.gov/pubmed/15911997>.
- Yeatts, A.B. et al., 2014. *In Vivo* Bone Regeneration Using Tubular Perfusion System Bioreactor Cultured Nanofibrous Scaffolds. *Tissue Engineering Part A*, 20(1–2), pp.139–146. Available at: <http://online.liebertpub.com/doi/abs/10.1089/ten.tea.2013.0168>.
- Yeatts, A.B. & Fisher, J.P., 2011. Bone tissue engineering bioreactors: dynamic culture and the influence of shear stress. *Bone*, 48(2), pp.171–81. Available at: <http://www.ncbi.nlm.nih.gov/pubmed/20932947> [Accessed July 27, 2012].
- Yin, Y. et al., 2003. Preparation and characterization of macroporous chitosan-gelatin/beta-tricalcium phosphate composite scaffolds for bone tissue engineering. *Journal of biomedical materials research. Part A*, 67(3), pp.844–55. Available at:

- <http://www.ncbi.nlm.nih.gov/pubmed/14613233>.
- You, F. et al., 2016. 3D Printing of Porous Cell-laden Hydrogel Constructs for Potential Applications in Cartilage Tissue Engineering. *ACS Biomaterials Science & Engineering*, 2, pp.1200–1210.
- You, L. et al., 2001. A model for strain amplification in the actin cytoskeleton of osteocytes due to fluid drag on pericellular matrix. *Journal of Biomechanics*, 34(11), pp.1375–1386.
- You, L.-D. et al., 2004. Ultrastructure of the osteocyte process and its pericellular matrix. *The anatomical record. Part A, Discoveries in molecular, cellular, and evolutionary biology*, 278(2), pp.505–513.
- Yu, X. et al., 2015. Biomaterials for Bone Regenerative Engineering. *Advanced Healthcare Materials*, 4(9), pp.1268–1285.
- Yuan, H. et al., 2010. Osteoinductive ceramics as a synthetic alternative to autologous bone grafting. *Proceedings of the National Academy of Sciences of the United States of America*, 107(31), pp.13614–9. Available at: <http://www.pubmedcentral.nih.gov/articlerender.fcgi?artid=2922269&tool=pmcentrez&rendertype=abstract> [Accessed October 24, 2013].
- Yung, C. & Wu, L., 2007. Transglutaminase crosslinked gelatin as a tissue engineering scaffold. *Journal of biomedical Materials Research Part A*. Available at: <http://onlinelibrary.wiley.com/doi/10.1002/jbm.a.31431/full> [Accessed December 3, 2013].
- Zaman, M. & Trapani, L., 2006. Migration of tumor cells in 3D matrices is governed by matrix stiffness along with cell-matrix adhesion and proteolysis. *Proceedings of the National Academy of Sciences*, 103(15), pp.10889–10894. Available at: <http://www.pnas.org/content/103/29/10889.short> [Accessed November 15, 2013].
- Zang, R. et al., 2012. Cell-Based Assays in High-Throughput Screening for Drug Discovery. *International Journal of Biotechnology for Wellness Industries*, 1, pp.31–51. Available at: <http://www.lifescienceglobal.com/pms/index.php/ijbwi/article/view/94>.
- Zeng, Y., Cowin, S.C. & Weinbaum, S., 1994. A fiber-matrix model for fluid-flow and streaming potentials in the canaliculi of an osteon. *Annals of Biomedical Engineering*, 22(3), pp.280–292.
- Zhang, K. et al., 2006. E11/gp38 selective expression in osteocytes: regulation by mechanical strain and role in dendrite elongation. *Molecular and cellular biology*, 26(12), pp.4539–52. Available at: <http://www.pubmedcentral.nih.gov/articlerender.fcgi?artid=1489126&tool=pmcentrez&rendertype=abstract> [Accessed August 14, 2014].
- Zhang, Z.Y. et al., 2009. A biaxial rotating bioreactor for the culture of fetal mesenchymal stem cells for bone tissue engineering. *Biomaterials*, 30(14), pp.2694–2704. Available at: <http://dx.doi.org/10.1016/j.biomaterials.2009.01.028>.
- Zhao, F., Vaughan, T.J. & McNamara, L.M., 2014. Multiscale fluid-structure interaction modelling to determine the mechanical stimulation of bone cells in a tissue engineered scaffold. *Biomechanics and Modeling in Mechanobiology*, pp.231–243.
- Zhao, F., Vaughan, T.J. & McNamara, L.M., 2015. Quantification of fluid shear stress in

- bone tissue engineering scaffolds with spherical and cubical pore architectures. *Biomechanics and Modeling in Mechanobiology*. Available at: <http://link.springer.com/10.1007/s10237-015-0710-0>.
- Zheng, R. et al., 2013. The influence of Gelatin/PCL ratio and 3-D construct shape of electrospun membranes on cartilage regeneration. *Biomaterials*, pp.1–13. Available at: <http://www.ncbi.nlm.nih.gov/pubmed/24135269> [Accessed October 21, 2013].
- Zheng, W., Thorne, N. & McKew, J.C., 2013. Phenotypic screens as a renewed approach for drug discovery. *Drug Discovery Today*, 18(21–22), pp.1067–1073. Available at: <http://dx.doi.org/10.1016/j.drudis.2013.07.001>.
- Zhou, H., Weir, M.D. & Xu, H.H.K., 2011. Effect of cell seeding density on proliferation and osteodifferentiation of umbilical cord stem cells on calcium phosphate cement-fiber scaffold. *Tissue engineering. Part A*, 17(21–22), pp.2603–13. Available at: <http://www.pubmedcentral.nih.gov/articlerender.fcgi?artid=3204200&tool=pmcentrez&rendertype=abstract> [Accessed September 30, 2014].
- Zisch, A.H. et al., 2003. Cell-demanded release of VEGF from synthetic, biointeractive cell ingrowth matrices for vascularized tissue growth. *The FASEB Journal*, 17(15), pp.2260–2262.
- Zouani, O.F. et al., 2013. Insights into the osteoblast precursor differentiation towards mature osteoblasts induced by continuous BMP-2 signaling. *Biology open*, 2(9), pp.872–81. Available at: <http://www.pubmedcentral.nih.gov/articlerender.fcgi?artid=3773333&tool=pmcentrez&rendertype=abstract> [Accessed January 23, 2014].

Appendix 1

1.1 Bioreactor in-house fabrication and construction

Bioreactor fabrication and construction was performed in-house at NUI Galway Engineering Building. The main components of the bioreactor, such as motor mounts, bearing holders and frames were fabricated using computer numeric control (CNC) machining, required G-code development, tools selection, cutting speeds and feed rates. Manual machining was performed to finishes off parts, such as tapping, cutting and drilling.

1.1.1.1 CNC machining

Automated CNC machining was carried out using a Haas TM1P Toolroom mill, capable of multiple tool changes during operation, high machining accuracy of 0.001 mm and precise machining profiles, see Figure 1-1. The Haas CNC mill is capable of 2.5 axis machining of one side of a part at a time before removing and rotating the part to the new machining side.



Figure 1-1: Haas TM1P CNC Toolroom mill used to automatically machine bioreactor parts

1.1.1.2 Material machining requirements and tool selection, G-codes, toolpath types and machine/workpiece setup

Machining of polycarbonate and aluminium required identifying appropriate cutters, spindle speeds and feed rates to achieve a clean finished cut. Polycarbonate and aluminium manufactures recommend using high speed steel (HSS) cutters, with cutting speed of ~200 m/min and max feed per tooth of ~0.2 mm along with climb milling as the main cutting technique. For different diameter tools and number of teeth, equations 2.2 – 2.4 were used to determine the appropriate cutting speeds, table feed rate and feed per tooth. The appropriate size and selection of machining tools was determined from the geometry of the slots, pockets and holes within the bioreactor design, requiring drill bits, end mills, thread mills and cutters compatible with polycarbonate and aluminium machining, see Table 4 for table cutting information.

$$V_c = \frac{\pi \times \text{cutting Diameter} \times n}{1000} \quad (2.2)$$

V_c = Cutting speed (m/min), n = spindle speed

$$V_f = V_f \times n \times ZEFF \quad (3.3)$$

V_f = Table feed (mm/min), n = spindle speed, ZEFF = number of teeth

$$f_z = \frac{V_f}{n \times ZEFF} \quad (4.4)$$

f_z = Feed/tooth (min), V_f = Table feed (mm/min), n = spindle speed, ZEFF = number of teeth

No.	Description	Cutter Diameter (mm)	No. of flutes	Cutting speed (m/min)	Feed/tooth (mm)	Ramp Feed rate (mm/min)	Lead in/out Feed rate (mm/min)	Plunge Feed rate (mm/min)	Spindle (Rpm)	Cutting Feed rate (mm/min)
1	M3 Thread Mill (D2.4)	2.4	3	45.23893	0.0155	379	500		6000	279
2	Chamfer (45 deg)	20	10	125.6637	0.01	300	500	50	2000	200
3	14mm Flat End mill	14	2	175.9292	0.014	212	500	100	4000	112
4	2mm Flat long series	2	2	31.41593	0.014	240	500	100	5000	140
5	1mm Flat CarbideMicro100	1	2	15.70796	0.014	240	500	100	5000	140
6	4mm Flat long series	4	2	62.83185	0.014	240	500	100	5000	140
7	6mm Flat spiral Clarkson	6	2	94.24778	0.015	250	500	100	5000	150
8	20mm Flat End mill	20	4	188.4956	0.014	268	500	100	3000	168
9	50mm Face mill	50	5	157.0796	0.014	170	500	100	1000	70
10	M2x0.4 Machine Tap	2							250	
11	1.6 drill bit	1.6					500	125	1750	
12	3.3 drill bit	3.3					500	125	1750	
13	4 drill bit	4					500	100	1500	
14	3 drill bit long series	3					500	125	1750	
15	2.5 drill bit long series	2.5					500	125	1750	
16	2 drill long series	2					500	125	1750	
17	Counter sink	20					500	50	1000	

Table 4: Table of different tools, spindle speeds and feed rates used in the fabrication of bioreactor parts.

G-codes to operate the CNC were developed through HSM Inventor CAM software. Firstly, a model of the CNC vice was imported into CAD software to assist in identifying boundary conditions such as work piece surrounding area, tool operating position and the zero reference coordinate, see Figure 1-2 (A). Subsequently, specific tool machining paths were developed, involving “toolpaths” such as thread milling, pocket milling, contour milling and slot milling, see Figure 1-2 (B). This allowed for the formation of geometries such as threaded shafts, gasket gland channels (1.4 x 0.7 mm), 45° chambers, 2mm fluid flow channels and automatic threading of M2 x 0.4 mm holes.

Fabrication of the bioreactor chamber required the machining of 13 complex parts from polycarbonate, which if individually setup within the CNC would result in a lengthy processing time. Therefore, the bioreactor chamber parts were split-up into three sections that were machined from three stock blocks. This involved using a “plastic model” technique, with parts manufactured using a “sprue” frame surrounding the various parts, allowing for precise machining of parts, while also reducing the time associated with the setup of individual parts, see Figure 1-2 (C). G-codes were developed for each of these three parts. Fabrication of the compression loading rig required the machining of the polycarbonate loading frame and

aluminium, consisting of 3 motor mounts and 2 compression arms parts. The same “sprue” method was used to manufacture the aluminium parts and the associated g-codes.

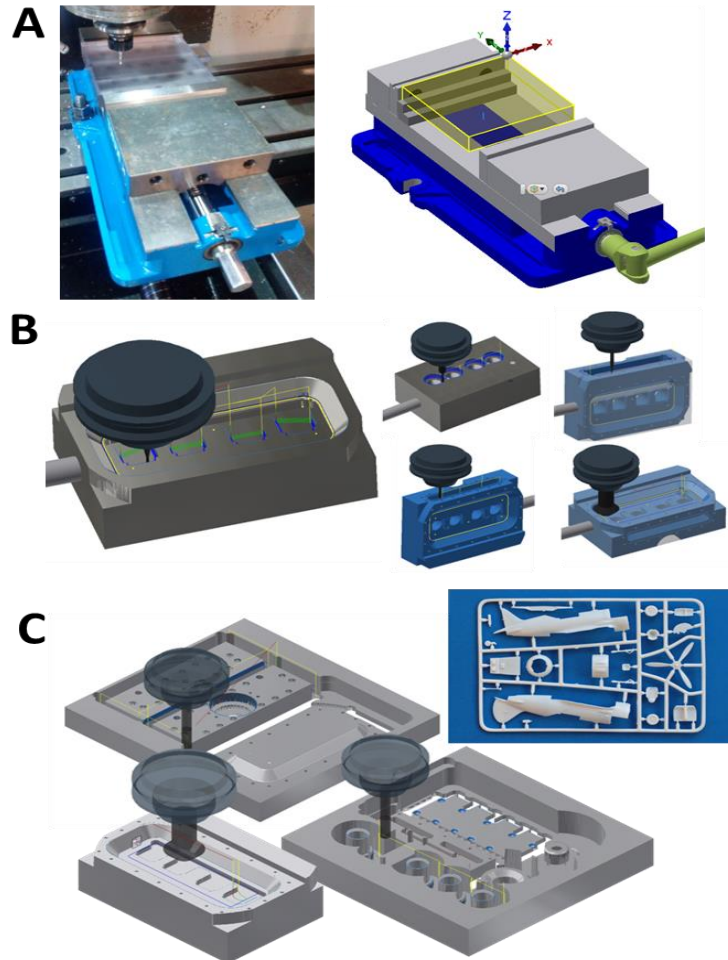


Figure 1-2: A model of CNC vice used for the development machining paths boundary conditions and zero coordinate offset (A). Sample toolpaths generated for machining out geometries bioreactor (B). Multiple bioreactor chamber parts, machined out using a “Sprue” machining approach from three different stock blocks (C).

1.1.1.3 CNC machine setup

After G-code development, the CNC mill was setup for machining, requiring the loading of machining tools within the carousel and zeroing of tool heights to the same offset, see Figure 1-3 (A). The CNC vice was set parallel to work table using the pressure probe. During polycarbonate cutting compressed air was used as

coolant, and as a method to clear waste material (swarf) from the cutter preventing tool overheating. Furthermore, detergent was used for tapping reducing friction during threading. While, water oil based coolant was used for aluminium. Finally, stock blocks were loaded in the CNC vice with zero (x,y,z) reference coordinate zeroed using a pressure probe, see Figure 1-3 (E).

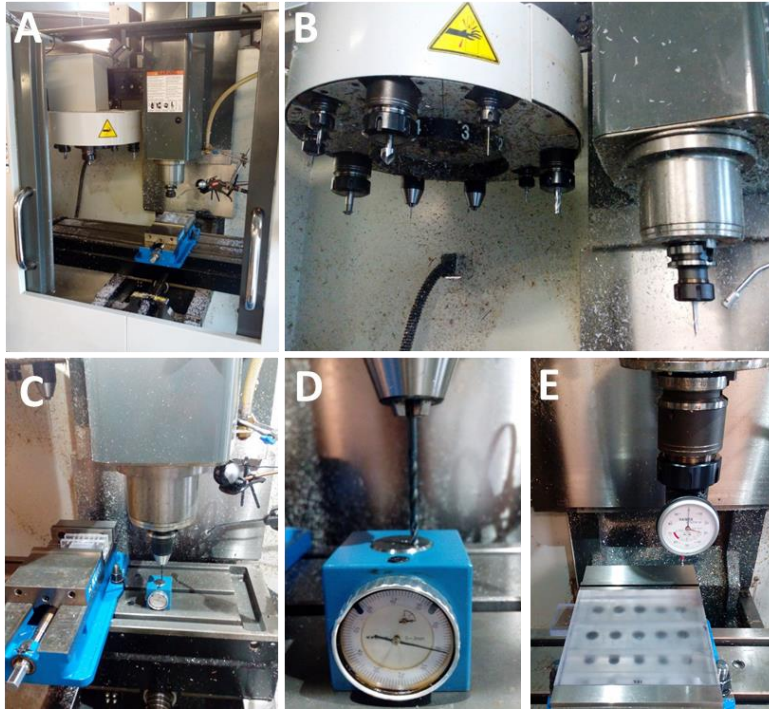


Figure 1-3: Tools setup on carousel (A&B) and hence all tool heights to the same offset using a pressure height gauge (C&D). Stock coordinate position and parameters setup with CNC vice and zero reference coordinate taken from fixed end of vice (E).

1.1.1.4 Cutting and face milling stock blocks

In preparation for CNC machining, purchased material was cut to rough stock dimensions, using a horizontal band and vertical table saw, see Figure 1-4 (B&C). After initial machining, stock parts were CNC machined to precise dimensions of the stock block, using face milling, producing parallel sides and flat surfaces finished to a high standard, see Figure 1-4 (E&F).

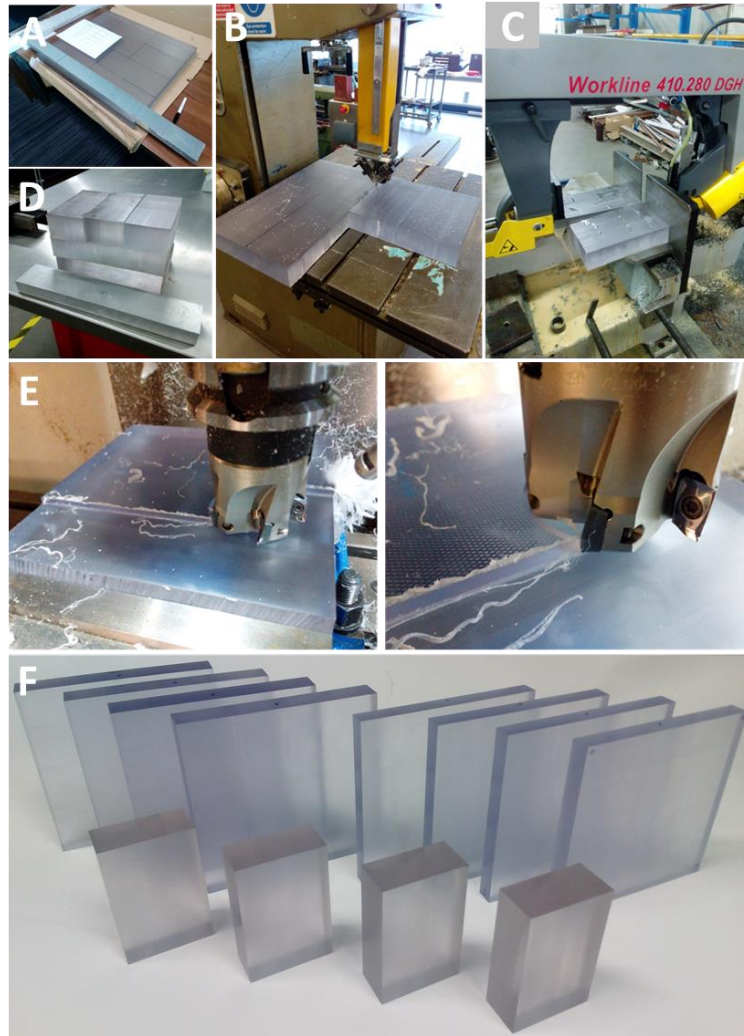


Figure 1-4: Polycarbonate and aluminium stock purchased parts (A) cut to rough stock dimensions using vertical (B) and horizontal band saw (C). Subsequently, precise face milling (E) carried out of stock parts forming parallel sides and smooth surfaces (F) for CNC machining.

1.1.1.5 Machining bioreactor components

CNC machining was carried out firstly on the bioreactor chamber components. Small components were machined initially, allowing for tolerance testing of moving components within larger parts, such as fitting of the compression chamber and the observation windows within the bioreactor chamber. Complicated geometries required detail machining profiles, such as 2 mm high channels for fluid flow and observation window threading for screw compression sealing, see Figure 1-5. After CNC machining, manual processing was carried out to finalise parts, involving thread tapping and swarf clearing, see Figure 1-6.



Figure 1-5: Machining of bioreactor chamber parts using the “sprue” technique. Precise stock blocks were loaded in the CNC vice with machining performed on two sides. Nine parts were created from A and three from B.

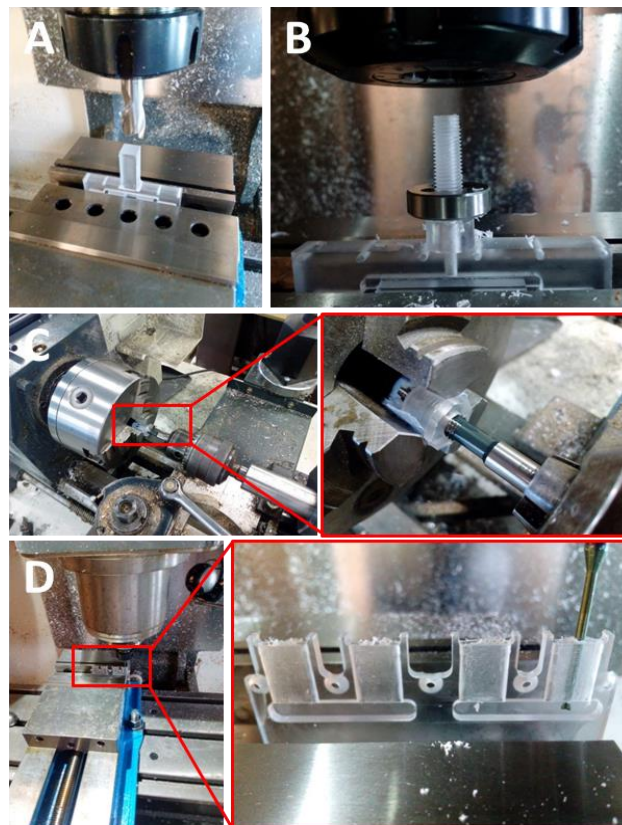


Figure 1-6: After removal of parts from the “sprue” further machining was performed (A), such as threading of the compression arm and nut (B & C). To allow

for fluid flow 2 mm high channels were machined out with a 2mm end mill cutter (D).

CNC machining of the main bioreactor chamber frame, required machining on four sides of the stock block, see Figure 1-7. Each side was tested for tolerances by testing the fit of corresponding parts in their homes, such as the compression arm and objective windows. Finally, the compression frame was machined of polycarbonate along with the aluminium motor mounts and the compression arm, see Figure 1-8.



Figure 1-7: CNC machining carried out on four sides of the bioreactor chamber stock block. Bioreactor windows were first machined out with thread milling performed (A-C). Machining of side 2 formed a slot for the compression chamber (D-F). Machining of side 3 formed 2 mm channels for fluid flow (G-I). Finally machining of side 4 preformed for observation window and 1 mm channels for calibration points through 1 mm End mill and 45° chambering (J-K).

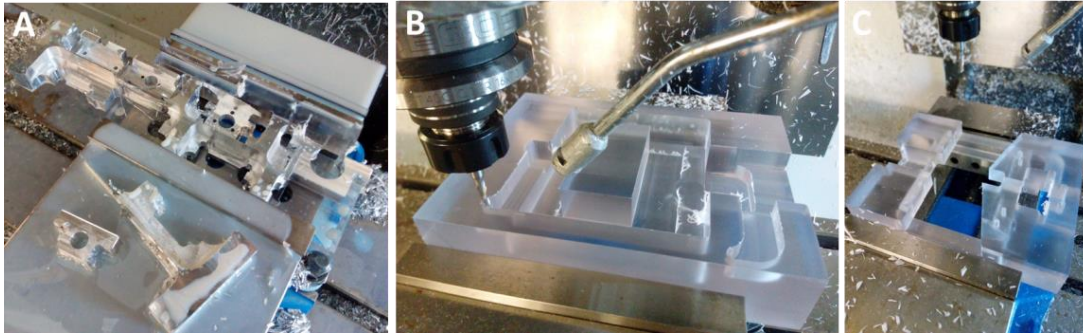


Figure 1-8: Fabrication of the compression rig. Five aluminium parts machined out using the “sprue” method (A). Subsequently, machining performed on two side of the polycarbonate compression rig frame (B-C)

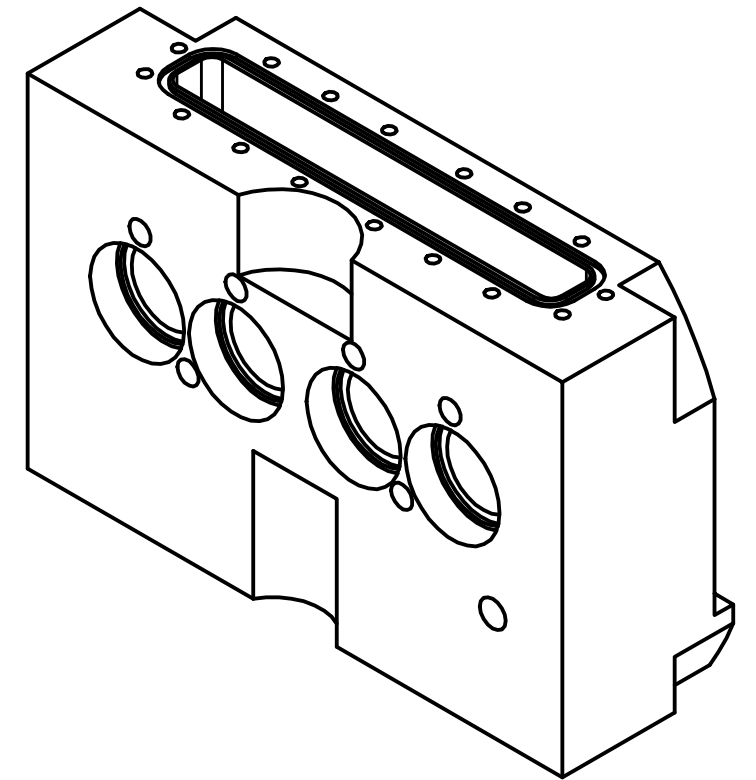
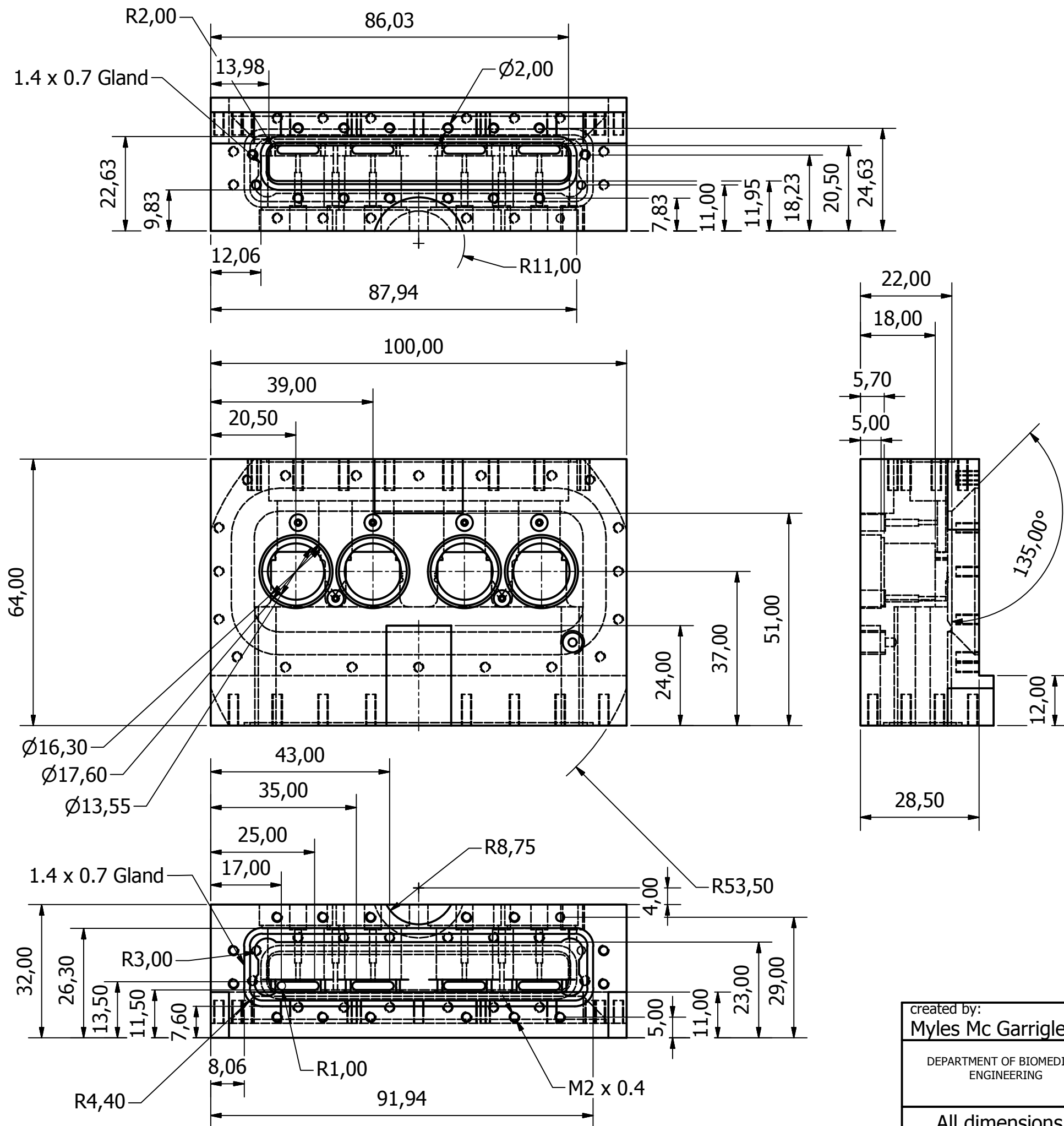
1.1.2 Bioreactor fabrication cost

It was estimated the total cost of the components required in the assembly of one bioreactor was approximately EUR 2,500, see Table 5. However, these costs were based on one off purchases, which would significantly reduce based on the volume of the orders. Manufacturing a single bioreactor took approximately 3 weeks at 7 hours a day, equating to 35 hours. Research online identified an average labour cost per hour of EUR 100 for out-source CNC machining. It was approximated that the current manufacturing process and the cost of machining tools equated to EUR 4000 for the fabrication of parts for one bioreactor. However, using properly setup manufacturing assembly lines, such as injection moulding and 3D printing this cost would significantly reduce. Overall, fabricating a bioreactor prototype costs approximately EUR 6,500. However, it is assumed in the case of bulk ordering and streamlined manufacturing processes bioreactor fabrication could be significantly reduced. Future work could look at refining the manufacturing process or identify possible alternatives such as injection moulding or 3D printing.

Description	Category	Total (Euro)
Programmable Syringe Pump (PUMP-NE-1000)	Equipment	€900.50
Precision Ball Screw and machining requirements	Bioreactor Parts	€735.70
Pillow ball bearing mount and support bearing	Bioreactor Parts	€116.87
Stepper Motor & Gearbox	Bioreactor Parts	€111.50
Stepper driver (SMCI 12 RS485)	Bioreactor Parts	€71.79
Cable set for stepper driver (ZK-SMCI12, ZK-XHP4-300, ZK-RS485-USB)	Electronics	€111.56
Electronic control box and connectors	Electronics	€48.03
Sealing gaskets	Bioreactor Parts	€135.00
Purchasing and cutting sintered porous platens	Bioreactor Parts	€80.00
Elbows fittings	Bioreactor Parts	€32.00
Material (Polycarbonate and Aluminium)	Bioreactor Parts	€150.00
Bolts	Bioreactor Parts	€30.00
		€2,522.95

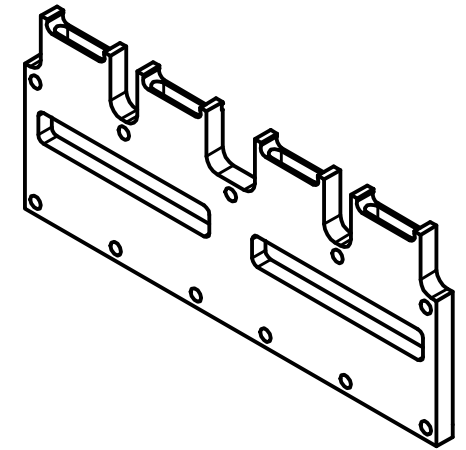
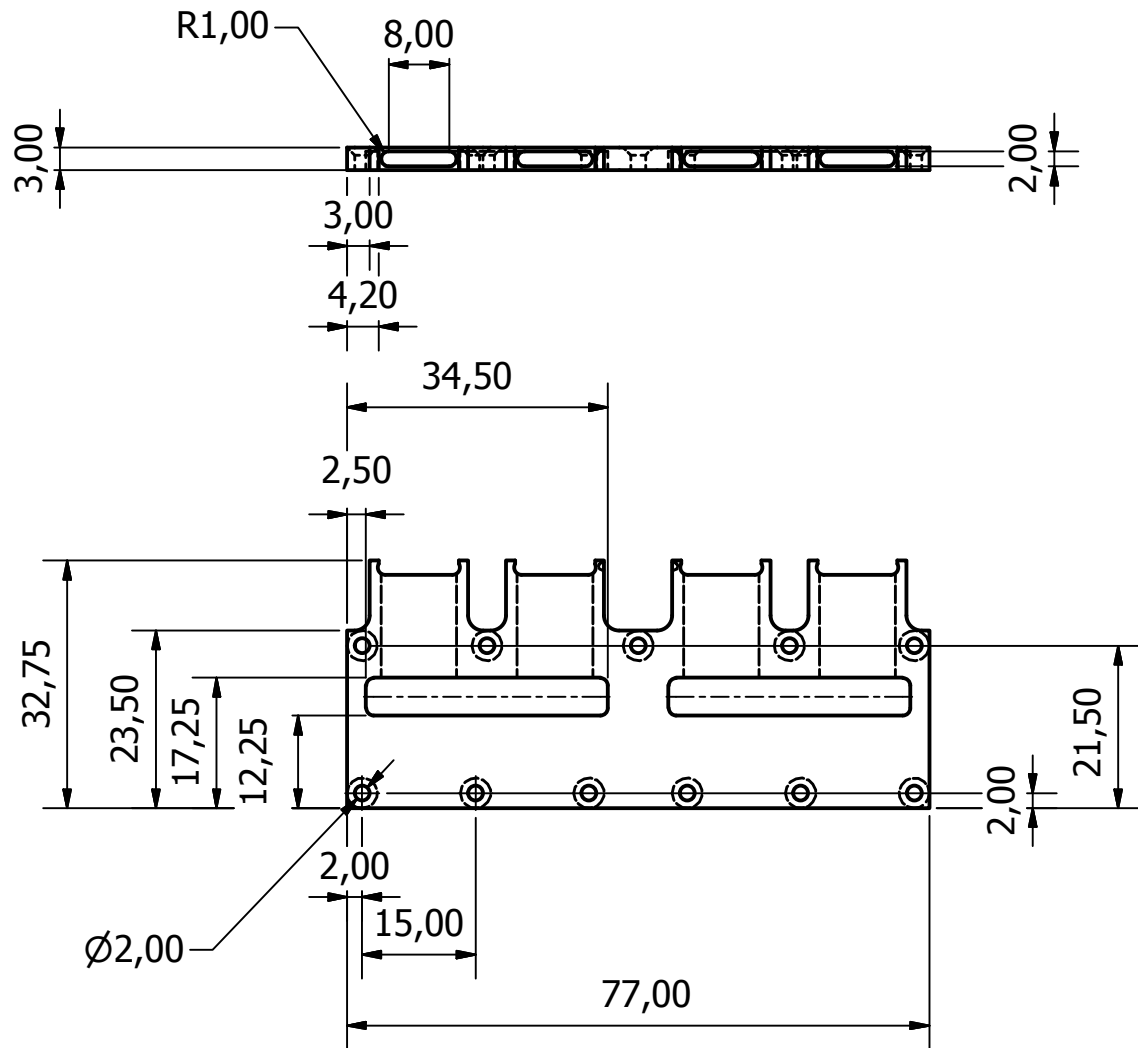
Table 5: Illustrates the approximate amount of the components and equipment required to fabricate one bioreactor device. This does not include labour and manufacturing costs.

Appendix 2



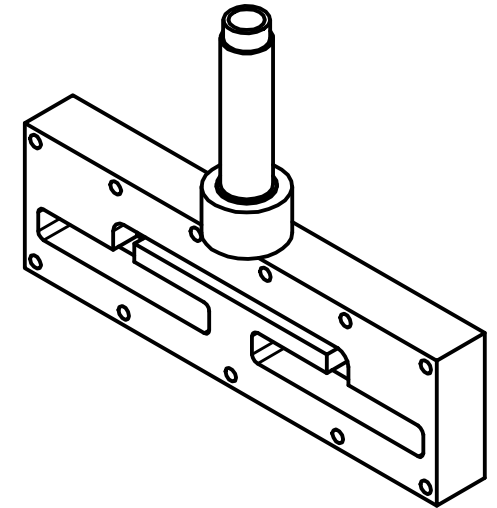
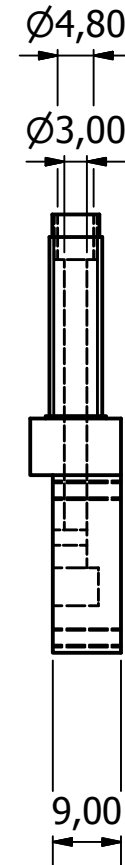
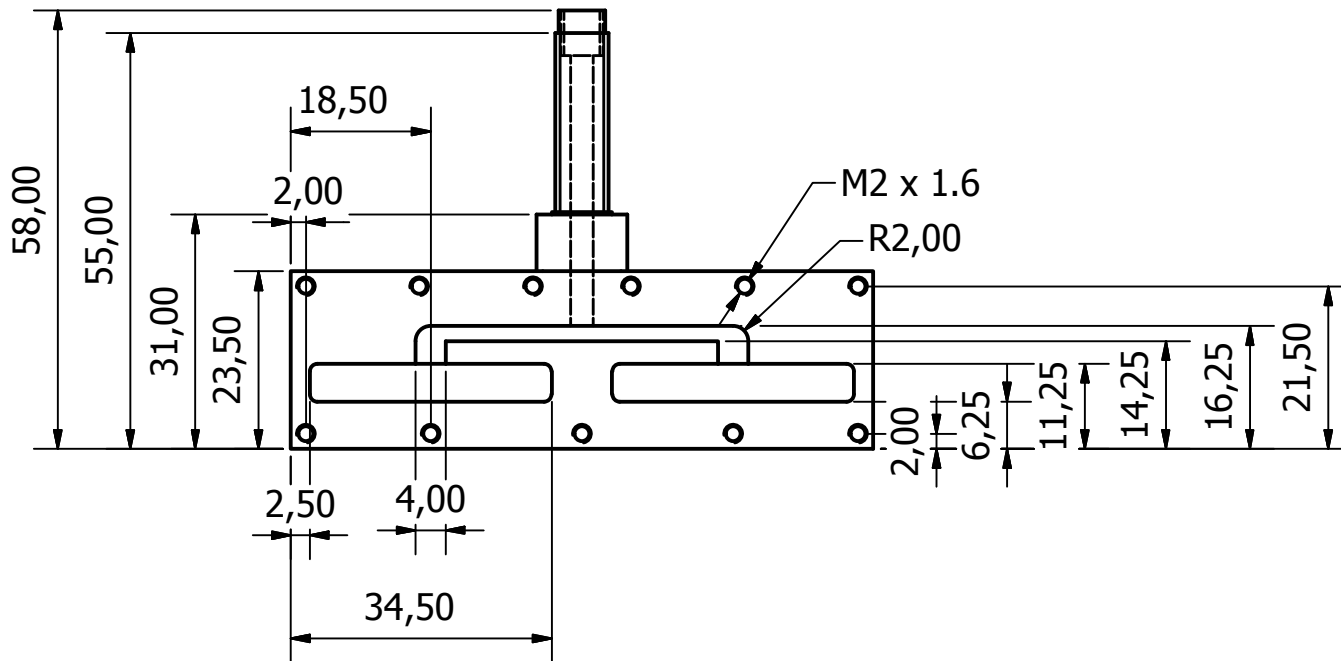
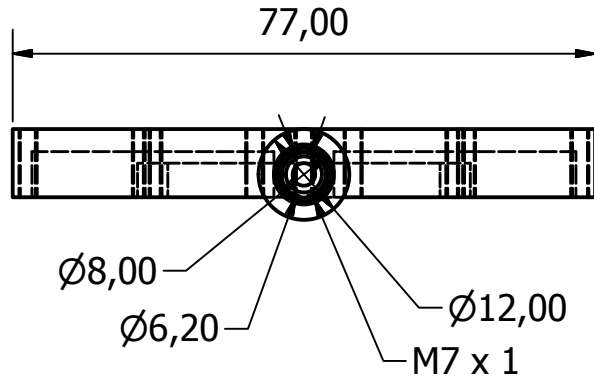
created by: Myles Mc Garrigle	approved by	Document type IDW	ID 08307598
DEPARTMENT OF BIOMEDICAL ENGINEERING		Title: 1:2	Scale: 1:2
All dimensions in mm		Date 17/08/2015	Sheet: 1 of 1
		Drawing no. CPB-16-1-P	

Material: Polycarbonate



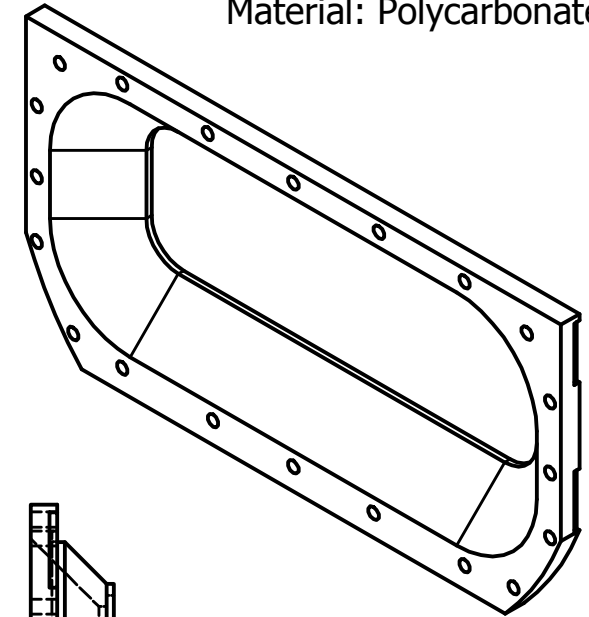
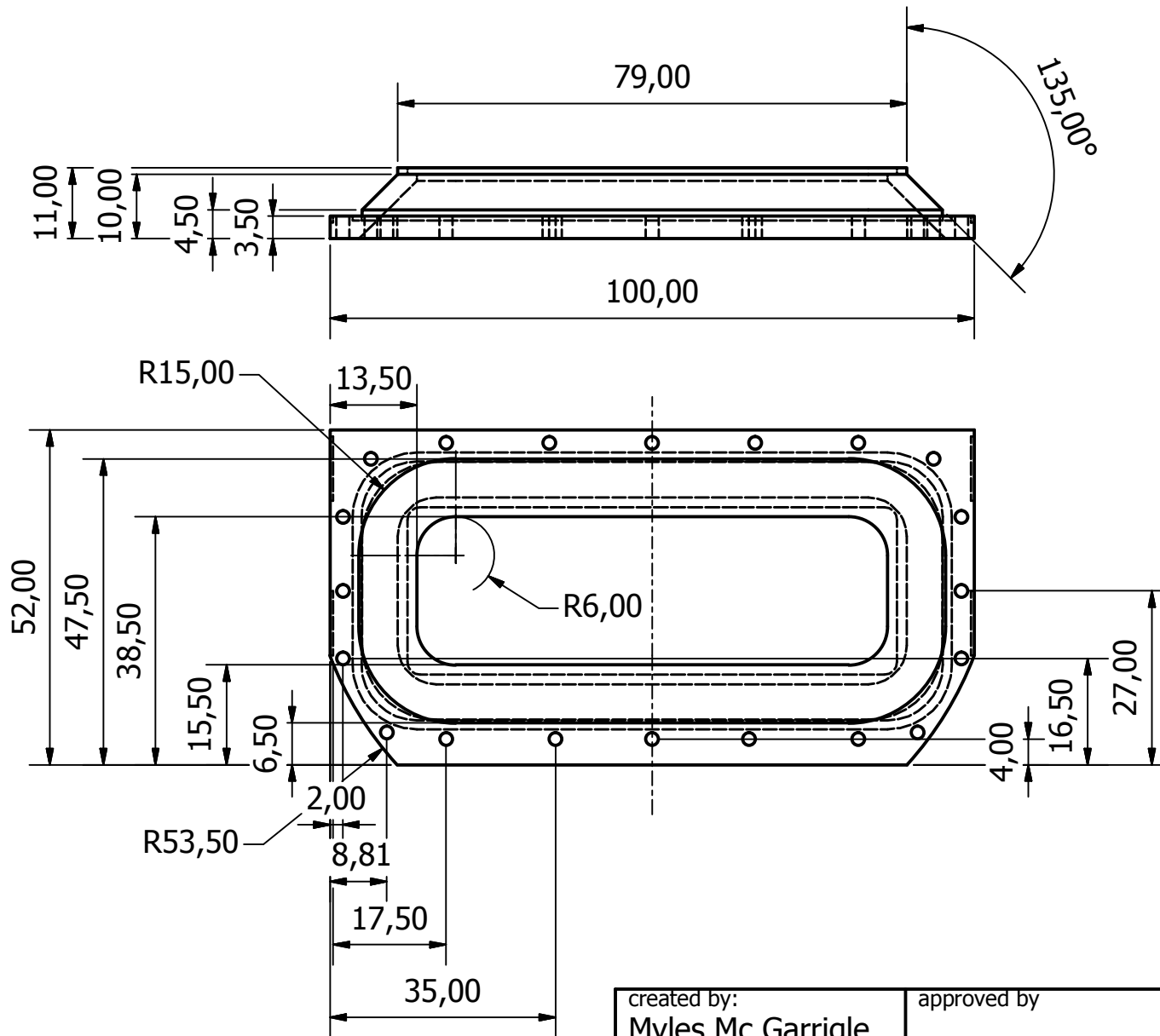
created by: Myles Mc Garrigle	approved by	Document type IDW	ID 08307598
DEPARTMENT OF BIOMEDICAL ENGINEERING		Title: CPB-16-2-P (MultiCompressionPlaten4Channel)	
		Scale: 1:1	Sheet: 1 of 1
All dimensions in mm	Date 24/06/2015	Drawing no. CPB-16-2-P	

Material: Polycarbonate



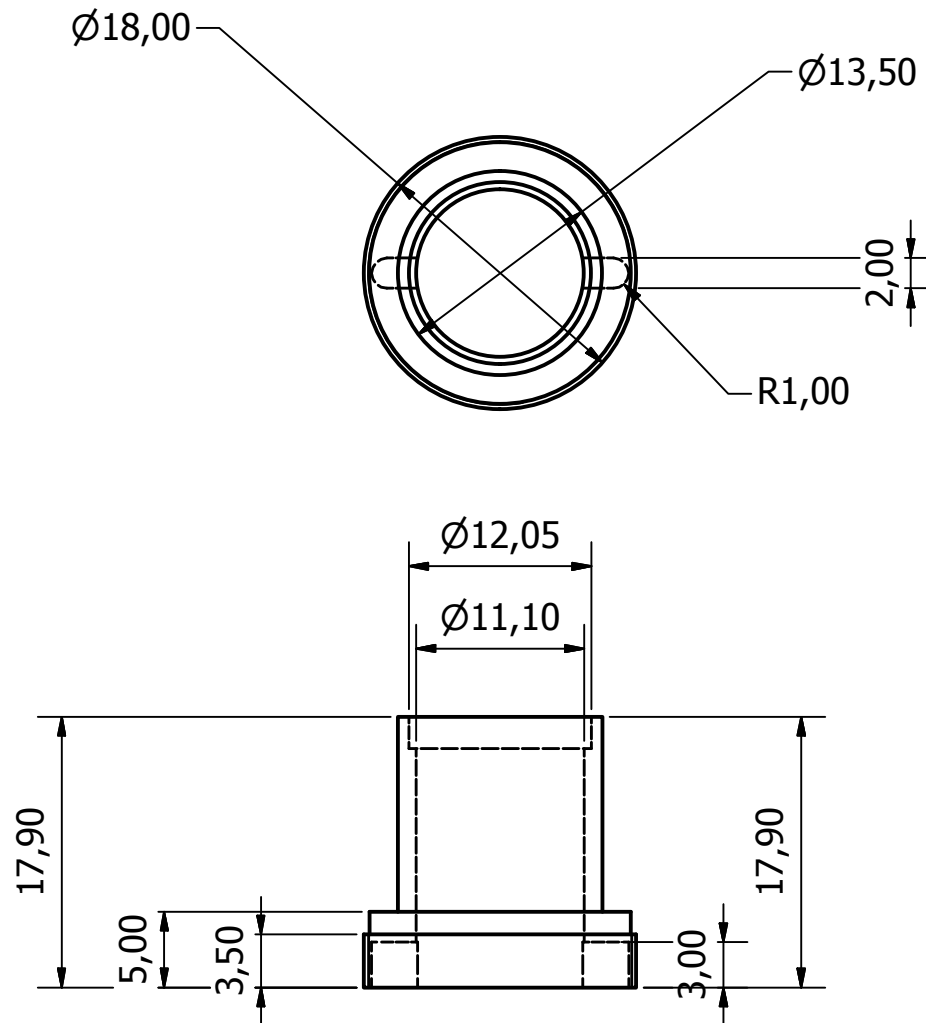
created by: Myles Mc Garrigle	approved by	Document type IDW	ID 08307598
DEPARTMENT OF BIOMEDICAL ENGINEERING		Title: CPB-16-3-P (MultiCompressionPlaten)	
		Scale: 1:1	Sheet: 1 of 1
All dimensions in mm		Date 25/06/2015	Drawing no. CPB-16-3-P

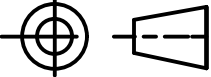
Material: Polycarbonate

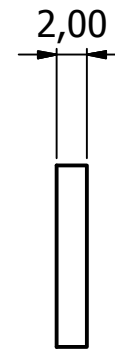
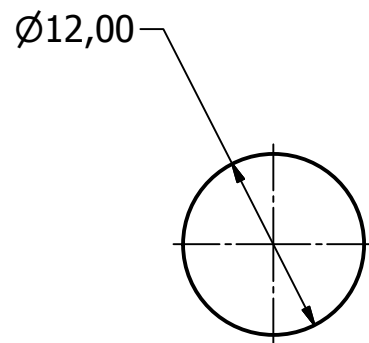


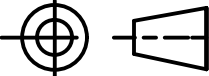
created by: Myles Mc Garrigle	approved by	Document type IDW	ID 08307598
DEPARTMENT OF BIOMEDICAL ENGINEERING		Title: CPB-16-4-P(ObjectiveViewWindow)	
		Scale: 1:1	Sheet: 1 of 1
All dimensions in mm		Date 07/05/2015	Drawing no. CPB-16-4-P

Material: Polycarbonate

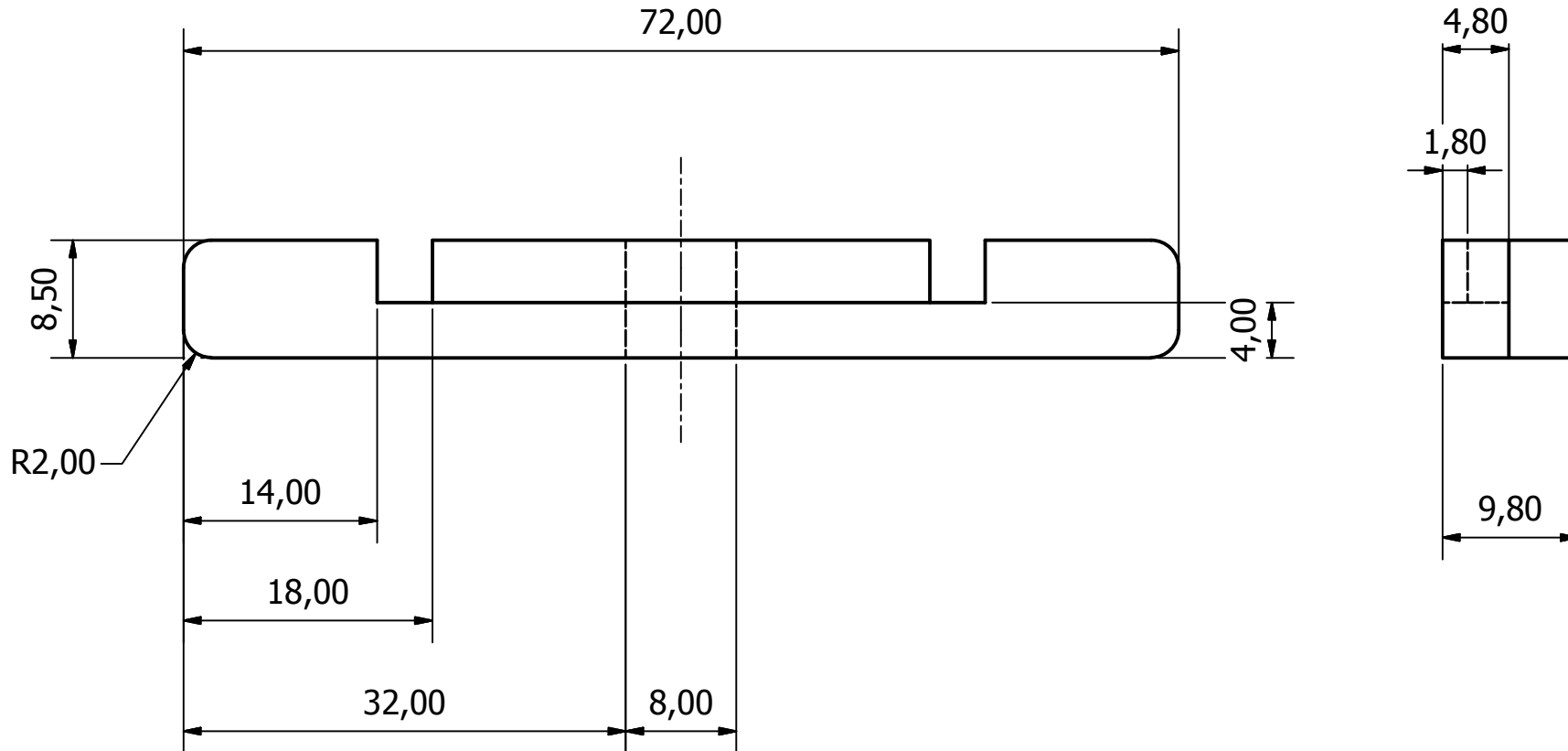


created by: Myles Mc Garrigle	approved by	Document type IDW	ID 08307598
DEPARTMENT OF BIOMEDICAL ENGINEERING		Title: CPB-16-5-P (TopViewWindow)	
		Scale: 2:1	Sheet: 1 of 1
All dimensions in mm		Date 07/05/2015	Drawing no. CPB-16-4-P



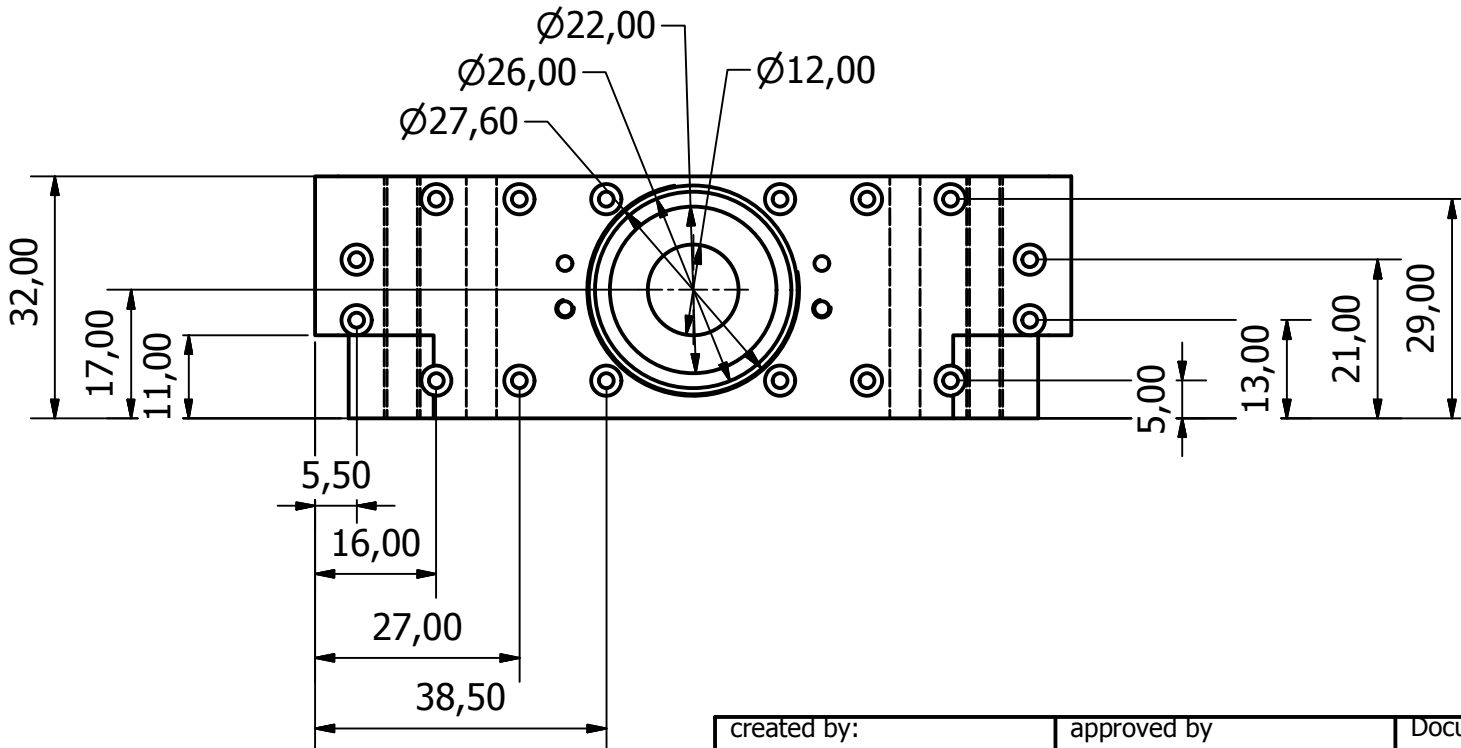
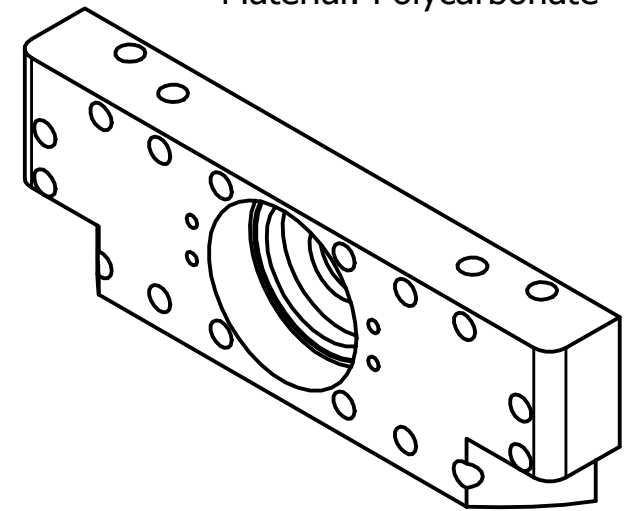
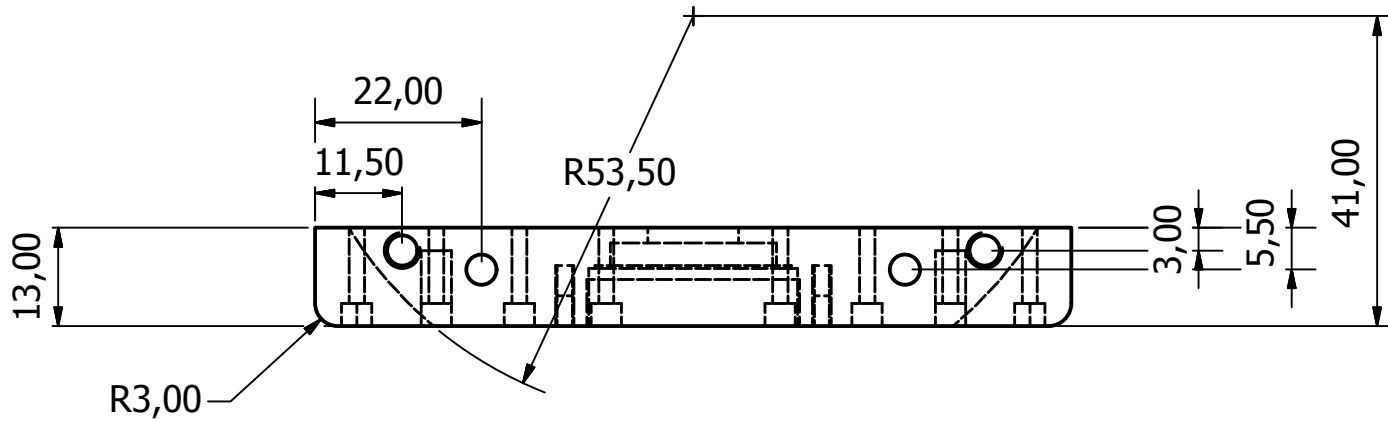
created by: Myles Mc Garrigle	approved by	Document type IDW	ID 08307598
DEPARTMENT OF BIOMEDICAL ENGINEERING		Title: CPB-16-6-P (TopWindowTransDisk)	
		Scale: 2:1	Sheet: 1 of 1
All dimensions in mm	Date 07/11/2015	Drawing no. CPB-16-1-P	

Material: Polycarbonate



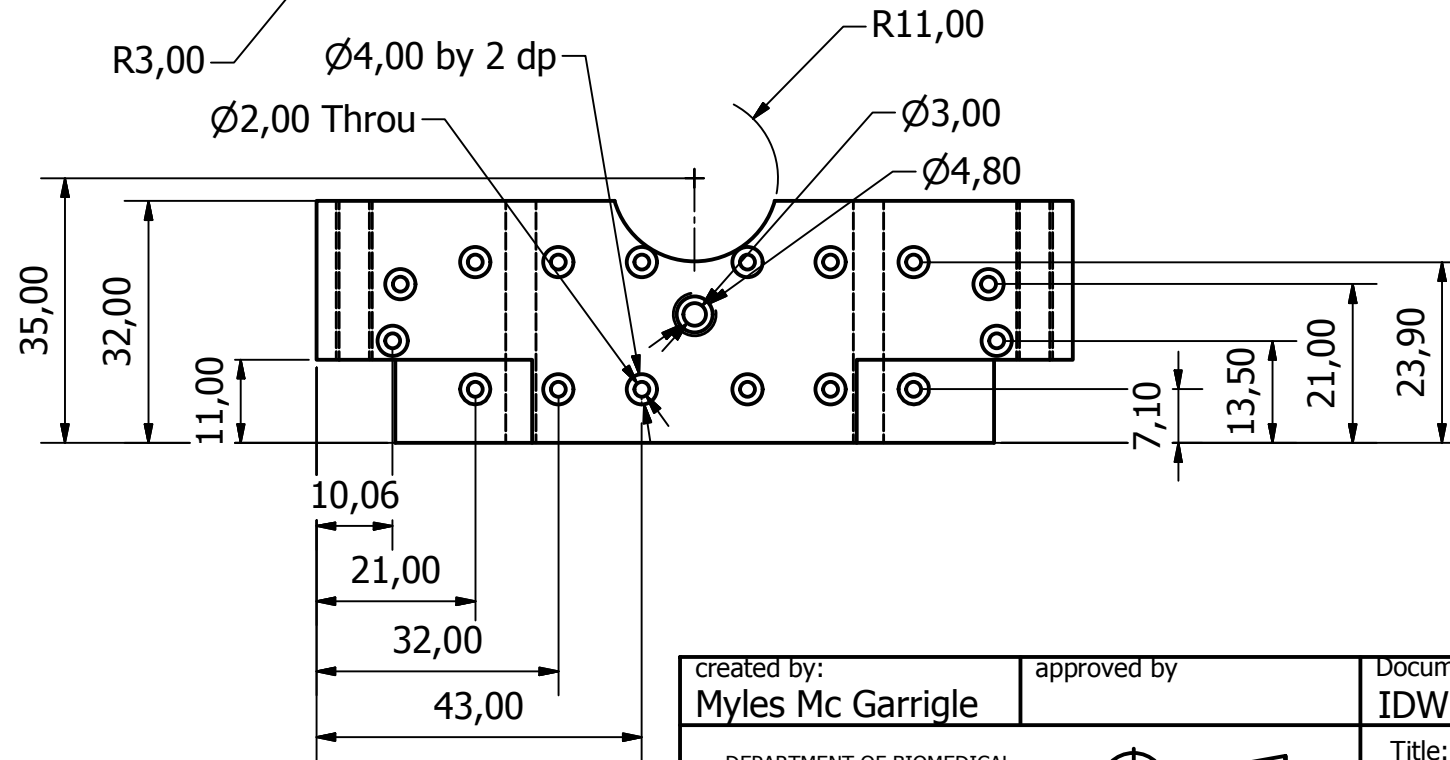
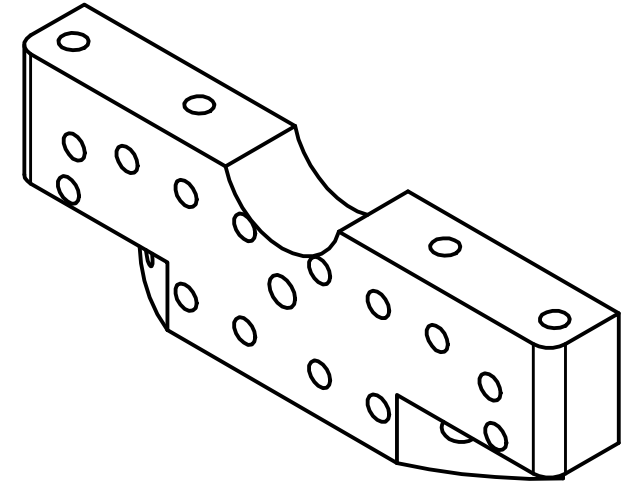
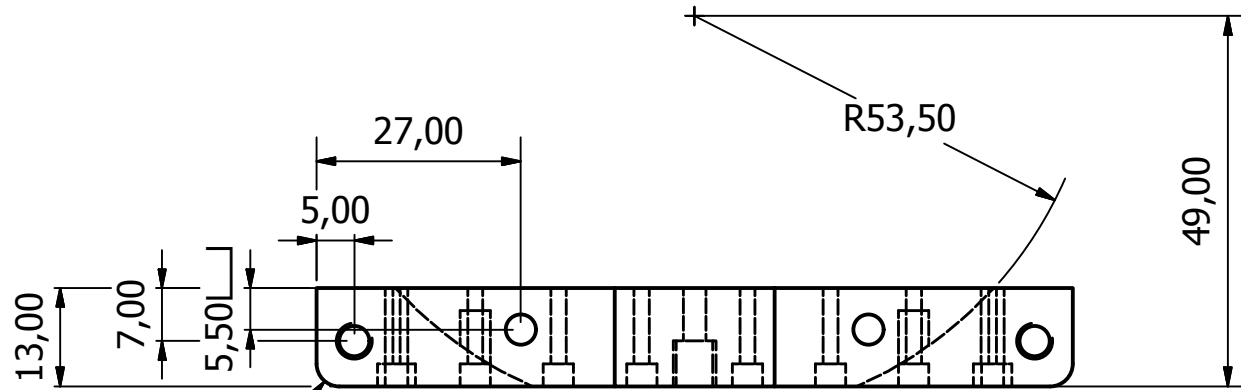
created by: Myles Mc Garrigle	approved by	Document type IDW	ID 08307598
DEPARTMENT OF BIOMEDICAL ENGINEERING	 	Title: CPB-16-7-P (OutletFlowGeometry)	Scale: 2:1
All dimensions in mm	Date 19/04/2016	Sheet: 1 of 1	Drawing no. CPB-16-7-P

Material: Polycarbonate

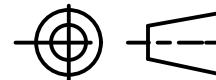


created by: Myles Mc Garrigle	approved by	Document type IDW	ID 08307598
DEPARTMENT OF BIOMEDICAL ENGINEERING		Title: CPB-16-8-P (BioreactorChamberLidInlet)	
 		Scale: 1:1	Sheet: 1 of 1
		All dimensions in mm	
Date 01/07/2015		Drawing no. CPB-16-8-P	

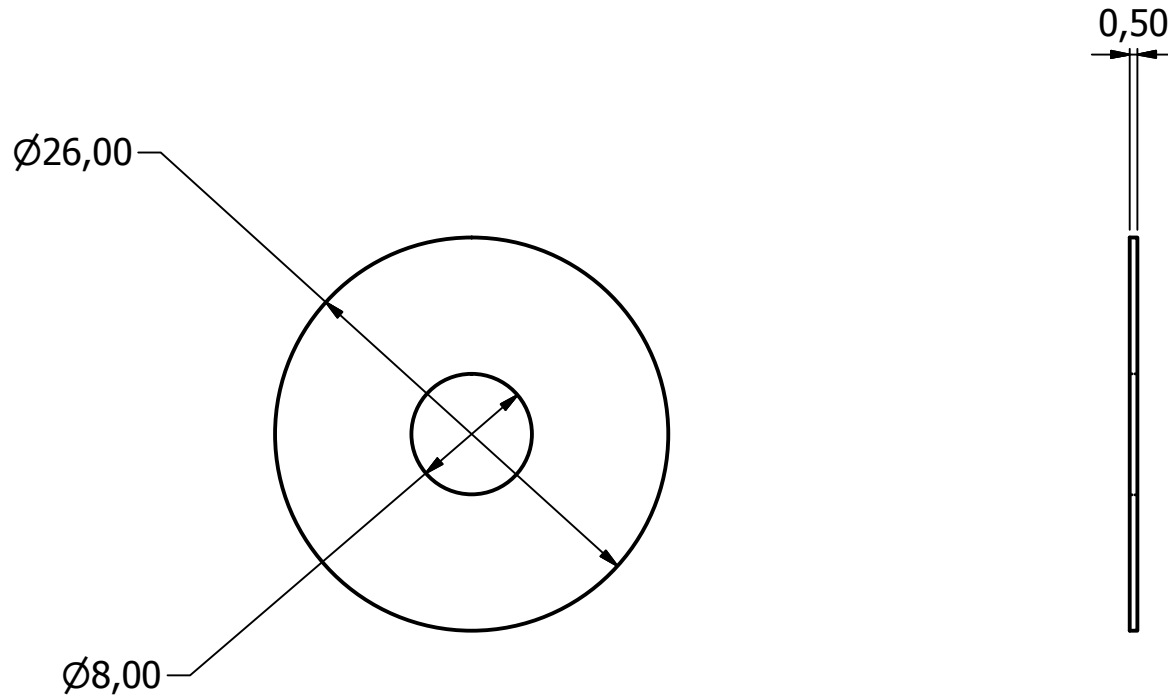
Material: Polycarbonate

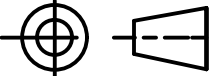


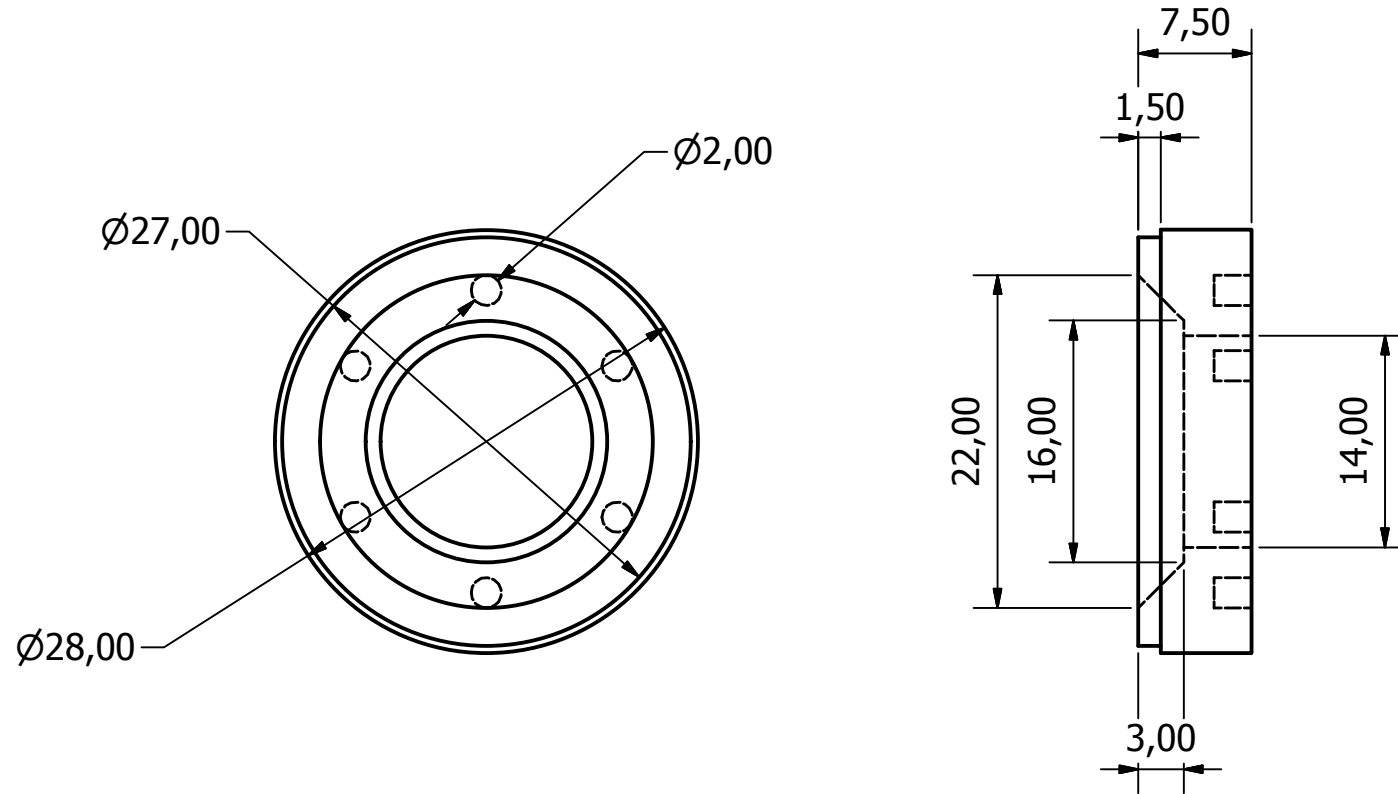
created by: Myles Mc Garrigle	approved by	Document type IDW	ID 08307598
DEPARTMENT OF BIOMEDICAL ENGINEERING		Title: CPB-16-9-P (BioreactorChamberLidOutlet)	
		Scale: 1:1	Sheet: 1 of 1
All dimensions in mm		Date 01/07/2015	Drawing no. CPB-16-9-P



Material: Silicon Shore Hardness A60

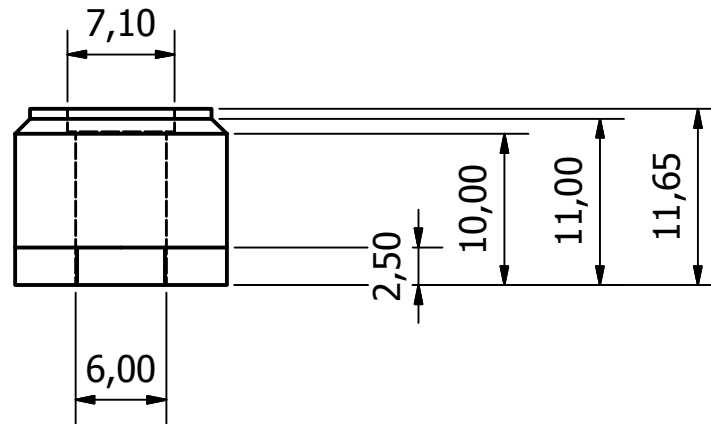
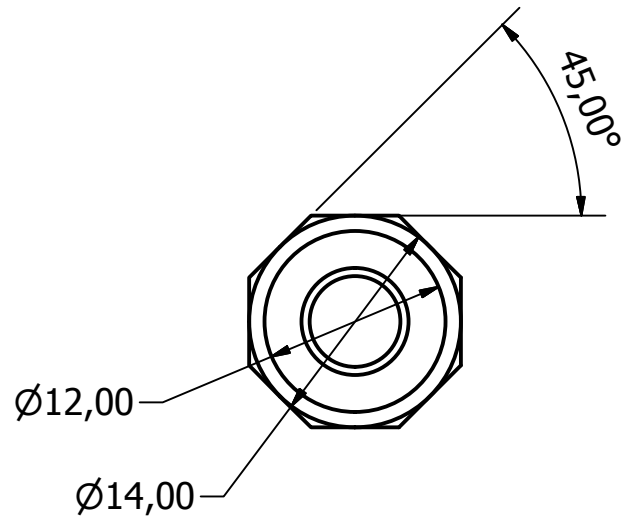


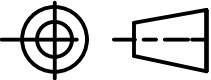
created by: Myles Mc Garrigle	approved by	Document type IDW	ID 08307598
DEPARTMENT OF BIOMEDICAL ENGINEERING		Title: CPB-16-10-P (DiaphragmSeal)	
		Scale: 2:1	Sheet: 1 of 1
All dimensions in mm	Date 06/01/2013	Drawing no. CPB-16-10-P	



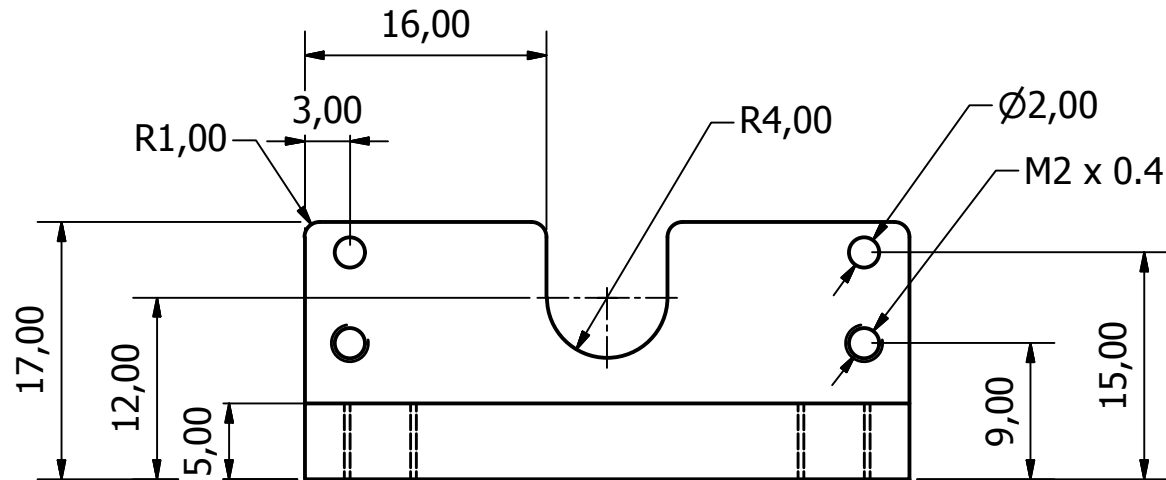
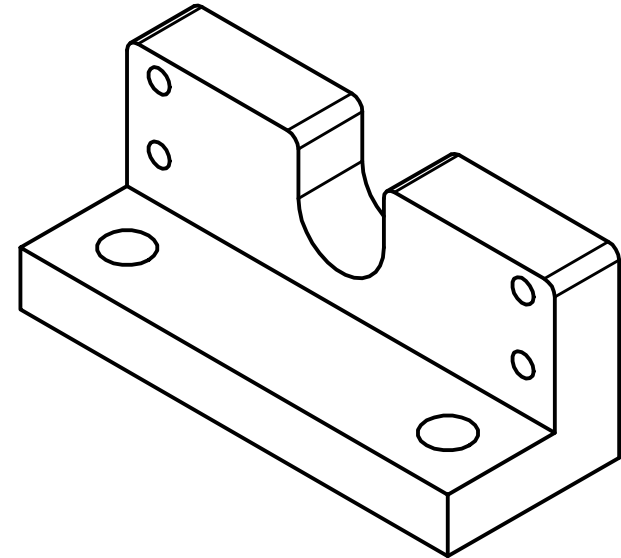
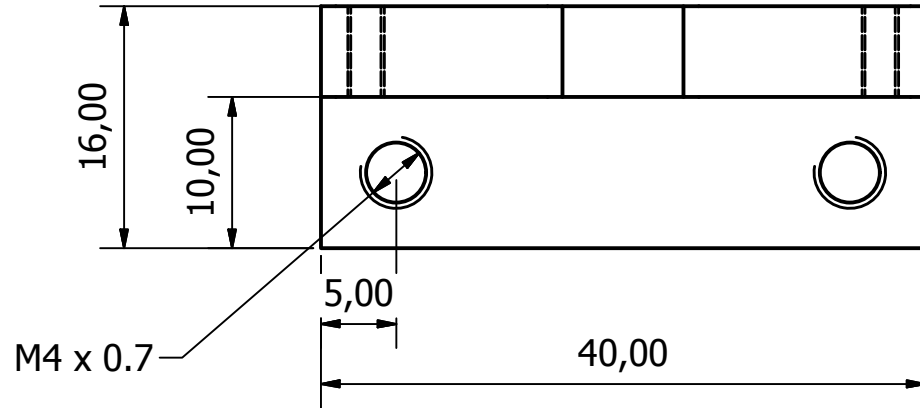
created by: Myles Mc Garrigle	approved by	Document type IDW	ID 08307598
DEPARTMENT OF BIOMEDICAL ENGINEERING		Title: CPB-16-11-P (DiaphragmClampExternal)	
		Scale: 2:1	Sheet: 1 of 1
All dimensions in mm	Date 09/07/2013	Drawing no. CPB-16-1-P	

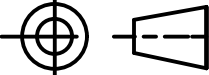
Material: Polycarbonate



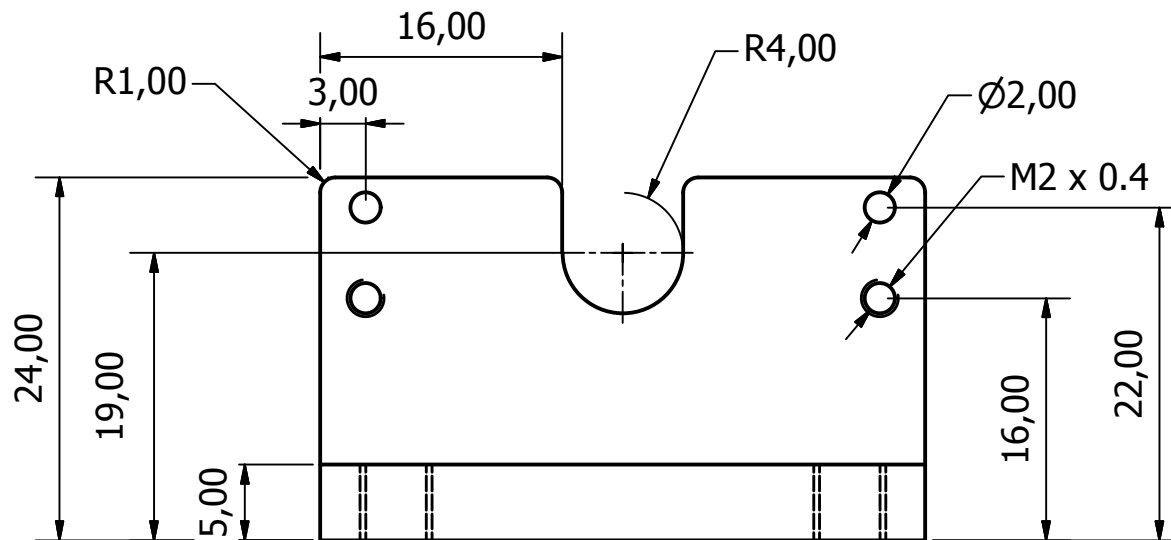
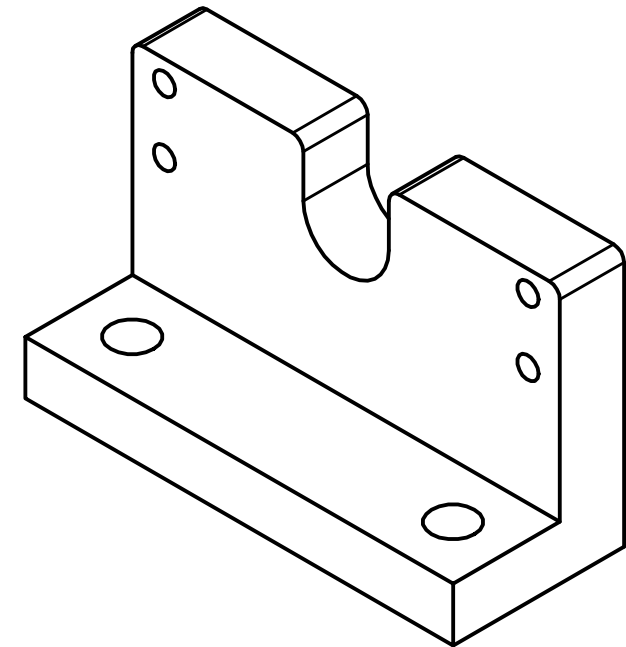
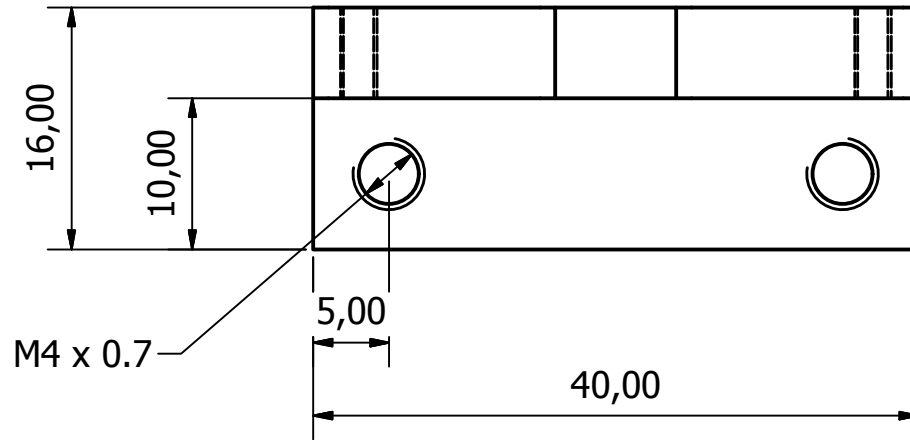
created by: Myles Mc Garrigle	approved by	Document type IDW	ID 08307598
DEPARTMENT OF BIOMEDICAL ENGINEERING		Title: CPB-16-12-P (DiaphragmClampInternal)	Scale: 2:1
All dimensions in mm		Date 09/07/2013	Sheet: 1 of 1
			Drawing no. CPB-16-12-P

Material: Aluminium

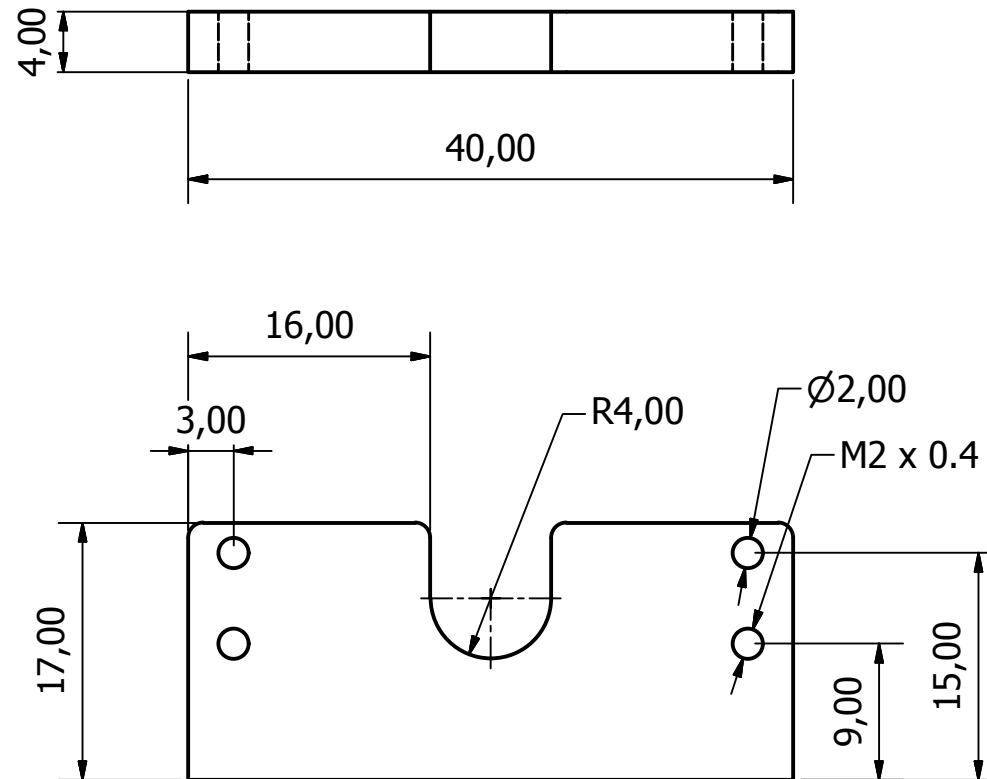


created by: Myles Mc Garrigle	approved by	Document type IDW	ID 08307598
DEPARTMENT OF BIOMEDICAL ENGINEERING		Title: CPB-16-13-P (CompressionArmBrakeDynamic)	Scale: 2:1
All dimensions in mm		Date 08/07/2015	Sheet: 1 of 1
Drawing no. CPB-16-13-P			

Material: Aluminium

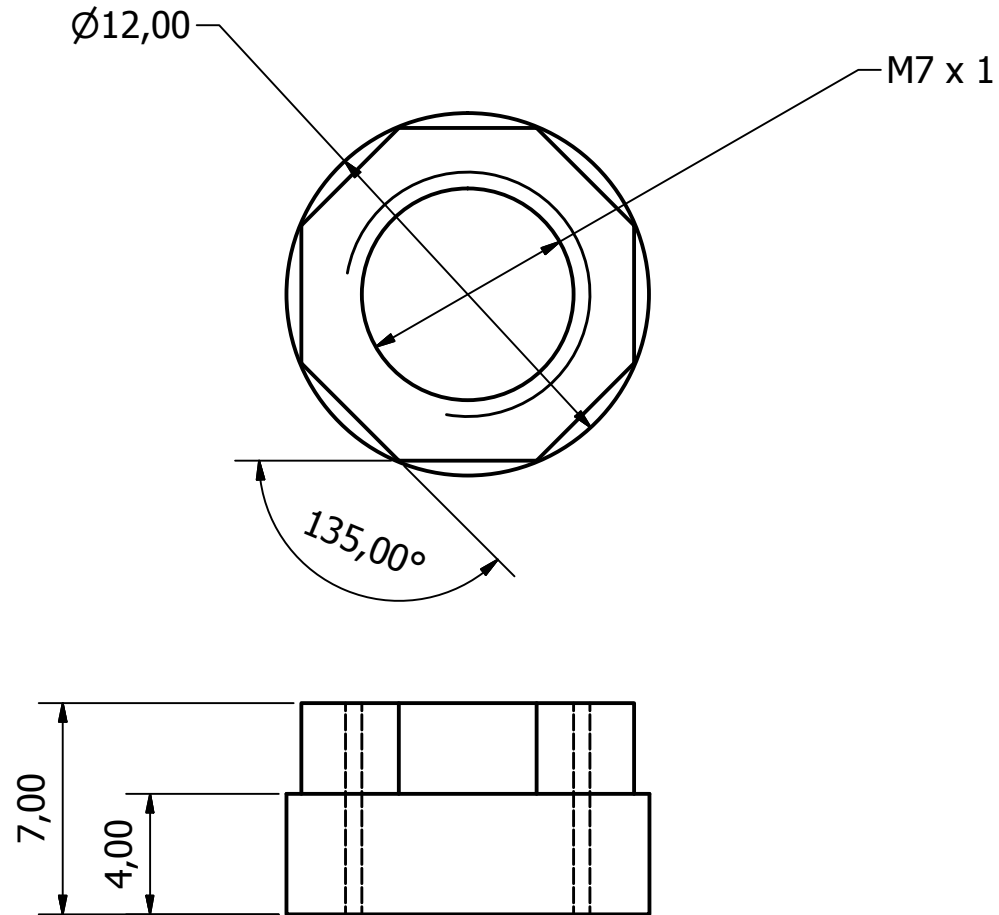


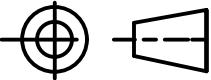
created by: Myles Mc Garrigle	approved by	Document type IDW	ID 08307598
DEPARTMENT OF BIOMEDICAL ENGINEERING		Title: CPB-16-14-P (CompressionArmBrakeDynamic2)	
		Scale: 2:1	Sheet: 1 of 1
All dimensions in mm		Date 08/07/2015	Drawing no. CPB-16-1-P



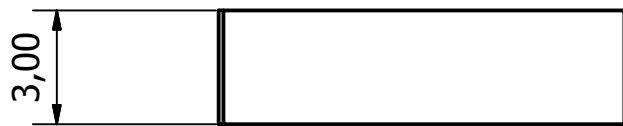
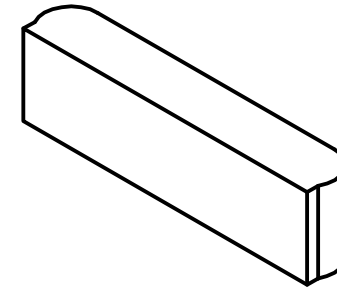
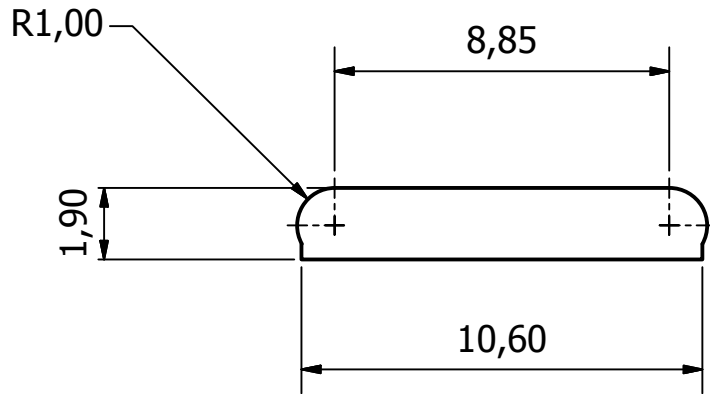
created by: Myles Mc Garrigle	approved by	Document type IDW	ID 08307598
DEPARTMENT OF BIOMEDICAL ENGINEERING		Title: CPB-16-15-P (CompressionArmBrakeStatic)	
		Scale: 1:2	Sheet: 1 of 1
All dimensions in mm	Date 07/11/2016	Drawing no. CPB-16-15-P	

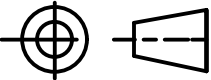
Material: Polycarbonate



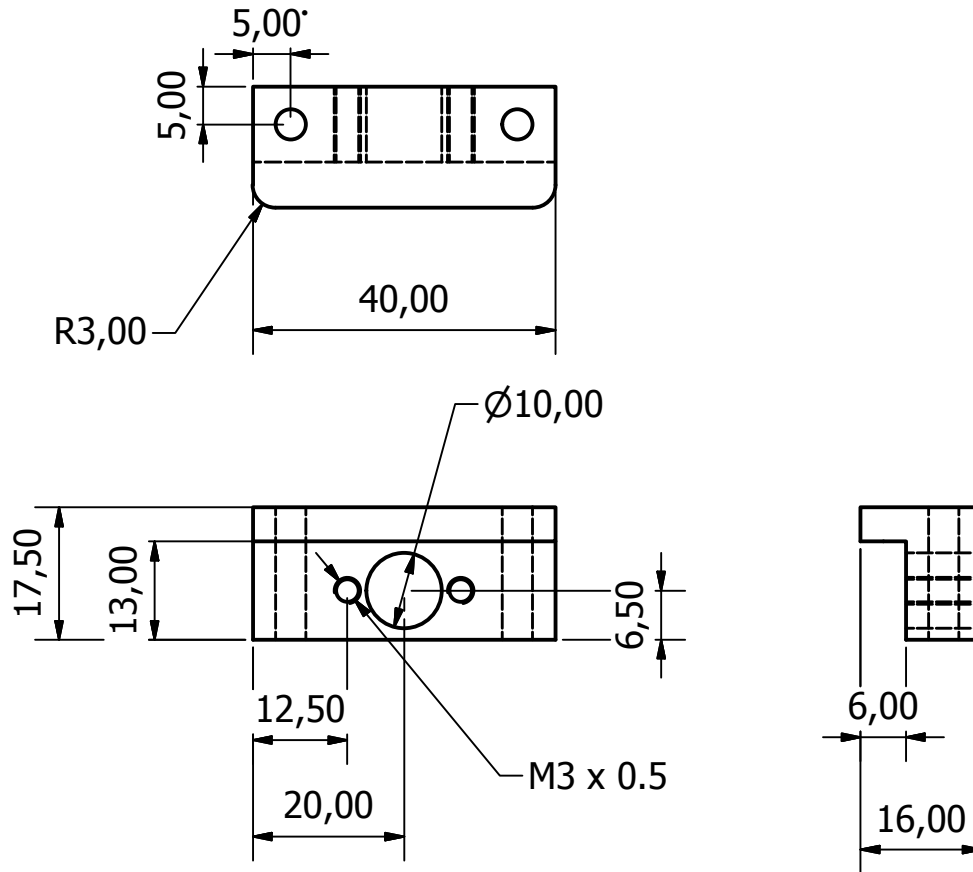
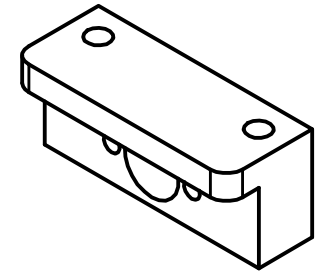
created by: Myles Mc Garrigle	approved by	Document type IDW	ID 08307598
DEPARTMENT OF BIOMEDICAL ENGINEERING		Title: CPB-16-16-P (CompressionArmPistonBolt)	Scale: 4:1
All dimensions in mm	Date 09/07/2013	Sheet: 1 of 1	
		Drawing no. CPB-16-16-P	

Material: Stainless steel 316L



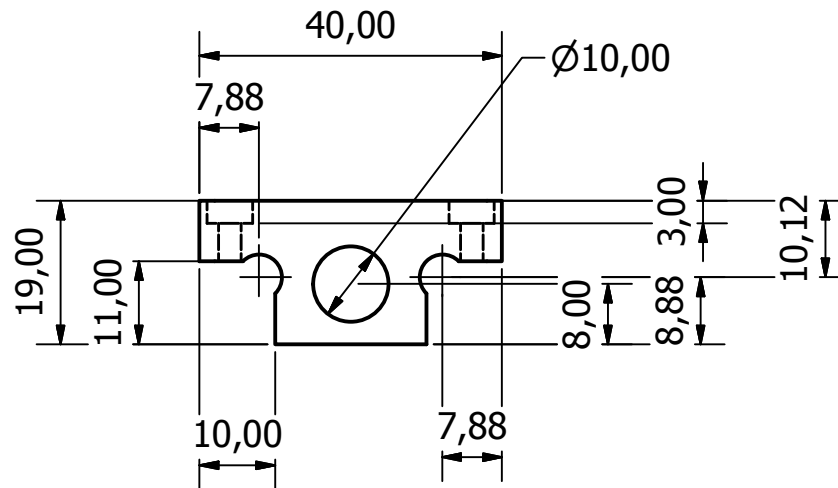
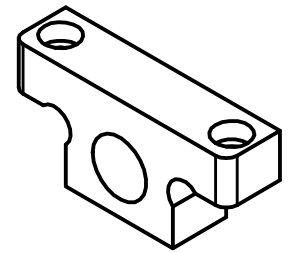
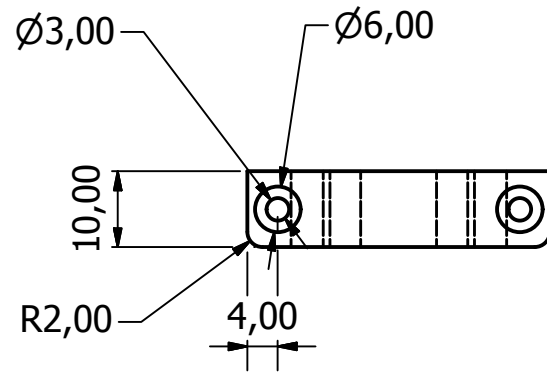
created by: Myles Mc Garrigle	approved by	Document type IDW	ID 08307598
DEPARTMENT OF BIOMEDICAL ENGINEERING		Title: CPB-16-17-P (CompressionPlatenPorous(Sintered))	
All dimensions in mm		Scale: 5:1	Sheet: 1 of 1
Date 05/05/2015		Drawing no. CPB-16-1-P	

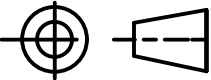
Material: Aluminium



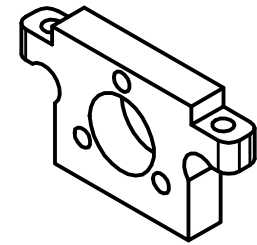
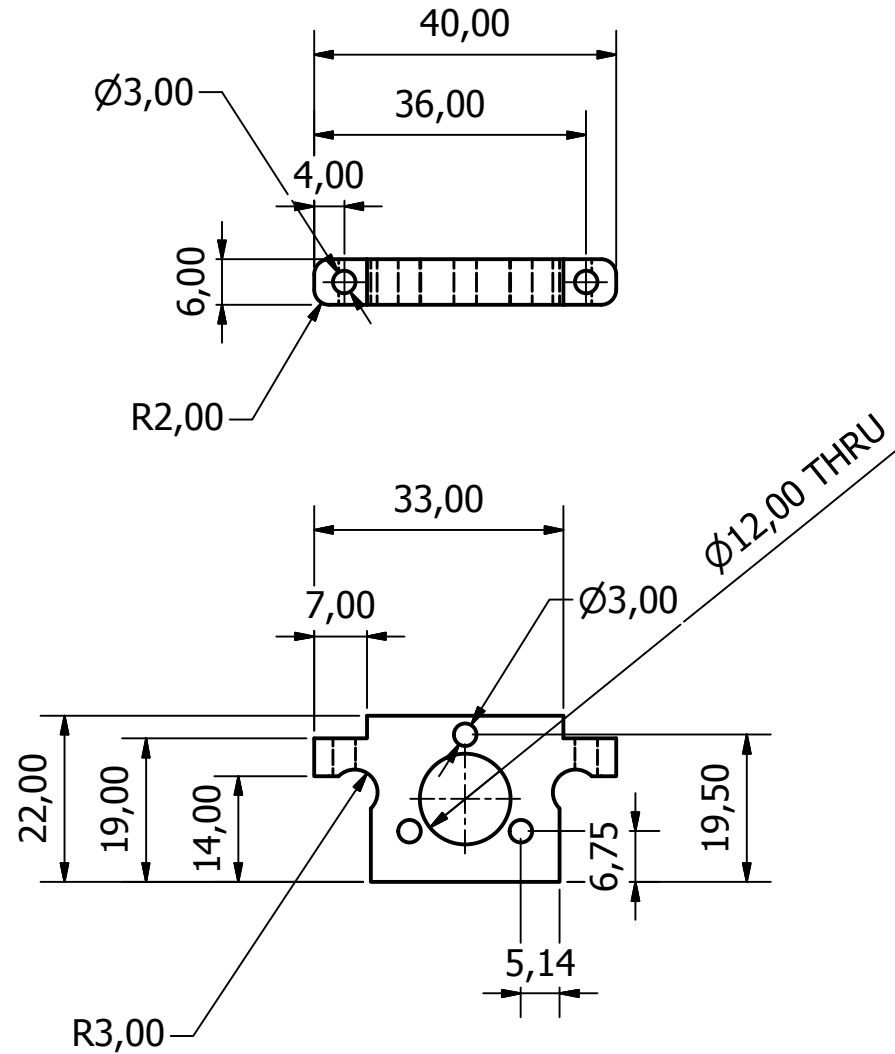
created by: Myles Mc Garrigle	approved by	Document type IDW	ID 08307598
DEPARTMENT OF BIOMEDICAL ENGINEERING		Title: CPB-16-18-P (PowerscrewMountDyanmic)	
		Scale: 1:2	Sheet: 1 of 1
All dimensions in mm	Date 08/07/2015	Drawing no. CPB-16-18-P	

Material: Aluminium



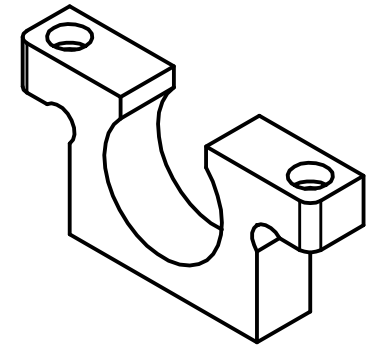
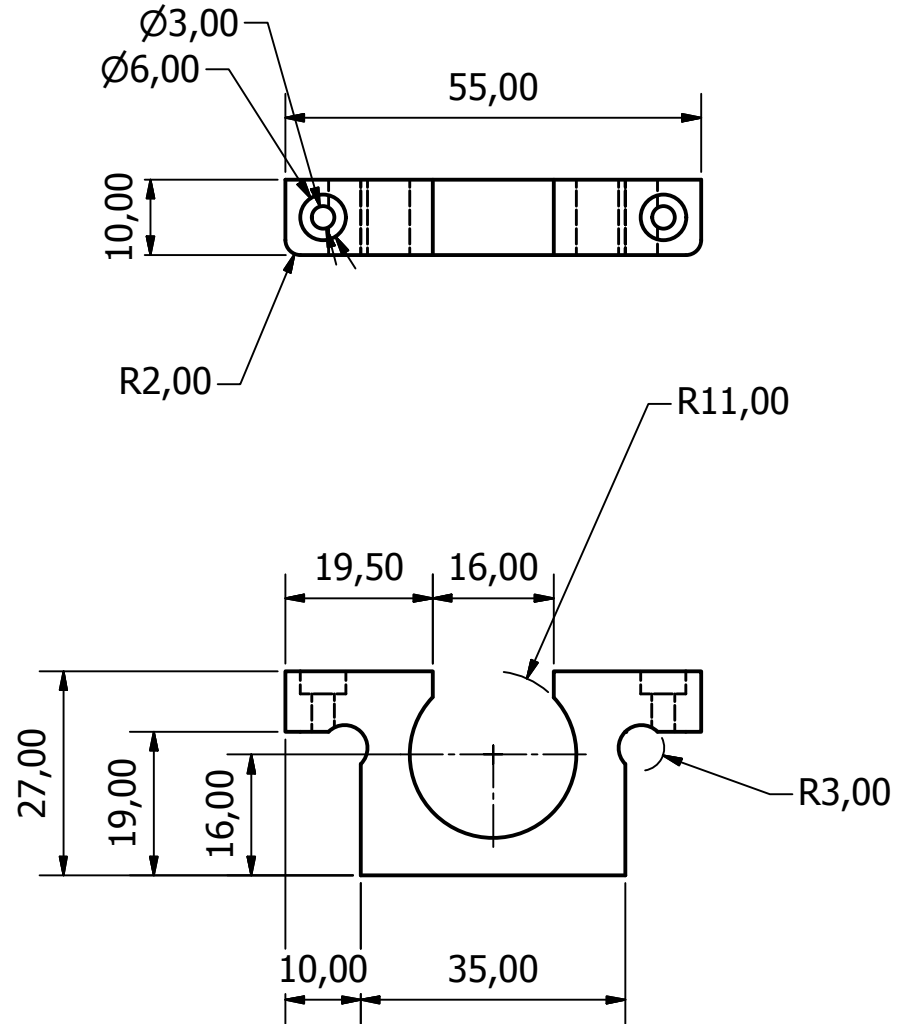
created by: Myles Mc Garrigle	approved by	Document type IDW	ID 08307598
DEPARTMENT OF BIOMEDICAL ENGINEERING		Title: CPB-16-19-P(PowerscrewMountSupport)	Scale: 1:1
All dimensions in mm		Date 29/08/2015	Sheet: 1 of 1
			Drawing no. CPB-16-19-P

Material: Aluminium



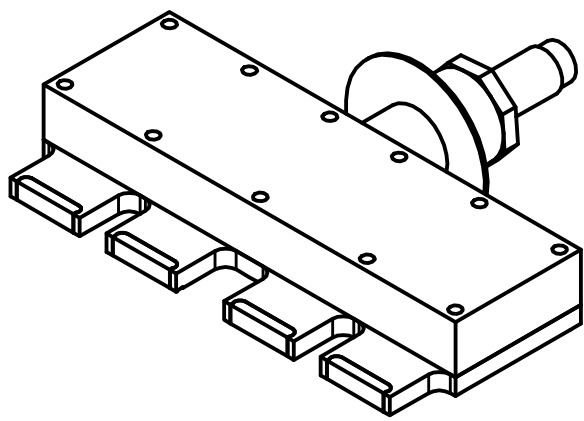
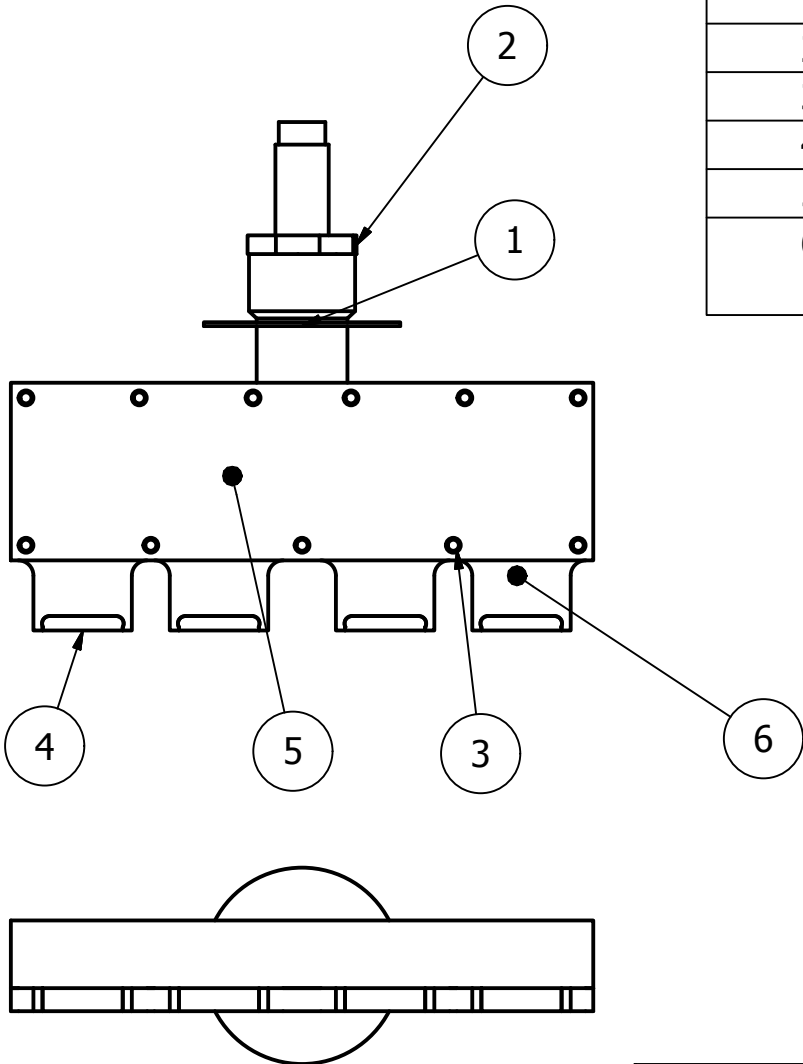
created by: Myles Mc Garrigle	approved by	Document type IDW	ID 08307598
DEPARTMENT OF BIOMEDICAL ENGINEERING		Title: CPB-16-20-P (GearMount)	
		Scale: 1:1	Sheet: 1 of 1
All dimensions in mm		Date 28/08/2015	Drawing no. CPB-16-20-P

Material: Aluminium

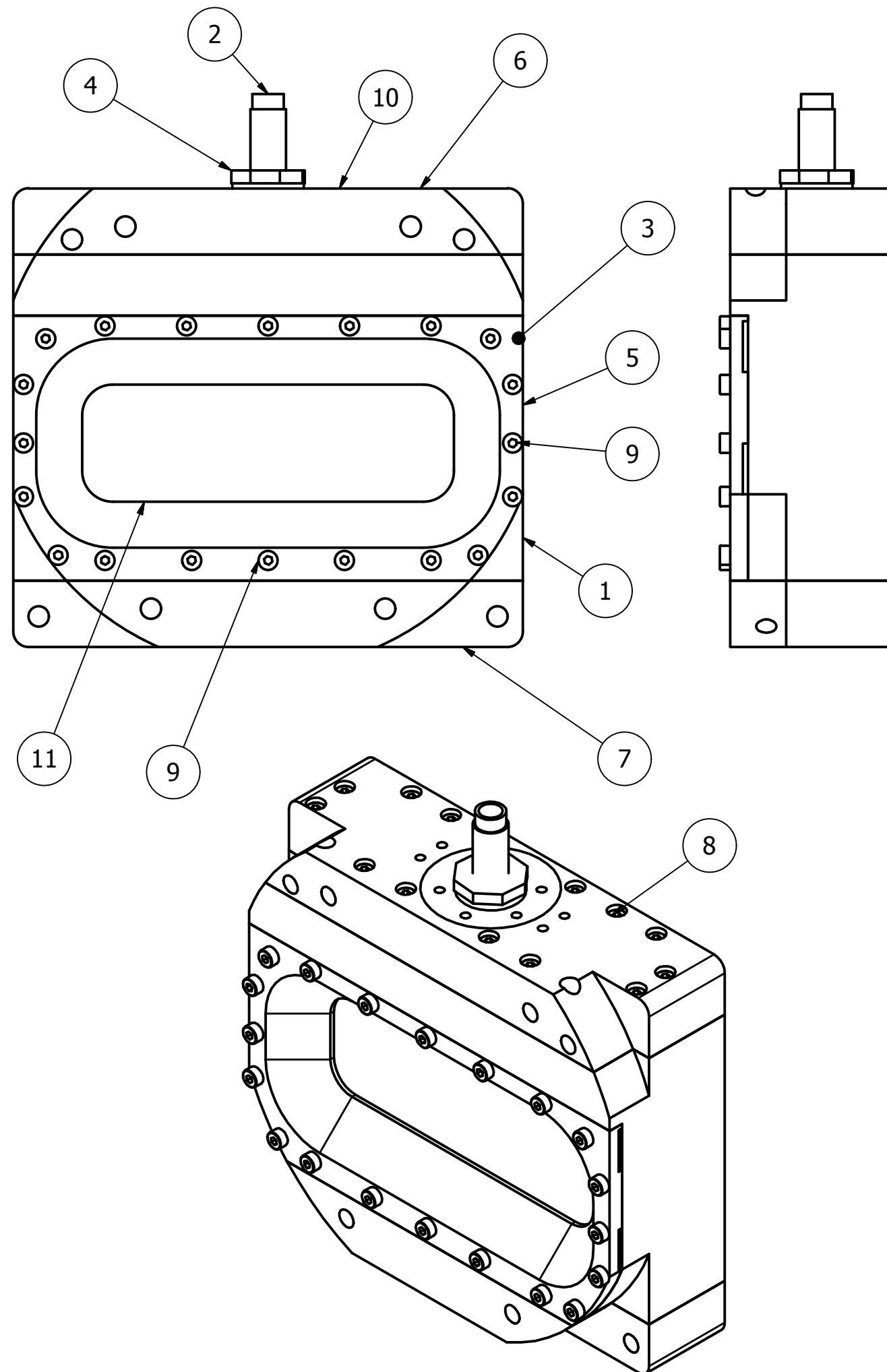


created by: Myles Mc Garrigle	approved by	Document type IDW	ID 08307598
DEPARTMENT OF BIOMEDICAL ENGINEERING		Title: CPB-16-21-P (MotorMount)	
		Scale: 1:1	Sheet: 1 of 1
All dimensions in mm	Date 28/08/2015	Drawing no. CPB-16-21-P	

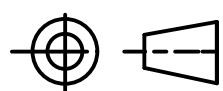
PARTS LIST			
ITEM	QTY	PART NUMBER	DESCRIPTION
1	1	CPB-16-10-P	Diaphragm seal
2	1	CPB-16-12-P	DiaphragmClampInternal
3	11	DIN 963 - M2 x 10	Countersunk Screw
4	4	CPB-16-17-P	CompressionPlatenPorous(Sintered)
5	1	CPB-16-3-P	MultiCompressionPlaten
6	1	CPB-16-2-P	MultiCompressionPlaten4Channel

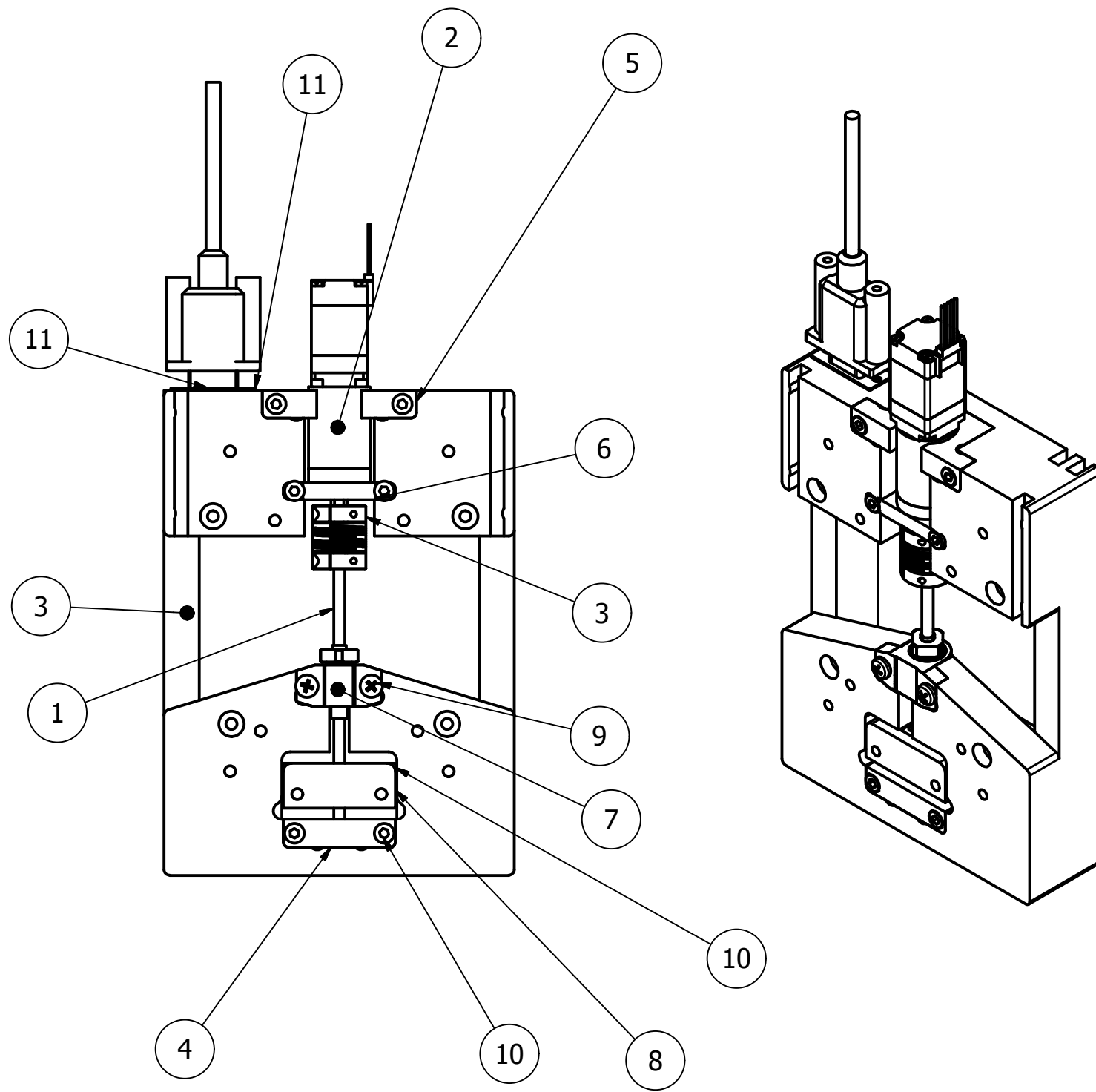


created by: Myles Mc Garrigle	approved by	Document type IDW	ID 08307598
DEPARTMENT OF BIOMEDICAL ENGINEERING		Title: CPB-16-1-SA (CompressionChamberPlaten)	
		Scale: 1:1	Sheet: 1 of 1
All dimensions in mm		Date 14/12/2014	Drawing no. CPB-16-1-SA



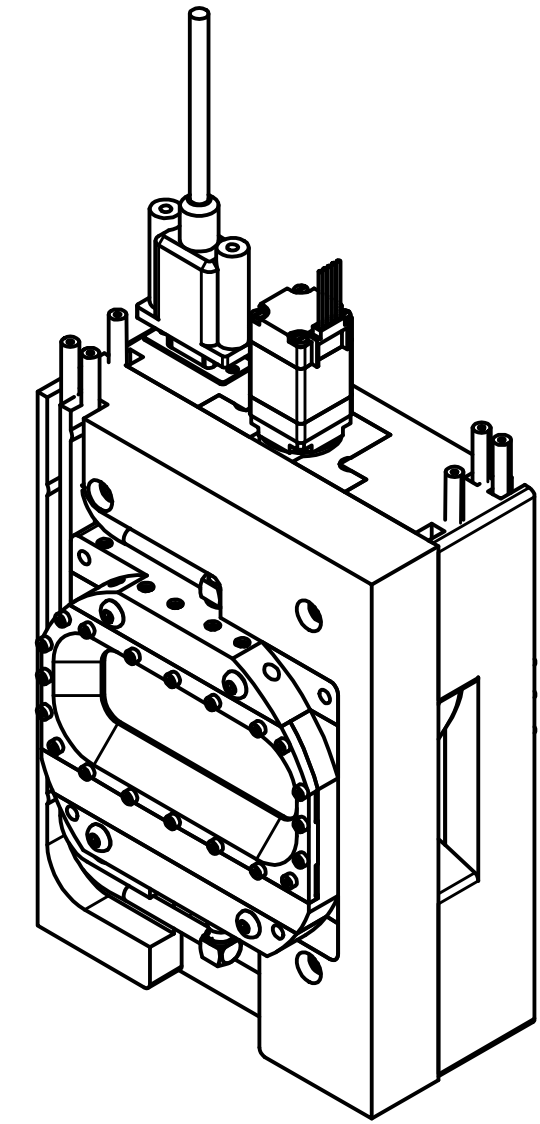
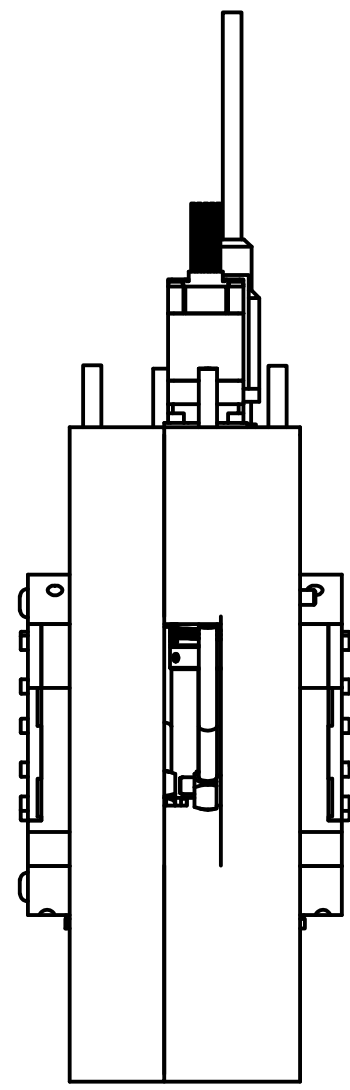
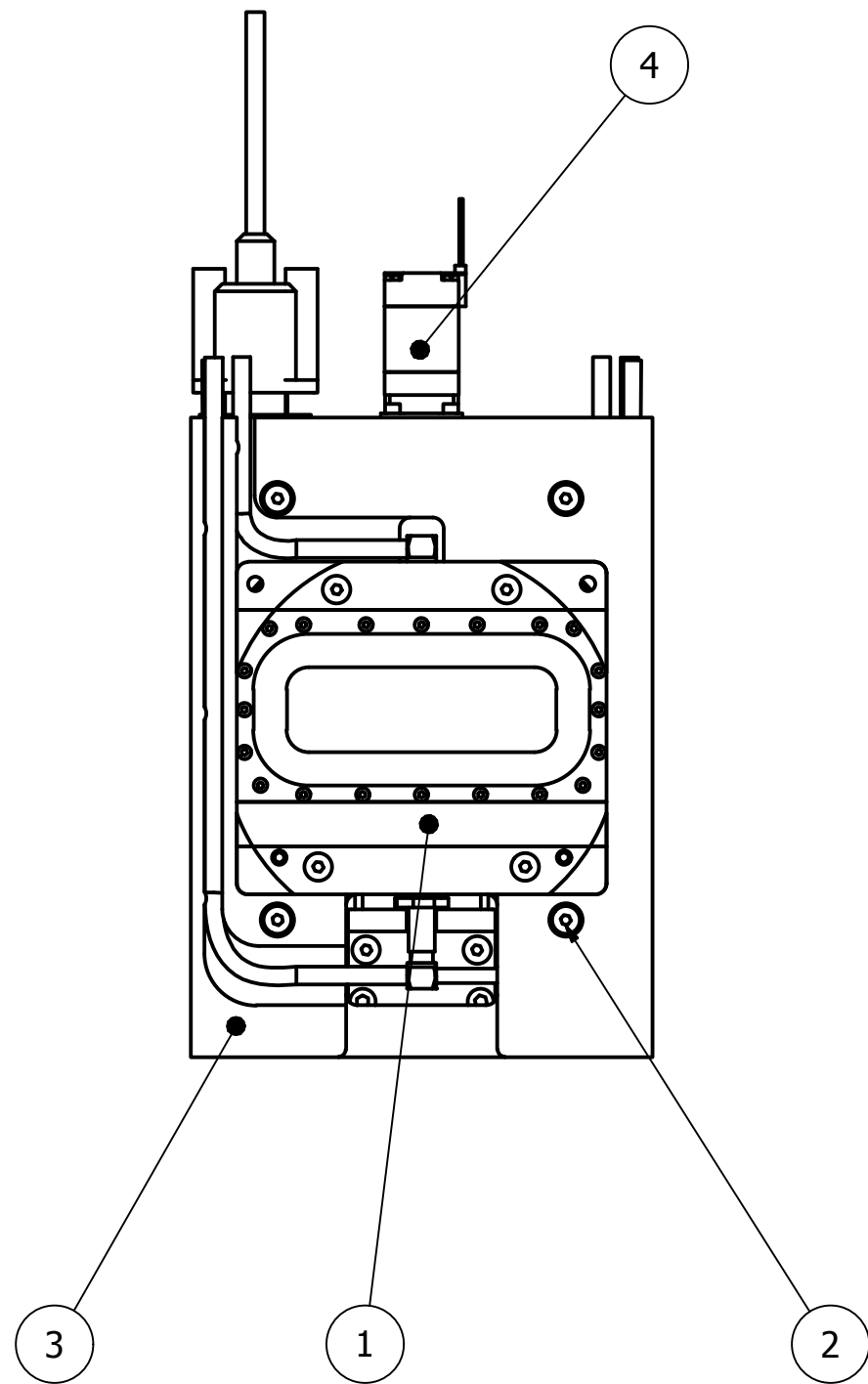
PARTS LIST			
ITEM	QTY	PART NUMBER	DESCRIPTION
1	1	CPB-16-1-P	BioreactorChamber
2	1	CPB-16-4-P	ObjectiveViewWindow
3	4	CPB-16-5-P	TopViewWindow
4	1	CPB-16-6-P	TopWindowTransDisk
5	1	CPB-16-7-P	OutletFlowGeometry
6	1	CPB-16-8-P	BioreactorChamberLidInlet
7	4	CPB-16-9-P	BioreactorChamberLidOutlet
8	28	ISO 4762 - M2 x 16	Hexagon Socket Head Cap Screw
9	24	ISO 4762 - M2 x 8	Hexagon Socket Head Cap Screw
10	1	CPB-16-11-P	DiaphragmClampExternal
11	1	CPB-16-24-P	Glass Silde Window

created by: Myles Mc Garrigle	approved by	Document type IDW	ID 08307598
DEPARTMENT OF BIOMEDICAL ENGINEERING		Title: 1:1	Sheet: 1 of 1
All dimensions in mm	Date 18/08/2015	Scale: 1:2	Drawing no. CPB-16-1-P



PARTS LIST			
ITEM	QTY	PART NUMBER	DESCRIPTION
1	1		BallscrewAssembly
2	1		Motor&GearAssembly
3	1	CPB-16-22-P	CompressionFrame
4	1	CPB-16-19-P	PowerscrewMountSupport
5	1	CPB-16-21-P	MotorMount
6	1	CPB-16-20-P	GearMount
7	1		FixedBearing
8	1	CPB-16-18-P	PowerscrewMountDynamic
9	2	ISO 7045 - M4 x 14 - 4.8 - H	Pan head screw with type H cross recess - product grade A
10	6	ISO 4762 - M4 x 20	Hexagon Socket Head Cap Screw
11	2	9-PinMaleConnector	
12	1	9-PinMaleConnectorCover	
13	4	DIN 963 - M2 x 10	Countersunk Screw
14	1	ANSI B27.7 - 3	General Purpose Tapered and Reduced Cross Section Retaining Rings - E-Ring External Series 3CM1 Retaining Rings

created by: Myles Mc Garrigle	approved by	Document type IDW	ID 08307598
DEPARTMENT OF BIOMEDICAL ENGINEERING		Title: CPB-16-3-SA (Compression Rig Assembly)	
All dimensions in mm		Scale: 1:2	Sheet: 1 of 1
Date 12/08/2015		Drawing no. CPB-16-3-SA	



PARTS LIST			
ITEM	QTY	PART NUMBER	DESCRIPTION
1	2	CPB-16-5-SA	Perfusion Chamber Assembly
2	14	ANSI B18.3.4M - M4 x 0.7 x 35	Broached Hexagon Socket Button Head Cap Screw - Metric
3	1	CPB-16-6-SA	Compression Rig Assembly
4	1		Geared Stepper Motor

created by: Myles Mc Garrigle	approved by	Document type IDW	ID 08307598
DEPARTMENT OF BIOMEDICAL ENGINEERING		Title: CPB-17-1-A(Full Assembly)	
All dimensions in mm		Scale: 1:2	Sheet: 1 of 1
		Date 12/08/2015	Drawing no. CPB-16-1-P